

Czech Technical University in Prague
Faculty of Electrical Engineering

Doctoral Thesis

December 2022

Václav Grim

Czech Technical University in Prague

Faculty of Electrical Engineering
Department of Measurement

***OPTIMIZATION OF MAGNETIC
SENSORS***

Doctoral Thesis

Václav Grim

Prague, December 2022

Ph.D. Programme: Electrical Engineering and Information Technology P2612
Branch of study: Measurement and Instrumentation 2601V006

Supervisor: *Pavel Ripka*
Supervisor-Specialist: *Vojtěch Petrucha*

Abstract

Sensors of magnetic field are able to, directly or indirectly, measure a broad range of physical quantities such as pressure, displacement or electric current. This dissertation focuses on application in three principal categories: wire-based sensors, position and speed sensors, and current sensors. Original research papers, both theoretical and experimental, are presented with additional explanatory text, together with literature review that mentions the most remarkable achievements in similar fields of research published in recent years.

The research led to several noteworthy results in the field of contactless current sensors: the Rogowski coil with composite core provides high sensitivity and low noise, extending its use case down to moderate currents of tens of Amperes. Another interesting innovation is the single-winding closed-loop fluxgate current sensor, which provides low energy consumption and greatly reduced complexity of the magnetic circuit.

Anotace

Senzory magnetického pole lze využít k přímým či nepřímým měřením mnoha fyzikálních veličin, např. tlaku, výchylky, úhlu či elektrického proudu. Tato disertace se zabývá senzory založenými na magnetických mikro- a nanodrátech, senzory polohy a rychlosti a bezkontaktními senzory elektrického proudu. Původní výzkum je zde prezentován ve formě publikovaných článků doplněných vysvětlujícím textem. V každé kapitole je rovněž uveden přehled nejzajímavějších světových publikací z poslední doby, zabývajících se podobnou problematikou a na něž vlastní výzkum navazoval.

Výsledkem výzkumu bylo několik vylepšení existujících principů bezkontaktního měření elektrického proudu. Rogovského cívky s kompozitním jádrem dosahují vyšší citlivosti a nižšího šumu ve srovnání se standardním uspořádáním, čímž je umožněno jejich nasazení do aplikací pracujících s nižšími proudy v řádu desítek Ampérů. Druhým významným výsledkem byla konstrukce zpětnovazebního fluxgate proudového senzoru s jedním vinutím, jenž se vyznačuje snadnou výrobou magnetického obvodu a nízkou spotřebou energie.

Klíčová slova

senzor, magnetické pole, magnetometr, inverzní úloha, měření elektrického proudu, nanostruktura, fluxgate, metoda konečných prvků

Keywords

sensor, magnetic field, magnetometer, inverse problem, electric current measurement, nanostructure, fluxgate, finite element method

Declaration

I hereby declare that the presented thesis is my own work and that I have cited all sources of information in accordance with the Guideline for adhering to ethical principles when elaborating an academic final thesis.

I acknowledge that my thesis is subject to the rights and obligations stipulated by the Act No. 121/2000 Coll., the Copyright Act, as amended, in particular that the Czech Technical University in Prague has the right to conclude a license agreement on the utilization of this thesis as a school work under the provisions of Article 60 (1) of the Act.

Prague on December 20, 2022

.....

Contents

1	Introduction	1
2	State of the Art	3
2.1	Wire-based Sensors and Wire Arrays	3
	Theoretical Works Regarding Wire Arrays	3
	Magnetic Microwire Manufacturing and Characterization	3
	Applications of Ferromagnetic Microwires	3
	Magnetic Nanowire Manufacturing	4
	Applications of Nanowires	4
2.2	Position and Speed Sensors	5
	Inductance-based Linear Position Sensors	5
	Linear Variable Differential Transformers	5
	Other Types of Transformer-based Linear Sensor	5
	Wiegand Sensors	6
	Applications Regarding Hydraulic and Pneumatic Cylinders	6
	Applications in Drilling	7
2.3	Current Sensors	8
	Current Transformers	8
	Magneto-Optical Current Sensors	9
	Magnetostrictive and Piezoelectric Current Sensors	9
	Yokeless Circular Sensor Arrays	10
	Rogowski Coils and Induction Sensors	11
3	Thesis objectives	13
4	Magnetic material modeling and nanowire-based sensors	15
4.1	Modelling and Measurement of Magnetically Soft Nanowire Arrays for Sensor Applications	16
4.2	The apparent permeability and the amplification factor of magnetic wires and wire arrays	34
4.3	A Simplified 2D Equivalent Model for Magnetic Wire Array	43
4.4	Multiwire Parallel Fluxgate Sensors	49
5	Position and speed sensors	55
5.1	Design and Modeling of a Linear Speed Sensor with a Flat Type Structure and Air Coils	56
5.2	A Position Sensor with Novel Configuration of Linear Variable Differential Transformer	67
5.3	An Axial Airgap Eddy Current Speed Sensor	77
6	Current Sensors	89
6.1	Rogowski Coil with Ferromagnetic Powder Core	90
6.2	Self-oscillating DC Current Transformer with Nanocrystalline Core	95
6.3	DC Current Sensor Using Switching-Mode Excited In-situ Current Transformer	100
6.4	A Busbar Current Sensor with Frequency Compensation	107
6.5	A 3-Phase Current Transducer Based on Microfluxgate Sensors	113
6.6	Characterization of circular array current transducers	120

Contents

7	List of all co-authored publications	127
7.1	Publications in Impacted Journals	127
7.2	Publications in Conference Proceedings	128
8	Conclusion	131
8.1	Review of Objective Fulfillment	131
8.2	Suggestions for Further Research	132
9	References	133

1 Introduction

This thesis is a collection of research papers on which I participated during my studies at the Department of Measurement. It covers a broad range of topics related to magnetic materials, low-frequency magnetic measurements and construction of electronic devices and instruments. It is divided into three sections, each of them revolving around one common topic.

Chapter 4 describes novel methods of magnetic material modeling which were used to calculate demagnetization factors of nanowire arrays containing millions of wires. The manufacturing and measurement of such arrays is also a part of this section.

Chapter 5 is devoted to the design and modeling of novel position and speed magnetic sensors, based on differential inductance between multiple excitation and pickup windings.

The earliest papers related to current measurement eventually became the foundation for Chapter 6, containing two journal papers where I am the first and main author.

The aim of my efforts was simply to come up with a new type of magnetic sensor, different from everything else presented before, whose properties would constitute an improvement over the standards set by commercially available devices.

The search was initially not restricted to a particular class of sensors. Priority was given to application of novel design methodologies not available to previous generations of designers – rapid prototyping with 3D printers, detailed computer simulations, or real-time data processing with microprocessors.

Eventually the scope was narrowed down to position sensors and non-contact current sensors, in particular fluxgate-based current sensors and Rogowski coils with ferromagnetic core.

2 State of the Art

2.1 Wire-based Sensors and Wire Arrays

Theoretical Works Regarding Wire Arrays

A detailed study of demagnetization factor of single, isolated cylinder is given in [S1]. Analytical equations are provided together with pre-calculated values for different diameter-to-length ratios and different permeabilities. It is a macroscopic model, independent of the absolute size and the presence of magnetic domains. The same authors later amended the paper with a more detailed table of results [S2].

The modeling of the magnetization reversal is based on the Landau–Lifshitz–Gilbert equation, which is possible with micromagnetic simulation software (e.g. MAPGAR [S3]). The results for single, isolated wire of varying size and composition is presented in [S4]. This micromagnetic simulation was extended to quasi-infinite arrays of wires in [S5], where the relation between the anisotropy of each wire and the anisotropy of the whole array is investigated for different fill factors.

Magnetic Microwire Manufacturing and Characterization

Microwires are made by melting a mixture of high-purity metal powders by in-rotating-water spinning for massive wires ([S6], Fig. 1), or by glass-coated melt spinning, which produces wires embedded in non-conductive glass sheath ([S7], Fig. 2). The thinnest wires are made by glass-coated method, with diameters down to 185 nm (20 μm including the glass layer) [S8]. Additional manufacturing steps, e.g. annealing, are needed to obtain the required magnetic properties. Wires for GMI are annealed under mechanical stress (by applying weights) to maximize the magnetoimpedance effect [S9]. In the case of coil-less fluxgate sensors, the required anisotropy is created by the application of torsional stress during annealing [S10].

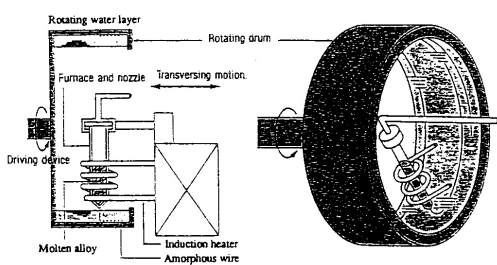


Figure 1: In-rotating-water spinning method principle [S6]

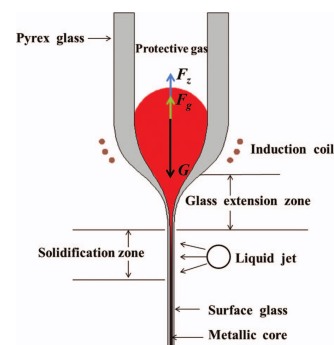


Figure 2: Glass-coated melt spinning method principle [S11]

Applications of Ferromagnetic Microwires

The most widely published application area of microwires at the moment of writing are giant magnetoimpedance (GMI) sensors. A chip-scale GMI sensor is presented in [S12], with microfabricated solenoidal coil around the wire. The coil is made by electrodeposition of copper into thick photoresist.

Another group of microwire sensors measure the domain wall propagation speed. The speed is dependent on mechanical stress, and a weight sensor can be built by embedding an array of microwires inside a block of concrete, with excitation and pickup windings loosely coupled from outside [S13].

Magnetic Nanowire Manufacturing

Nanowires are created by electrodeposition into a non-magnetic matrix. The electrolyte is a solution of metal salts, usually iron and nickel. In addition, the solution commonly contains boric acid as a pH buffer, citric acid as a complexing agent, saccharin as a grain refiner or ascorbic acid as an anti-oxidizer. Paper [S14] provides a detailed description of the deposition mechanism, as well as an overview of driving methods – DC, pulsed and reverse-pulsed. The deposition matrix is either a track-etched polycarbonate membrane made of solid sheet by heavy ion bombardment ([S15], Fig. 3) or an anodic alumina membrane ([S16], Fig. 4).

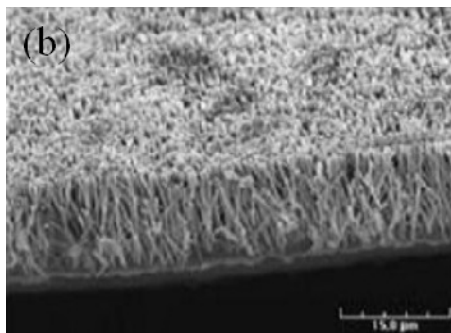


Figure 3: SEM photograph of a nanowire array deposited into track-etched membrane [S15]

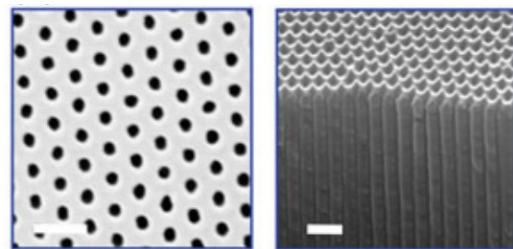


Figure 4: SEM photograph of an anodic alumina membrane (top view and cross section) [S17]

Applications of Nanowires

Nanowires can be made of thin, alternating layers of two different materials, and this structure is the base of the CPP-GMR (giant magnetoresistance, current perpendicular to the layer plane) effect ([S18], Fig. 5). There were attempts for using CPP-GMR nanowires in the read heads of magnetic data storage devices [S19].

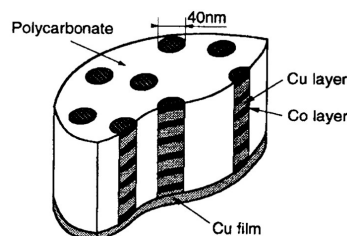


Figure 5: Cross section of a membrane with deposited multi-layer nanowires. In reality, their aspect ratio is much larger and they are not perpendicular to the surface [S18]

A completely different application field is the controlled destruction of cells within a body not by hyperthermia, but by mechanical ablation with nanowires spinning in externally generated magnetic field. The nanoscopic diameter of such wires allows them to simply dissolve after the treatment is over [S20].

2.2 Position and Speed Sensors

Inductance-based Linear Position Sensors

An overview of principles used in modern, industrial position sensors is given e.g. in [S21], with particular emphasis on inductive sensors and their associated circuitry. In order to achieve usable stability and temperature coefficient, inductive sensors usually use differential arrangement with at least two identical coils. Paper [S22] presents one possible solution with coplanar, side-by-side coils manufactured on a common PCB substrate. Inductive sensors detect both ferromagnetic and non-magnetic (paramagnetic) metals. Comparison of different materials used for sensor targets is given in [S23]. Aluminium is usually preferred over steel for its linearity and lack of hysteresis. The material of magnetic core is selected depending on the required precision and sensitivity. Air-cored coils do not suffer from temperature dependent permeability or hysteretic losses. Ferrite or other low-loss ferromagnetic material is used where high sensitivity is preferred over long-term stability. The geometry of a ferrite pot core is analyzed and optimized in [S24]. There have also been attempts to sense distance by measuring the self-inductance of a solenoidal coil with a movable ferromagnetic core [S25]. This particular design tries to improve linearity by gradually adjusting the pitch of the winding along its length.

Linear Variable Differential Transformers

LVDTs are traditionally used for high precision contact measurements, with accuracy under one micrometer. The classic cylindrical arrangement with one excitation coil in the center and two antiseriably connected pickup coils at the ends has been in use at least since 1946, when the design was published under its current name. Schematic diagram of a traditional LVDT is shown in Fig. 6. LVDTs are simple and rugged enough even for space applications, where the lifetime is limited only by the robustness of the associated electronic circuits [S26].

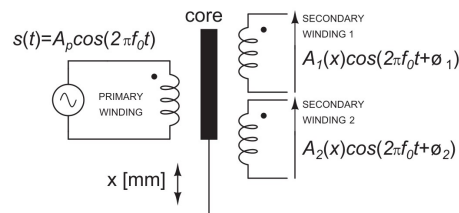


Figure 6: Schematic arrangement of the LVDT [S26]

To separate the effects of mutual inductance and core loss, a synchronous detector locked onto the primary current is used in high-performance applications. Either a physical synchronous rectifier [S27] or a synthetic rectifier working on sampled and digitized data [S28] is used.

The static transfer characteristic for a finite-length transducer is not perfectly linear. Compensation for “end effects” is done by digital post-processing [S29], or more exotically with an analog circuit, whose transfer function is inverse to the one of the sensor [S30].

Other Types of Transformer-based Linear Sensor

Sensors of this kind transform physical movement into changes in mutual inductance between an excitation coil and a pickup coil. Although only one pickup winding is needed in theory,

such sensor is robust enough only for the most simplistic applications [S31]. In real-world scenarios, at least two antiseriably connected windings are needed.

A noteworthy example of sensor based on the difference in mutual inductances is the Ironless Inductive Position sensor (I2PS, Fig. 7). Its construction and performance is similar to the LVDT, but it does not contain any ferromagnetic material, nor does it need electrical connection with the moving parts [S32]. The fixed part contains two excitation and two pickup coil segments, with the coupling coefficient between them controlled by the position of a fifth, short-circuited winding affixed to a movable plunger. The only limit for increasing the excitation frequency (and therefore the dynamic response) is the proximity and skin effect in the winding, which was modeled and tested up to 50 kHz [S33]. It was deployed as a part of a particle detector in the Large Hadron Collider, and its long-term stability proved comparable to LVDT with the benefit of immunity to stray magnetic fields [S34].

Another variation on the LVDT principle is the Permanent Magnetic Linear Contactless Displacement Sensor (PLCD, Fig. 8), where the ferromagnetic core stays stationary, but the balance of magnetic flux is disturbed by a permanent magnet creating a small saturated zone in the core [S35].

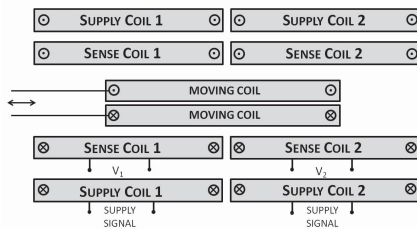


Figure 7: Ironless Inductive Position Sensor (I2PS) operating principle [S32]

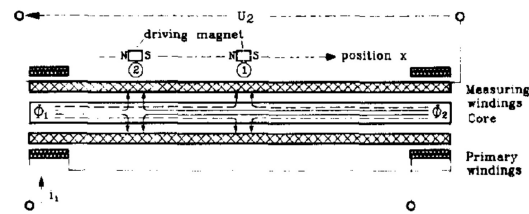


Figure 8: Permanent Magnetic Linear Contactless Displacement Sensor (PLCD) operating principle [S35]

Wiegand Sensors

The central part of a Wiegand sensor is a specially prepared wire that has an area of low coercivity in the center and high coercivity at the surface. The high-coercivity area is subject to abrupt and complete domain reversal when the external field intensity exceeds a particular threshold level. This reversal is visible in Fig. 9 as a discontinuity on the material's hysteresis loop. The resulting step in magnetic flux causes a voltage spike in winding wound around the wire. The threshold value is not constant enough to be used for measurement, but it can be used as an incremental encoder, counting pulses induced by a code wheel with permanent magnets [S36]. A design of a rotary Wiegand encoder including a soft magnetic yoke is given in [S37]

A big advantage of Wiegand sensors is their ability to work from zero speed, because the flux step caused by domain reversal is independent on the rate of change of the external driving field. For this reason can Wiegand sensor be used also for energy harvesting, where each passing of a magnet generates a fixed amount of charge [S38]. This is useful e.g. in turbine flow meters [S39].

Applications Regarding Hydraulic and Pneumatic Cylinders

A specific application area of hydraulic and pneumatic cylinders is covered by various sensing principles. The main challenge in cylinder position sensing are the geometrical constraints, because the sensor cannot be placed inside the cylinder or along the outer piston rod. A

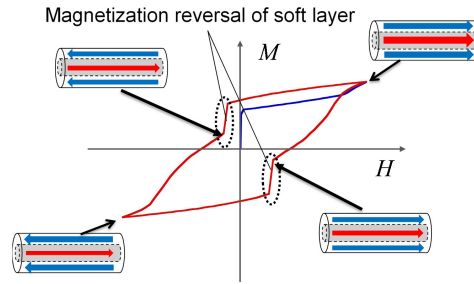


Figure 9: Typical hysteresis loop of a Wiegand wire. The instantaneous reversal of the outer, magnetically soft layer causes steps in the observed loop [S38]

simple solution applicable to non-magnetic, non-conductive (e.g. fiberglass) cylinders is a long solenoidal coil covering the whole outer surface of the cylinder, whose self-inductance changes with the movement of the steel piston rod inside [S40].

Applications in Drilling

Horizontal directional drilling (HDD) is a method used in construction as well as in mining operations, that allows making underground boreholes following an arbitrary trajectory, most often entering from the surface diagonally and then continuing horizontally, up to several kilometers in length. The drill string is hollow, carrying a supply of hydraulic fluid (mud with a specific composition) to power a hydraulic motor at the end of the string. The fluid returns to the surface through the gap between the drill string and the borehole wall, carrying away the removed material.

A common task in HDD is drilling holes from both ends, in this case a precise direction monitoring and control is necessary to ensure the two segments meeting in the center. Flux-gate magnetometers are used for this purpose for their sensitivity and long-term stability. A solution presented in [S41] uses two excitation coils on one drill and two 3D magnetometers on the other for a complete 6-axis positioning system (Fig. 10).

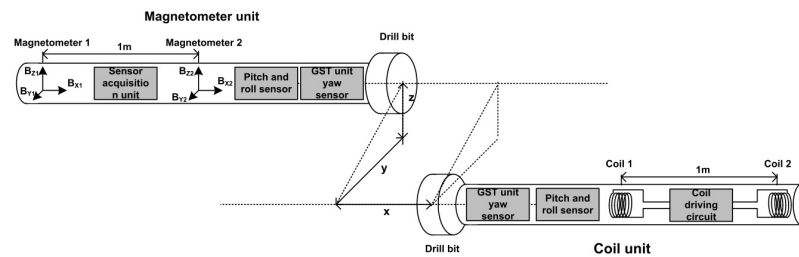


Figure 10: Block diagram of a navigation system used in drilling operations, consisting of inertial sensors, excitation coils and magnetometers for mutual position estimation [S41]

The drill bit is mounted at a fixed angle (approx. 2°) at the end of the drill string, to control its direction by simply rotating the string. Proposal for a motorized self-leveling sensor platform is presented in [S42], keeping the reference frame aligned with the drilling direction.

The 3D fluxgate sensors need to be calibrated, this is usually done by rotating in all directions and fitting an ellipsoid onto the measured points. Although the part of the drill string around the sensors is non-magnetic, it is preferable to perform the magnetic calibration in situ, after integration to the whole system [S43]

2.3 Current Sensors

Current Transformers

Traditional AC current transformers are very robust and have very good rejection of external fields. High precision current transformers are used e.g. for the measurement of energy consumption in power distribution networks. In this application it is necessary to ensure that no DC current is present, which can permanently affect the instrument precision. Direct current in AC network can be induced by the Earth's field variations. They can also be caused by unbalanced transformerless inverters or may appear as a result of outage in HVDC lines, when only one conductor remains in operation and the returning ground current causes differences in earth potential [S44]. Changes in permeability and phase error due to core magnetization and proposed methods of correction are presented in [S45]. One of the methods is further elaborated in [S46], where the effective value of the burden resistor is dynamically adjusted by shorting one of its sections with a semiconductor switching circuit. The advantage of this solution is that it works with existing current transformers with only one secondary winding and without disconnecting the primary side.

Current transformers are also used at higher frequencies e.g. in power inverters or AC oscilloscope current probes. At frequencies in the range of megahertz and above, the length of the winding is no longer negligible compared to the signal wavelength. Individual turns of the winding, as well as the shielding layers have to be treated as transmission lines matched to the impedance of the connected cables and instruments. High frequency field solvers (e.g. Ansys HFSS) are needed for the design of such devices [S47].

Highly compact transformers were manufactured using planar technology, laminating a sheet of ferromagnetic material (Permalloy) between two polyimide films. The windings are then made by etching the copper-coated substrate ([S48], Fig. 11 and 12) or by screen printing with silver ink in a continuous, reel-to-reel process [S49]. The finished flat structure is rolled into a loop around the measured conductor.

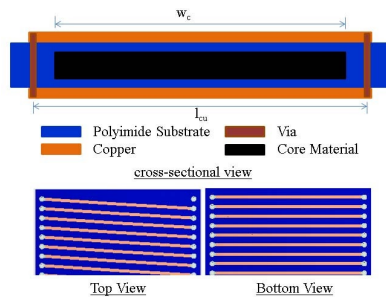


Figure 11: Cross-section of planar current transformer made with modified PCB manufacturing process [S48]

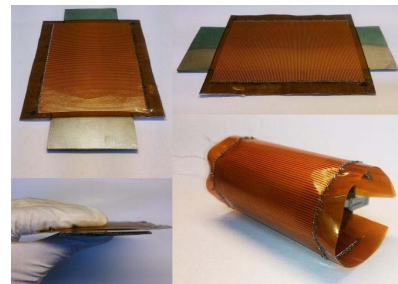


Figure 12: Photograph of a planar current transformer [S48]

After a closer inspection, design flaws in [S48], which negate the design's real-world viability are easily identified: The core material is unsuitable for this type of application for its low permeability and high core loss. The contact between the two loose core ends is poorly defined and will cause undesirable increase in reluctance. The core is not protected from mechanical stress, which has strong influence on its magnetic properties. The secondary current is measured with a resistor and an oscilloscope, which is a method unacceptable for the characterization of such devices. The most important error is the high resistance of the secondary winding, which causes the core to saturate from the beginning of the tested current range.

Magneto-Optical Current Sensors

Magneto-optical fiber sensors are the most advanced method for the measurement of large currents (hundreds of Amperes and more). Their advantage lies in the complete galvanic isolation of the measured object from the instruments and immunity to spurious electric fields. The underlying physical phenomenon is the Faraday rotation i.e. the gradual change of polarization plane along the fiber length (Fig. 13). The operating principle together with considerations regarding their installation in outdoor environment is presented in [S50]. The polarization-maintaining (PM) fibers are not rotationally symmetric and they are very sensitive to the misalignment at fiber connectors. Possible methods of reduction of this sensitivity are presented in [S51].

Extremely large currents inside the ITER nuclear fusion reactor in the order of megaamperes, are also being measured with magneto-optical fiber sensors [S52].

A different application of MO effect is the visualization of in-plane currents by application of MO film on top of the sample and observing with a setup similar to a Kerr microscope [S53].

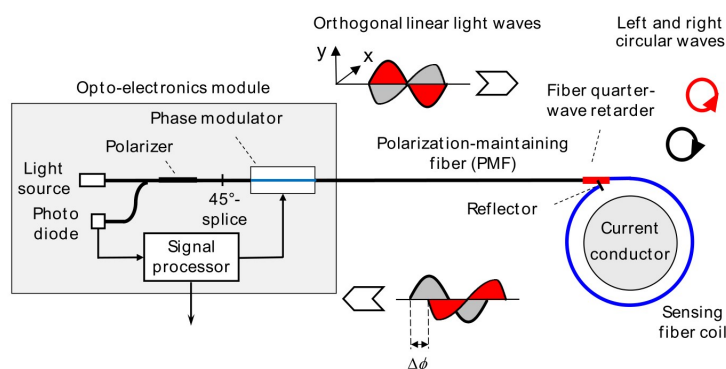


Figure 13: Principle of operation of fiber optic current sensor [S50]

Magnetostrictive and Piezoelectric Current Sensors

Resonant beam sensor is an example of a micromechanical system adapted for electric current measurement. Such sensor, suitable for AC applications is presented in [S54] or [S55]. A cantilever beam with a permanent magnet at its end is covered with PZT piezoelectric plates serving as a pickup (Fig. 14). The excitation is provided by a nearby current-carrying conductor. The vibrating beam has one self-resonant frequency, rejecting all other exciting fields. Geometry optimization and sensitivity to manufacturing inaccuracy, together with measurement on samples, is presented in [S56].

Magnetostrictive sensors with optical readout work by compressing an optical fiber bonded to a magnetostrictive substrate, typically Terfenol-D. In [S57] a fiber Bragg mirror (FBG) is bonded to a Tb-Dy-Fe giant magnetostrictive substrate and its central wavelength is measured. Two orthogonal cuts of the magnetostrictive material are used for temperature compensation. Another possible approach is to use a loop of standard singlemode fiber and measure the strain through Rayleigh backscattering [S58].

Most magnetolectric sensors use a multi-layer laminate consisting of magnetostrictive layer providing strain in magnetic field, and piezoelectric layer converting strain into charge (Fig. 15). In some exotic designs the magnetostrictive layer is missing and out-of-plane force is exerted with a pair of permanent magnets, modulated with additional flux generated by the measured conductor [S59]. Piezoelectric layer by itself cannot detect static strain, and for

DC-capable sensors an additional AC excitation is needed [S60]. Linearity and sensing range is improved with the addition of compensation winding that maintains the total magnetic flux in the yoke close to zero [S61].

Magneto-acoustic sensors are a variant of surface acoustic wave (SAW) circuits, where the external field modulates the speed of sound in the magnetostrictive layer [S62]. The active material does not have to form a continuous layer, and dividing it into thin strips helps with the reduction of hysteresis errors [S63].

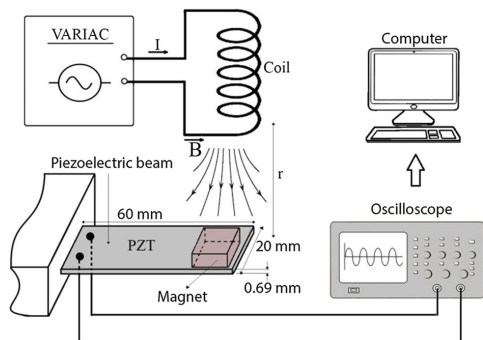


Figure 14: Resonant beam AC current sensor with piezoelectric sensing [S55]

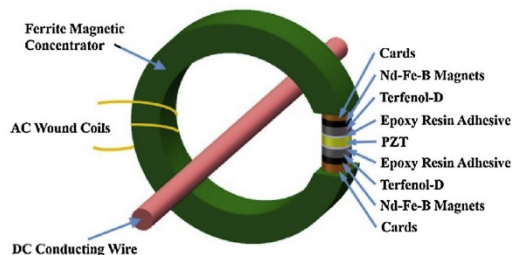


Figure 15: Magnetostrictive current sensor with piezoelectric sensing, with ferromagnetic yoke [S60]. Nonlinearity of the sensor allows for DC current measurement with an additional AC excitation winding

Yokeless Circular Sensor Arrays

Yokeless sensors are a lightweight, simpler alternative to sensors with closed magnetic yoke, their operation is based on piecewise approximation of the Ampere's law. In ideal case, the sensitivity inside the sensor circle is constant and independent on the angular displacement of the conductor. This assumption does not hold if the number of sensing element is not infinite. Analytical calculation of the relation of sensor count and accuracy [S64], calculation of errors caused by off-center and off-axis position of the conductor [S65], and the influence of external currents [S66] were thoroughly studied in literature.

In order to minimize the disturbances from external currents, it is favorable to place the sensor as closely to the measured conductor as possible. Hall effect sensors, which can measure high field intensity, are the most suitable for measurement on closely spaced wire bundles [S67]. Limited measurement range of AMR sensors may be overcome with closed-loop mode of operation, using the on-chip compensation coils connected in series [S68].

The sensitivity distribution inside the sensor circle is not exactly uniform, but it is constant and methods were developed for compensation of this irregularity. Position estimation algorithm and 2D look-up table is presented e.g. in [S69] for AMR sensors or in [S70] for Hall sensors.

An unusual non-circular arrangement of sensing elements was used for flat busbars [S71], in this case each sensing element has a different weight due to the non-symmetrical geometry.

It was shown that multiple conductors may be measured simultaneously using circular sensors, e.g. in [S72], the values for three different conductors inside one cable are separated from the data measured by four sensors. Careful three-layer shielding is necessary to exclude any external fields. A modification of this method without the need for shielding uses 18 sensors arranged in three concentric rings ([S73], Fig. 16 and 17).

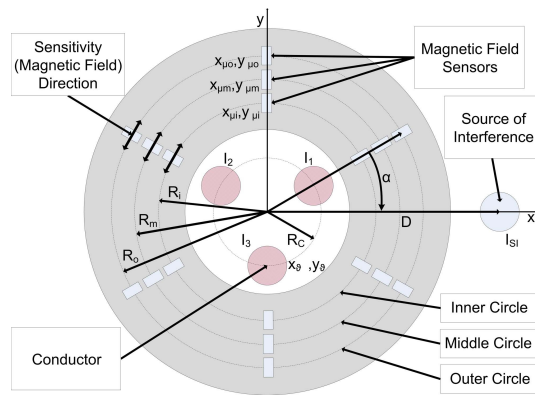


Figure 16: Schematic depiction of an 18-element, yokeless sensor [S73]. Three different conductors can be resolved from the output data, even in the presence of external disturbing fields

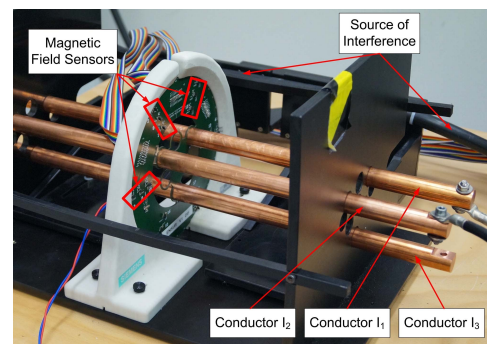


Figure 17: Photograph of an 18-element three-phase yokeless sensor in a test fixture [S73]

Rogowski Coils and Induction Sensors

Alternating current on outer layers of a PCB can be measured with a solenoidal coil made on its internal layers [S74]. Arrays of planar PCB coils can be used for the measurement of external wires with partial compensation of outside fields, if the distance is fixed [S75]. An array of five induction coils under a three-phase overhead lines is enough to reconstruct all three currents [S76]. Ring sensor with six 2-D coils can be used to separate the phase currents inside a three-phase cable [S77].

Rogowski coils are very sensitive to deformation and thermal expansion of its nonmagnetic core. For applications in which absolute accuracy is not critical, they can easily be fabricated with printed circuit technology. In [S78], a miniature PCB-based Rogowski Coil is integrated into IGBT modules for high-speed current monitoring (Fig. 19). It uses analog integrator to reconstruct the primary current from the induced voltage.

The outer surface of Rogowski coils is usually electrostatically shielded for protection against interference. The shielding layer adds additional capacitance to the coil, dependent on the size of air gap and the location of the grounding connection. A schematic diagram containing various parasitic elements is shown in Fig. 18. Different shielding styles are discussed in [S79], together with proposal of differential winding method of RCs, which can further reduce the susceptibility to external electromagnetic interference.

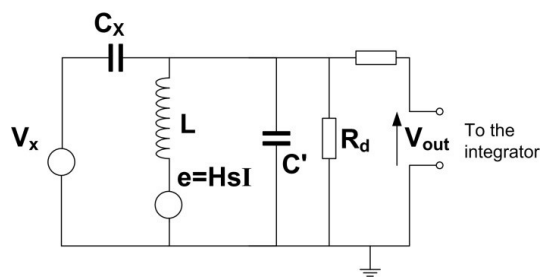


Figure 18: Equivalent schematic diagram of a Rogowski coil [S79]. External interference V_X is coupled to the integrator through the stray capacitance C_X

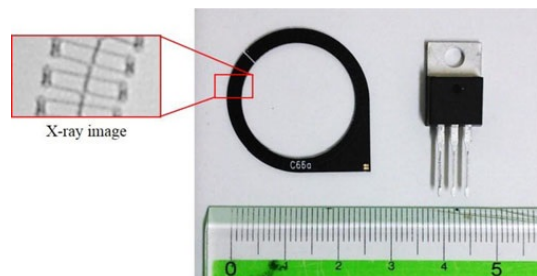


Figure 19: Miniature PCB-based Rogowski coil [S78]

3 Thesis objectives

1. Select magnetic materials suitable for sensor applications (including amorphous and nanocrystalline) and choose suitable numeric models for their analysis, fitting to the measured characteristics in wide range of fields.
2. Utilize these models for FEM simulation of novel magnetic position sensors and electric current sensors, building upon and extending standard simulation software tools.
3. Optimize the sensors performance using parametric design methods and controlled iterative approach.
4. Build physical demonstrators and measurement fixtures with the help of modern, fast prototyping methods (in particular 3D printing).
5. Measure the properties of the demonstrators and compare them with simulations. Identify the shortcomings of computer simulations or measurement methods that cause the observed discrepancy between expectation and reality.

4 Magnetic material modeling and nanowire-based sensors

Most of the papers included in this chapter are dealing with sensors based on arrays of soft magnetic nanowires. Nanowire fabrication and applications were the central point of the GAČR Nanofluxgate project. The concept of electrodeposition into a nonmagnetic, nanostructured matrix had already been thoroughly studied, but the novelty of this project lied in the application of such nanostructures into the area of magnetic field sensors, as a replacement of magnetic cores normally consisting of metallic strips made by bulk electrodeposition or by etching of amorphous ribbons.

The nanowires are thin enough to not form multiple magnetic domains and therefore the associated Barkhausen noise is low. Utilization of the micro-scale shape anisotropy was attempted, as the (local) demagnetization factor of the wires in longitudinal direction is much lower than in transverse direction. This property was studied with the intention of constructing a core for a planar fluxgate sensor which senses the magnetic field in vertical direction.

The nanowires are too small to be handled individually and because their size is less than the wavelength of visible light, SEM imaging has to be used to verify the deposition result. For the purpose of quick evaluation of various geometrical wire arrangements a large-scale model was used. The wires in this model are no longer a single magnetic domain, but the fill ratios and demagnetization factors are the same.

4.1 Modelling and Measurement of Magnetically Soft Nanowire Arrays for Sensor Applications




This paper covers research carried out over the course of several years as a cooperation among three institutions. The research of nanowires was started at the University of Applied Sciences Aschaffenburg, where they have all the necessary process equipment available. The key instrument in manufacturing the samples was the sputter coater, used to create the conductive backside on the substrates prior to electrodeposition. I personally spent two months at their laboratory studying and optimizing the deposition process.

The magnetic measurement requiring a SQUID measurement system were done at the Institute of Physics, Czech Academy of Sciences. All remaining tasks, including subsequent electrodeposition on new types of membranes and FEM simulations, were carried out at the Department of Measurement.

My contribution was the preparation of samples and FEM simulations (some of my results were verified by Dr. Mirzaei, who independently arrived to similar results).

Article

Modelling and Measurement of Magnetically Soft Nanowire Arrays for Sensor Applications

Pavel Ripka^{1,*} , Vaclav Grim¹ , Mehran Mirzaei¹, Diana Hrakova¹, Janis Uhrig², Florian Emmerich², Christiane Thielemann², Jiri Hejtmanek³, Ondrej Kaman³ and Roman Tesar³ 

¹ Faculty of Electrical Engineering, Czech Technical University in Prague, Technicka 2, 166 27 Praha 6, Czech Republic; vaclav.grim@fel.cvut.cz (V.G.); mirzameh@fel.cvut.cz (M.M.); hrakodia@fel.cvut.cz (D.H.)

² Biomems Lab, Faculty of Engineering, Technische Hochschule Aschaffenburg, 63743 Aschaffenburg, Germany; s130567@h-ab.de (J.U.); florian.emmerich@h-ab.de (F.E.); christiane.thielemann@h-ab.de (C.T.)

³ Fyzikální Ústav AV ČR, v. v. i, Cukrovarnicka 10/112, 162 00 Praha 6, Czech Republic; hejtman@fzu.cz (J.H.); kaman@fzu.cz (O.K.); tesar@fzu.cz (R.T.)

* Correspondence: ripka@fel.cvut.cz; Tel.: +420-736-760-601

Abstract: Soft magnetic wires and microwires are currently used for the cores of magnetic sensors. Due to their low demagnetization, they contribute to the high sensitivity and the high spatial resolution of fluxgates, Giant Magnetoimpedance (GMI), and inductive sensors. The arrays of nanowires can be prepared by electrodeposition into predefined pores of a nanoporous polycarbonate membrane. While high coercivity arrays with square loops are convenient for information storage and for bistable sensors such as proximity switches, low coercivity cores are needed for linear sensors. We show that coercivity can be controlled by the geometry of the array: increasing the diameter of nanowires (20 µm in length) from 30 nm to 200 nm reduced the coercivity by a factor of 10, while the corresponding decrease in the apparent permeability was only 5-fold. Finite element simulation of nanowire arrays is important for sensor development, but it is computationally demanding. While an array of 2000 wires can be still modelled in 3D, this is impossible for real arrays containing millions of wires. We have developed an equivalent 2D model, which allows us to solve these large arrays with acceptable accuracy. Using this tool, we have shown that as a core of magnetic sensors, nanowires are efficiently employed only together with microcoils with diameter comparable to the nanowire length.

Keywords: magnetic nanowires; soft magnetic wires; magnetic sensors



Citation: Ripka, P.; Grim, V.; Mirzaei, M.; Hrakova, D.; Uhrig, J.; Emmerich, F.; Thielemann, C.; Hejtmanek, J.; Kaman, O.; Tesar, R. Modelling and Measurement of Magnetically Soft Nanowire Arrays for Sensor Applications. *Sensors* **2021**, *21*, 3. [https://dx.doi.org/10.3390/s21010003](https://doi.org/10.3390/s21010003)

Received: 24 November 2020

Accepted: 18 December 2020

Published: 22 December 2020

Publisher's Note: MDPI stays neutral with regard to jurisdictional claims in published maps and institutional affiliations.



Copyright: © 2020 by the authors. Licensee MDPI, Basel, Switzerland. This article is an open access article distributed under the terms and conditions of the Creative Commons Attribution (CC BY) license (<https://creativecommons.org/licenses/by/4.0/>).

1. Introduction

Magnetic wires have been used as functional materials of fluxgate magnetic field sensors since the 1930s, and some of these devices are still in production. The magnetic core of these sensors is typically a permalloy (NiFe) wire with a diameter of 0.2 mm, but some fluxgates and induction sensors use core in the form of rod with length up to 1 m [1]. While wire-core fluxgates usually do not achieve the low noise and the high offset stability of ring-core fluxgate sensors made of thin tape, wire cores of Vacquier type show several fundamental advantages [2]:

1. The sensing direction is defined by the direction of the sensor core and not by the direction of the pickup coil. This allows the construction of highly stable gradiometers of the Foerster type [3].
2. The wire-core sensor has high spatial resolution, and it is therefore convenient for measurements of small field sources such as microbeads [4,5].
3. The high shape anisotropy reduces the Crossfield error (a non-linearity response to fields perpendicular to the primary sensing direction) [6].
4. The low demagnetization of the sensor core increases sensitivity and thus allows miniaturization of sensors.

Wires have low cross-sectional area, but the decreased sensitivity can be compensated by increasing of the excitation frequency, as the effect of eddy currents is less pronounced [7]. Magnetic wires have been also used for other sensors such as Wiegand sensors used for position detectors, speed sensors, security labels and for energy harvesting [8].

A new era of magnetic wires started in 1976 with the invention of amorphous microwires. These wires, typically 50 μm to 150 μm in diameter, are mechanically strong and exhibit magnetically soft properties even without annealing [9,10]. They are therefore well suited for applications in fluxgate and GMI magnetic field sensors, and for strain measurements [11]. The magnetic properties of these wires depend on their chemical composition and cooling rate; they can be further tailored by field annealing or by stress annealing. Helical anisotropy can be established by annealing under torsion [12], allowing for the construction of coil-less fluxgate sensors [13,14], whereas other sensors use domain-wall velocity [15]. Passive wireless strain sensors based on microwires can be embedded into composite structures [16]. Glass-covered wires are produced by the Taylor method, which allows the production of diameters from below 1 μm up to 50 μm [17]. In as-cast form, these wires suffer from internal stresses causing non-repeatability and increased noise level. These stresses can be released by current annealing [18]. Both crystalline structures and amorphous structures can be achieved by this technique. Amorphous wires can be subsequently nanocrystallized by thermal treatment [19].

The first sensor application of amorphous wire was the GMI sensor [20,21], where the high-frequency impedance of the wires depends on the DC field that is applied, due to a change in the magnetic permeability. GMI sensors can detect fields down to the nT range, noise level of 35 pT/ $\sqrt{\text{Hz}}$ at 1 Hz has been recently reported [22]. GMI sensors based on amorphous wire have reversible and reproducible stress sensitivity [23]. The main problem of GMI sensor is their poor DC offset stability, caused by the fact that their magnetic core is not saturated. Thus, the sensor can be magnetized by a strong magnetic field, which causes an offset shift. It is also difficult to stabilize the bias field which is necessary to achieve linear operation [24]. Despite these disadvantages, GMI sensors are being used for the detection on nanoparticles [25] and integrated GMI sensors are used in mobile phones [26].

A promising application could be the use of a microwire as a core for a miniature fluxgate sensor, which can even be flexible [27,28]. Fluxgate sensors utilize non-linearity of the magnetization characteristics of the soft magnetic core. In the presence of the measured DC field, the characteristics shifts, and even harmonic components of the excitation frequency appear in the induced voltage. The output signal asymmetry can also be detected in the time domain [29,30]. Fluxgates are usually excited by a strong AC field, which magnetizes the core deeply into saturation during each excitation cycle. Due to this fact, the magnetic state of the core is restored, and the sensor has a DC stability of typically 1 nT. This is true for the longitudinal fluxgate, for which the wire core is excited in the longitudinal direction by a solenoid coil [31]. By contrast, the transverse fluxgate is excited by an electric current through the wire. In order to fully saturate the magnetic core, composite wires consisting of a copper core and a ferromagnetic shell were fabricated by electrodeposition [32]. Microwires are also used as security labels and in microwave metamaterials [33]. Magnetic microwires have low coercivity, high permeability, and may achieve near-zero magnetostriction. In this regard they are superior to thin-film cores which are manufactured by sputtering or electrodeposition. The mentioned properties make microwires ideal for microfluxgate sensors [34,35] which have applications in mobile devices, motion tracking, medical devices, non-destructive testing and in the mining industry [36]. A 20 mm long fluxgate sensor based on a single amorphous microwire achieved a noise of 1.4 nT/ $\sqrt{\text{Hz}}$ at 1 Hz [37].

In 2009, we studied transverse fluxgates with cores made of several microwires. We found that the performance is strongly affected by the magnetostatic coupling between the wires, which depends on their distance [38]. The demagnetization factor of the microwire core was studied in [39]. At that time, 3D Finite Element Modelling (FEM) of a

multiwire core was computationally challenging, so that the study was limited to several wires only.

Nanowire arrays have been fabricated by electrodeposition of a magnetic material into the pores of nanoporous membranes [40]. These arrays exhibit ferromagnetic resonance in the GHz range, and they have large potential for microwave applications such as tunable filters, circulators, and nanoantennas up to THz range [41,42]. Individually functionalized nanowires can also be used in biomedical applications [43]. Another important application of nanowire arrays is in perpendicular magnetic recording [44]. Magnetic nanowires have been fabricated in several laboratories, but to the best of our knowledge they have never been used as functional materials for magnetic field sensors, as most of the fabricated wires have high coercivity. For CoNiP material system the minimum achieved coercivity was 64 kA/m [45]. A systematic study based on micromagnetic simulations of the remagnetization process for cylindrical nanowires with different crystalline structure was conducted in [46].

In this paper, we show progress that has been made in the fabrication, testing and modelling of magnetically soft nanowires. In detail, we examine the effect of the nanowire array geometry on the global magnetic properties. Finite element simulations of nanowire arrays are performed with a simplified 2D equivalent model, which allows for the modelling of large arrays, and the results are verified with the experimental data.

2. Nanowire Fabrication

Our magnetic nanowires are grown by electrodeposition of a magnetic permalloy (NiFe) into the pores of a nanoporous membrane. Here, we use polycarbonate (PC) membranes for the fabrication of nanowires of various diameters and lengths, but alumina and silicon membranes can be used as well.

The general production process of magnetic nanowire arrays is schematically depicted in Figure 1. At first, a glass substrate is metallized with a 200 nm thick copper layer by using a sputter process. In the next step, a photoresist SU8 (MicroChem Corp., Westborough, MA, USA) is structured on top to form an insulation layer, determining the nanowires growth area (Figure 1a). Subsequently, an ion track etched PC membrane (Merck KGaA, Darmstadt, Germany) is placed on the prepared substrate and is gently pressed with a sponge (Figure 1b). This is necessary to avoid any voids between the membrane and the prepared structure, which would result in irregular deposition. Controlled filling of the holes between substrate and membrane is performed by a galvanic growth process (Figure 1c). The electrochemical deposition of the permalloy is carried out at 35 °C in a three-electrode setup, where a platinum wire is used as a counter electrode and Ag/AgCl is used as a reference electrode. Two hours prior to deposition and during deposition, the electrolyte was bubbled with nitrogen to avoid oxidation of Fe²⁺ ions. During pulsed electrochemical deposition, the composition of the nanowires' material is controlled by the parameters of the voltage pulses. This technique has been shown to achieve homogeneous growth of the wires [47]. The delay time between pulses ensures constant material transport through the pores and helps to renew the concentration of the metal ions at the pore-electrolyte interface. All deposition processes were carried out by using VersaStat4 (Princeton Applied Research, Oakridge, TN, USA), since this instrument allows for very precise adjustment of the required parameters. For the pulsed deposition, an aqueous electrolyte was developed which consists of the following components: 300 g/L NiSO₄·6H₂O, 45 g/L NiCl₂·6H₂O, 43.27 g/L FeSO₄·7H₂O, 45 g/L H₃BO₃ [48].

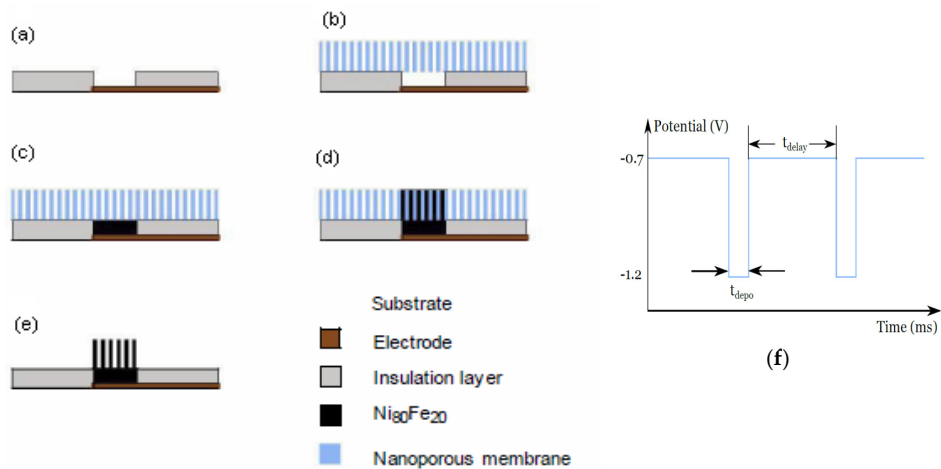


Figure 1. Fabrication of nickel-iron nanowires using nanoporous membranes: (a) insulation layer (photoresist) on top of sputtered Cu electrode, (b) membrane placed, (c) Filling of the holes by electrodeposition, (d) growing nanowires, (e) optional dissolving of the membrane not used in this study, (f) waveform used for electrodeposition.

Boric acid was used to enhance the ion transport and the solubility of all components. During pulsed deposition, a constant deposition pulse time (t_{depo}) of 10 ms and a delay time (t_{delay}) of 100 ms were applied, with voltage amplitude of -1.2 V and -0.7 V, respectively (Figure 1f), which resulted in uniform nanowire growth. The morphology and the size of the nanowires were characterized by scanning electron microscopy (SEM) (Phenom ProX), and the micrographs are shown in Figure 2. The chemical composition of the wires was determined to $Ni_{80}Fe_{20}$ by energy dispersive X-ray spectroscopy (EDX) attached to the SEM. An EDX spectrum of the $Ni_{80}Fe_{20}$ nanowires grown in the PC template is shown in Figure 3 (see the red line).

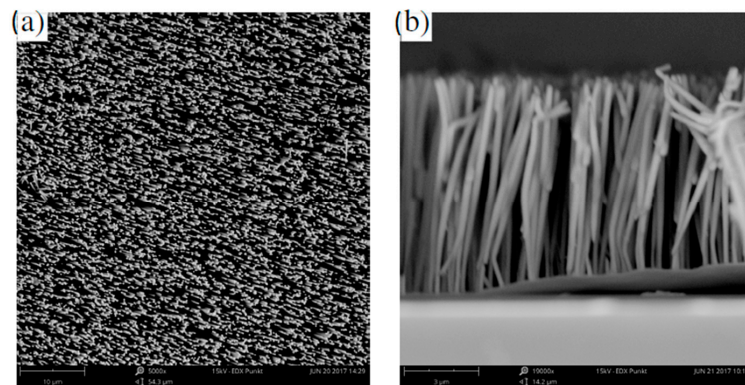


Figure 2. SEM micrographs of a NiFe wire array with a wire diameter of 200 nm, length of 20 μm , and an aspect ratio of 100. (a) top view and (b) lateral view.

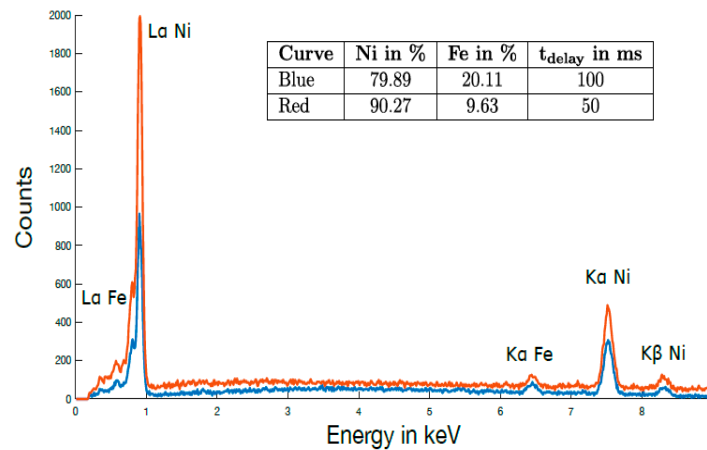


Figure 3. Energy dispersive X-ray spectroscopy (EDX) spectrum of the Ni₈₀Fe₂₀ and Ni₉₀Fe₁₀ nanowire arrays. Differences in the composition were achieved by using different delay times in the pulsed deposition process.

In another experiment, we varied the composition of the nanowire material by decreasing the pulse delay time during electrochemical deposition from $t_{\text{delay}} = 100$ ms to $t_{\text{delay}} = 50$ ms, which resulted in a reduction in iron content of 10%, leading to Ni₉₀Fe₁₀, see Figure 3. In both samples, no signatures of oxygen contamination were found, as they were kept under a constant nitrogen atmosphere. The nanowire lengths were controlled by monitoring the current during deposition and adjusting the deposition time, as the length increased linearly with time. In addition to the nanowire arrays depicted in Figure 2, we fabricated nanowires with diameters of 30 nm and 400 nm by employing the same process. The nanowire length was always 20 μm . In summary, we have presented a method for fabrication of permalloy nanowires that allows the geometry and the composition of the nanowires to be controlled. The quality of the membrane is very important, as it determines the density and the geometry of the wires.

Finally, as an optional step, the membrane can be dissolved with acetone, which would release free-standing nanowires (Figure 1e). However, in this study we kept the nanowires inside the membrane to ensure that they were immovable.

3. Nanowire Magnetic Characterization

Magnetic measurements in DC fields at a temperature of 300 K were performed by SQUID magnetometry on a MPMS XL (Magnetic Property Measurement System, Quantum Design, Inc.). In order to evaluate the effect of demagnetization, we measured samples of two diameters, 1 mm and 3 mm, from each type of nanowire arrays. The measuring sequence was programmed to achieve high precision of the coercivity measurement and to keep the measurement time reasonably short: at first the magnet reset option (controlled quench) was applied to remove any remnant fields in the superconducting winding of the magnetometer, and a full magnetization loop was measured within the range ± 159 kA/m (± 200 mT) with no-overshoot approach and stabilization of particular fields during the field scan, close to zero field the linear regression mode for fitting SQUID scans was used instead of the iterative regression mode. After the measurement of these low-field loops, the magnetization curves were measured up to higher fields of 3180 kA/m (4T) to determine the saturation magnetization.

The complete hysteresis loop in the high-field range is shown on arrays with different wire diameters in Figure 4. Figure 5 shows examples of the detailed low-field hysteresis loop measured on 30 nm, 200 nm and 400 nm diameter wire arrays. Importantly, knowing the saturated magnetic moment of each sample and the saturated magnetic flux density B_s

of the electrodeposited permalloy with known chemical composition, we can rescale the y axis in units of B (Figure 5b) and to calculate the apparent permeability of the measured nanowire array.

The measured coercivity values are shown in Table 1. The coercivity of samples A (30 nm diameter wires) occurs in the range $\approx 30\text{--}40$ kA/m. Its value drops significantly with increasing the wire diameter, specifically to ≈ 5 kA/m and below for diameters of 200 nm and 400 nm. The coercivity does not show significant dependence on the sample size (a diameter of 1 mm or 3 mm). The magnetic moment per unit area is proportional to the amount of magnetic material present in the sample, which depends on the wire diameter. Sample-to-sample variations are probably caused by the random character of the pores in the polycarbonate membrane, as the chemical composition of the wires was quite stable. The apparent permeability was calculated as a slope of the BH curve. The values of flux density B were calculated from the measured magnetic moment, supposing that the saturated magnetic moment is always equivalent to $B = 0.7$ T, which is the saturated flux density of the permalloy that was employed in the present study.

The origin of the reduction in coercivity with growing the wire diameter can be explained by the increased magnetostatic coupling between wires together with an increase in demagnetization, which leads to the decrease in shape anisotropy. This is demonstrated by the hysteresis loop measured in the direction perpendicular to the wires (Figure 6). For the selected wire diameter of 200 nm, the coercivity in the perpendicular direction is $H_{c\perp} = 8.5$ kA/m, while the coercivity in the longitudinal direction is only $H_{c\parallel} = 2.6$ kA/m (Figure 5, Table 1). Also, the relative permeability in the perpendicular direction is $\mu_{\perp} = 5.4$ and in the longitudinal direction it is $\mu_{\parallel} = 3.3$, which indicates that the easy direction is already perpendicular to the wire axis.

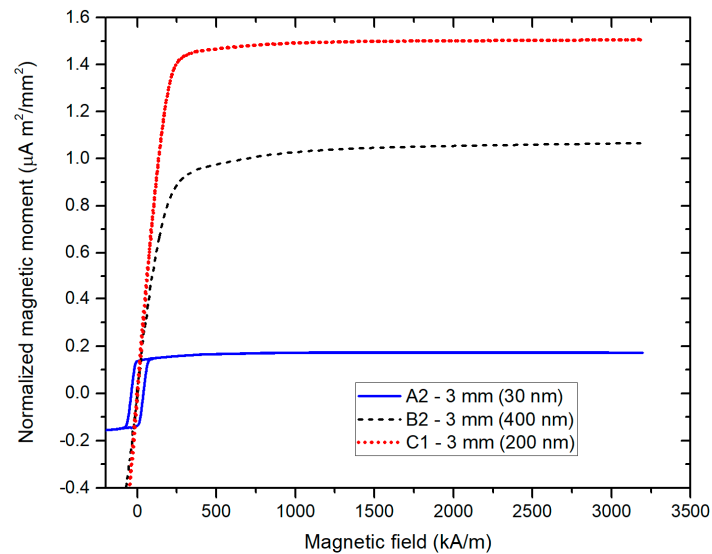


Figure 4. High-field hysteresis loops of the arrays of 20 μm long wires with different diameters.

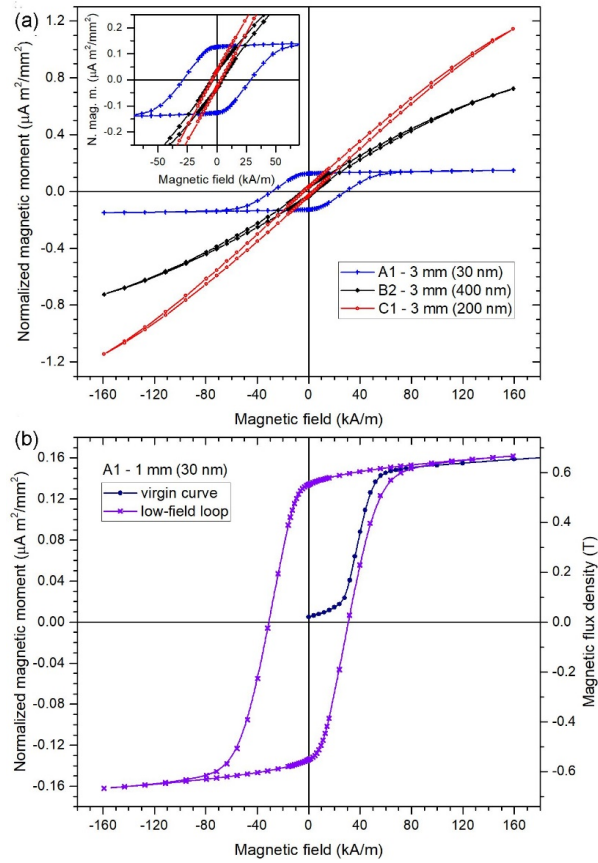


Figure 5. Low-field hysteresis loops of (a) 3 mm diameter circular arrays of Permalloy wires with different diameters. The wire length is always 20 μm . The inset shows the low-field details of the same loops. (b) 1 mm diameter array of 30 nm diameter wires also showing the virgin curve.

Table 1. Measured coercivity and calculated permeability values of arrays of 20 μm long permalloy nanowires.

#	Sample	Hc [kA/m]	μ_a
1	A1-1mm 30 nm	31	20
2	A1-3mm 30 nm	29	18
3	A2-3mm 30 nm	39	16
4	A4-1mm 30 nm	31	14
5	B2-1mm 400 nm	3.9	3.3
6	B2-3mm 400 nm	4.5	3.4
7	C1-1mm 200 nm	4.6	3.7
8	C1-3mm 200 nm	2.6	3.3

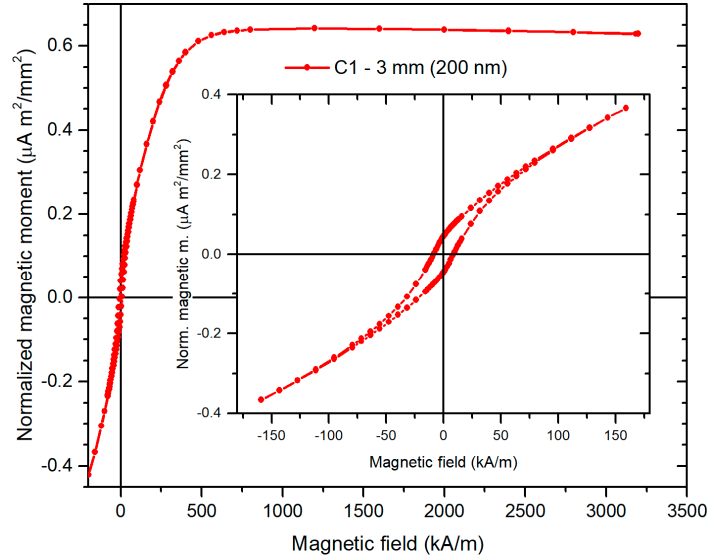


Figure 6. Low-field hysteresis loop of the array of 200 nm diameter 20 μm long permalloy wires measured in the direction perpendicular to wires.

4. Modelling Nanowire Arrays

4.1. Demagnetization, Apparent Permeability and Amplification Factor

The demagnetization factor of a single wire was calculated with high accuracy by Chen et al., assuming a constant permeability [49]. We verified his calculation by 3D FEM modelling, and we calculated more datapoints to improve the interpolation errors.

We also calculated the values of the (magnetometric) apparent permeability μ_a , which is defined as:

$$\mu_a = \frac{B_{\text{mean}}}{\mu_0 H_0} \quad (1)$$

where B_{mean} is the average value of magnetic flux density within the wire volume that was inserted into the homogeneous field with intensity H_0 .

The relation between the magnetometric demagnetization factor D and apparent permeability is described by the formula [50]

$$\mu_a = \frac{\mu_r}{1 + D(\mu_r - 1)} \quad (2)$$

where μ_r is relative permeability of the material.

While the apparent permeability of ring and racetrack cores have been extensively studied, we are not aware of any paper analyzing the effects of the coil geometry and core geometry on the sensitivity of a multicore sensor.

Verification of our calculations was performed by measurements on the array of crystalline permalloy microwires. The models should also be extended to include non-linear magnetization curves of the material under study. We defined the amplification factor a of the induction coil with a multiwire core:

$$a = \frac{\Phi_{\text{cored}}}{\Phi_{\text{air}}} \quad (3)$$

where Φ_{cored} and Φ_{air} is the coil flux with and without the core, respectively.

For very slim coils wound tightly around a rod core, the amplification factor is roughly equal to the apparent permeability μ_a ; this is not valid for wire cores with large coil area.

Better approximation of the amplification factor a considers the coil cross-sectional area A_{air} and core cross-section A_{core} . This formula was derived by Primdahl for fluxgate sensors and it is commonly used in literature [51]:

$$a = \frac{\Phi_{cored}}{\Phi_{air}} = \frac{A_{air} - A_w + \mu_a A_w}{A_{air}} = 1 + (\mu_a - 1) \frac{A_w}{A_{air}} \quad (4)$$

where A_w/A_{air} is array density.

We have already shown by FEM simulations and verified by measurement that for small wire arrays the real values of the amplification factor are much lower [50].

In this paper we examine the apparent permeability and amplification factor of nanowire arrays as a function of distance between the wires, i.e., wire density. At first, we make this analysis for a single wire, then for a small wire array and finally we model and calculate very large arrays.

4.2. 2D Model for Single Wire

Figure 7 shows the amplification factor of a single permalloy wire with a diameter of 200 nm, length of 20 μm , and relative permeability $\mu_r = 500$ inside a 20 μm long pick-up coil as a function of the coil diameter d . As the system is rotationally symmetrical, the calculation was made by 2D FEM.

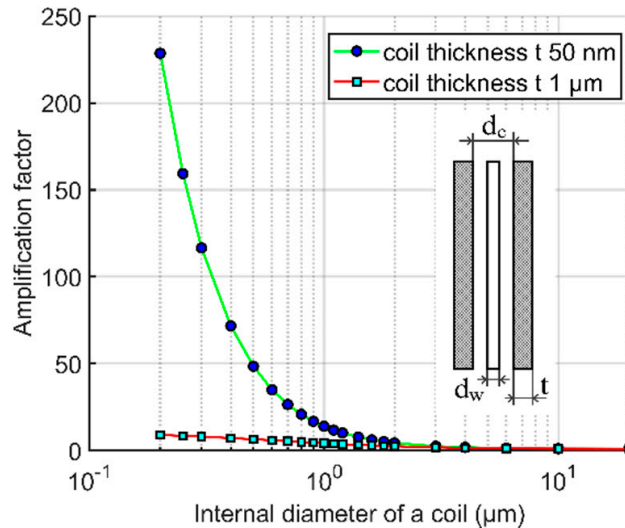


Figure 7. Amplification factor of a single 20 μm long permalloy wire with a diameter of 200 nm inside a 20 μm long pick-up coil with two different thicknesses as a function of the coil diameter d (FEM simulation). The wire material relative permeability is $\mu_r = 500$ and apparent permeability $\mu_a = 361$.

The apparent permeability of this wire was also calculated by 2D FEM as $\mu_a = 361$. Figure 7 shows that high values of the amplification factor can be achieved only when thin coil is fabricated tightly around the magnetic nanowire core. Even though, the achievable value of amplification factor is only 230, which is significantly lower value than the apparent permeability. When increasing the coil diameter, the amplification factor decreases rapidly; for 500 nm internal coil diameter and 50 nm coil thickness, the amplification factor calculated by FEM is only 50, while using Equation (4) the expected value would be $a = 81$. The reason of this behavior is that the magnetic flux density B around the magnetic wire core is weaker than the measured homogenous B_0 . The profile of B in the wire midplane is shown in Figure 8. When going from the wire center in radial direction, magnetic flux

density B steeply drops upon crossing the boundary of the high-permeability core and air. The magnified part outside the wire shows that the field in the wire vicinity is weaker because the field lines are concentrated in the high-permeability region and this shielding effect is decreasing with distance.

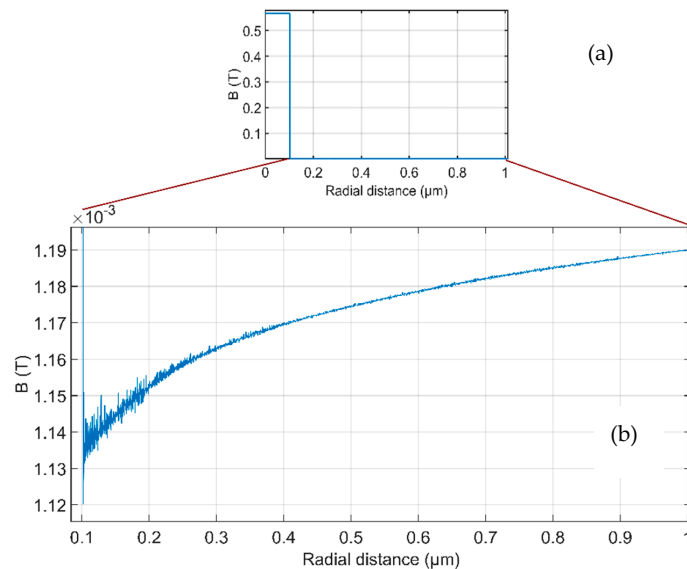


Figure 8. Magnetic flux density B in the midplane of a 200 nm diameter wire as a function of radial distance from the wire center: (a) inside and outside the wire (b) the outside part enlarged to show decrease in B close to the wire surface.

4.3. 3D Model for Small Wire Array

Figure 9 shows apparent permeability and amplification factor as a function of wire array density A_w/A_{air} , of a small array of permalloy wires with a diameter of 200 nm, length of 20 μm , and relative permeability $\mu_r = 500$. The wire array diameter is $D = 20 \mu\text{m}$, and the single-turn pickup coil has internal diameter of 22 μm , length of 20 μm and thickness of 1 μm or 50 nm. The apparent is decreasing with decreasing wire distance due to increasing magnetostatic coupling. For very small density the coupling is minimum and apparent permeability is approaching its maximum value of $\mu_a = 361$ for single wire. The minimum value of $\mu_a = 4$ is reached for 100% density, i.e., for solid permalloy cylinder with diameter of 20 μm , and length of 20 μm (Figure 9a). If we calculate the amplification factor using the simplified Equation (4), we obtain maximum amplification for 12% wire density (500 nm wire pitch). However, more accurate results obtained by FEM modelling show monotonous increase of the amplification factor with array wire density. The maximum value for both calculation methods is $a = 3$ for solid cylinder. The amplification factor only slightly depends on the coil thickness (Figure 9b).

4.4. Equivalent 2D Model for Large Wire Arrays

For the FEM simulations of large wire arrays, we proposed a simplified 2D equivalent model based on hollow cylinders. We also verified this model on small wire arrays of up to 90 wires [37] by comparison with 3D simulation and by measurement.

In the present paper, we extend these simulations to the nanowire arrays described in Section 2. As these arrays contain millions of wires, 3D FEM is impossible due to the computational complexity. Although we use symmetry to reduce the problem, even for 2521 wires in an array the number of elements is already 1.5 million and the computational time on a conventional PC (i7, 3.4 GHz, 8 cores with 32.0 GB RAM) reaches 43 min. Our 2D

computational model attempts to overcome this problem-computation time for the same task was only 7 s.

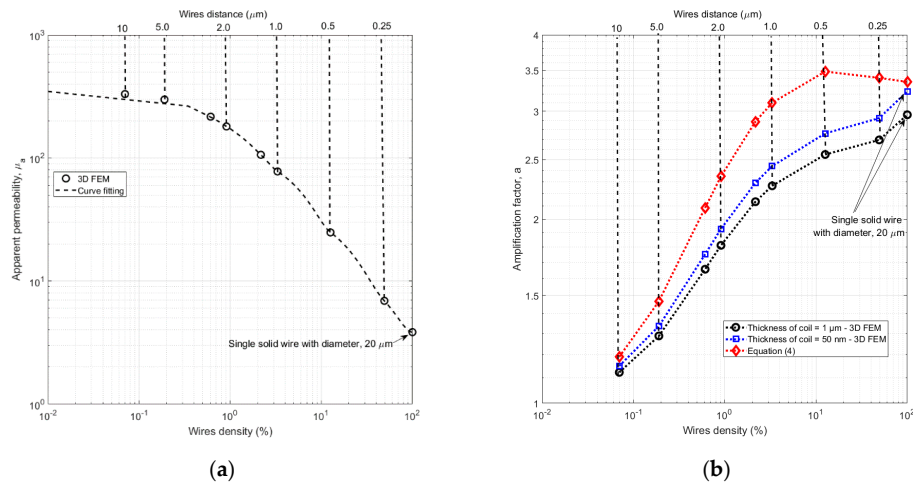


Figure 9. Apparent permeability (a) and amplification factor (b) of a small wire array as a function of wire density (FEM simulation). The array diameter $D = 20 \mu\text{m}$ is the same as the wire length.

Figure 10a shows a model of part of a hexagonal array of nanowires with diameter D_w , length L , and distance d_w . Figure 10b shows a similar square lattice model.

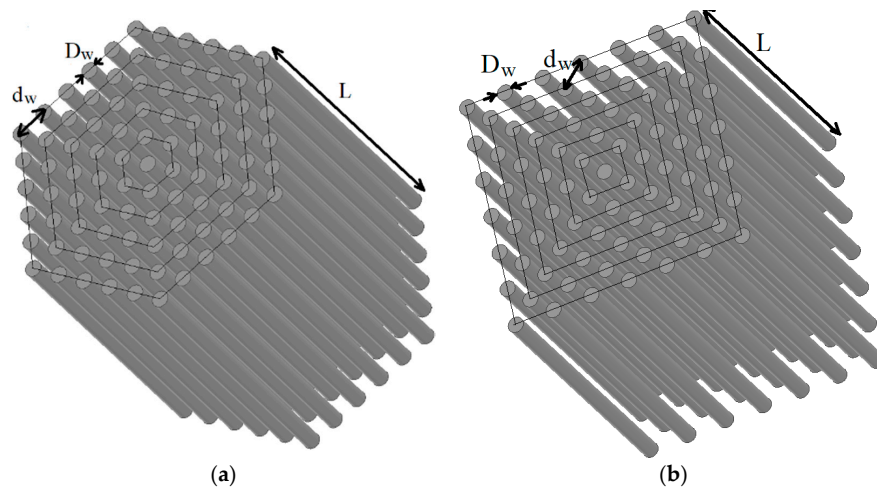


Figure 10. Part of the model of the wire array (a) with a hexagonal arrangement and (b) with a square arrangement.

Figure 11 shows the equivalent 2D model that replaces wires by hollow cylinders. The height of the hollow cylinders is the same as the height of the wires. The mean radius of the hollow cylinders, R_c , is calculated according to Equations (1) and (2), which are based on the assumption that the circle with radius R_c has the same area as the red color hexagon/square shown in Figure 11a,b. The red color lines connect the centers of the wires into a single hexagonal/square “shell” of wires. The thickness, t_c , of the hollow cylinders is

calculated based on the assumption that the volume of the hollow cylinder must be equal to the volume of the wires that belong to the same shell.

$$R_c = \sqrt{3 \cdot R_{h-c} \cdot R_{h-i} / \pi} = \sqrt{3 \cdot \sqrt{3} / 2 / \pi} \cdot R_{h-c}, R_{h-i} = \sqrt{3} / 2 R_{h-c}, \quad (5)$$

$$d_c = \sqrt{3 \cdot \sqrt{3} / 2 / \pi} \cdot d_w, t_c = 3D_w^2 / 4 / d_c$$

$$R_c = \sqrt{4 \cdot R_{r-i} \cdot R_{r-c} / \pi} = \sqrt{2 / \pi} R_{r-c}, R_{r-i} = \sqrt{2} / 2 R_{r-c}, \quad (6)$$

$$d_c = \sqrt{2 / \pi} d_w, t_c = D_w^2 / 2 / d_c$$

where, R_{h-c} and R_{h-i} are the outer (circumference) radius of the hexagon and the inner radius of the hexagon, respectively. R_{r-c} and R_{r-i} are the outer (circumference) radius of the square and the inner radius of the square, respectively. The distance, d_c , between the hollow cylinders is the same between all cylinders, as it is proportional to the distance of the wires, d_w , as mentioned in Equations (1) and (2).

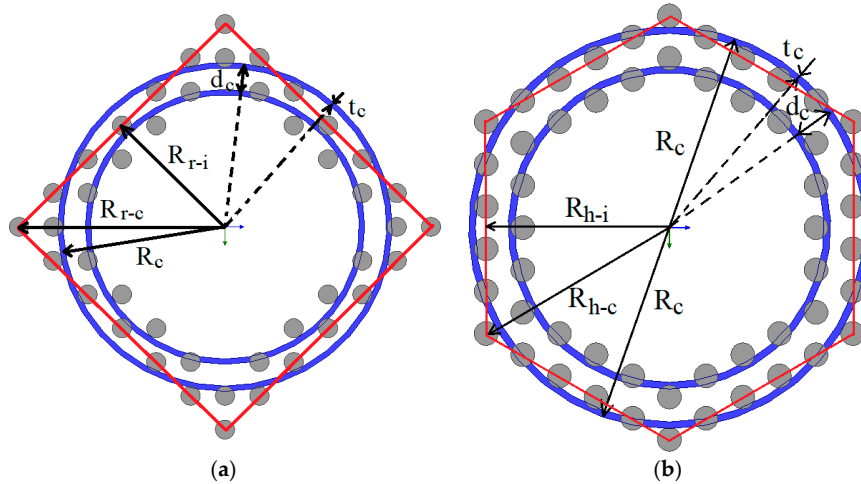


Figure 11. Equivalent hollow cylinders (a) for a hexagonal arrangement and (b) for a square arrangement of the wires.

4.5. Verification of the 2D Model on Arrays of Thousands of Wires

In the first phase, we verified our 2D equivalent model by comparing it with a true 3D model. The calculation was performed for 20 μm wires 200 nm in diameter and for several distances between the wires. The wire lattice was either hexagonal (for 2791 wires) or square (for 2521 wires).

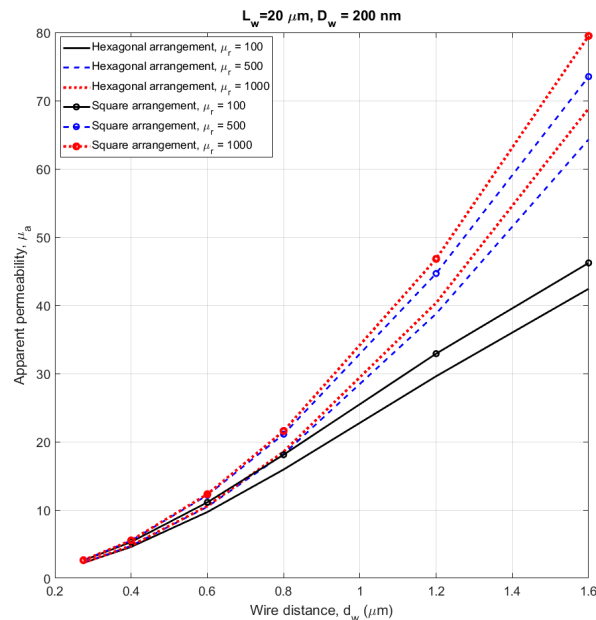
The calculated results are shown in Table 2. The maximum difference between the 3D model and the 2D model is 4%, showing that the 2D simplified equivalent model can be used with reasonable accuracy.

Table 2. Apparent Permeability Comparison between 3D and 2D.

Case- $\mu_r = 500$ $D_w = 200$ nm, $L_w = 20$ μm	μ_a 3D	μ_a 2D	Rel. Diff. (%)
2791 wires–Hexagon, $d_w = 1.6$ μm	85.75	88.39	3.1
2791 wires–Hexagon, $d_w = 1.2$ μm	59.40	60.24	1.4
2791 wires–Hexagon, $d_w = 0.8$ μm	34.91	34.94	0.1
2791 wires–Hexagon, $d_w = 0.6$ μm	24.13	23.97	−0.7
2791 wires–Hexagon, $d_w = 0.4$ μm	14.72	14.51	−1.4
2791 wires–Hexagon, $d_w = 0.275$ μm	9.68	9.49	−2.0
2521 wires–Square, $d_w = 1.6$ μm	97.06	98.98	2.0
2521 wires–Square, $d_w = 1.2$ μm	67.13	67.90	1.1
2521 wires–Square, $d_w = 0.8$ μm	39.84	39.52	−0.8
2521 wires–Square, $d_w = 0.6$ μm	27.83	27.13	−2.5
2521 wires–Square, $d_w = 0.4$ μm	16.92	16.40	−3.1
2521 wires–Square, $d_w = 0.275$ μm	11.13	10.70	−3.9

4.6. Using the 2D Model on Very Large Arrays

In the next phase, we modelled a 1 mm diameter membrane with embedded 200 nm wires (equivalent to Sample 1) by using the 2D-equivalent model. The wire length was again 20 μm . These arrays already contain from 200,000 up to 9 million wires, so that 3D FEM cannot be performed. In order to observe the effect of the material permeability and the geometry of the lattice, we performed simulations for hexagonal and square arrays and for relative permeability of 100, 500 and 1000. The simulation results are shown in Figure 12. For small distances, the apparent permeability depends neither on material permeability nor on lattice geometry, supposing that the permeability is 100 or more. For the minimum distance of $d_w = 275$ nm, the apparent permeability is 2.25 for a hexagonal lattice and 2.6 for a square lattice. For the permeability 3.7 measured on Sample 1 (Table 1) the corresponding distance between wires is $d_w = 350$ nm, which is only slightly lower value than the mean distance estimated from micrographs (500 nm).


Figure 12. Apparent permeability versus wire distance with hexagonal and square arrangements—Membrane diameter, $D_m = 1$ mm. Calculated by FEM using the 2D-equivalent model.

As we already mentioned in Section 4.1, the multiwire induction sensor sensitivity depends not only on the apparent permeability of the core, but also on the coil geometry. The first approximation of the amplification factor a , calculated by using Equation (4), is shown in Figure 13. The values of the apparent permeability were calculated by FEM as a function of wire distance for a constant array diameter.

We have also used 2D equivalent FEM to calculate the amplification factor according to the definition in Equation (3). The resulting values are plotted in Figure 14 for the same parameters as in Figure 13. These results show that Equation (4) cannot be used for large arrays, as it gives unrealistic results. The estimates based on calculated flux are more precise.

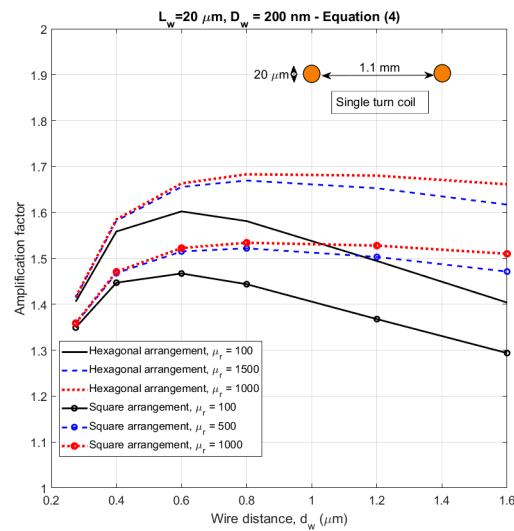


Figure 13. Amplification factor of a 1 mm diameter array of nanowires as a function of wire density—calculated by the approximate Equation (4).

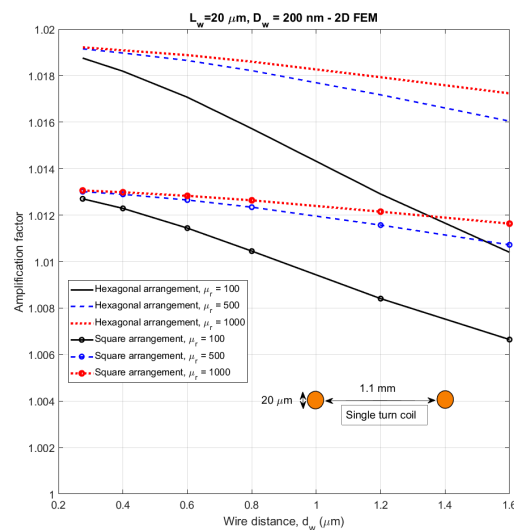


Figure 14. Amplification factor of a 1 mm diameter array of nanowires as a function of wire density—calculated by FEM.

Even though the apparent permeability of less dense large wire arrays can realistically reach the value of 80, the overall amplification factor of very large arrays is very small. This shows the non-intuitive result, that the sensors based on magnetic wires should have a diameter of the wire array lower than the wire length. This rule is applicable both for single-wire and multiwire cores. Several isles of such sub-arrays with their own pickup coils serially interconnected can be used in order to increase the sensitivity, but there should be distances reducing their magnetostatic coupling.

5. Conclusions

While soft magnetic wires of millimeter and micrometer size are successfully used in magnetic sensors, nanowire arrays have been developed mainly for magnetic storage applications and as microwave materials. This study has aimed to analyze possible applications of microwires and nanowires as sensor cores or field concentrators.

We have shown that magnetically soft nanowire arrays can be fabricated by controlling their shape anisotropy. The achieved coercivity value was as low as 4 kA/m. Future work will be targeted on further lowering the coercivity by applying a magnetic field during electrodeposition. Magnetic softening can also be accomplished by successive field annealing. High-temperature annealing may be possible after replacing the polymer membrane by an alumina membrane.

FEM magnetic modelling is essential for the design of future sensors. We have introduced a simplified 2D equivalent model, which allows the modelling of large arrays. The 2D model has been verified by comparison to full 3D model up to 2000 wires. According to simulations, for small pitch and very large arrays, demagnetization caused by magnetostatic coupling reduces the apparent permeability to small values regardless of the permeability of the material. The simulation results fit the values of $\mu_a = 3$ measured by SQUID magnetometer for an array of millions of 200 nm diameter wires.

We have also shown that the widely used apparent permeability can be employed to characterize single-core sensors with slim coil, but it gives misleading results for multicore sensors. Therefore, we use the amplification factor, which is directly related to the sensitivity of the induction sensor based on a given combination of core and coil. We have shown that only for single wire and very small wire arrays the amplification factor can be estimated by the popular simplified formula. For larger arrays, the simplified formula gives unrealistic results (false maximum appears even for 91 wires) and the amplification factor should be calculated by FEM. While for a small array inside a 20 μm diameter microcoil the amplification factor is 3.2, for a 1 mm diameter coil the correct amplification factor drops down to 1.02. This indicates that another key challenge for the future development of nanowire-based magnetic sensors is to fabricate microcoils small enough to be able to efficiently capture the signal from nanowire array.

Author Contributions: Conceptualization, P.R., C.T. and J.H.; methodology, O.K.; FEM modelling, M.M.; fabrication, J.U. and F.E.; measurements, V.G., D.H., O.K. and R.T.; writing—original draft preparation, P.R., C.T., M.M. and O.K.; writing—review and editing, O.K. All authors have read and agreed to the published version of the manuscript.

Funding: This study was supported by the Grant Agency of the Czech Republic within the Nanofluxgate project (GACR GA20-27150S). The authors also gratefully acknowledge financial support from the Bundesministerium für Bildung und Forschung in the frame of FHproUnt2015 (HARVIS 03FH003PX5). Furthermore, the authors from the Institute of Physics, CAS would like to acknowledge the support by the Operational Programme Research, Development and Education financed by European Structural and Investment Funds and the Czech Ministry of Education, Youth and Sports (Project No. SOLID21-CZ.02.1.01/0.0/0.0/16_019/0000760).

Conflicts of Interest: The authors declare no conflict of interest.

References

1. Jordan, J.W.; Sternberg, B.; Dvorak, S.L. Size, Weight and Power Efficiency for High-power, Nonlinear, Geophysical-transmitter, Rod-core Antennas. *J. Environ. Eng. Geophys.* **2011**, *16*, 1–12. [[CrossRef](#)]
2. Janosek, M. Parallel fluxgate magnetometers. In *High Sensitivity Magnetometers*; Grosz, A., Haji-Sheikh, M., Mukhopadhyay, S., Eds.; Springer: Berlin/Heidelberg, Germany, 2017.
3. Foerster, F. A method for the measurement of d-c field differences and its application to nondestructive testing. *Nondestruct. Test.* **1955**, *13*, 31–41.
4. Lei, J.; Wang, T.; Lei, C.; Zhou, Y. Detection of Dynabeads using a micro-electro-mechanical-systems fluxgate sensor. *Appl. Phys. Lett.* **2013**, *102*, 022413. [[CrossRef](#)]
5. Murzin, D.; Mapps, D.J.; Levada, K.; Belyaev, V.; Omelyanchik, A.; Panina, L.; Rodionova, V. Ultrasensitive Magnetic Field Sensors for Biomedical Applications. *Sensors* **2020**, *20*, 1569. [[CrossRef](#)]
6. Ripka, P.; Janosek, M.; Butta, M.; Billingsley, S.W.; Wakefield, E.; IEEE. *Crossfield Effect in Magnetic Sensors*; IEEE: New York, NY, USA, 2009; p. 1860. [[CrossRef](#)]
7. Delevoye, E.; Audoin, A.; Beranger, A.; Cuchet, R.; Hida, R.; Jager, T. Microfluxgate sensors for high frequency and low power applications. *Sens. Actuators A Phys.* **2008**, *145*, 271–277. [[CrossRef](#)]
8. Sun, X.Y.; Yamada, T.; Takemura, Y. Output Characteristics and Circuit Modeling of Wiegand Sensor. *Sensors* **2019**, *19*, 2991. [[CrossRef](#)] [[PubMed](#)]
9. Vazquez, M.; Chiriac, H.; Zhukov, A.; Panina, L.; Uchiyama, T. On the state-of-the-art in magnetic microwires and expected trends for scientific and technological studies. *Phys. Status Solidi A Appl. Mater. Sci.* **2011**, *208*, 493–501. [[CrossRef](#)]
10. Zhukov, A.; Ipatov, M.; Corte-Leon, P.; Gonzalez-Legarreta, L.; Blanco, J.M.; Zhukova, V. Soft magnetic microwires for sensor applications. *J. Magn. Magn. Mater.* **2020**, *498*, 166180. [[CrossRef](#)]
11. Alimohammadi, S.; Meydan, T.; Williams, P. Strain sensing by exploiting the Matteucci effect in amorphous wire. *Int. J. Appl. Electromagn. Mech.* **2019**, *59*, 115–121. [[CrossRef](#)]
12. Fuzer, J.; Brauer, P.; Nielsen, O.V. Magnetic behaviour of amorphous ribbons with creep-induced helical anisotropy and their fluxgate properties. *J. Magn. Magn. Mater.* **1998**, *188*, 286–290. [[CrossRef](#)]
13. Atalay, S.; Ripka, P.; Bayri, N. Coil-less fluxgate effect in (Co_{0.94}Fe_{0.06})(72.5)Si_{12.5}B₁₅ amorphous wires. *J. Magn. Magn. Mater.* **2010**, *322*, 2238–2243. [[CrossRef](#)]
14. Butta, M.; Ripka, P.; Infante, G.; Badini-Confalonieri, G.A.; Vazquez, M. Magnetic microwires with field-induced helical anisotropy for coil-less fluxgate. *IEEE Trans. Magn.* **2010**, *46*, 2562–2565. [[CrossRef](#)]
15. Chizhik, A.; Zhukov, A.; Gonzalez, J.; Stupakiewicz, A. Control of the domain wall motion in cylindrical magnetic wires. *Appl. Phys. Lett.* **2016**, *109*, 4. [[CrossRef](#)]
16. Olivera, J.; Aparicio, S.; Hernandez, M.G.; Zhukov, A.; Varga, R.; Campusano, M.; Echavarria, E.; Velayos, J.J.A. Microwire-Based Sensor Array for Measuring Wheel Loads of Vehicles. *Sensors* **2019**, *19*, 4658. [[CrossRef](#)] [[PubMed](#)]
17. Chiriac, H.; Ovari, T.A. Amorphous glass-covered magnetic wires: Preparation, properties, applications. *Prog. Mater. Sci.* **1996**, *40*, 333–407. [[CrossRef](#)]
18. Murata, N.; Nomura, R.; Matsuoka, A. Current annealing of amorphous wire core for performance improvement of fundamental mode orthogonal fluxgate. *J. Magn. Magn. Mater.* **2019**, *484*, 497–503. [[CrossRef](#)]
19. Chiriac, H.; Lupu, N.; Stoian, G.; Ababei, G.; Corodeanu, S.; Ovari, T.A. Ultrathin Nanocrystalline Magnetic Wires. *Crystals* **2017**, *7*, 13. [[CrossRef](#)]
20. Knobel, M.; Vazquez, M.; Kraus, L. Giant magnetoimpedance. In *Handbook of Magnetic Materials*; Buschow, K., Ed.; Elsevier: Amsterdam, The Netherlands, 2003.
21. Sayad, A.; Skafidas, E.; Kwan, P. Magneto-Impedance Biosensor Sensitivity: Effect and Enhancement. *Sensors* **2020**, *20*, 5213. [[CrossRef](#)]
22. He, D.F. PT-Level High-Sensitivity Magnetic Sensor with Amorphous Wire. *Sensors* **2020**, *20*, 161. [[CrossRef](#)]
23. Nabias, J.; Asfour, A.; Yonnet, J.P. The Impact of Bending Stress on the Performance of Giant Magneto-Impedance (GMI) Magnetic Sensors. *Sensors* **2017**, *17*, 640. [[CrossRef](#)]
24. Zhang, D.S.; Pan, Z.M.; Zhou, H.; Zhang, W.N. Magnetic sensor based on giant magneto-impedance effect using the self-regulating technology on the bias magnetic field. *Sens. Actuators A Phys.* **2016**, *249*, 225–230. [[CrossRef](#)]
25. Garcia-Arribas, A. The Performance of the Magneto-Impedance Effect for the Detection of Superparamagnetic Particles. *Sensors* **2020**, *20*, 1961. [[CrossRef](#)] [[PubMed](#)]
26. Chen, J.W.; Li, J.H.; Li, Y.Y.; Chen, Y.L.; Xu, L.X. Design and Fabrication of a Miniaturized GMI Magnetic Sensor Based on Amorphous Wire by MEMS Technology. *Sensors* **2018**, *18*, 732. [[CrossRef](#)]
27. Trigona, C.; Sinatra, V.; Ando, B.; Baglio, S.; Bulsara, A.R. Flexible Microwire Residence Times Difference Fluxgate Magnetometer. *IEEE Trans. Instrum. Meas.* **2017**, *66*, 559–568. [[CrossRef](#)]
28. Schoinas, S.; El Guamra, A.M.; Moreillon, F.; Passeraub, P. Fabrication and Characterization of a Flexible Fluxgate Sensor with Pad-Printed Solenoid Coils. *Sensors* **2020**, *20*, 2275. [[CrossRef](#)] [[PubMed](#)]
29. Chen, S.Y.; Wang, Y.Z.; Lin, J. A SFTD Algorithm for Optimizing the Performance of the Readout Strategy of Residence Time Difference Fluxgate. *Sensors* **2018**, *18*, 3985. [[CrossRef](#)] [[PubMed](#)]

30. Pang, N.; Cheng, D.F.; Wang, Y.Z. A High Stability Time Difference Readout Technique of RTD-Fluxgate Sensors. *Sensors* **2017**, *17*, 2325. [[CrossRef](#)]
31. Ripka, P.; Janošek, M. Advances in magnetic field sensors. *IEEE Sens. J.* **2010**, *10*, 1108–1116. [[CrossRef](#)]
32. Kraus, L.; Butta, M.; Ripka, P. Magnetic anisotropy and giant magnet impedance in NiFe electroplated on Cu wires. *Sens. Lett.* **2013**, *11*, 53–55. [[CrossRef](#)]
33. El Kammouni, R.; Infante, G.; Torrejon, J.; Britel, M.R.; Brigui, J.; Vazquez, M. Microwave behavior in CoFe-based single- and two-phase magnetic microwires. *Phys. Status Solidi A Appl. Mater. Sci.* **2011**, *208*, 520–525. [[CrossRef](#)]
34. Lu, C.C.; Huang, J.; Chiu, P.K.; Chiu, S.L.; Jeng, J.T. High-Sensitivity Low-Noise Miniature Fluxgate Magnetometers Using a Flip Chip Conceptual Design. *Sensors* **2014**, *14*, 13815–13829. [[CrossRef](#)] [[PubMed](#)]
35. Ciudad, D.; Diaz-Michelena, M.; Perez, L.; Aroca, C. Small Fluxgate Magnetometers: Development and Future Trends in Spain. *Sensors* **2010**, *10*, 1859–1870. [[CrossRef](#)] [[PubMed](#)]
36. Gooneratne, C.P.; Li, B.D.; Moellendick, T.E. Downhole Applications of Magnetic Sensors. *Sensors* **2017**, *17*, 2384. [[CrossRef](#)] [[PubMed](#)]
37. Can, H.; Svec, P.; Tanriseven, S.; Bydzovsky, J.; Birlikseven, C.; Sozeri, H.; Topal, U. Optimizing the sensing performance of a single-rod fluxgate magnetometer using thin magnetic wires. *Meas. Sci. Technol.* **2015**, *26*. [[CrossRef](#)]
38. Ripka, P.; Li, X.P.; Fan, J. Multiwire core fluxgate. *Sens. Actuators A Phys.* **2009**, *156*, 265–268. [[CrossRef](#)]
39. Ripka, P.; Butta, M.; Jie, F.; Li, X. Sensitivity and noise of wire-core transverse fluxgate. *IEEE Trans. Magn.* **2010**, *46*, 654–657. [[CrossRef](#)]
40. Vázquez, M. *Magnetic Nano- and Microwires: Design, Synthesis, Properties and Applications*; Elsevier Science: Amsterdam, The Netherlands, 2015.
41. Ghaddar, A.; Gloaguen, F.; Gieraltowski, J. Magnetic properties of ferromagnetic nanowire arrays: Theory and experiment. In Proceedings of the International Conference on Magnetism (ICM 2009), Karlsruhe, Germany, 26–31 July 2010.
42. Dmytriiev, O.; Al-Jarah, U.A.S.; Gangmei, P.; Kruglyak, V.V.; Hicken, R.J.; Mahato, B.K.; Rana, B.; Agrawal, M.; Barman, A.; Matefi-Tempfli, M.; et al. Static and dynamic magnetic properties of densely packed magnetic nanowire arrays. *Phys. Rev. B* **2013**, *87*, 174429. [[CrossRef](#)]
43. Martinez-Banderas, A.I.; Aires, A.; Teran, F.J.; Perez, J.E.; Cadenas, J.F.; Alsharif, N.; Ravasi, T.; Cortajarena, A.L.; Kosel, J. Functionalized magnetic nanowires for chemical and magneto-mechanical induction of cancer cell death. *Sci. Rep.* **2016**, *6*, 35786. [[CrossRef](#)]
44. Fert, A.; Piroux, L. Magnetic nanowires. *J. Magn. Magn. Mater.* **1999**, *200*, 338–358. [[CrossRef](#)]
45. Lee, Y.C.; Chao, C.T.; Li, L.C.; Suen, Y.W.; Horng, L.; Wu, T.H.; Chang, C.R.; Wu, J.C. Magnetic tunnel junction based out-of-plane field sensor with perpendicular magnetic anisotropy in reference layer. *J. Appl. Phys.* **2015**, *117*, 3. [[CrossRef](#)]
46. Ivanov, Y.P.; Vazquez, M.; Chubykalo-Fesenko, O. Magnetic reversal modes in cylindrical nanowires. *J. Phys. D Appl. Phys.* **2013**, *46*, 485001. [[CrossRef](#)]
47. Salem, M.S.; Sergelius, P.; Zierold, R.; Moreno, J.M.M.; Gorlitz, D.; Nielsch, K. Magnetic characterization of nickel-rich NiFe nanowires grown by pulsed electrodeposition. *J. Mater. Chem.* **2012**, *22*, 8549–8557. [[CrossRef](#)]
48. Torabinejad, V.; Aliofkhaezai, M.; Assareh, S.; Allahyarzadeh, M.H.; Rouhaghdam, A.S. Electrodeposition of Ni-Fe alloys, composites, and nano coatings—A review. *J. Alloys Compd.* **2017**, *691*, 841–859. [[CrossRef](#)]
49. Chen, D.X.; Pardo, E.; Sanchez, A. Fluxmetric and magnetometric demagnetizing factors for cylinders. *J. Magn. Magn. Mater.* **2006**, *306*, 135–146. [[CrossRef](#)]
50. Li, J.P.; Liu, S.B.; Feng, W.G.; Guo, B. Analysis of a fluxgate incorporating demagnetization field. In *New Materials and Processes, Pts 1–3*; Chen, W.Z., Li, Q., Chen, Y.L., Dai, P.Q., Jiang, Z.Y., Eds.; Trans Tech Publications Ltd.: Stafa-Zurich, Switzerland, 2012; Volume 476–478, pp. 1425–1428.
51. Primdahl, F.; Petersen, J.R.; Olin, C.; Andersen, K.H. The short-circuited fluxgate output current. *J. Phys. E Sci. Instrum.* **1989**, *22*, 349–354. [[CrossRef](#)]

4.2 The apparent permeability and the amplification factor of magnetic wires and wire arrays

As a continuation of the theoretical analysis of ordered magnetic structures, the focus was placed on systems with low number of wires, where the overall aspect ratio is not extremely low. For the purpose of convenience, much larger wire specimens (length and diameter both 1000 times larger than the deposited samples) was used. Different arrangements with 1 to 91 wires were simulated and measured.

The properties of the wires apart from their composition were mostly unknown, for this reason measurements were done also for the case of single-wire core (which would not be practical on nano-scale wires). The simulations of Mr. Mirzaei have shown that the results are close to prior works regarding demagnetization factor of solid cylinders.

I contributed with design and manufacture of test fixtures, coil winding, and with measurement of B-H loops using a high-resolution PXI digitizer system.



Research articles

The apparent permeability and the amplification factor of magnetic wires and wire arrays

P. Ripka^{*}, V. Grim, M. Mirzaei

Czech Technical University in Prague, Technická 2, 166 27 Praha 6, Czech Republic

ARTICLE INFO

Keywords:

Magnetic wire
Magnetic sensor
Demagnetization
Wire array

ABSTRACT

We have calculated and plotted the apparent permeability and the demagnetization factor of single magnetic wires. We have also confirmed the accuracy of the analytical formula for the conversion between the apparent permeability and the demagnetization factor. We also show that, as regards wire geometry, the effective permeability calculated from the inductance does not provide a good estimate of the apparent permeability, but that it is close to the amplification factor for induction sensors.

We extend the concept of apparent permeability to a wire array. This will allow us to design multiwire magnetic sensors, mainly induction sensors and fluxgates. FEM calculations have been verified on physical models with up to 91 wires. Finally, we show a simplified 2D model for studies of larger wire arrays, and we verify the accuracy of the model.

1. Introduction

Soft magnetic wires are an essential component of many magnetic sensors. The main advantages of the wire geometry are as follows:

- low demagnetization in the longitudinal direction
- high maximum operating frequency
- high spatial resolution in the radial direction

Apparent permeability and demagnetization factor of ferromagnetic rods and wires was calculated by Bozorth [1]. His nomograms were reproduced by many textbooks and they have been used by several generations of developers as a very practical tool. Much later Chen et al. calculated the demagnetization factors of wires with higher precision, but only for small number of points [2]. One of the results of this paper is creation of more precise nomograms thanks to finite element simulation tools and computational power which were not available before.

Permalloy wires with a typical diameter of 0.2 mm have been used for the core of Foerster-type fluxgate sensors. Thanks to the low demagnetization in the longitudinal direction and the very high demagnetization in the perpendicular direction, the sensitivity direction of the Foerster sensor is given by the direction of the core, and not by the direction of the coil axis. This is a principal difference from fluxgates with ring core geometry, where the sensitivity direction is mainly given

by the pick-up coil geometry [3]. Foerster used this advantage in his single-axis gradiometer, which achieved high stability by attaching both wire cores of the differential fluxgate pair to the same non-magnetic string.

First description of the field dependence of ac resistance of permalloy wires was reported in [4]. This was later called Giant magnetoimpedance effect (GMI) and used for magnetic field sensors [5].

Copper wire covered by electrodeposited permalloy were used for many applications from computer memories, inductors to GMI elements [6–10]. They are also used as the core of orthogonal fluxgates, as they allow the sensor to be excited by the current flowing through the copper wire [11].

Amorphous wires produced by water quenching have a typical diameter of 120 μm . They exhibit interesting magnetoelastic properties that make them suitable candidates for strain sensors. Cobalt-based amorphous wires may have near-zero magnetostriction. These wires are used in magnetic field sensors such as giant magnetoimpedance (GMI) and fluxgate sensors. These magnetic microwires are widely used in the cores of orthogonal fluxgates, which are excited by the current flowing through the magnetic wire. A fluxgate based on amorphous wire reached a noise level of $1\text{pT}/\sqrt{\text{Hz}}$ @ 1Hz [12]. Nanocrystalline wires can be produced from amorphous precursors.

Another group are glass-coated amorphous microwires with a typical diameter of 5–20 μm . First descriptions of glass-coated microwires were

^{*} Corresponding author.

E-mail address: ripka@fel.cvut.cz (P. Ripka).

<https://doi.org/10.1016/j.jmmm.2021.167726>

Received 23 June 2020; Received in revised form 29 December 2020; Accepted 1 January 2021

Available online 22 January 2021

0304-8853/© 2021 Elsevier B.V. All rights reserved.

reported in [13], their magnetic bistability was explained in [14] and their sensor applications reviewed in [15]. Glass-coated microwires may have quite interesting dynamic properties and work as metamaterials being lashed together as assay [16,17].

Magnetic nanowires are mainly produced by electroplating into the pores in a membrane. Until now, these nanowires have not been used much for sensor cores due to their rather high coercivity [18]. However it has been found that densely-packed nanowire arrays may have anhysteretic characteristics [19]. Glass-covered amorphous and nanocrystalline nanowires were also produced [20]. The properties and the sensor applications of magnetic microwires and nanowires are reviewed in a book by Vazquez [21].

As the cross-sectional area of a single wire is small, several studies describe sensors with multiwire cores. Robbes developed an experimental longitudinal fluxgate using (5 + 5) 2 cm long, 20 μm diameter microwires. The noise of this experimental device was around 30pT/ $\sqrt{\text{Hz}}$ @1Hz, and the main advantage was the high bandwidth due to the high excitation frequency [22]. A transverse fluxgate with a core made of 1 to 16 microwires was studied by Li [23], and it was found that the sensitivity increases almost exponentially with the number of wires. Later studies have shown that this effect depends strongly on the wire pitch, and an important consideration is the increase in the quality factor of the tuned output with an increasing number of wires. Increasing the number of wires also reduces the sensor noise [24]. An array of 10 glass-coated amorphous microwires was used in GMI sensor for the detection of magnetic microparticles [25]. Using multiple cores for GMI sensor may improve the directional dependence and sensor characteristics [26]. Magnetic dynamic interaction in amorphous microwire array were studied by Fan Jie [27]. The transverse anisotropy of microwire arrays has been enhanced as the number of wires increases. Longitudinal hysteresis loops show decreasing permeability with number of wires.

Single-core inductive, GMI and fluxgate sensors have been described well and are well understood, but this is not the case for multiwire sensors. To the best of our knowledge, all existing studies of magnetic field sensors based on multiwire cores are experimental, and the conclusions are empirical. In this paper we investigate the demagnetization and the corresponding apparent permeability of the wire array. This is necessary for the analysis and design of sensors based on wire arrays. An example is the development of sensors based on nanowire arrays: the optimum wire length and pitch can be found and the corresponding membrane can be produced in one or two steps, which would significantly reduce the considerable experimental development costs.

We define the collective apparent permeability of the multiwire core as a design parameter for sensors, and we calculate this parameter by finite-element modelling (FEM). For the simulation, we need the magnetization characteristics of the wire material. We will show how the material characteristics can be measured on a straight wire. We also build a physical model using an array of permalloy wires, and we verify the FEM results by measurements.

1.1. Finite-element modelling (FEM)

For 3-D modelling we used Ansys. The modelling is challenging, as the high aspect ratio of the wire requires a large number of nodes. However, the arrays are periodical and we often simulated only a part of the array and made use of symmetry. When the number of wires in the array exceeds 100, the 3-D calculation becomes challenging. We therefore replaced the wires by the equivalent hollow cylinders in order to create a rotationally symmetrical model and reduce the problem to 2-D. We tested this simplified 2-D model for a moderate number of wires, and we believe that the simplified model can be used for large arrays.

1.2. Experimental verification

In all experiments presented in this paper we used permalloy wires 0.2 mm in diameter and 36 mm in length. Each wire was encased in a

glass capillary with an outside diameter of 1.1 mm to protect it from bending during handling (Fig. 1). We first characterized a single wire using a long coil and a short coil, then we made a calculation and measurements for an array of 7 wires with different pitches, and finally we experimented with arrays of up to 91 wires.

2. Demagnetization and apparent permeability

Let us consider a ferromagnetic object with relative material permeability μ inserted into a homogeneous magnetic field H_0 . If the shape is rotational ellipsoid, both B and H remain homogeneous and the magnetic field H inside the object is smaller than H_0 due to the demagnetization field $H_D = DM$

$$H = H_0 - DM = \frac{H_0}{1 + D(\mu_r - 1)} \quad (1)$$

where M is magnetization

D is the demagnetization factor, $0 < D < 1$

μ_r is relative permeability

and for the internal flux density B we can write

$$B = \mu_A \mu_0 H_0 \quad (2)$$

where μ_A is the apparent permeability

μ_0 is the permeability of the free space

and therefore

$$\mu_A = \frac{\mu_r}{1 + D(\mu_r - 1)} \quad (3)$$

If the shape is not ellipsoid, neither H nor B is homogeneous and we should use averaging. If the averaging is performed over the midplane of the core, the resulting demagnetizing factor D_f is called fluxmetric. If the averaging is over the whole volume of the core, the resulting

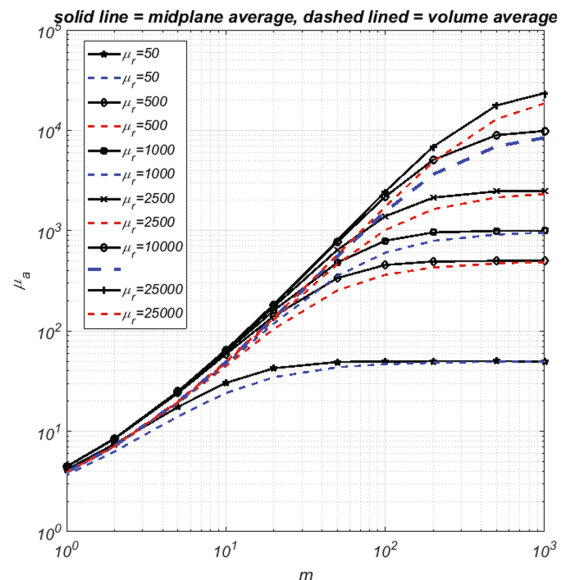


Fig. 1. Magnetometric/fluxmetric apparent permeability (solid line/dashed line) of a ferromagnetic wire, calculated by FEM as a function of the aspect ratio m and the relative permeability μ_r of the wire material.

demagnetizing factor D_m is called magnetometric.

The demagnetization factor of a single wire was calculated by Bozorth [1] and later, with improved accuracy, by Chen [2]. The demagnetization factor was also evaluated for other sensor core shapes, e.g. ring-cores [28,29], race-track cores [30] and stripe cores. To the best of our knowledge, all these calculations were made only for constant material permeability.

The demagnetization factor and the corresponding apparent permeability can also be measured using a coil. In this case, we measure effective values, which depend not only on the core shape and the material properties, and also on the geometry of the measurement coil. It is reasonable to call these coil-related parameters effective demagnetization factor D_e and effective permeability μ_e , in conformity with the IEC standard terminology, in which μ_e is calculated from the coil inductance for the simple case of a toroidal core shape.

Primdahl [28] derived a formula for calculating the effective permeability from the inductance L_{core} of a solenoid coil with the core inserted and L_{air} with the core removed.

$$\mu_e = \frac{L_{core} - L_{air}}{L_{air}} \times \frac{A_{coil}}{A_{core}} \quad (4)$$

where A_{coil} is the cross-sectional area of the solenoid and A_{core} is the cross-sectional area of the core. The corresponding effective demagnetization factor can be calculated using (3). For coils tightly wound around the core and having the same length, the effective permeability and the demagnetization factor are believed to be close to the apparent magnetometric permeability and the corresponding demagnetization factor. One of the aims of this study is to verify this correspondence.

For wire arrays, we can similarly define, calculate and measure the collective effective permeability and the effective demagnetization factor D_e related to the solenoid coil around the wire array. In order to avoid confusion, we rather use the term Amplification factor. The amplification factor is then an important parameter in the design of inductive and fluxgate magnetic sensors, as it is directly related to the sensor sensitivity and also to the sensor impedance, which influence the magnetometer noise.

2.1. FEM simulations of a single wire

Using 2D FEM, we calculated the apparent permeability and the demagnetization factor as a function of m and μ_r . The results are plotted in Figs. 1 and 2. We compared the calculated values with the demagnetization factors precisely calculated by a completely different method in [2], and we found good agreement, as shown in Table 1. We therefore believe that our results are more precise than the values calculated by Bozorth [1], which have been reproduced in many textbooks [11].

The demagnetization factors calculated in [2] are very precise, and the estimated error is 0.1%. The precise values are very useful for metrological applications (measurements of the magnetic moment, magnetization or susceptibility of samples), while accuracy of few percent is sufficient for the sensor design. While [2] covers a wide range of permeabilities, from 0 (for superconductors) up to ∞ , and also a wide range of aspect ratios from 0.001 to 500, the number of calculated points is rather low and only a few of them fit into the practical range for sensors. For this reason, some of the datapoints in Table 1 are missing in [2] and they were only calculated by us. We believe it is a strong point in our approach that the datapoints calculated in our charts are quite dense, and the interpolation error is therefore very low. While the datapoints in [2] are calculated very precisely, they are quite sparse (only 12 values fall into our area of interest), and we can expect large interpolation errors for the charts in. The relative errors for the 12 mentioned datapoints are calculated in table 1: with the exception of one extreme point (very low permeability and high aspect ratio), the error is below 1.8%.

Table 1 Demagnetization factor D numerically calculated by the

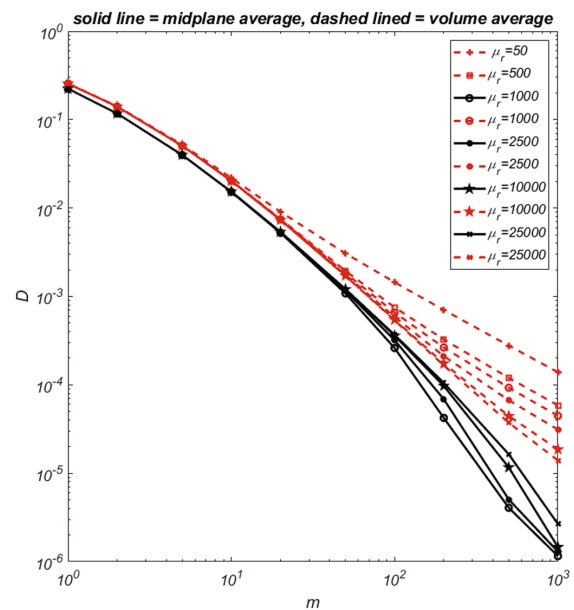


Fig. 2. Demagnetization factor (fluxmetric solid line, magnetometric dashed line) of a ferromagnetic wire.

surface pole method in [6] and by FEM simulation (in our work), and the relative error as the difference between these values. Apparent permeability μ_A calculated by FEM (our work) and calculated from D , using (3) and the relative error of (3). All these values are calculated for several points within the area of interest for magnetic sensors.

Fig. 3 shows the dependence between the apparent permeability and the relative permeability for several values of m , including $m = 190$, which is the shape factor of the wire that we later use in experiments. It is clear that the difference between μ_r and magnetometric μ_{am} is only 0.2% for $\mu_r = 1\,000$, and 4.7% for $\mu_r = 1\,000$, but it increases dramatically to 52% for $\mu_r = 10\,000$. This dependence can be used to reconstruct the material permeability from the measured permeability. Fig. 3b shows the flux lines for wire in homogenous magnetic field.

2.2. Measurements on a single wire

As the first step, the average and local B-H loops were measured to estimate the material characteristics to be used in the simulations. A magnetic field was generated by Helmholtz coils with mean diameter $D = 520$ mm, powered by a sinewave current source. The flux was measured by coils wound around the capillary. The Helmholtz coil current and also the induced voltage were sampled by 24 bit PXI ADC module at 100 kSPS, and the voltage was numerically integrated. The average (magnetometric) flux was measured by a single-layer solenoid of the same length as the wires, while the local flux was measured by the short coil. The coil parameters are presented in Table 2. The magnetic wire with the short coil inside a plastic holder is shown in Fig. 4.

After A/D conversion, the induced voltage was numerically integrated to obtain the flux.

The correction that had to be made for the air flux of the pick-up coil was $A_{coil}/A_{core} = 45$ for a short coil and 30.25 for a long coil. Thanks to the low demagnetization, the H inside the wire is almost the same as H_0 , so that the H in the pickup coil is homogeneous and the correction is straightforward.

The average hysteresis loop measured with the long coil is shown in Fig. 5 for several wires from the same annealing batch.

Table 1
The magnetometric demagnetization factor and the apparent permeability, calculated in [6] and calculated by us.

μ_r	M	M				
		100	130	200	500	1000
100	D in [2]	1.1656 E-3		5.5515 E -4	2.1595 E-4	
	D our calc.	1.1834E-3	8.9011E-4	5.6517E-4	2.2490E-4	1.1199E-4
	error (%)	-1.53		-1.77		-4.19
	μ_A by FEM	89.5126	91.9016	94.7013	97.8566	98.9006
	μ_A by (3)	89.5130	91.9016	94.7013	97.8220	98.9035
1 000	error (ppm)	-0.4	0.1	0.0	35.4	-2.9
	D in [2]	6.5513 E-4		2.6360 E-4	9.2506 E-5	
	D our calc.	6.6286E-4	4.6220E-4	2.6682E-4	9.4152E-5	4.5227E-5
	error (%)	-1.20		-1.29		-1.78
	μ_A by FEM	601.6128	684.116	789.5438	914.4916	956.7692
2 500	μ_A by (3)	601.6134	684.1172	789.5444	914.0285	956.7714
	error (ppm)	-0.1	-0.2	-0.1	50.6	-0.2
	D in [2]					
	D our calc.	5.9132E-4	3.9615E-4	2.1317E-4	6.7748E-5	3.1493E-5
	μ_A by FEM	1008.9985	1256.293	1631.0830	2139.4091	2317.5812
5 000	μ_A by (3)	1009.0	1256.3	1631.1	2138.0	2317.6
	error (ppm)	0.2	-0.1	-0.8	64.6	-0.9
	D in [2]					
	D our calc.	5.6417E-4	3.6983E-4	1.8959E-4	5.4122E-5	2.4146E-5
	μ_A by FEM	1308.7985	1755.145	2567.0465	3938.5221	4461.4314
10 000	μ_A by (3)	1308.8	1755.1	2567.1	3935.3	4461.5
	error (ppm)	-0.3	0.4	-0.2	82.2	-1.0
	D in [2]	5.4334 E-4		1.7390 E-4	4.4268E -5	
	D our calc.	5.4983E-4	3.5557E-4	1.7600E-4	4.4815E-5	1.8791E-5
	error (%)	-1.23		-1.21		-1.20
100 000	μ_A by FEM	1538.9901	2195.248	3623.3668	6913.1814	8418.1913
	μ_A by (3)	1539.0	2195.2	3623.4	6905.6	8418.3
	error (ppm)	-0.3	1.1	-1.5	110.0	-1.0
	D in [2]	5.3007 E-4		1.6042E -4	3.2775 E-5	
	D our calc.	5.3644E-4	3.4200E-4	1.6240E-4	3.3130E-5	1.0536E-5
100 000	error (%)	-1.12		-0.98		-1.08
	μ by FEM	1830.0486	2840.969	5800.4474	23248.2336	48693.9768
	μ_A by (3)	1830.0	2840.9	5800.5	23185.9	48695.2
	error (ppm)	0.2	1.1	-1.2	268.1	-2.6

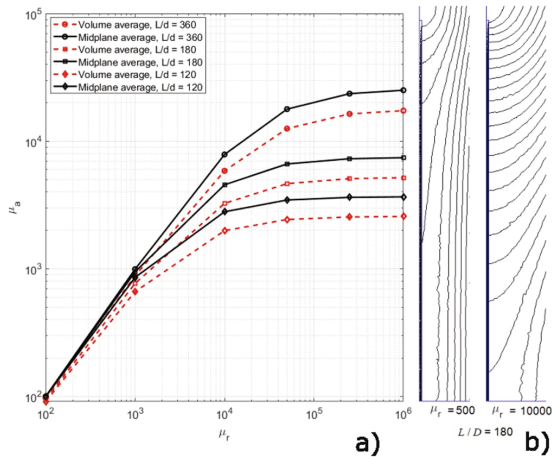


Fig. 3. a) Apparent permeability vs relative permeability (FEM simulation) for various m b) flux lines for $L/D = 180$ and two values of material permeability.

The local hysteresis loop was measured for several positions of the short pickup coil with respect to the wire midplane. The loop becomes flatter when the coil is moved towards the end of the wire, because the corresponding local demagnetization field increases (Fig. 6). These measured loops and the conversion factors between the apparent and relative permeability (plotted in Fig. 3) can be used to reconstruct the loop of the material itself, without the demagnetization effect.

Table 2
Coils for the characterization of a single wire.

	Long coil	Short coil
Length (mm)	27.5	4
Effective diameter (mm)	1.1	1.34
Cu wire diameter (mm)	0.32	0.056
Number of turns N	76	500
Magnetic wire diameter (mm)	0.2	
Magnetic wire length (mm)	38	
Aspect ratio m	36/0.2 = 180	
A_{coil}/A_{core}	30.25	45

For the central position of the short coil, we measured the amplitude magnetization curve and we calculated the amplitude permeability (Fig. 7). The maximum amplitude (relative) permeability in this figure is 6 000 (Fig. 8).

Using Fig. 3 for maximum fluxmetric apparent permeability of 6000, we estimate the maximum material permeability of the wire $\mu_{rmax} = 30 000$. This fits well with the magnetometric apparent permeability of 4150. Similar verification can be made for other material permeabilities corresponding to other values of H_m in Fig. 7.

We also measured the inductance of the long coil, or of the short coil, with and without the wire core, in order to estimate the accuracy of (4) for an estimate of the apparent permeability of the magnetometric, or fluxmetric, demagnetization factor and the corresponding apparent permeability. A Kepco BOP power amplifier and an SR830 lock-in amplifier together with the resistance standard were the instruments that were used. The inductance of the long core without a wire core was $L_{air} = 0.4 \mu H$, and the inductance L_{core} is shown in Fig. 7 as a function of H in the center of the wire. It should be noted that, according to FEM analysis, the field intensity H decreases to approximately one half at the

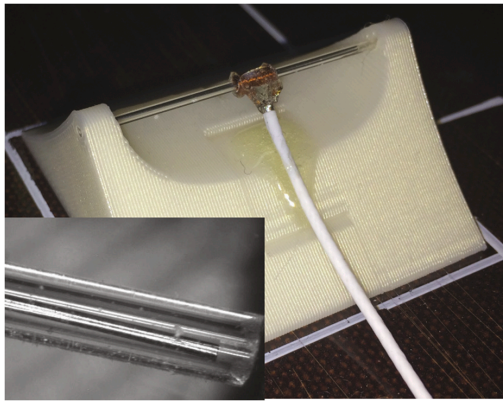


Fig. 4. A single 0.2 mm wire in glass capillary, with a short 500-turn pickup coil (the detail of the wire end in the inset).

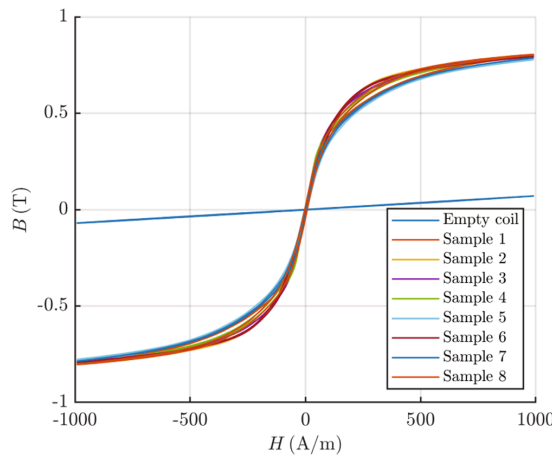


Fig. 5. Average hysteresis loop of a single wire (the number of measured points was 20 000).

wire ends. From the maximum inductance $L_{\text{core}} = 41 \mu\text{H}$ we can calculate, using (4), that the maximum effective magnetometric permeability is

$$\mu_{em} = \frac{41 - 0.4}{0.4} * 30.25 = 3070$$

Similarly, for the short coil we measured $L_{\text{air}} = 0.92 \mu\text{H}$, $L_{\text{core}} = 3.32 \text{ mH}$ and the maximum effective fluxmetric permeability was

$$\mu_{ef} = \frac{3.32 - 0.092}{0.092} * 45 = 1579$$

It is clear that in this case the effective permeability does not provide a good estimate of the real magnetometric apparent permeability. The large difference can be explained by the fact that the source field of the solenoid is far from homogeneous: the field at the end is only one half of the field in the center.

It should be noted that the permeability values at higher frequencies drop due to the eddy currents – this is documented by the frequency dependence of the inductance, shown in Fig. 9. Both the material non-linearity and the frequency dependence should be considered in the future for a precise simulation. However, this non-trivial task is beyond

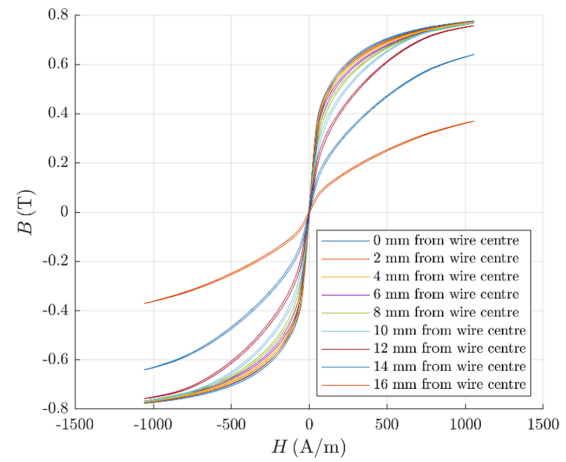


Fig. 6. Local B-H loops measured at different positions of the short coil. The measurement frequency was 1 Hz (the number of measured points was 20 000).

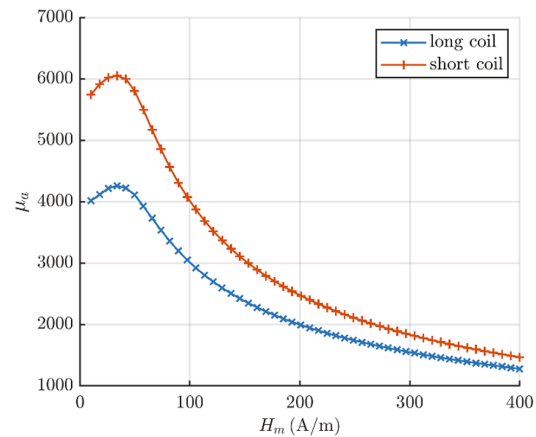


Fig. 7. The amplitude “fluxmetric” permeability of the central part of the wire (measured with the short coil) and the magnetometric apparent permeability (measured with the long coil).

the scope of the present paper, and in all calculations and simulations presented in this paper we only consider the constant permeability.

2.3. A miniature induction sensor with a single wire

An important application of magnetic wires is in a small induction sensor with high spatial resolution. These coils are used in non-destructive evaluation and in speed sensors. Amplification factor a is a measure of the effect of the core

$$a = \Phi_{\text{cored}} / \Phi_{\text{air}} \quad (5)$$

The amplification factor depends on permeability, and it is therefore field dependent.

A good estimate for the amplification factor is

$$a = L_{\text{core}} / L_{\text{air}} \quad (6)$$

If we use the maximum inductance of our long coil, the estimated $a_{\text{max}} = 39.2 / 0.4 = 98$.

The precise value of amplification factor a should be measured for a

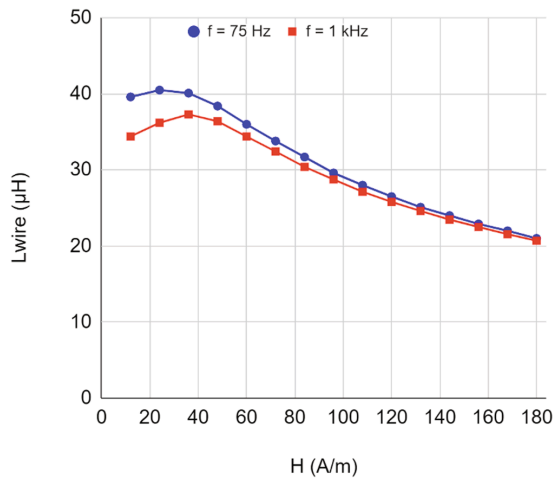


Fig. 8. The inductance L_{core} of the long coils. AC measurement field intensity (calculated from the measurement current).

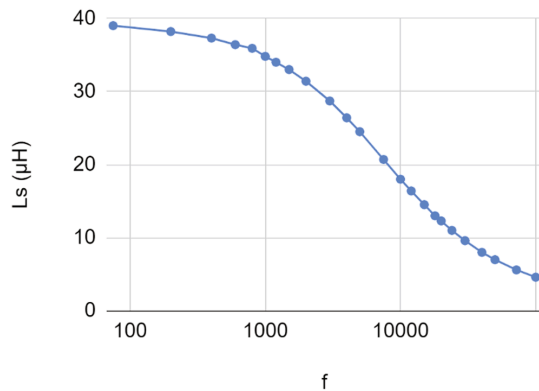


Fig. 9. Inductance vs. Frequency for the “100 mV” measurement range.

homogeneous external field. We measured the field dependence of a in a Helmholtz coil pair (Fig. 10). The measured value fits the estimate very well. It is clear that a simple induction sensor of this type can be used

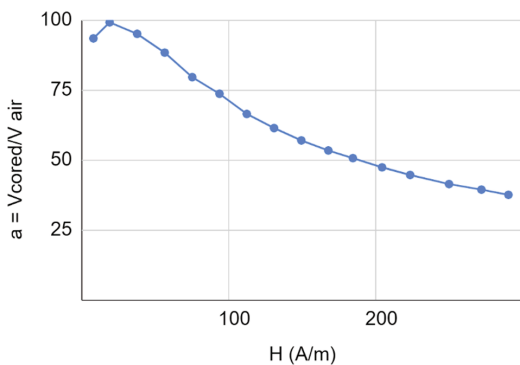


Fig. 10. Amplification factor for a single wire.

only for small fields in the range of the Earth’s field (about 50 A/m). For larger fields, the core starts to be saturated and its sensitivity drops. The sensitivity of an uncompensated sensor is also frequency dependent. For these two reasons, induction sensors usually work in short-circuited mode or with magnetic feedback [31].

Amplification factor a is much smaller than μa , because core cross-sectional area A_{core} is only a fraction of the cross-sectional area of solenoid A_{coil} . On the other hand increasing diameter of the wire core would decrease m and thus increase demagnetization and decrease the sensitivity. Better way how to increase the sensitivity is by using a multi-wire core, as analyzed in the next section.

2.4. FEM simulations of wire arrays

We have performed conventional simulations for a wire array with up to 100 wires.

The time harmonic finite element method is used for the simulations [FEMM, MAXWELL/ANSYS]. 2D FEM is enough with an axisymmetric configuration for a no wire model (including only a coil) and with a single wire in the center. 3D FEM analysis is necessary for modeling multi wires. The adaptive mesh generation method is used to reduce the energy error of the model below 0.125% and to obtain precise magnetic results. As the wires are distributed in a hexagonal-shape form, we consider only 1/12th of the whole model in the simulations, due to symmetry. This helps to reduce the size of the model and to decrease the simulation time, especially in 3D.

2.5. Measurement on a small wire array (7 wires)

The effects of different geometric arrangements of multi-wire cores were evaluated on a large-scale model consisting of the permalloy wires mentioned above into a 3D printed honeycomb matrix (Fig. 11). The matrix can contain up to 91 wires with pitch $p = 1.6$ mm. A pickup coil ($D = 18.1$ mm, $l = 30$ mm, $N = 303$ turns) is wound around the cores.

First, we measured the sensitivity of the pickup coil with a 7-wire array core with a different pitch. An example of two array configurations is shown in Fig. 12, and the measured results are shown in Fig. 12. The amplification factor defined in (5) is shown on the right axis. The absolute voltages were 1.98 mV for the air coil, 2.73 mV for the coil with 1 wire, and from 4.07 mV to 6.19 for the coil with 7 wires, depending on their pitch. The increase in sensitivity with increasing pitch is due to the decrease in magnetostatic coupling and the corresponding decrease in demagnetization (Fig. 13).

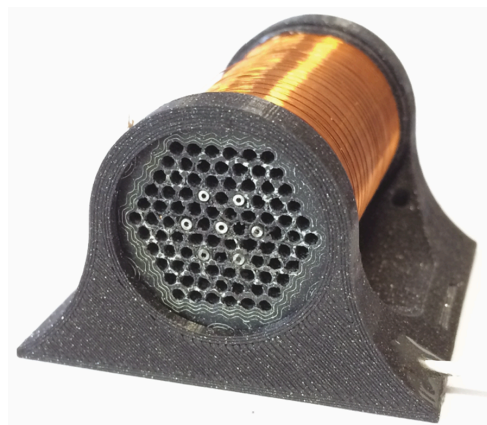


Fig. 11. A plastic matrix with seven wires spaced at 3 mm.

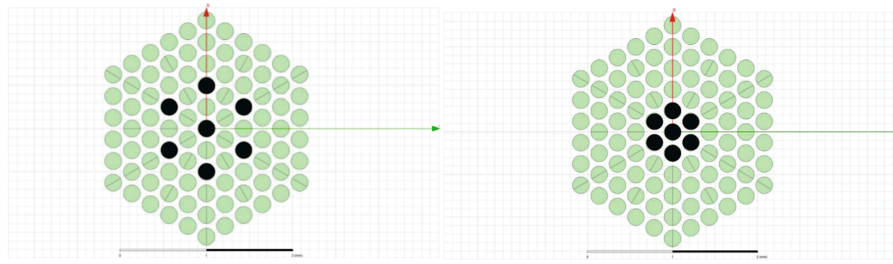


Fig. 12. Seven wires in a honeycomb matrix: an example of two configurations with different pitches.

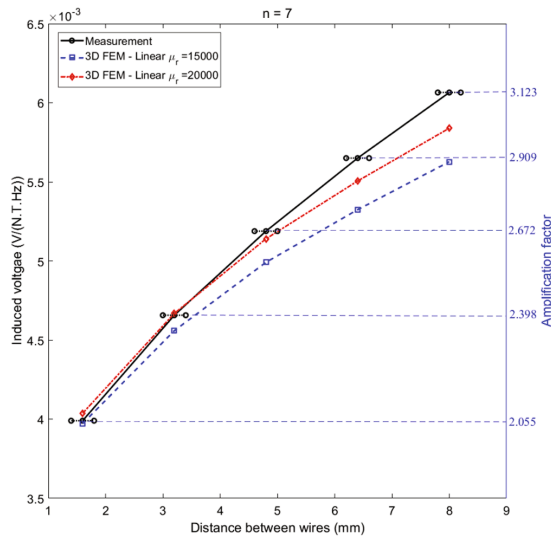


Fig. 13. The measured normalized induced voltage (left axis) and the calculated amplification factor (right axis) as a function of the wire pitch for 7 wires. The horizontal error bars represent ± 0.4 mm uncertainty of the wire distance. The measured field was 30.6 A/m (38 μ T), 97 Hz.

2.6. Measurements for medium-size wire arrays (up to 91 wires)

For these measurements we used the honeycomb matrix shown in Fig. 11. Starting from an empty matrix, we added wires starting from the center, and we measured the voltage induced into the pickup coil (Fig. 14). From these values, we can again calculate and measure amplification factor a and the apparent permeability for the central wire (both magnetometric and fluxmetric). For a wire array, the amplification factor is the collective apparent permeability of the whole core as seen by the pickup coil. This means that the coil will have the sensitivity of a if it is filled by a homogeneous medium with effective permeability of a .

3. Conclusions

We have calculated and plotted the magnetometric and fluxmetric apparent permeability and the demagnetization factor of single magnetic wires using FEM. Our results fit well with the demagnetization factors calculated by a completely different method in [6]. Unlike [6], we have also calculated the apparent permeability, and we have provided more datapoints for geometries and permeability values relevant to sensors. We have verified the accuracy of eq. (3) as a universal relation between the demagnetization factor and the apparent permeability.

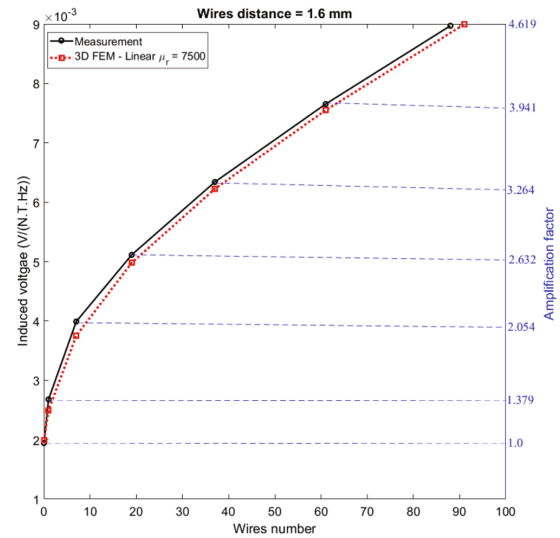


Fig. 14. Induced voltage vs. number of wires measured in a 30.6 A/m, 97 Hz field.

The maximum deviation between this simple analytical formula and our FEM calculations was 0.03%. We have also shown that, as concerns the wire geometry, the effective permeability calculated from the inductance is not a good estimate for the apparent permeability, but that the effective permeability is close to the amplification factor for inductive sensors. We have only briefly mentioned the influence of the non-linearity and the frequency dependence the magnetic material on the apparent permeability and demagnetization factor, which we will plan to investigate in a separate study. We have also shown that wire-based induction sensors should work either in a short-circuited mode or with magnetic feedback.

We have extended the concept of apparent permeability to a wire array, which will allow the systematic design of multiwire magnetic sensors, mainly induction sensors and fluxgates. FEM calculations have been verified on physical models for two scenarios: an array of 7 sensors with changing pitch, and an array of 1 to 91 sensors with a constant pitch. The achieved accuracy of 10% was limited by the fact that we used a linear model of the material.

CRediT authorship contribution statement

P. Ripka: Conceptualization, Formal analysis, Methodology, Writing - review & editing. V. Grim: Data curation. M. Mirzaei: Writing - review & editing.

Declaration of Competing Interest

The authors declare that they have no known competing financial interests or personal relationships that could have appeared to influence the work reported in this paper.

Acknowledgement

This work was supported by the Grant agency of the Czech Republic within the framework of the "NanoFluxGate" project (GACR 20-27150S).

References

- [1] R.M. Bozorth, D.M. Chapin, Demagnetizing factors of rods, *J. Appl. Phys.* 13 (1942) 7.
- [2] D.X. Chen, E. Pardo, A. Sanchez, Fluxmetric and magnetometric demagnetizing factors for cylinders, *J. Magn. Magn. Mater.* 306 (1) (2006) 135–146.
- [3] P. Ripka, *Magnetic sensors and magnetometers*, Artech House, Boston, London, 2001.
- [4] E.P. Harrison, G.L. Turney, H. Rowe, Electrical Properties of Wires of High Permeability, *Nature* 135 (1935) 1.
- [5] M. Knobel, M. Vazquez, and L. Kraus, "Giant magnetoimpedance," *Handbook of Magnetic Materials*, K. Buschow, ed.: Elsevier, 2003.
- [6] R.S. Beach, N. Smith, C.L. Platt, et al., Magneto-impedance effect in NiFe plated wire, *Appl. Phys. Lett.* 68 (19) (1996) 2753–2755.
- [7] H. Garcia-Miquel, S.M. Bhagat, S.E. Lofland, et al., Ferromagnetic resonance in FeCoNi electroplated wires, *J. Appl. Phys.* 94 (3) (2003) 1868–1872.
- [8] G.V. Kuryandskaya, R. El Kammouni, S.O. Volchkov, et al., Magnetoimpedance Sensitive Elements Based on CuBe/FeCoNi Electroplated Wires in Single and Double Wire Configurations, *IEEE Trans. Magn.* 53 (4) (2017) 15.
- [9] S.V. Shcherbinin, R. Perez, M. Vazquez, et al., Ferromagnetic Resonance in Electroplated CuBe/FeCoNi and Amorphous CoFeSiB Wires, *IEEE Trans. Magn.* 56 (4) (2020).
- [10] F.E. Atalay, H. Kaya, S. Atalay, Giant magnetoimpedance effect in electroplated CoNiFe/Cu wires with varying Ni, Fe and Co content, *J. Alloy. Compd.* 420 (1–2) (2006) 9–14.
- [11] M. Butta, P. Ripka, G. Infante et al., "Bi-metallic magnetic wire with insulating layer as core for orthogonal fluxgate," *IEEE Transactions on Magnetics*, vol. 45, no. 10, pp. 4443–4446, 2009, 2009.
- [12] M. Janosek, M. Butta, M. Dressler, et al., 1-pT Noise Fluxgate Magnetometer for Geomagnetic Measurements and Unshielded Magnetocardiography, *IEEE Trans. Instrum. Meas.* 69 (5) (2020) 2552–2560.
- [13] R. Gemperle, L. Kraus, J. Schneider, Magnetization Reversal in Amorphous $(\text{Fe}_{1-x}\text{Ni}_x)_{80}\text{P}_{10}\text{B}_{10}$ Microwires, *Czech J. Phys.* 28 (10) (1978) 1138–1145.
- [14] J. Gonzalez, N. Murillo, V. Larin, et al., Magnetic bistability of glass-covered Fe-rich amorphous microwire: influence of heating treatments and applied tensile stress, *Sens. Actuators A-Phys* 59 (1–3) (Apr 1997) 97–100.
- [15] A. Zhukov, M. Ipatov, P. Corte-Leon, et al., Soft magnetic microwires for sensor applications, *J. Magn. Magn. Mater.* 498 (2020).
- [16] H. Garcia-Miquel, J. Carbonell, J. Sanchez-Dehesa, Left handed material based on amorphous ferromagnetic microwires tunable by dc current, *Appl. Phys. Lett.* 97 (9) (2010).
- [17] G.S. Makeeva, O.A. Golovanov, The electrodynamic analysis of propagation constants of electromagnetic waves in 3D magnetic nanowire lattices under the magnetic resonance conditions at microwaves, *J. Commun. Technol. Electron.* 61 (1) (2016) 1–9.
- [18] S.G. Cho, B. Yoo, K.H. Kim, et al., Magnetic and Microwave Properties of NiFe Nanowires Embedded in Anodized Aluminum Oxide (AAO) Templates, *IEEE Trans. Magn.* 46 (2) (2010) 420–423.
- [19] O. Dmytriiiev, U.A.S. Al-Jarah, P. Gangmei, et al., Static and dynamic magnetic properties of densely packed magnetic nanowire arrays, *Phys. Rev. B* 87 (17) (2013).
- [20] H. Chiriac, N. Lupu, G. Stoian, et al., Ultrathin Nanocrystalline Magnetic Wires, *Crystals* 7 (2) (2017) 13.
- [21] M. Vázquez, *Magnetic Nano- and Microwires: Design, Synthesis, Properties and Applications*: Elsevier Science, 2015.
- [22] D. Robbes, C. Dolabdjian, Y. Monfort, Performances and place of magnetometers based on amorphous wires compared to conventional magnetometers, *J. Magn. Magn. Mater.* 249 (1–2) (2002) 393–397.
- [23] X.P. Li, J. Fan, J. Ding, et al., Multi-core orthogonal fluxgate sensor, *J. Magn. Magn. Mater.* 300 (1) (2006) E98–E103.
- [24] F. Jie, N. Ning, W. Ji, et al., Study of the Noise in Multicore Orthogonal Fluxgate Sensors Based on Ni-Fe/Cu Composite Microwire Arrays, *IEEE Trans. Magn.* 45 (10) (2009) 4451–4454.
- [25] H. Chiriac, D.D. Herea, S. Corodeanu, Microwire array for giant magnetoimpedance detection of magnetic particles for biosensor prototype, *J. Magn. Magn. Mater.* 311 (1) (2007) 425–428.
- [26] V.M. De La Prida, H. Garcia-Miquel, G.V. Kuryandskaya, Wide-angle magnetoimpedance field sensor based on two crossed amorphous ribbons, *Sens. Actuators A-Phys.* 142 (2) (2008) 496–502.
- [27] J. Fan, J. Wu, N. Ning, et al., Magnetic Dynamic Interaction in Amorphous Microwire Array, *IEEE Trans. Magn.* 46 (6) (2010) 2431–2434.
- [28] F. Primdahl, B. Hernando, O.V. Nielsen, et al., Demagnetizing Factor and Noise in the Fluxgate Ring-core Sensor, *Journal of Physics E-Scientific Instruments* 22 (12) (1989) 1004–1008.
- [29] M. De Graef, M. Beleggia, The fluxgate ring-core demagnetization field, *J. Magn. Magn. Mater.* 305 (2) (Oct 2006) 403–409.
- [30] J. Kubik, P. Ripka, Racetrack fluxgate sensor core demagnetization factor, *Sensors and Actuators A-Physical* 143 (2) (2008) 237–244.
- [31] S. Tumanski, Induction coil sensors - a review, *Meas. Sci. Technol.* 18 (3) (2007) R31–R46.

4.3 A Simplified 2D Equivalent Model for Magnetic Wire Array

This paper provides further elaboration on the multi-wire geometry and its differences from a bulk magnetic core. Again, wire counts ranging from 1 to 91 were analyzed by FEM and compared to experimental results. Operation only in linear region is considered here, with permeability set as a constant during simulations. Experiments were done also in the linear region, with the generated flux significantly below the saturation flux density of the material.

The key point of this paper is the derivation and verification of dimension reduction mechanism, which transform a 3D structure into two dimensions (r and z). This transformation is needed to keep the number of nodes within the limits of computer memory in case of arrays significantly larger than 91 wires (the whole electrodeposited membrane contains millions of wires).

My work consisted of mechanical design of the experimental bobbins, coil winding, and performing the experimental verification.

A Simplified 2-D Equivalent Model for Magnetic Wire Array

Mehran Mirzaei^{1b}, Pavel Ripka^{1b}, and Vaclav Grim^{1b}

Faculty of Electrical Engineering, Czech Technical University in Prague, 16627 Prague, Czech Republic

Demagnetization factor and corresponding apparent permeability for multiwire arrays using the 3-D finite element method (FEM) are calculated in this article. The effect of distance between magnetic wires on the demagnetization factor and apparent magnetic permeability is studied for various values of relative magnetic permeability. The simulations are compared with experimental results on arrays up to 91 wires. A novel simplified equivalent 2-D model for wire arrays is presented in this article, as a fast method for calculations. The simplified axisymmetrical model consists of a set of hollow cylinders with equivalent volume. The results of the proposed simplified 2-D model fit very well the full 3-D FEM simulations and experimental results. Two different hexagonal and square arrangements for wires are considered both for the simulations and the measurements.

Index Terms—2-D and 3-D finite element method (FEM), apparent permeability, demagnetization, multiwires.

I. INTRODUCTION

THE calculation of demagnetization factor and apparent permeability of the magnetic core is essential for induction and fluxgate sensor design [1]. Demagnetization factors for ellipsoidal and non-ellipsoidal shapes of a single element were studied in detail in various publications [1]–[13]. For instance, the demagnetization factor for the sphere can be analytically calculated and it is 1/3 [2]. The demagnetization factor for single ellipsoidal has closed-form equation and does not depend on permeability [1]. The apparent permeability is independent of permeability only for very high relative permeability values. The demagnetization factor for the non-ellipsoidal shape of a single element, for example, solid cylindrical wire and hollow cylinder, cannot be described in single closed-form formula; however, approximations using curve fitting were used [1], [4], [6]. The magnetic permeability of wire has a high impact on the demagnetization [7], [8]. The finite element method (FEM) or complex analytical modeling is common methods to take into account magnetic permeability effects on the demagnetization. The demagnetization factors are categorized into two cases: fluxmetric (ballistic or central) and magnetometric, which consider the whole volume. Magnetometric demagnetization factor is of interest in this article. In our recent article [14], we analyzed the induced voltage of a pickup coil with a core consisting of a hexagonal wire array of up to 91 wires using 3-D FEM. Magnetic nanowire arrays are fabricated by electroplating into the pores in membranes [15]. These arrays contain millions of wires in every square millimeter. 3-D FEM analysis of such complex arrays is not possible due to the computational complexity. We therefore used intuitive simplified 2-D model to estimate the demagnetization factor of these arrays.

The aim of this article is to rigorously define the equivalent 2-D model and verify it both by 3-D modeling and by

experiment on the wire arrays up to 91 wires. We examine the induced voltage in the pickup coils, demagnetization, and apparent permeability for hexagonal and square lattices. Magnetometric demagnetization factor and corresponding apparent permeability are analyzed and calculated using 3-D FEM and 2-D equivalent model. Various numbers of wires are considered and both linear magnetic permeability and nonlinear $B-H$ curve are used for the simulations. The effect of distance between magnetic wires (pitch) on the demagnetization factor and apparent magnetic permeability is studied for various values of relative magnetic permeability.

Using equivalent hollow cylinders instead of wire array would help to simplify the 3-D model to a 2-D model to simulate: 1) large number of wires and 2) model with very fine mesh for higher accuracy, which is problematic in 3-D modeling because of limited memory issue.

II. HOLLOW CYLINDER VERSUS SOLID CYLINDER

Equation (1) depicts the relationship between apparent permeability μ_a , demagnetization N , and relative magnetic permeability μ_r

$$\begin{aligned} \mu_a &= \mu_r / (1 + N \cdot (\mu_r - 1)), \quad \mu_r \rightarrow \infty \Rightarrow \mu_a \approx 1/N \\ N &= (\mu_r / \mu_a - 1) / (\mu_r - 1). \end{aligned} \quad (1)$$

To compare demagnetization and apparent permeability of solid cylinder and hollow cylinder with the same volume, we first used approximate equation of fluxmetric demagnetization factor N_s according to the formula derived in [4] and [5] for the solid cylinder

$$\begin{aligned} N_s(m, \chi) &= N_1(m) \cdot 2/\pi \cdot \tan^{-1}(22\chi/m^{1.3}) + N_2(m) \\ &\quad \cdot (1 - 2/\pi \cdot \tan^{-1}(22\chi/m^{1.3})) \\ \chi &= \mu_r - 1, \quad m = L/D \end{aligned} \quad (2)$$

$$E(m) = 1/(1 - m^2) \cdot (1 - m/\sqrt{1 - m^2} \cos^{-1}(m)), \quad 0 \leq m < 1 \quad (3)$$

$$E(m) = 1/(m^2 - 1) \cdot (m/\sqrt{m^2 - 1} \ln(m + \sqrt{m^2 - 1}) - 1), \quad m > 1 \quad (4)$$

Manuscript received March 16, 2021; revised May 17, 2021; accepted May 26, 2021. Date of publication June 2, 2021; date of current version January 20, 2022. Corresponding author: M. Mirzaei (e-mail: mirzameh@fel.cvut.cz).

Color versions of one or more figures in this article are available at <https://doi.org/10.1109/TMAG.2021.3085485>.

Digital Object Identifier 10.1109/TMAG.2021.3085485

0018-9464 © 2021 IEEE. Personal use is permitted, but republication/redistribution requires IEEE permission. See <https://www.ieee.org/publications/rights/index.html> for more information.

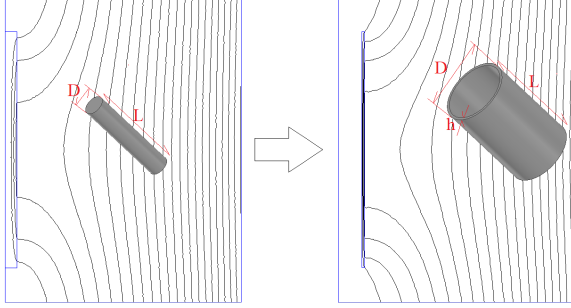


Fig. 1. Magnetic flux distributions in solid cylindrical wire and hollow cylinder or wire with same axial length and volume.

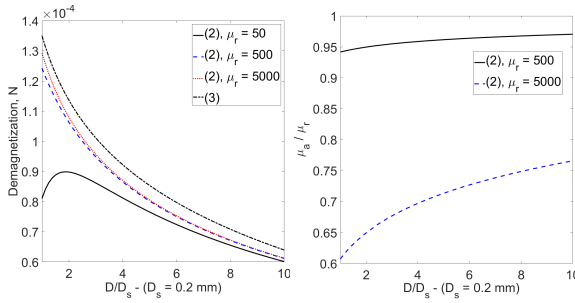


Fig. 2. Demagnetization factor (left) and apparent permeability to relative permeability ratio (right) of the hollow cylinder versus normalized diameter D/D_s ($D_s = 0.2$ mm) calculated by (2)–(7)— D (mm) is the outer diameter of the hollow cylinder and length $L = 36$ mm (solid cylinder diameter is 0.2 mm and the hollow cylinder has an equal cross-sectional area as a solid cylinder).

$$N_1(m) = E(m) \cdot (1 + 2.35 \ln(1 + 0.137m)) / (1 + 2.28 \ln(1 + 0.284m)), \quad \mu_r > 1 \quad (5)$$

$$N_2(m) = E(m) \cdot 1 / (1 + 2.15 \ln(1 + 0.326m)), \quad \mu_r \approx 1. \quad (6)$$

This simplifies for infinite permeability to

$$N_s(m) = 1/m^2 \cdot (\ln(1.2m) - 1) \quad (7)$$

where D is the diameter of the wire and L is the axial length of the wire as shown in Fig. 1.

The demagnetization factor N_h of the hollow cylinder with shell thickness h is calculated according to [4]

$$N_h = (D^2 - (D - 2h)^2) / D^2 N_s = (1 - (1 - 2h/D)^2) N_s. \quad (8)$$

From (8), it is clear that $N_h < N_s$.

In Section II, we consider 0.2 mm diameter (D) and 36 mm (L) long magnetic wire ($m = L/D = 180$) and calculate the demagnetization factor and apparent permeability of hollow cylinder with the equal cross-sectional area as a solid cylinder or wire.

The magnetic flux distribution in Fig. 1 shows that flux is distributed more uniform in a hollow cylinder than a solid cylinder because the shell thickness is smaller than solid cylinder radius. Fig. 2 shows that the demagnetization factor N_h of

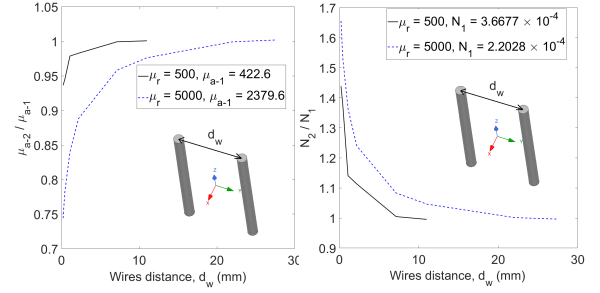


Fig. 3. Ratio of apparent permeability μ_{a-2} and demagnetization factor N_2 of two cylindrical wires to those of single wire (μ_{a-1} and N_1) as a function of the wire distance.

the hollow cylinder calculated using (8) is decreasing versus normalized hollow cylinder diameter D with original solid cylinder diameter $D_s = 0.2$ mm, and apparent permeability increases with increasing normalized diameter D/D_s (Fig. 2).

III. WIRE ARRAY

A. Two Wires

Permalloy wires with 36 mm length and diameter 0.2 mm are used for the physical modeling and measurement in this section. Apparent permeability and magnetometric demagnetization factor are calculated based on the averaging formula for volume integral of the axial component of flux density B_z in wire volume V_w using (9). B_{air} is the magnetic flux density in the air

$$\mu_a = \left(\int B_z dV \right) / (B_{\text{air}} V_w). \quad (9)$$

First, only two wires are considered to evaluate their magnetostatic coupling. The results are shown in Fig. 3 calculated using magnetostatic 3-D FEM, which shows increasing apparent permeability and decreasing demagnetization with increasing the distance of the wires. The magnetostatic coupling is stronger for higher relative magnetic permeability $\mu_r = 5000$ in comparison with $\mu_r = 500$ and therefore, the apparent permeability μ_{a-2} reduces, and demagnetization N_2 decreases more for the same wire distance.

B. Multiwires

Two possible regular arrangements of wires with equal distances could be hexagonal or square lattices [16], [17]. It is obvious that for the same wire distance (pitch), the wire density is higher for the hexagonal arrangement in comparison with the square arrangement.

The experimental setup was built to test experimentally the effects of the number of magnetic wires and their distances. Fig. 4 shows a solenoid coil wound around seven wires with the hexagonal arrangement and five wires with the square arrangement. The coils with wires are placed in the Helmholtz coils to measure the induced voltage (Fig. 5).

Time harmonic method is used for 3-D FEM simulations to calculate induced voltages, apparent permeability, and demagnetization. The wires and pickup coil are only considered in

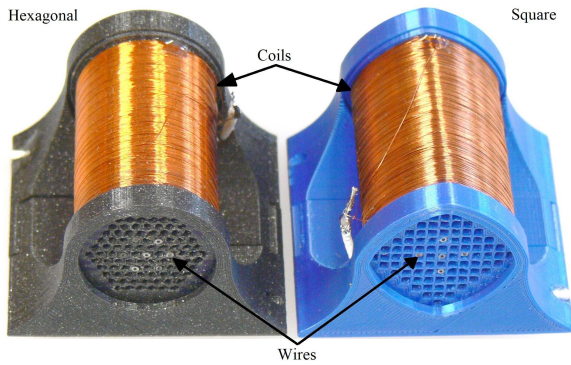


Fig. 4. Experimental model of pickup coils and permalloy wires with the hexagonal and square arrangement.

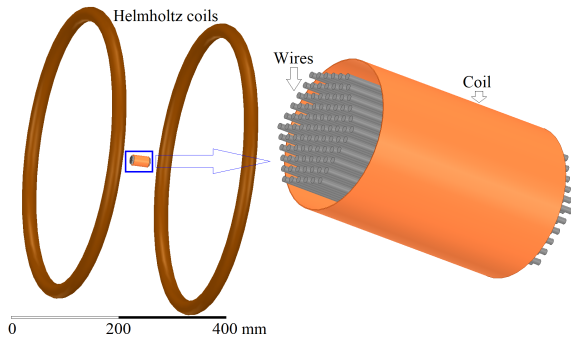


Fig. 5. Computational model of pickup coil and permalloy wires with the Helmholtz coils to generate a uniform field.

the model and the Helmholtz coils are substituted by a smooth source field in the air with a value of $34.4 \mu\text{T-rms}$ as wires and pickup coil dimensions are very small in comparison with Helmholtz coil dimensions. The computational model in 3-D FEM is reduced to 1/24th of the full model for hexagonal array and 1/16th for a square array to decrease the amount of mesh because of axial and circumferential symmetry. The values of induced voltage (normalized by the number of turns of the coil, magnetic flux density generated by Helmholtz coil and frequency) shown in Fig. 6 increase with increasing wire distance as apparent permeability of magnetic core increases and demagnetization decreases. The magnetic simulation is shown for $\mu_r = 17500$, which gives the best match between measurements and 3-D FEM for both hexagonal and square arrays of wires.

The apparent permeability is higher, and demagnetization is lower for the square array with five wires in comparison with the hexagonal array with seven wires. The lower number of wires causes higher apparent permeability and lower demagnetization. The influence of the increasing distance of wires on demagnetization and apparent permeability is the same as increasing hollow cylinder diameter in Figs. 1 and 2.

C. 2-D Equivalent Model

Regular hexagonal and square distribution of permalloy wires could be substituted using a hollow cylinder as shown

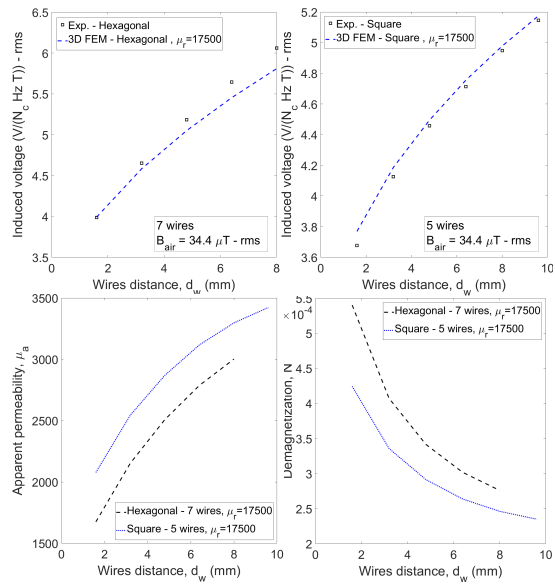


Fig. 6. Normalized induced voltage versus wire distance for hexagonal (seven wires in Fig. 4) and square (five wires in Fig. 4) array of wires (up) and their apparent permeability and demagnetization (bottom)—3-D FEM with constant permeability.

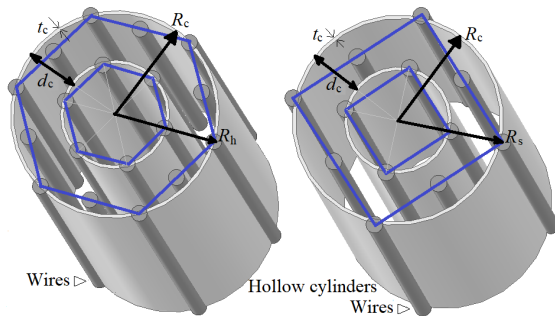


Fig. 7. Schematic model of wires for hexagonal array (left) and square array (right) and their equivalent hollow cylinder model for 2-D analysis.

in Fig. 7 to simplify the 3-D FEM model to a 2-D FEM model with axisymmetric configuration.

The mean radius R_c of each hollow cylinder is calculated in (10) for hexagon and (11) for square so that the corresponding circle area has the same value as areas of the depicted hexagon and square in Fig. 7 for each array of wires. The thickness of the hollow cylinder t_c in (10) and (11) is calculated that each hollow cylinder volume is equal to the corresponding array of wires. Practically, all hollow cylinders have the same distance d_c between each other and the same thickness t_c because of the regular hexagonal and square distribution of wires

$$R_c = \sqrt{\frac{3\sqrt{3}}{2\pi}} \cdot R_h, \quad d_c = \sqrt{\frac{3\sqrt{3}}{2\pi}} \cdot d_w, \quad t_c = \frac{3D_w^2}{4d_c} \quad (10)$$

$$R_c = \sqrt{\frac{2}{\pi}} \cdot R_s, \quad d_c = \sqrt{\frac{2}{\pi}} \cdot d_w, \quad t_c = \frac{D_w^2}{2d_c} \quad (11)$$

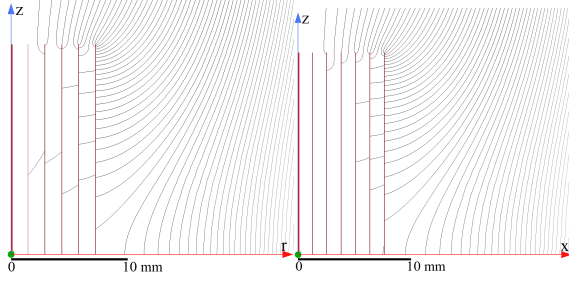


Fig. 8. Magnetic flux distribution in a 2-D axisymmetric model of hexagonal distributions of 91 wires with five arrays (left) and square distribution of 85 wires with six arrays (right).

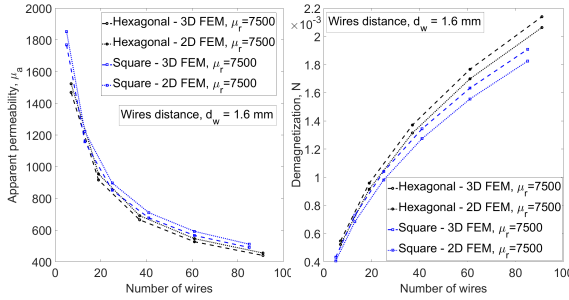


Fig. 9. Apparent permeability and demagnetization calculated using 2-D and 3-D FEM versus the number of wires with hexagonal and square distribution—constant permeability.

where d_w and D_w are the distance of wires and diameter of wires, respectively. R_h and R_s are circumradius of hexagon and square, respectively.

Fig. 8 presents 2-D magnetic flux distribution for a hexagonal array of wires with 91 wires and a square array of wires with 85 wires using 2-D axisymmetric time harmonic FEM.

The calculated hollow cylinders corresponding to the square array of wires with $d_w = 1.6$ mm distance have a $d_c = 1.28$ mm distance and $t_c = 15.7$ μm thickness, and they are 1.46 mm and 20.6 μm for a hexagonal array of wires. The comparisons between 3-D FEM and 2-D axisymmetric FEM for apparent permeability and demagnetization versus the number of wires are shown in Fig. 9. The small discrepancy is mainly caused by less fine mesh in 3-D model in comparison with 2-D model.

IV. INDUCED VOLTAGE

The calculated induced voltages using the 2-D equivalent model versus the number of wires with wire distance $d_w = 1.6$ mm are investigated. The linear magnetic permeability and nonlinear $B-H$ curve are both considered for the modeling to evaluate the accuracy of the 2-D equivalent model based on hollow cylinders for the multiwire arrays.

A. Linear Simulations and Constant Permeability

Fig. 10 shows normalized induced voltage versus the number of wires, comparing experimental results, 3-D FEM and

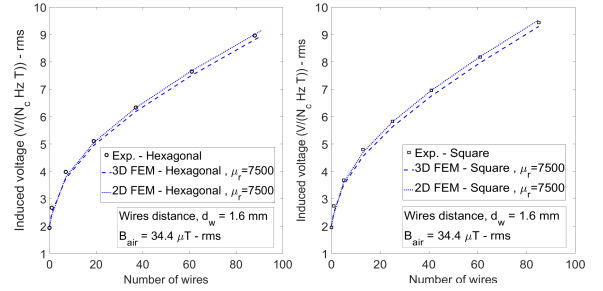


Fig. 10. Induced voltage versus the number of wires for hexagonal (up to 91 wires in Fig. 5) and square (up to 85 wires) array of wires—3-D FEM and 2-D FEM with constant permeability versus experimental results.

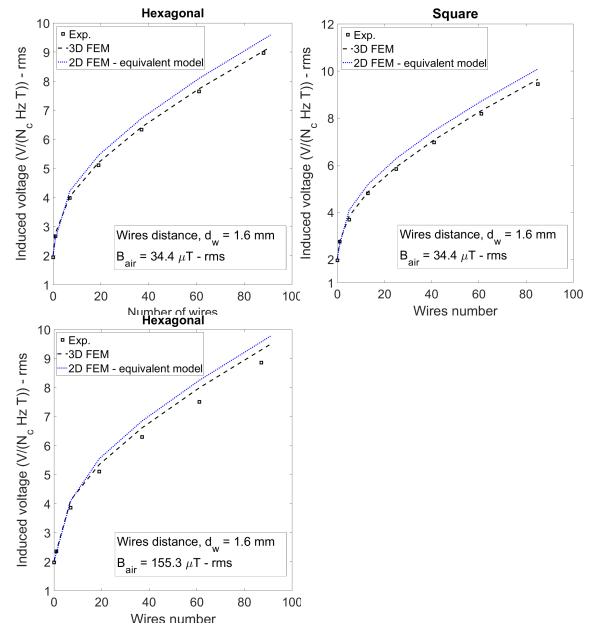


Fig. 11. Induced voltage versus the number of wires for hexagonal (up to 91 wires in Fig. 5) and square (up to 85 wires) array of wires—3-D FEM and 2-D FEM with nonlinear $B-H$ curve versus experimental results.

2-D FEM, using equivalent model under homogenous magnetic field in the air with $B_{air} = 34.4$ μT -rms. The 2-D FEM matches with 3-D FEM and experiments with higher accuracy for induced voltage in comparison with results shown in Fig. 9. The reason is that the induced voltage in the pickup coil is less sensitive to the mesh quality.

B. Nonlinear $B-H$ Curve

A typical $B-H$ curve for permalloy material of measured wires in this article is utilized to model nonlinearity [18]. The following analytical formulas [19] in (12) and (13) are used in FEM simulations for smooth modeling of the $B-H$ curve. Using analytical functions in (12) and (13) helps to generate a $B-H$ data for smooth magnetization curve, which is essential

for accurate FEM analysis of permalloy wires

$$B = J + \mu_0 H, \quad \mu_r = \frac{1}{\mu_0} \frac{B}{H} = \frac{1}{\mu_0} \frac{J}{H} + 1 \quad (12)$$

$$\mu_r = \frac{1}{\mu_0} \frac{a_1 H^{b_1-1} + a_2 H^{b_2-1}}{c_1 H^{b_1} + c_2 H^{b_2} + 1} + 1. \quad (13)$$

The parameters a_1 , a_2 , c_1 , c_2 , b_1 , and b_2 in (13) are $14.1 \cdot 10^{-3}$, $3.11 \cdot 10^{-3}$, $43.2 \cdot 10^{-3}$, $5.48 \cdot 10^{-3}$, 2.17, and 3.78, respectively. The results of the induced voltage at applied fields 34.4 and 155.3 μT are shown in Fig. 11. The discrepancy is higher between 3-D FEM and 2-D FEM for nonlinear simulations in comparison with the linear simulations in Fig. 10. However, the accuracy of the equivalent 2-D model is in an adequate range in comparison with experimental results. Utilizing a 2-D equivalent model could help to decrease simulation time especially when a nonlinear B - H curve should be used, for example, for fluxgate sensors analysis, design, and optimization.

V. CONCLUSION

Apparent permeability and magnetometric demagnetization factors of cylindrical wire arrays were analyzed and calculated. The distance between wires is a critical factor for apparent permeability and demagnetization. Two different wire lattices are considered: hexagonal and square. The difference of apparent permeability and demagnetization factor for hexagonal and square arrangements of wires decreases when wire distance decreases as magnetostatic coupling between wires becomes higher and multiwire performs as a single solid wire. Increasing wire distance increases the apparent permeability and decreases the demagnetization factor, which is similar to the comparison between the solid cylinder and hollow cylinder.

The novel 2-D equivalent model based on hollow cylinders to replace the 3-D model was proposed and verified by measurement. 2-D model could save the time of simulations and number of cells in the mesh and speedup design and optimization of magnetic sensors with multiwire core.

ACKNOWLEDGMENT

This work was supported by the Grant Agency of the Czech Republic through the Nanofluxgate Project under Grant GACR GA20-27150S.

REFERENCES

- [1] P. Ripka, *Magnetic Sensors and Magnetometers*. Norwood, MA, USA: Artech House, Jan. 2001.
- [2] M. Staff, *Electrodynamics of Electrical Machines*. London, U.K.: Iliffe, Mar. 1968.
- [3] S. G. Sandomirskii, "Calculation of short hollow cylinders under magnetization parallel to the generatrix," *Russian Electr. Eng.*, vol. 80, no. 2, pp. 109–112, Feb. 2009.
- [4] S. G. Sandomirskii, "Errors in the classical calculation of the demagnetizing factor for a cylinder," *Russian Electr. Eng.*, vol. 84, no. 7, pp. 376–381, Jul. 2013.
- [5] V. F. Matyuk, A. A. Osipov, and A. V. Strelyukhin, "Central demagnetization coefficient for hollow cylindrical bars made of soft magnetic materials," *Russian J. Nondestruct. Test.*, vol. 43, no. 3, pp. 154–162, Mar. 2007.
- [6] M. Nirei, S. Suzuki, K. Tashiro, and H. Wakiwaka, "Constitution of an approximate equation of demagnetizing factors for cylinder using multiple regression analysis," *J. Jpn. Soc. Appl. Electromagn. Mech.*, vol. 17, no. 3, pp. 449–452, 2009.
- [7] D.-X. Chen, J. A. Brug, and R. B. Goldfarb, "Demagnetizing factors for cylinders," *IEEE Trans. Magn.*, vol. 27, no. 4, pp. 3601–3619, Jul. 1991.
- [8] D.-X. Chen, E. Pardo, and A. Sanchez, "Fluxmetric and magnetometric demagnetizing factors for cylinders," *J. Magn. Magn. Mater.*, vol. 306, no. 1, pp. 135–146, Nov. 2006.
- [9] M. Beleggia, D. Vokoun, and M. De Graef, "Demagnetization factors for cylindrical shells and related shapes," *J. Magn. Magn. Mater.*, vol. 321, no. 9, pp. 1306–1315, May 2009.
- [10] J. Prat-Camps, C. Navau, D.-X. Chen, and A. Sanchez, "Exact analytical demagnetizing factors for long hollow cylinders in transverse field," *IEEE Magn. Lett.*, vol. 3, 2012, Art. no. 0500104.
- [11] B. K. Pugh, D. P. Kramer, and C. H. Chen, "Demagnetizing factors for various geometries precisely determined using 3-D electromagnetic field simulation," *IEEE Trans. Magn.*, vol. 47, no. 10, pp. 4100–4104, Oct. 2011.
- [12] S. H. Im and G. S. Park, "Research on the demagnetization and demagnetizing factors for normal shape of magnetic materials," in *Proc. Compumag*, Daejeon, South Korea, Jun. 2017. [Online]. Available: [https://www.compumag.org/Proceedings/2017_Daejeon/papers/\[PD-A7-11\]_434.pdf](https://www.compumag.org/Proceedings/2017_Daejeon/papers/[PD-A7-11]_434.pdf)
- [13] S. H. Im and G. S. Park, "A research on the demagnetizing factors for magnetic hollow cylinders," in *Proc. 21st Int. Conf. Electr. Mach. Syst. (ICEMS)*, Jeju, South Korea, Oct. 2018, pp. 2629–2632. [Online]. Available: <https://ieeexplore.ieee.org/stamp/stamp.jsp?tp=&arnumber=8548969>
- [14] P. Ripka, V. Grim, and M. Mirzaei, "The apparent permeability and the amplification factor of magnetic wires and wire arrays," *J. Magn. Magn. Mater.*, vol. 527, no. 1, Jun. 2021, Art. no. 167726.
- [15] P. Ripka *et al.*, "Modelling and measurement of magnetically soft nanowire arrays for sensor applications," *Sensors*, vol. 21, no. 1, p. 3, Dec. 2020.
- [16] A. Woodworth, R. Jansen, K. P. Duffy, P. Naghipour, and E. E. Shin, "Creating a multifunctional composite stator slot material system to enable high power density electric machines for electrified aircraft applications," in *Proc. AIAA/IEEE Electr. Aircr. Technol. Symp.*, Cincinnati, OH, USA, Jul. 2018, pp. 1–8.
- [17] P. A. Kyaw, M. Delhommais, J. Qiu, C. R. Sullivan, J.-L. Schanen, and C. Rigaud, "Thermal modeling of inductor and transformer windings including litz wire," *IEEE Trans. Power Electron.*, vol. 35, no. 1, pp. 867–881, Jan. 2020.
- [18] J. Kubik, L. Pavel, P. Ripka, and P. Kaspar, "Low-power printed circuit board fluxgate sensor," *IEEE Sensors J.*, vol. 7, no. 2, pp. 179–183, Feb. 2007.
- [19] M. Mirzaei and P. Ripka, "Analytical functions of magnetization curves for high magnetic permeability materials," *IEEE Trans. Magn.*, vol. 54, no. 11, pp. 1–5, Nov. 2018.

4.4 Multiwire Parallel Fluxgate Sensors

The final paper of this chapter is built upon all preceding publications, but this time the wires are operated in non-linear fashion as a fluxgate sensor. Of particular interest was the noise performance, especially the noise cross-spectrum, because the coupling between adjacent cores is a function of their relative distance.

I contributed to this paper with design of the reconfigurable bobbin with bifilar winding, as well as with verifying the sometimes counterintuitive simulation results (e.g. overunity efficiency in Fig. 5 is not a numerical error, but a result of a difference in integration bounds).

Multiwire Parallel Fluxgate Sensors

Pavel Ripka¹, Diana Hrakova, Vaclav Grim¹, and Mehran Mirzaei¹

Department of Measurements, Faculty of Electrical Engineering, Czech Technical University in Prague, 166 36 Prague, Czech Republic

Fluxgate sensors with straight wire or rod cores are used in nondestructive testing (NDT), portable gradiometers, and sensor arrays and for the detection of small objects. We show that their sensitivity at the voltage output mode depends on the excitation parameters, properties of the core material and geometry, pick-up coil length, but only slightly on the pick-up coil diameter. This finding allows one to design multiwire cores with large wire pitch, which decreases their magnetic interactions and thus reduces demagnetization and correlation of their noise. As a result, using N wires theoretically increases sensitivity N -times, which is not achievable with dense cores. We have demonstrated this tendency for N up to 8 and one type of permalloy wire.

Index Terms—Demagnetization, fluxgate sensors, magnetic field sensors.

I. INTRODUCTION

SOME of the early parallel fluxgate sensors had cores made of straight magnetic wires, and this design is still used in many devices, including portable gradiometers and low-cost sensor arrays in magnetoelastic torque meters [1]. In this article, we deal with fluxgates of parallel type, which have the same direction of the excitation field and the measured field. The other type is transverse fluxgate, which is excited by current flowing through the wire [2]. The magnetic core of parallel type open-core fluxgates typically consists of crystalline permalloy wire with a diameter of around 0.2 mm.

Although straight wire-core fluxgates usually do not achieve the low noise and high offset stability of ring-core fluxgate sensors made of thin tape, they have very small demagnetization due to their slim shape. This brings several advantages which keep these sensors on the market [3].

- 1) Their sensing direction is precisely defined by the direction of the sensor core.
- 2) They have excellent spatial selectivity which is important for the detection of magnetic particles [4], [5].
- 3) High sensitivity allows decreasing the core length.
- 4) The large shape anisotropy gives them low crossfield error [6].

There are also important disadvantages of straight-wire-based sensors: sensor cores with open ends are usually noisier and their offset is less stable with temperature and time than the closed-core sensors. The open rods are more difficult to saturate, so these sensors are also consuming more energy and are more susceptible to perming effects (i.e., offset change after a shock of a large field).

The fluxgate sensitivity depends on magnetic characteristics of the core, excitation parameters, and geometry of the core and the windings. The sensitivity of ring-core and race-track

fluxgate sensors is well understood and described in the literature both for voltage output [7]–[9] and current (short-circuited output) [10], while we are not aware of specific study on the sensitivity of the straight-wire-cored fluxgate sensors. We offer such study in this article for the case of voltage output.

The existing straight-wire-core parallel fluxgate sensors are of the basic two types: single and double wire sensors.

A. Single-Wire Sensors

Sensors with a single open core are utilized for magnetometers using time-domain detection—the device described by Sonoda and Ueda [11], Blazek *et al.* [12], and Ando *et al.* [13] being typical examples—and it is often used for auto oscillation or magnetic multivibrator (or self-oscillating) sensors, such as in [14]. Multiple single-coil fluxgates with a wire core can also be connected in series to measure the field gradient or to provide averaging of the measured magnetic field. This is used in magnetoelastic torque sensors manufactured by Methode. Single cores are also used for some fluxgate-based sensors of electric current [15]. The main problem of the single-core fluxgates is the large spurious voltage at their output which is caused by a large mutual inductance between the excitation and output winding. This spurious voltage at the excitation frequency and odd harmonics can overload the processing electronics, and together with some nonlinearity in the measuring chain, it can create second harmonic signal, which is falsely interpreted as sensor offset.

B. Double-Wire Sensors

The large part of the spurious signal is eliminated in the double-core sensor consisting of wires excited in opposite directions so that their output without field is near zero. An advanced double-rod sensor with a common pick-up coil (Vacquier type) was developed by Moldovanu *et al.* [16] for the INTERBALL satellite instrument [13] and later tested with various kinds of core materials [14]. Foerster [15] used two individual identical pick-up coils connected serially; such a configuration allows easier adjustment of the sensor balance by moving the cores with respect to their coils. A 50 cm long

Manuscript received March 16, 2021; revised May 31, 2021 and June 21, 2021; accepted June 23, 2021. Date of publication June 28, 2021; date of current version January 20, 2022. Corresponding author: P. Ripka (e-mail: ripka@fel.cvut.cz).

Color versions of one or more figures in this article are available at <https://doi.org/10.1109/TMAG.2021.3093017>.

Digital Object Identifier 10.1109/TMAG.2021.3093017

0018-9464 © 2021 IEEE. Personal use is permitted, but republication/redistribution requires IEEE permission.

See <https://www.ieee.org/publications/rights/index.html> for more information.

fluxgate of this type with 10 pT resolution was constructed for a geophysical observatory [16].

Multiple wires have been used for the cores of transverse fluxgates. It was found that the sensor performance is strongly affected by the magnetostatic coupling between the wires which depends on their distance [17]. The demagnetization factor of the core made of several microwires was studied in [18].

In this article, we analyze the possibility to use multiple straight wires or rods in the cores of parallel-type fluxgate. The idea is obvious, but as far as we know it has neither been described in the literature nor applied in the industry. The article is based on measurements of the model cores made of permalloy wires. The model can be upscaled for magnetic rods and downscaled for bundles of microwires and arrays of nanowires.

II. EXPERIMENTAL SETUP

Our model cores consist of 36 mm long, 0.2 mm diameter Permalloy wires with chemical composition $\text{Ni}_{78}\text{Fe}_{15}\text{Cu}_4\text{Mn}_3$. The wires were annealed for 3 h in a dry hydrogen atmosphere at 1080 °C to obtain near-zero magnetostriction. The wires are kept inside the glass tube to protect them from mechanical stress. Five experimental sensor types were designed:

S1: Single-core sensor: both excitation coil and pick-up coil are wound directly on the glass capillary or cylindrical bobbins of various diameters [Figs. 1(a) and 2].

V(1+1): Double-core sensor of Vacquier type: the same excitation coils are connected antiseriably. The cores are inserted into the larger glass pipe serving as a bobbin for pick-up coil around both cores [Fig. 1(b)].

F(1+1): Double-core sensor of Förster type: excitation coils are connected either antiseriably or serially, but each core has its own pick-up coil. These pick-up coils are connected serially or antiseriably [Fig. 1(c)].

Ln: n -Wire core sensor with individual excitation coils and one large common pick-up solenoid using honeycomb array made by 3-D printing.

L(n+n): Two n -wire sensors connected antiseriably.

The parameters of selected sensors and measured sensitivity values are shown in Table I.

Fig. 2 shows examples of the measured fluxgates. The multiwire type has a 3-D printed honeycomb bobbin which allows insertion of different configurations of wires in glass capillaries. Fig. 3 shows examples for dense and loose positioning of eight wires inside the honeycomb.

III. EFFECT OF PICK-UP COIL GEOMETRY

The effect of the pick-up coil diameter and length is shown on the single-wire fluxgate in Fig. 4. Flux line “a” returns back inside pick-up turns 1 and 2 and does not cross pick-up turn 3; therefore, it does not contribute to the flux of these coils. Line “b” contributes only to 2, “c” contributes to 2 and 3, and “d,” and “e” contribute to all 1, 2, and 3.

From that, we may conclude that with the given number of turns, the pick-up coil should be short and slim to maximize the sensitivity. However, also other design aspects should be considered: a shorter coil has higher capacitance and a very

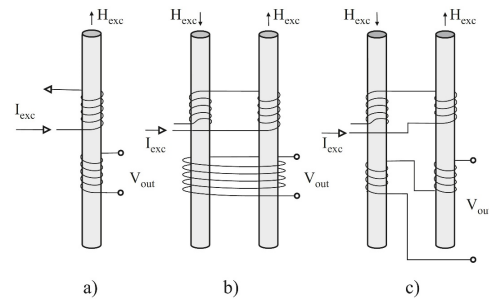


Fig. 1. Fluxgate sensors with wire cores (a) single, (b) Vacquier, and (c) Foerster.

TABLE I
SENSITIVITY OF THE TESTED WIRE-CORE FLUXGATE
SENSORS AT 4 KHZ EXCITATION

sensor	D/d	D	N pick	Max sens (mV/47 μ T)	at V _{exc} (V)
SI-1.5	7.5	1.5	220	10.1	0.91
SI-2.15	10.75	2.15	235	10.6	0.77
SI-11	55	11	235	9.4	0.91
V(1+1)	17.5	3.5	235	24	1
F(1+1)	7.5	1.5	470	28.6	1.05
Ln ... large pickup coil					
1 wire			514	21	1.8
2 w	90	18	514	39	2.2
4 w			514	71	2.8
8 w			514	124	4.5

D is the magnetic wire diameter, D is the diameter and N_{pick} is number of turns of the pickup coil

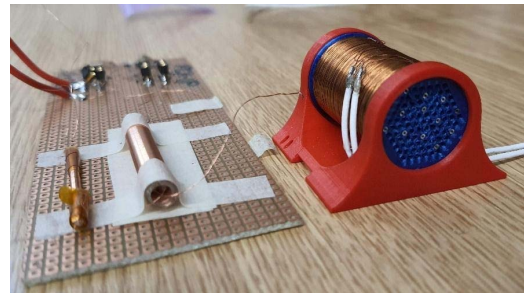


Fig. 2. Experimental fluxgate sensors: S1 single core, V2 Vacquier, and Ln multiwire.

short coil with the same number of turns also cannot be physically slim.

Using 2-D finite element modeling (FEM) simulation, we calculated the pick-up coil flux as a function of pick-up coil diameter D for several material permeabilities. The wire diameter was always $d = 0.2$ mm, and the field source was the excitation coil with an internal diameter of 1.1 mm. Fig. 5 shows the result for the long pick-up coil. Displayed are relative values $\Phi_{\text{pick}}/\Phi_{\text{exc}}$ where Φ_{exc} is the total flux of the excitation coil and Φ_{pick} is the total flux of the

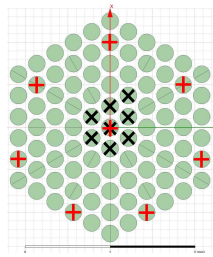


Fig. 3. Multiwire sensors with eight wires with distance (pitch) of 1 (x) and 4 (+).

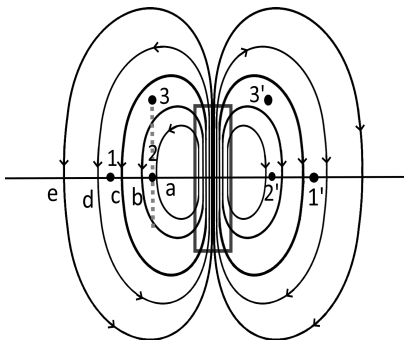


Fig. 4. Single-wire fluxgate: with flux lines a, b, c, d, and e, and three different pick-up turns 1, 2, and 3.

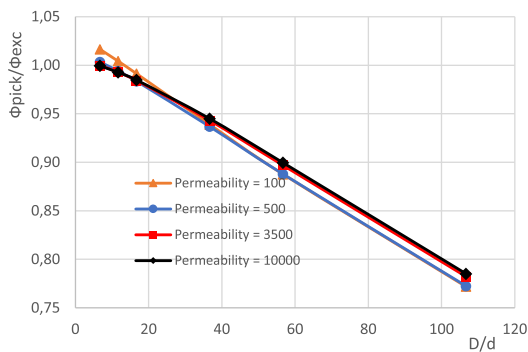


Fig. 5. Relative flux of the long pick-up coil as a function of its relative diameter—values calculated by 2-D FEM.

pick-up coil. The flux of the pick-up coil decreases with an increasing diameter as intuitively expected for fluxgate sensors. This dependence is very similar regardless of the wire permeability. The sensitivities measured on single-wire fluxgate sensors are marked for comparison. Both simulated and measured sensitivity values change only by about 20% in this large range of diameters. This is very different from current-output fluxgate, which shows a much steeper decrease in sensitivity. This finding is fundamental for the design of multicore fluxgate.

As mentioned, a shorter pick-up coil with the same number of turns located in the central part of the core is more sensitive. The reason is that some of the flux lines (type b in Fig. 1) do

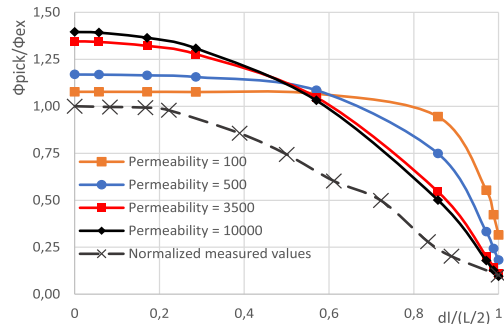


Fig. 6. Relative flux of the very short pick-up coil as a function of its relative position—calculated by 2-D FEM for several values of relative permeability. Lower trace (x): measured relative sensitivity of short coil.

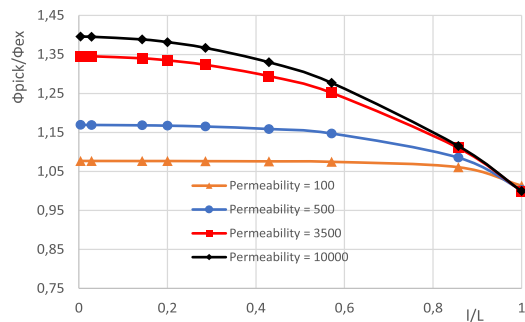


Fig. 7. Relative flux of a pick-up coil as a function of its relative length—values calculated by 2-D FEM for constant number of turns.

not cross end turns of the long coil. In order to examine this effect quantitatively, we calculated by 2-D FEM the relative flux for the short pick-up coil as a function of its position (Fig. 6). In the same figure, we show the measured values of the relative sensitivity of fluxgate with a short coil, which roughly fits with the simulation.

We also calculated the total flux of the pick-up coil as a function of its length l (Fig. 7). In this case, the results depend on the wire permeability, but it is clear that the end parts of the pick-up coil do not contribute much to the sensor sensitivity. The reasonable length of the pick-up coil is 60%–80% of the core length. However, for the relative permeability of the core material $\mu_r = 10000$, the increase of sensitivity caused by shortening of the pick-up coil is only 25%. A similar effect was observed for ring-core and race-track fluxgates [10] and also for the cored induction sensor [21].

IV. EFFECT OF EXCITATION PARAMETERS

The fluxgate sensitivity depends on the frequency and amplitude of the excitation current, as well as on its shape. In our study, the sensor was excited from the generator with an internal resistance of 50 Ω . Due to the low inductance of the excitation coil, this is similar to the current source. The typical measured sensitivity values plotted in Fig. 8 correspond well with the elementary fluxgate theory: for a given frequency, the sensitivity is increasing with excitation amplitude, reaches the maximum, and slowly decreases. The sensitivity increases

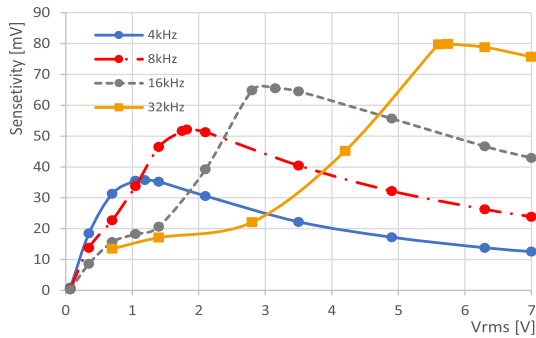


Fig. 8. Sensitivity of sensor $V(1+1)$ as a function of excitation amplitude, excitation frequency is a parameter.

with frequency (until it reaches the limit given by eddy currents and hysteresis losses). The excitation level for the maximum sensitivity is increasing with frequency [1], [23]. These rules do not take into account the parametric amplification which at higher frequencies can be caused by the parasitic capacitance of the pick-up coil. Many fluxgates also use a resonance excitation circuits; that solution reduces the excitation power but introduces strong non-linearity [23]. For open-core fluxgates these resonant effects are usually not important due to the low quality factor of the sensor coils.

V. EFFECT OF CORE GEOMETRY AND MULTIWIRE SENSORS

The sensor sensitivity depends on the core geometry that affects its effective demagnetization factor. With fixed core diameter d the sensitivity can be increased by increasing the core length l . However, for most practical applications l is limited. It is possible to increase core area by using a stack of several wires, however, the sensitivity increase is limited by demagnetization. The effective way to decrease the demagnetization factor is to decrease the magnetostatic coupling between the wires by increasing their distance. In order to do that one should use a larger pick-up coil diameter. This is possible because as shown in Section III, increasing the pick-up coil diameter reduces the sensitivity only very slightly. In order to verify this assumption, we made a 3-D FEM model in Ansys and calculated relative sensitivity as a function of a number of wires and their permeability. The results of this simulation are shown in Fig. 9 for the maximized wire distances (wire positions as shown by + marks in Fig. 3). In the same Fig. 9, we show sensitivities measured on sensors L1 to 8. The measured values fit well with the curve for $\mu_e = 10000$. It should be noted that the apparent permeability of fluxgate core is time-dependent and the effective permeability μ_e is its average value.

By increasing the number of wires in the core from 1 to 8 (sensor L1 versus L8 in Table I), the sensitivity is theoretically increased by a factor of 8, if the wire distance (pitch) is large enough to avoid magnetostatic interaction. In our case, the achieved sensitivity increase was only 6.

For each configuration of the sensor core, we found the optimum working point (excitation frequency and amplitude)

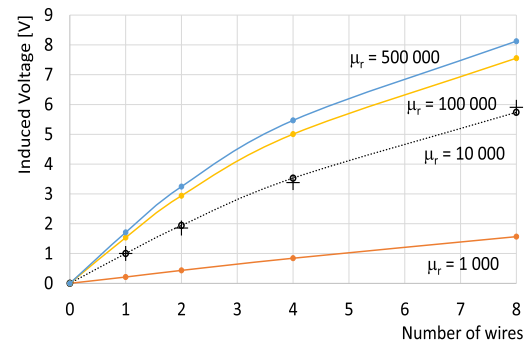


Fig. 9. Relative sensitivity of L1 to L8 sensors as a function of number of wires in the core. Calculated by FEM for several values of effective permeability. Values marked + are measured relative sensitivities.

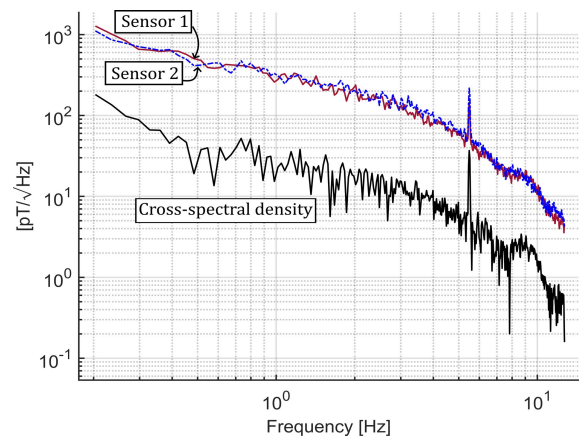


Fig. 10. Noise PSD and cross-spectral density of two single-wire sensors in 5 mm distance.

to maximize the sensitivity and minimize the noise. In general, the excitation amplitude for minimum noise was 10%–20% higher than the amplitude for maximum sensitivity.

According to the theory, the noise is reduced by the factor of \sqrt{N} for independent noise sources. We have observed a general decrease in noise with increasing of the wire number and with increasing wire distance. However, the decrease was significantly lower than \sqrt{N} . Fig. 10 shows typical noise spectra of the measured sensors and their cross-spectrum. The noise has $1/f$ character, drop at higher frequencies is caused by the low-pass filter of the lock-in amplifier with 30 ms time constant. Even for a distance of 5 mm between two wires the noise correlation is still high which explains that the achieved noise reduction was less than \sqrt{N} . Comparing an L1 with an L8 fluxgate, the measured noise level decreases by a factor of 0.53 (instead of $1/\sqrt{8} = 0.35$ which is the theoretical value for independent noise sources).

VI. CONCLUSION

We have shown that the sensitivity of the straight-wire-core fluxgate with voltage output depends only very slightly on the diameter of the pick-up coil. This opens up the possibility to design a multiwire fluxgate with a loose core.

The sensitivity of the multiwire fluxgate is increasing with the wire pitch. This is caused by the fact that with increasing wire distance their magnetostatic interaction is decreasing, which results in lower demagnetization. This initial study was limited to the single diameter and Permalloy material for the core wire. The achieved noise was $150 \text{ pT}\sqrt{\text{Hz}}$ at 1 Hz, which is acceptable for many applications such as portable gradiometers, position, and torque sensors, and detection of small objects. For the mentioned applications the straight wire core has significant advantages. We plan to improve the noise properties by the application of arrays of amorphous or nanocrystalline microwires.

ACKNOWLEDGMENT

This work was supported by the Grant Agency of the Czech Republic within the Nanofluxgate Project under Grant GACR GA20-27150S.

REFERENCES

- [1] P. Ripka, *Magnetic Sensors and Magnetometers*. Boston, MA, USA: Artech House, 2001.
- [2] M. Butta, M. Vazquez, R. P. del Real, and E. Calle, "Dependence of the noise of an orthogonal fluxgate on the composition of its amorphous wire-core," *AIP Adv.*, vol. 10, no. 2, Feb. 2020, Art. no. 025114.
- [3] M. Janosek, "Parallel fluxgate magnetometers," in *High Sensitivity Magnetometers*, A. Grosz, M. Haji-Sheikh and S. Mukhopadhyay, Eds. Berlin, Germany: Springer, 2017.
- [4] L. Guo, Z. Yang, S. Zhi, Z. Feng, C. Lei, and Y. Zhou, "Sensitive detection of cardiac troponin T based on superparamagnetic bead-labels using a flexible micro-fluxgate sensor," *RSC Adv.*, vol. 7, no. 82, pp. 52327–52336, 2017.
- [5] C. Lei *et al.*, "Detection of dynabeads in small bias magnetic field by a micro fluxgate-based sensing system," *J. Appl. Phys.*, vol. 116, no. 15, Oct. 2014, Art. no. 154701.
- [6] P. Ripka and S. W. Billingsley, "Crossfield effect at fluxgate," *Sens. Actuators A, Phys.*, vol. 81, nos. 1–3, pp. 176–179, Apr. 2000.
- [7] C. Hinrichs, J. Stahl, K. Kuchenbrandt, and M. Schilling, "Dependence of sensitivity and noise of fluxgate sensors on racetrack geometry," *IEEE Trans. Magn.*, vol. 37, no. 4, pp. 1983–1985, Jul. 2001.
- [8] E. Özkök, H. Can, F. Inanır, and U. Topal, "A comparative study for optimization of sensitivity and noise levels in race-track sensors," *J. Supercond. Novel Magn.*, vol. 30, no. 12, pp. 3555–3557, Dec. 2017.
- [9] L. Pérez, I. Lucas, C. Aroca, P. Sánchez, and M. C. Sánchez, "Analytical model for the sensitivity of a toroidal fluxgate sensor," *Sens. Actuators A, Phys.*, vols. 130–131, pp. 142–146, Aug. 2006.
- [10] F. Primdahl, P. Ripka, J. R. Petersen, and O. V. Nielsen, "The sensitivity parameters of the short-circuited fluxgate," *Meas. Sci. Technol.*, vol. 2, no. 11, pp. 1039–1045, Nov. 1991.
- [11] T. Sonoda and R. Ueda, "Distinctive features of magnetic field controlled type magnetic field sensor," *IEEE Trans. Magn.*, vol. 25, no. 5, pp. 3393–3395, Sep. 1989.
- [12] J. Blažek, D. Praslička, J. Hudák, A. Klinda, I. Mikita, and J. Marcin, "New generation of magnetic relaxation sensors based on the melt-spun FeCoBCu alloys," *Acta Phys. Polonica A*, vol. 118, no. 5, pp. 1010–1012, Nov. 2010.
- [13] B. Andó, S. Baglio, A. R. Bulsara, and C. Trígona, "Design and characterization of a microwire fluxgate magnetometer," *Sens. Actuators A, Phys.*, vol. 151, no. 2, pp. 145–153, Apr. 2009.
- [14] S. Takeuchi and K. Harada, "A resonant-type amorphous ribbon magnetometer driven by an operational amplifier," *IEEE Trans. Magn.*, vol. MAG-20, no. 5, pp. 1723–1725, Sep. 1984.
- [15] V. Grim, P. Ripka, and J. Bauer, "DC current sensor using switching-mode excited *in-situ* current transformer," *J. Magn. Magn. Mater.*, vol. 500, Apr. 2020, Art. no. 166370.
- [16] A. Moldovanu *et al.*, "Functional study of fluxgate sensors with amorphous magnetic materials cores," *Sens. Actuators A, Phys.*, vol. 59, nos. 1–3, pp. 105–108, Apr. 1997.
- [17] A. Moldovanu, E. D. Diaconu, E. Moldovanu, C. Macovei, B. O. Moldovanu, and G. Bayreuther, "The applicability of VITROVAC 6025 X ribbons for parallel-gated configuration sensors," *Sens. Actuators A, Phys.*, vol. 81, nos. 1–3, pp. 193–196, Apr. 2000.
- [18] F. Foerster, "A method for the measurement of DC field differences and its application to nondestructive testing," *Nondestruct. Test.*, vol. 13, no. 1, pp. 31–41, 1955.
- [19] T. Saito, T. Sakurai, K. Yumoto, T. Tamura, M. Seto, and T. Hayasaka, "Magnetometers for geophysical use—Part I. Fluxgate magnetometer with a 0.5-m length two-core sensor," *Sci. Rep. Tohoku Univ.*, vol. 27, no. 2, pp. 85–93, 1980.
- [20] P. Ripka, M. Butta, F. Jie, and X. Li, "Sensitivity and noise of wire-core transverse fluxgate," *IEEE Trans. Magn.*, vol. 46, no. 2, pp. 654–657, Feb. 2010.
- [21] S. Tumanski, "Induction coil sensors—A review," *Meas. Sci. Technol.*, vol. 18, no. 3, pp. R31–R46, Mar. 2007.
- [22] F. Primdahl, "The fluxgate mechanism, Part I: The gating curves of parallel and orthogonal fluxgates," *IEEE Trans. Magn.*, vol. MAG-6, no. 2, pp. 376–383, Jun. 1970.
- [23] P. Ripka and W. G. Hurley, "Excitation efficiency of fluxgate sensors," *Sens. Actuators A, Phys.*, vol. 129, nos. 1–2, pp. 75–79, May 2006.

5 Position and speed sensors

Most of the papers presented in this chapter are dealing with sensors based on induction principle, with differential pickup windings. This type of sensor can also directly measure movement velocity, because of the non-zero decay time of the eddy currents induced in the conductive core.

All of the papers include a thorough theoretical elaboration of the problem being solved, approximate solution obtained either by analytical calculation (for simple geometries) or by finite element method simulation. The simulated geometries do not contain enough symmetry to allow simplified 2D model simulation. Moreover, because the movement is altering the geometry, the simulator has to run in transient mode and perform re-meshing at every timestep. This, together with the low ratio of differential to common-mode pickup voltage, leads to very long simulation times in the order of days for each design variation.

Several of the presented designs are targeted toward pneumatic cylinders, while others are meant as a general purpose, industrial sensor, with robustness and simplicity given the highest priority.

5.1 Design and Modeling of a Linear Speed Sensor with a Flat Type Structure and Air Coils

An innovative linear speed sensor based on eddy currents is presented in this paper. A distinguishing feature of this type sensor is the completely smooth slider (or rotor for rotational versions) without any slots or embedded code strip. Movement is detected by observing the speed-dependent change in mutual inductance between the excitation and pickup windings. This is because the eddy currents circulating in the armature change their position (relative to the stator) as they decay and therefore the pickup winding on the trailing side is subjected to larger flux than the one on the leading side.

The sensitivity depends on the material's conductivity – aluminium is the usual compromise between electrical and mechanical properties. Steel can also be used with reduced performance. The paper does not include a method of reconstructing the speed information from the output voltage. It could be done e.g. with a lock-in amplifier with very sharp low-pass filter with cutoff frequency just below the excitation frequency, to accurately capture the speed transients.

I personally contributed to the mechanical construction of the sensor.



Research articles

Design and modeling of a linear speed sensor with a flat type structure and air coils



Mehran Mirzaei*, Pavel Ripka, Andrey Chirtsov, Jan Vyhnanek, Vaclav Grim

Faculty of Electrical Engineering, Czech Technical University, Prague 16627, Czech Republic

ARTICLE INFO

Keywords:

Flat type
Linear speed sensor
Eddy current
Aluminum
Iron
Analytical method and finite element method

ABSTRACT

This paper presents the design and modeling of a linear eddy current speed sensor with a flat type structure and an air coil configuration. The theory of the eddy current speed sensor is based on utilizing the speed component of the induced currents in a solid moving conductor under stationary or alternating source fields. The stationary part comprises one rectangular excitation coil and two antiseriably connected rectangular pick-up coils on the left and right sides of the excitation coil in the direction of the trajectory of the moving part. The moving part is considered firstly as a rectangular conductive ferromagnetic solid iron plate, and secondly as a rectangular aluminum plate. A 3D analytical model using Fourier series is developed to analyze the linear speed sensor in Cartesian coordinates. In addition, the 3D numerical finite element method is used for simulations of the linear speed sensor, and the results are compared with the results for analytical methods. The effects of iron permeability on the speed sensor are calculated for a rectangular ferromagnetic solid iron bar or conductor. The experimental results are presented for a linear speed sensor for a rectangular ferromagnetic solid iron plate and also for a rectangular aluminum plate, at variable speeds. The calculation and the experimental results show that the speed sensor outputs differ completely for solid iron conductive plates and for aluminum conductive plates, due to the different electrical conductivities and magnetic permeabilities.

1. Introduction

Speed sensors are needed for rotating and translational energy converters [1–5]. Non-magnetic optical sensors, variable reluctance sensors, eddy current-based sensors and Hall effect magnetic sensors can be developed for speed measurements. Magnetic sensors could have a moving or stationary permanent magnet or coil as the excitation source. The principles of magnetic sensors are based on the magnetic properties of the sensing material, or on a change in the parameters of the magnetic circuit [6]. Magnetic sensors are more reliable and more robust to dust and dirt than non-magnetic sensors [7,8], especially when the position and the speed of moving objects are being measured.

Eddy current-based speed sensors are widely used for various configurations and applications [6] and [9–15]. For example, the Faraday generator, the homopolar generator and magnetic flowmeters [6] and [15] are the earliest utilization of the speed effect in moving conductive objects subjected to magnetic fields. Perpendicular and non-perpendicular pick-up coils for eddy current speed sensors are analyzed using the Fourier transform in [9–11], as is presented later using a ferrite core in [12]. Aluminum moving part is used in [9–12], which has relative magnetic permeability equal to 1. An eddy current speed sensor with an

axisymmetric structure was developed and measured at variable speeds with a ferromagnetic iron rod [13]. It has three coils for excitation and pick-up voltage. The eddy current-based speed sensor has a quite simple and cost-effective structure, which is an essential consideration for industrial applications.

Our solution for flat type linear speed measurements is based on a single coil excitation coil with an AC current and two pick-up coils for measurements without using a ferromagnetic yoke. In order to analyze the eddy current speed sensor, a fast and precise 3D analytical method is presented for calculating the coil inductance and the induced voltages in the pick-up coils. This method takes into account the eddy currents in the moving conductive part caused by alternating current and the speed of the moving current part for a flat shape model, using Fourier series. General closed-form equations are also obtained for the output results. A 3D time-stepping finite element method (FEM) simulation taking into account the speed of the moving part is also presented for a comparison with analytical calculations. Various relative magnetic permeabilities and conductivities are considered for the solid iron moving part in order to evaluate the effects of the electrical and magnetic parameters on the performance of the eddy current speed sensor. The sensitivity of the eddy current speed sensor versus the gap between coils and moving

* Corresponding author.

E-mail address: mirzameh@fel.cvut.cz (M. Mirzaei).<https://doi.org/10.1016/j.jmmm.2019.165834>

Received 26 June 2019; Received in revised form 23 August 2019; Accepted 10 September 2019

Available online 20 September 2019

0304-8853/ © 2019 Elsevier B.V. All rights reserved.

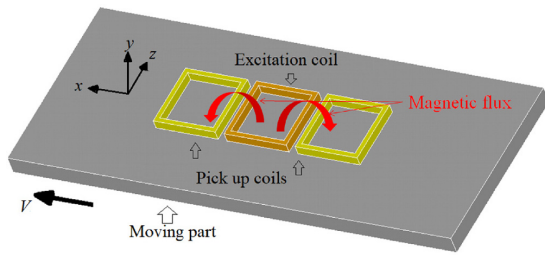


Fig. 1. Flat type eddy current speed sensor.

plate is also evaluated. Flat shape aluminum rectangular plates and solid ferromagnetic iron rectangular plates are both used in the measurements for the moving part, and the experimental results at variable speeds are compared with analytical calculations.

2. Model and coil configurations

Fig. 1 shows a 3D model of a flat type eddy current speed sensor coils and solid conductor moving part. The middle coil is the excitation coil, and the coils on the left and right sides are the pick-up coils, which are connected antiserially. The moving part is made of solid iron or of aluminum. Only 1-D movement is considered with speed, V in the direction of the x-axis (Fig. 1).

It is obvious that the induced voltage in the pick-up coils is zero at zero speed, because the net flux linkage is zero in the antiserially connected pick-up coils (Fig. 1).

Fig. 2 and Table 1 show the parameters and the dimensions of a linear speed sensor. Parameters $d, h, t, g, w_1, w_2, \sigma_{al}, \sigma_i$ and μ_{ri} are the thickness of the moving part, the coil height, the coil thickness, the gap between the coils and the moving part, the inner width of the coils in the x-direction, the inner width of the coils in the z-direction, the electrical conductivity of aluminum, the electrical conductivity of iron, and the relative magnetic permeability of iron, respectively. Regions 1, 2, 3, 4 and 5 in Fig. 2 (above) are the region

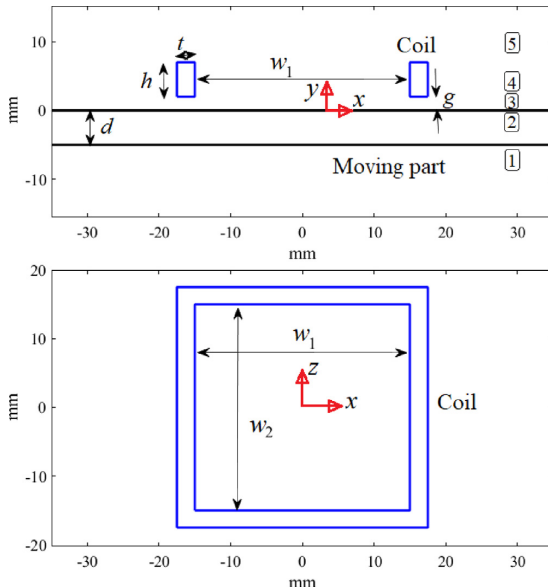


Fig. 2. Computational models – in the x-y plane (above) and in the x-z plane (below).

Table 1
Linear speed sensor parameters.

Parameters	Values
I	154 mA
N	100
d	5 mm and 10 mm
h	5.0 mm
t	2.5 mm
g	2 mm
w_1	30 mm
w_2	30 mm
σ_{al}	30.3 MS/m
σ_i	5.24 MS/m
μ_{ri}	100

below the moving part, in the moving part, the air region between the coils and the moving part, in the region of the coils, and the air region above the coils, respectively.

3. 3D modeling

3.1. Analytical

3D modeling and analysis is required for the proposed eddy current speed sensor, because the air coil configuration is used. 2D analysis is not accurate enough to take the 3D fluxes into account. The general partial differential equations in 3D, using the Maxwell equations, are as follows [16–18]:

$$\begin{aligned} \nabla \times H &= J, \quad B = \mu H, \quad \nabla \times J = -\sigma \frac{dB}{dt} \\ \nabla \cdot B &= 0 \rightarrow B = \nabla \times A, \quad \nabla \cdot A = 0 \rightarrow \frac{\partial A_x}{\partial x} + \frac{\partial A_z}{\partial z} = 0 \\ \nabla^2 A_x - \mu \sigma \frac{dA_x}{dt} &= -\mu J_{s,x} \\ \frac{dA_x}{dt} &= \frac{\partial A_x}{\partial t} + \frac{dx}{dt} \cdot \frac{\partial A_x}{\partial x} = \frac{\partial A_x}{\partial t} + V \cdot \frac{\partial A_x}{\partial x} \\ \frac{\partial^2 A_x}{\partial x^2} + \frac{\partial^2 A_x}{\partial y^2} + \frac{\partial^2 A_x}{\partial z^2} - \mu \sigma \left(\frac{\partial A_x}{\partial t} + V \cdot \frac{\partial A_x}{\partial x} \right) &= -\mu J_{s,x} \\ \nabla^2 A_z - \mu \sigma \frac{dA_z}{dt} &= -\mu J_{s,z} \\ \frac{dA_z}{dt} &= \frac{\partial A_z}{\partial t} + \frac{dx}{dt} \cdot \frac{\partial A_z}{\partial x} = \frac{\partial A_z}{\partial t} + V \cdot \frac{\partial A_z}{\partial x} \\ \frac{\partial^2 A_z}{\partial x^2} + \frac{\partial^2 A_z}{\partial y^2} + \frac{\partial^2 A_z}{\partial z^2} - \mu \sigma \left(\frac{\partial A_z}{\partial t} + V \cdot \frac{\partial A_z}{\partial x} \right) &= -\mu J_{s,z} \end{aligned} \quad (1)$$

where H is magnetic field strength, B is magnetic flux density, J is current density, A is magnetic vector potential, μ is relative magnetic permeability, σ is electrical conductivity, A_x and A_z are the x-axis and z-axis components of the magnetic vector potentials, and $J_{s,x}$ and $J_{s,z}$ are the x-axis and z-axis components of the source current densities in the excitation coil.

Only linear magnetic modeling using the initial permeability is considered here, due to the low magnetic fields in the sensor, and nonlinearity and hysteresis effects are neglected.

The y-component of the magnetic vector potential is assumed to be zero, because the excitation coil is parallel to the x-z plane, and the y-component of the source current density is therefore zero [9] and [16] and also the dimensions of conducting object are enough large in comparison with excitation coil. This assumption helps to solve analytically computational model of the eddy current sensor.

The method of separation of variables (the Fourier method) is used to solve (1) [16] and [19]. It is assumed that the magnetic fields change sinusoidally against time and anti-periodically in the x-direction with period length $2l$ and in the z-direction with period length $2L$. It is assumed that the computational model of eddy current sensor is artificially repeated in longitudinal direction and transversal direction as shown in Fig. 3. Therefore the derivations in (1) can therefore be replaced as follows using the method of separation of variables:

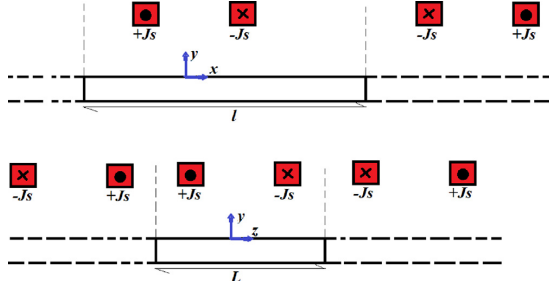


Fig. 3. Longitudinal view of anti-periodically repetition (above) and transversal view of anti-periodically repetition.

$$A_{x,z} = \sum_n \sum_m X_{x,z}^m(x) \cdot Y_{x,z}^{m,n}(y) \cdot Z_{x,z}^n(z) \cdot T(t) \quad (2)$$

$$X_{x,z}^m(x) \propto \exp(-jk_m \cdot x), \quad k_m = m \frac{\pi}{l}, \quad m = \pm 1, \pm 3, \pm 5, \dots$$

$$Z_{x,z}^n(z) \propto \exp(-jk_n \cdot z), \quad k_n = n \frac{\pi}{L}, \quad n = \pm 1, \pm 3, \pm 5, \dots$$

$$T(t) \propto \exp(j\omega \cdot t)$$

$$\frac{\partial A_{x,z}}{\partial t} = j\omega \cdot A_{x,z}$$

$$\omega = 2\pi f$$

$$\frac{\partial A_{x,z}^{m,n}}{\partial x} = -jk_m \cdot A_{x,z}^{m,n}, \quad \frac{\partial^2 A_{x,z}^{m,n}}{\partial x^2} = -k_m^2 \cdot A_{x,z}^{m,n}$$

$$\frac{\partial^2 A_{x,z}^{m,n}}{\partial z^2} = -k_n^2 \cdot A_{x,z}^{m,n} \quad (3)$$

$$-k_m^2 A_{x,z}^{m,n} + \frac{\partial^2 A_{x,z}^{m,n}}{\partial y^2} - k_n^2 A_{x,z}^{m,n} - j\mu\sigma(\omega - V \cdot k_m) A_{x,z}^{m,n} = -\mu J_{s,x,z}^{m,n} \quad (4)$$

where f is frequency. m and n are harmonic orders. The magnetic flux densities and eddy current densities are forced to be zero at boundaries $x = \pm l/2$ and $z = \pm L/2$ using assumptions of the model in Fig. 3. The solutions of (1) versus y for regions 1 ($A_{z,1}$, $A_{x,1}$), 2 ($A_{z,2}$, $A_{x,2}$), 3 ($A_{z,3}$, $A_{x,3}$), 4 ($A_{z,4}$, $A_{x,4}$) and 5 ($A_{z,5}$, $A_{x,5}$) are presented in (5).

Harmonic orders are only odd numbers as the computational model is symmetric and it is anti-periodically repeated.

$$\begin{aligned} A_{z,1} &= \sum_n \sum_m (C_{11} \exp(\gamma_1 y) + C_{12} \exp(\gamma_1 y)) \\ &\times \exp(j(\omega t - k_m x - k_n z)), \quad \sigma = 0, \quad J_{s,z} = 0 \\ \gamma_1 &= \gamma, \quad (\gamma = \sqrt{k_m^2 + k_n^2}), \quad A_{x,1} = -\frac{k_n}{k_m} A_{z,1} \\ A_{z,2} &= \sum_n \sum_m (C_{21} \exp(\gamma_2 y) + C_{22} \exp(\gamma_2 y)) \\ &\times \exp(j(\omega t - k_m x - k_n z)), \quad \sigma \neq 0, \quad \mu = \mu_2, \quad J_{s,z} = 0 \\ \gamma_2 &= \sqrt{\gamma^2 + j\mu_2 \sigma (\omega - k_m V)}, \quad A_{x,2} = -\frac{k_n}{k_m} A_{z,2} \\ A_{z,3} &= \sum_n \sum_m (C_{31} \exp(\gamma_3 y) + C_{32} \exp(\gamma_3 y)) \\ &\times \exp(j(\omega t - k_m x - k_n z)), \quad \sigma = 0, \quad J_{s,z} = 0 \\ \gamma_3 &= \gamma, \quad A_{x,3} = -\frac{k_n}{k_m} A_{z,3} \\ A_{z,4} &= \sum_n \sum_m \left(C_{41} \exp(\gamma_4 y) + C_{42} \exp(\gamma_4 y) + \frac{\mu_4 J_p^{m,n}}{\gamma_4^2} \right) \\ &\times \exp(j(\omega t - k_m x - k_n z)), \quad \sigma = 0, \quad \mu = \mu_4, \quad J_{s,z} \neq 0 \\ \gamma_4 &= \gamma, \quad A_{x,4} = -\frac{k_n}{k_m} A_{z,4} \\ A_{z,5} &= \sum_n \sum_m (C_{51} \exp(\gamma_5 y) + C_{52} \exp(\gamma_5 y)) \\ &\times \exp(j(\omega t - k_m x - k_n z)), \quad \sigma = 0, \quad J_{s,z} = 0 \\ \gamma_5 &= \gamma, \quad A_{x,5} = -\frac{k_n}{k_m} A_{z,5} \end{aligned} \quad (5)$$

where C_{11} , C_{12} , C_{21} , C_{22} , C_{31} , C_{32} , C_{41} , C_{42} , C_{51} and C_{52} are constants, and they are calculated by the boundary conditions between regions 1 to 5 in (6).

$$\begin{aligned} A_{z,1}(y = -\infty) &= 0 \\ A_{z,1}(y = -d) &= A_{z,2}(y = -d) \\ H_{x,1}(y = -d) &= H_{x,2}(y = -d) \\ A_{z,2}(y = 0) &= A_{z,3}(y = 0) \\ H_{x,2}(y = 0) &= H_{x,3}(y = 0) \\ A_{z,3}(y = g) &= A_{z,4}(y = g) \\ H_{x,3}(y = g) &= H_{x,4}(y = g) \\ A_{z,4}(y = g + h) &= A_{z,5}(y = g + h) \\ H_{x,4}(y = g + h) &= H_{x,5}(y = g + h) \\ A_{z,5}(y = \infty) &= 0 \\ H_x &= \frac{B_x}{\mu} = \frac{1}{\mu} \frac{\partial A_z}{\partial y} \end{aligned} \quad (6)$$

where H_x are B_x are the x -component of the magnetic flux density and magnetic field strength, respectively. Parameter $J_p^{m,n}$ in (5) for coil excitation is obtained as follows:

$$\begin{aligned} J_p^{m,n} &= 4 \frac{j}{n\pi l} C_J \cdot J_s \\ C_J &= \frac{1}{k_m + k_n} C_{J,1} C_{J,2} - \frac{1}{k_m - k_n} C_{J,3} C_{J,4} \\ C_{J,1} &= \cos\left(k_m \frac{w_1 + t}{2} + k_n \frac{w_2 + t}{2}\right) \\ C_{J,2} &= \sin\left(k_m \frac{t}{2} + k_n \frac{t}{2}\right) \\ C_{J,3} &= \cos\left(k_m \frac{w_1 + t}{2} - k_n \frac{w_2 + t}{2}\right) \\ C_{J,4} &= \sin\left(k_m \frac{t}{2} - k_n \frac{t}{2}\right) \\ J_s &= \frac{N \cdot I}{h \cdot t} \end{aligned} \quad (7)$$

where N and I are the number of turns per coil and the current amplitude (Table 1), respectively.

In this paper, it is considered that the excitation coil and the pickup coils have same dimensions and number of turns. The mutually-induced voltage, U_M , and the mutual inductance, L_M , can be calculated as follows [16,20,21]:

$$L_M = \frac{\Psi_M}{I} = \frac{N \int (\int A_4 \cdot dl) ds}{I \cdot h \cdot t}, \quad U_M = -j\omega \cdot L_M \quad (8)$$

where Ψ_M is the total average mutual flux linkage over the volume of the coils. Line integration of A_4 (magnetic vector potential in the coil region 4 in (5)) is applied to each coil in the current flow direction, as in an excitation coil. The surface integration in (8) is for the coil cross-section area, which is averaged over the coil cross-section area, $h \cdot t$.

The differential voltage between the left and right side pick-up coils (Fig. 1) is presented in (9) and (10). The polarity of the differential voltage changes with the changes in speed direction, according to (9) and (10).

$$U_d = U_{M,l} - U_{M,r} = j\omega \cdot (L_{M,r} - L_{M,l}) \cdot I \quad (9)$$

$$\begin{aligned} U_d &= U_{M,l} - U_{M,r} = \frac{2\omega N \cdot l \cdot I}{h \cdot t} \sum_n \sum_m (C_U C_J \sin(k_m w_3)) \\ C_U &= \frac{4j}{n\pi l} \left(1 + \left(\frac{k_n}{k_m} \right)^2 \right) \cdot (C_{U,1} + C_{U,2} + C_{U,3}) \\ C_{U,1} &= \frac{C_{41}}{\gamma_4} \cdot (\exp(\gamma_4 \cdot (h + g)) - \exp(\gamma_4 \cdot g)) \\ C_{U,2} &= -\frac{C_{42}}{\gamma_4} \cdot (\exp(-\gamma_4 \cdot (h + g)) - \exp(-\gamma_4 \cdot g)) \\ C_{U,3} &= \frac{\mu_0 J_p^{m,n}}{\gamma_4^2} \cdot h \end{aligned} \quad (10)$$

where w_3 is the distance between the centers of pick-up coils and the center of the excitation coil.

The magnetic flux lines distribution and the eddy current distribution for iron and aluminum moving parts at 100 Hz and 2 m/s are shown in Figs. 4–7. The magnetic flux lines distribution is corresponding to the contour plot of z -component of magnetic vector potential, A_z in the x - y plane ($z = 0$), which A_x is zero. The eddy current distribution is contour plot of streamline function, I_y in x - z plane

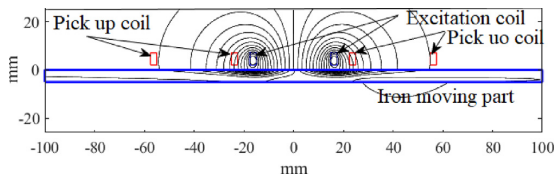


Fig. 4. Magnetic flux distribution in the x-y plane for the iron moving part at 100 Hz and 2 m/s.

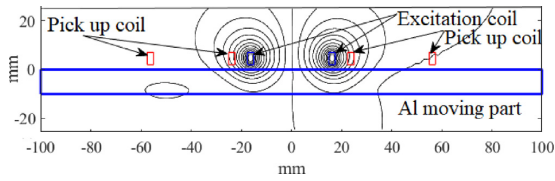


Fig. 5. Magnetic flux distribution in the x-y plane for the aluminum moving part at 100 Hz and 2 m/s.

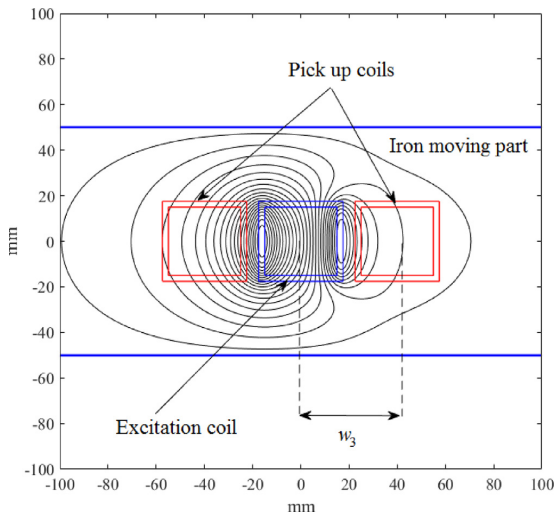


Fig. 6. Eddy current distribution in the x-z plane on the surface of the solid iron moving part at 100 Hz and 2 m/s – analytical method.

[19].

$$\begin{aligned}
 J &= \nabla \times I_y \\
 J_{x,2} &= -\sigma \left(\frac{\partial A_{x,2}}{\partial t} + V \cdot \frac{\partial A_{x,2}}{\partial x} \right), \quad I_y = -\int J_{x,2} dz \\
 J_{z,2} &= -\sigma \left(\frac{\partial A_{z,2}}{\partial t} + V \cdot \frac{\partial A_{z,2}}{\partial x} \right), \quad I_y = \int J_{z,2} dx \\
 I_y &= \frac{\sigma(\omega - V \cdot k_m)}{k_m} \times \\
 &\sum_n \sum_m (C_{21} \exp(\gamma_2 y) + C_{22} \exp(\gamma_2 y)) \\
 &\times \exp(j(\omega t - k_m x - k_n z))
 \end{aligned} \tag{11}$$

The iron moving part is 5 mm in thickness, and the aluminum moving part is 10 mm in thickness (Table 1). The skin depths are 2.2 mm for the iron moving part, and 9.1 mm for the aluminum moving part, at 100 Hz. The speed effect on the differential induced voltage could be higher for an aluminum moving part than for an iron moving part, as the skin depth is greater in aluminum (Fig. 5). The deformation and the extension of the induced eddy currents in the iron moving part due to the speed effect is larger, because of the higher relative

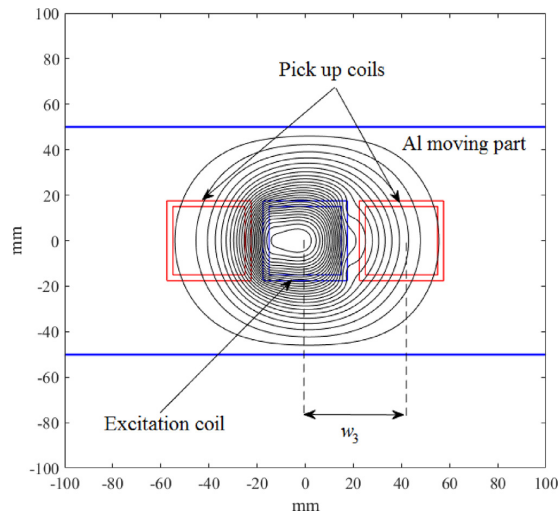


Fig. 7. Eddy current distribution in the x-z plane on the surface of the aluminum moving part at 100 Hz and 2 m/s – analytical method.

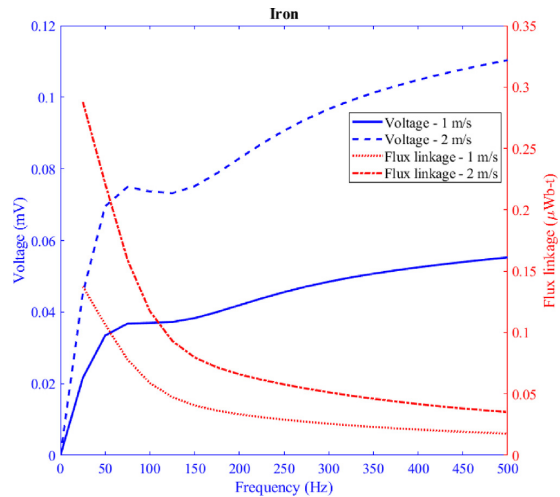


Fig. 8. Amplitude of differential induced voltage and flux linkage versus frequency for the iron moving part – airgap, $g = 2$ mm ($\mu_{ri} = 100$).

permeability. Figs. 8 and 9 show differential voltages and flux linkages versus frequency for iron and aluminum moving parts. The differential voltage for the iron moving part increases with frequency, with the exception of some fluctuation between 75 Hz and 125 Hz (Fig. 8). The maximum differential voltage value for the aluminum moving part is located at 75 Hz in Fig. 9, and the differential voltage decreases continuously at higher frequencies for the aluminum moving part. The flux linkages decrease at higher frequencies, which shows that lower frequencies or DC are best for obtaining maximum flux linkage or magnetic flux density, and the flux linkages are more sensitive to speed at lower frequencies.

The differential voltages and flux linkages versus the gap between the coils and the moving part are shown in Fig. 10. The differential voltage and the flux linkage decreases monotonically in the case of the aluminum moving part. The differential voltages and the flux linkages for the iron moving part have maximum values for a 3.5 mm gap. This is

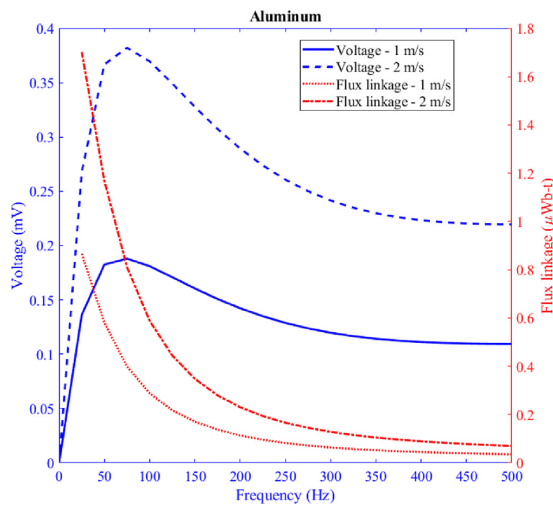


Fig. 9. Amplitude of the induced differential voltage and flux linkage versus frequency for the aluminum moving part – airgap, $g = 2$ mm.

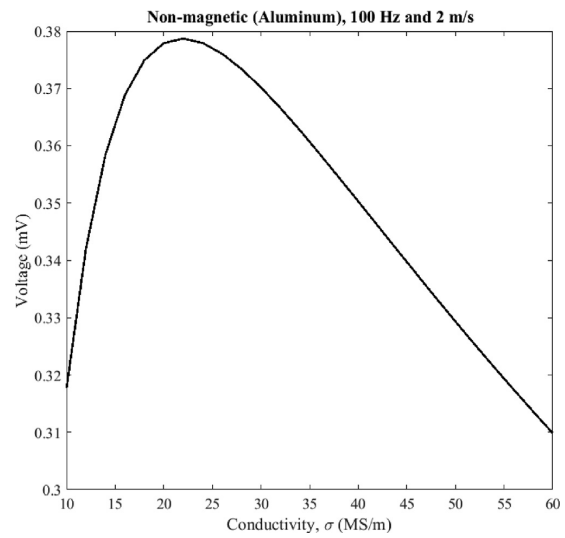


Fig. 11. Amplitude of the induced differential voltage versus conductivity for a nonmagnetic moving part, e.g. aluminum.

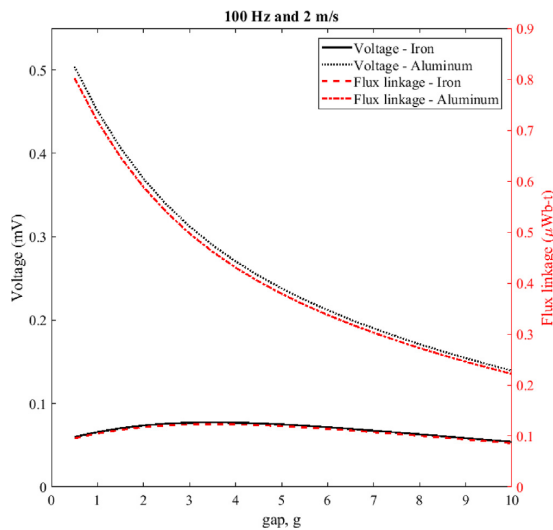


Fig. 10. Amplitude of the induced differential voltage and flux linkage versus gap, g ($\mu_r = 100$).

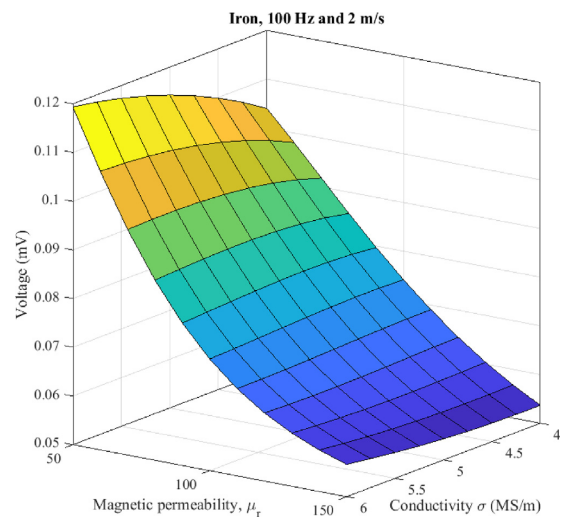


Fig. 12. Amplitude of the induced differential voltage versus conductivity and magnetic relative permeability for a magnetic moving part.

due to the high permeability of the iron moving part. The differential voltage and the flux linkage are higher for an aluminum moving part than for an iron moving part for different gaps and frequencies, see in Figs. 8–10.

The differential voltage for a non-magnetic moving part (for example in this paper, aluminum) versus conductivity is shown in Fig. 11. The maximum value is at 22.0 MS/m.

The differential voltage for a magnetic moving part versus conductivity and relative magnetic permeability is presented as a 3D plot in Fig. 12. The relative magnetic permeability varies between 50 and 150, which is an acceptable range for low magnetic fields. Nonlinearity is neglected in the simulations, and constant magnetic permeability is used in the simulations as the magnetic field in the eddy current speed sensor is small. The assumed range of conductivity is between 4 MS/m and 6 MS/m, which is an expected range for construction steels and

irons. The maximum and minimum differential voltage values for iron moving parts are located at conductivity = 6 MS/m, relative magnetic permeability = 50 and conductivity = 4 MS/m, relative magnetic permeability = 150, respectively. The sensitivity of the eddy current speed sensor to variations in magnetic permeability is much higher. The sensitivity for an aluminum moving part to variations in conductivity are much lower than for an iron moving part within the same range of conductivity variations (Fig. 11).

The sensitivity of an eddy current speed sensor to the thickness of the moving parts is dependent on the material of the moving part and on the excitation frequency (Fig. 13), because of the skin effects and the flux penetration depth in the conductive moving parts. The maximum values of the differential voltages for iron moving parts are located at a thickness of 4 mm for 100 Hz and at a thickness of 2 mm for 200 Hz. Thicknesses of 6 mm and 3 mm are the positions of the maximum values

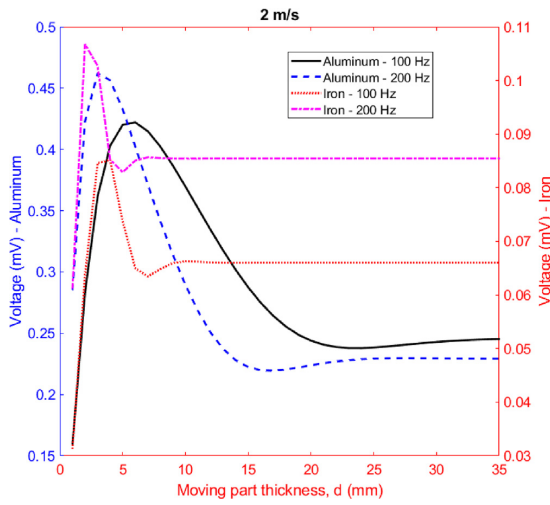


Fig. 13. Amplitude of the induced differential voltage versus moving part thickness – airgap, $g = 2 \text{ mm}$ ($\mu_{ri} = 100$).

of the differential voltages for an aluminum moving part at 100 Hz and 200 Hz, respectively.

Excellent linearity characteristics of a flat type eddy current speed sensor up to 2 m/s is shown in Fig. 14. The linear function equations between the differential voltage, U_d , and the moving part speed, V , are shown as follows:

$$U_d = K \cdot V \quad (12)$$

$$V = K' \cdot U_d, \quad K' = K^{-1} \quad (13)$$

Constant K is calculated in Fig. 14. An eddy current speed sensor with an iron moving part has greater sensitivity at 1000 Hz than at 100 Hz. However, it is not recommended to operate the sensor at very high frequencies due to the smaller skin depth and the greater sensitivity to the surface of an iron moving part, because iron and steel surfaces are affected by corrosion.

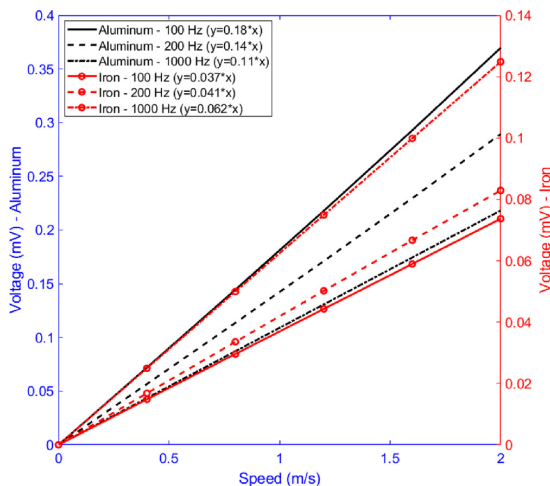


Fig. 14. Amplitude of induced differential voltage versus moving part thickness – airgap, $g = 2 \text{ mm}$ ($\mu_{ri} = 100$).

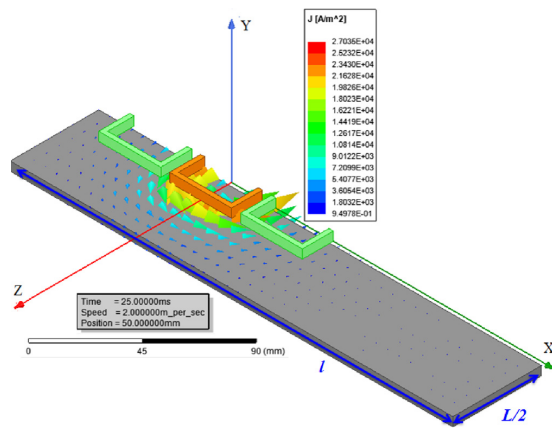


Fig. 15. Eddy current distribution in the x-z plane on the surface of a solid iron moving part at 100 Hz and 2 m/s ($\mu_{ri} = 100$) – FEM.

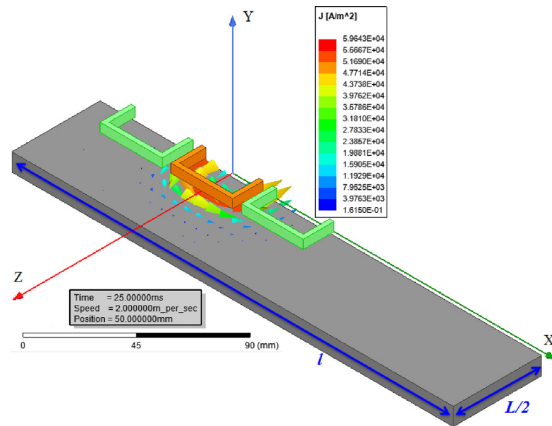


Fig. 16. Eddy current distribution in the x-z plane on the surface of an aluminum moving part at 100 Hz and 2 m/s – FEM.

3.2. FEM

Time-stepping 3D FEM is used to model a flat type eddy current speed sensor, taking into account the speed of the moving part. Figs. 15 and 16 show the eddy current distributions in the iron and aluminum moving parts. The eddy currents are weaker in the iron moving part, and they are located closer to the surface than in the case of the aluminum moving part. Only one half of the FEM model is analyzed, as the model is symmetric to the X-Y plane. A comparison between 3D FEM and the 3D analytical calculations shows that the 3D analytical calculations, which are much faster than 3D FEM, are highly accurate (Tables 2–6). The difference between 3D FEM and the 3D analytical

Table 2
Comparison between analytical and 3D FEM at different speeds – differential voltage (amplitude).

$g = 2 \text{ mm}$ $f = 100 \text{ Hz}$	Iron ($d = 5 \text{ mm}$) Analytical/FEM	Aluminum ($d = 10 \text{ mm}$) Analytical/FEM
$V = 0.5 \text{ m/s}$	0.019/0.017 mV	0.090/0.080 mV
$V = 1.0 \text{ m/s}$	0.037/0.034 mV	0.181/0.161 mV
$V = 2.0 \text{ m/s}$	0.074/0.069 mV	0.370/0.333 mV

Table 3
Comparison between analytical and 3D FEM at higher frequency – differential voltage (amplitude).

$g = 2 \text{ mm}$ $V = 2.0 \text{ m/s}$	Iron ($d = 5 \text{ mm}$) Analytical/FEM	Aluminum ($d = 10 \text{ mm}$) Analytical/FEM
$f = 200 \text{ Hz}$	0.083/0.078 mV	0.289/0.263 mV

Table 4
Comparison between analytical and 3D FEM for higher gap – differential voltage (amplitude).

$V = 2.0 \text{ m/s}$ $f = 100 \text{ Hz}$	Iron ($d = 5 \text{ mm}$) Analytical/FEM	Aluminum ($d = 10 \text{ mm}$) Analytical/FEM
$g = 4 \text{ mm}$	0.077/0.075 mV	0.27/0.247 mV

Table 5
Comparison between analytical and 3D FEM for different moving part thickness – differential voltage (amplitude).

$g = 2 \text{ mm}$ $f = 100 \text{ Hz}$ $V = 2.0 \text{ m/s}$	Iron Analytical/FEM	Aluminum Analytical/FEM
$d = 5 \text{ mm}$	–	0.42/ 0.376 mV
$d = 10 \text{ mm}$	0.066/0.064 mV	–

Table 6
Comparison between analytical and 3D FEM for different material data – differential voltage (amplitude).

$g = 2 \text{ mm}$ $f = 100 \text{ Hz}$ $V = 2.0 \text{ m/s}$	Iron ($d = 5 \text{ mm}$) Analytical/FEM	Aluminum ($d = 10 \text{ mm}$) Analytical/FEM
$\sigma_{\text{al}} = 58 \text{ MS/m}$	–	0.314/0.286 mV
$\sigma_{\text{al}} = 22 \text{ MS/m}$	–	0.379/0.342 mV
$\sigma_{\text{f}} = 4.0 \text{ MS/m}$ ($\mu_{\text{ri}} = 150$)	0.054/0.051 mV	–
$\sigma_{\text{f}} = 6.0 \text{ MS/m}$ ($\mu_{\text{ri}} = 50$)	0.119/0.108 mV	–

calculations can be reduced by using a finer mesh and a larger number of mesh elements and a smaller time step for the simulations. However, this significantly increases the 3D FEM simulation time. The relative magnetic permeability of iron is considered to be equal to 100 in the simulations.

Parameters l and L in Figs. 15 and 16 correspond to the parameters for the analytical calculations, which are mentioned in (3) and Fig. 3. These parameters are used in the analytical calculations. Parameter l is selected equal to 250 mm, and parameter L is 100 mm, which is similar to the width of the iron and aluminum plates. The maximum values for harmonic orders m and n are selected to be 200 and 100, respectively. These values are a compromise between accuracy and simulation time for the analytical method.

4. Experiments

Figs. 17 and 18 show the experiment set-up elements with the coils and with iron and aluminum moving parts and measurement devices, oscilloscope, reference position sensor and signal generator. The high accuracy of the analytical method for calculating the mutual induced voltage in one of the pick-up coils using (14) is shown in Table 7, in comparison with measurements at zero speed of the moving part. Table 8 also presents a comparison between the analytical calculations using (15) and (16) and the experimental values for the self-inductances of the excitation coil. This illustrates the high precision of the proposed analytical method.

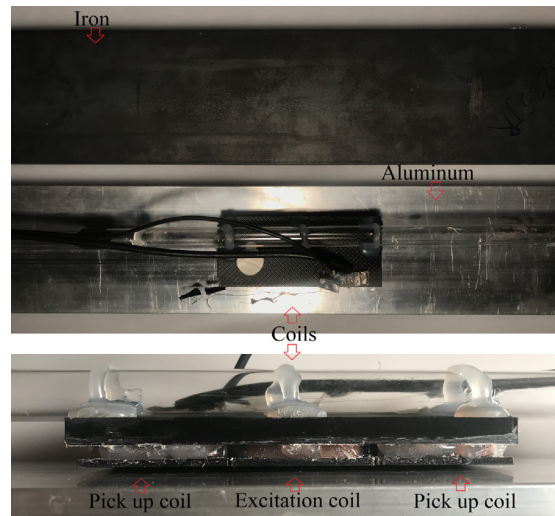


Fig. 17. Experiments elements – excitation and pick-up coils and aluminium plate (10 mm in thickness) and iron plate (5 mm in thickness).

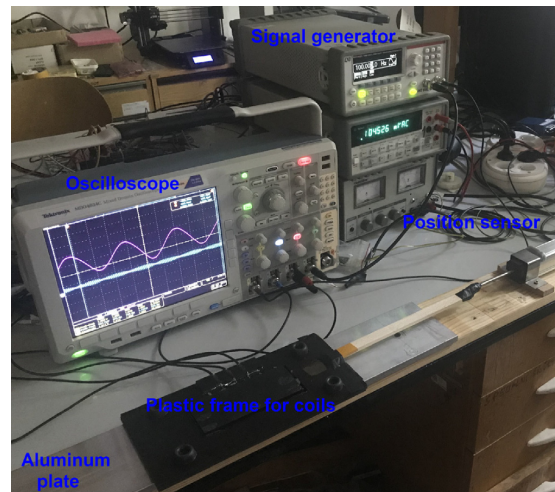


Fig. 18. Measurement devices – oscilloscope, signal generator and reference position sensor.

Table 7
Comparison between the analytical and experimental – induced voltage of one of the pick-up coils (rms value).

	Iron ($g = 2 \text{ mm}$) Analytical/Exp.	Air Analytical/Exp.
$f = 100 \text{ Hz}$	3.320/3.488 mV	2.192/2.253 mV

$$U_{M,l} = U_{M,r} = \frac{j\omega N \cdot L \cdot l}{h \cdot t} \sum_n \sum_m (C_U C_j \exp(jk_m w_3)) = \frac{j\omega N \cdot L \cdot l}{h \cdot t} \sum_n \sum_m (C_U C_j \exp(-jk_m w_3)) \quad (14)$$

$$L_S = \frac{\Psi_S}{I} = \frac{N \int (\int A_4 \cdot dl) ds}{I \cdot h \cdot t} \quad (15)$$

Table 8
Comparison between analytical and experimental – self inductances.

$f = 100 \text{ Hz}$	Iron	Air
	Analytical/Exp.	Analytical/Exp.
$g = -$	-	583.3/613.0 μH
$g = 1.0 \text{ mm}$	820.8/843.0 μH	-
$g = 2.0 \text{ mm}$	771.6/785.0 μH	-
$g = 6.0 \text{ mm}$	673.0/698.0 μH	-
$g = 7.0 \text{ mm}$	659.8/682.0 μH	-

$$L_s = \frac{N \cdot L \cdot I}{h \cdot t \cdot I} \sum_n \sum_m (C_U C_J) \quad (16)$$

In Tables 7 and 8, ‘Air’ means that there is no conductive moving part, ‘Iron’ means that the iron moving part is located in the gap, g and g is the distance between coils and iron moving part.

Eqs. (17) and (18) are used for the analytical calculations of transient differential voltages at variable speeds. Acceleration effects (the second term in (17)) are neglected in (18). The parameter, K in (18) at 100 Hz are calculated equal to 0.18 mV/m/s for the aluminum moving part and 0.037 mV/m/s for the iron moving part as presented in Fig. 14.

$$U_d = \frac{d((L_{M,r} - L_{M,l}) \cdot I_s)}{dt} = \frac{\partial((L_{M,r} - L_{M,l}) \cdot I \cdot \sin(\omega t))}{\partial t} + \frac{\partial((L_{M,r} - L_{M,l}) \cdot I_s)}{\partial V} \cdot \frac{dV}{dt} \quad (17)$$

$$U_d \approx \frac{\partial((L_{M,r} - L_{M,l}) \cdot I \cdot \sin(\omega t))}{\partial t} = \omega \cdot (L_{M,r} - L_{M,l}) \cdot I \cdot \cos(\omega t) = K \cdot V \cdot \cos(\omega t) \quad (18)$$

The analytically calculated results and the experimental values for differential voltages versus time at various speeds (Fig. 19 and Fig. 22) are shown in Figs. 20, 21 and Figs. 23, 24. The relative instantaneous positions of coils and moving parts are measured by a Senpos MRTM500 type potentiometric linear position sensor (Fig. 18) with a measurement range of 500 mm and linearity error of 0.05%.

The relative speed is calculated numerically using differentiation of relative positions of moving part and the coils versus time. The experimental differential voltage results and instantaneous relative positions of moving part and the coils are saved by a digital oscilloscope as

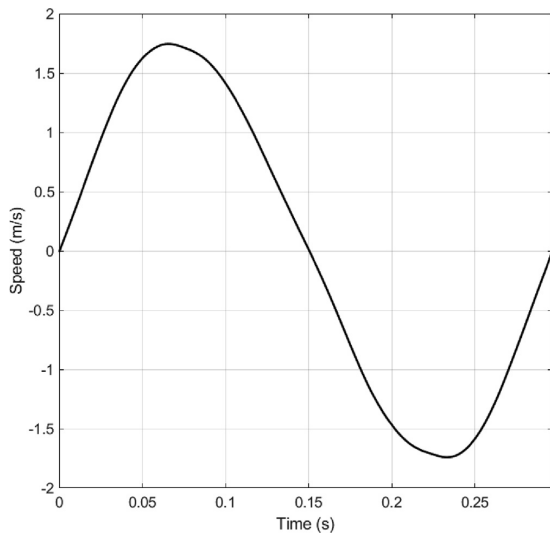


Fig. 19. Applied experimental speed versus time for an aluminium moving part.

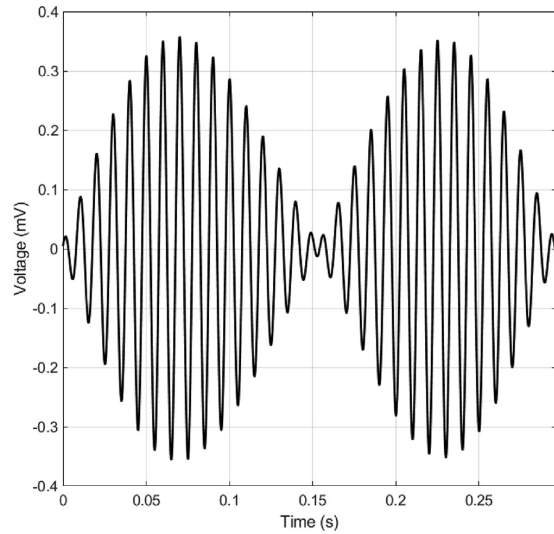


Fig. 20. Experimental differential voltage versus time for an aluminium moving part – 100 Hz.

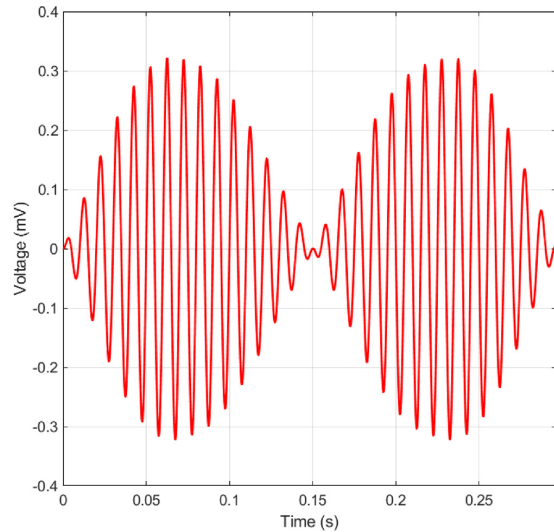


Fig. 21. Analytically calculated differential voltage versus time for an aluminium moving part – 100 Hz.

shown in Fig. 18. Signal generator (Fig. 18) with internal resistance 50 Ω and voltage amplitude 10 V is connected to the excitation coil. The speed is variable function versus time, which affects the differential voltage of eddy current speed sensor. The analytical induced voltages coincide well with the experimental results, showing the accuracy of the proposed analytical method. The main sources of differences between the experimental calculations and the analytical calculations may be the tolerances of the elements in the experimental set up, for example, the gap (lift off) between the coils and the moving parts and the relative magnetic permeability for the iron moving part (Fig. 24).

The direction (sign) of the speed could not be calculated from the amplitude of the induced voltage, but it could be obtained by calculating the phase angle relative to the excitation current. The speed values could be calculated by the voltage peaks or by the voltage RMS

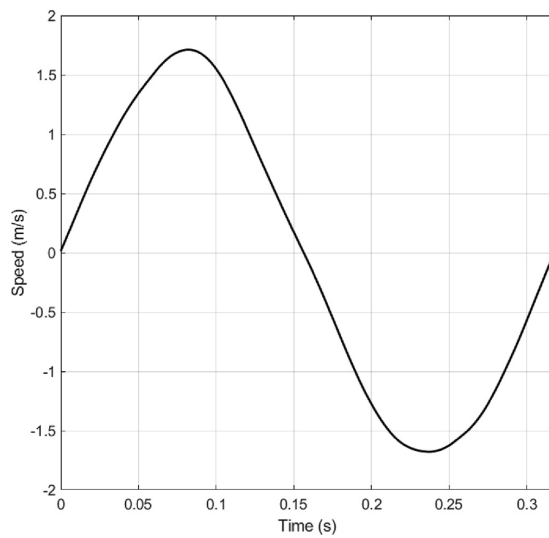


Fig. 22. Applied experimental speed versus time for an iron moving part.

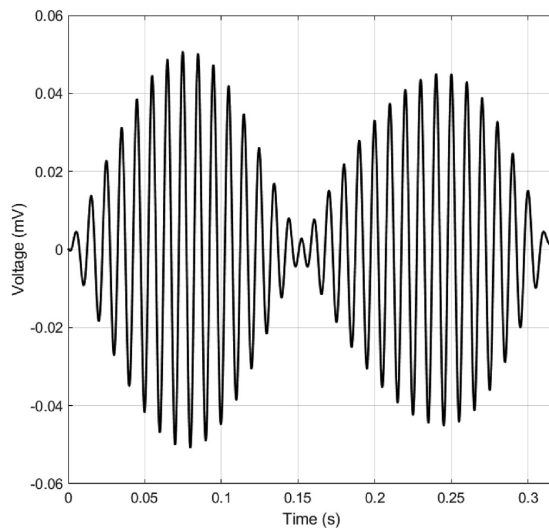


Fig. 23. Experimental differential voltage versus time for an iron moving part - 100 Hz.

or the rectified DC value in each half period can be used. Minima and maxima of the differential voltage in Figs. 20 and 23 correspond to the zero crossing and maximums of speed in Figs. 19 and 20.

The parameter, K in (18) for iron moving part changes from 0.037 mV/m/s for relative magnetic permeability, $\mu_{ri} = 100$ to 0.027 mV/m/s for $\mu_{ri} = 150$ at 100 Hz. The parameter, K ($=0.18$ mV/m/s) for the aluminum moving part is a fixed value for constant gap. The speeds of moving parts in Figs. 19 and 22 are changing between -1.75 m/s to $+1.75$ m/s. The induced voltage is higher for aluminum moving part in the same speed range in comparison with iron moving part.

Using ratiometric output $U_1 - U_2 / (U_1 + U_2)$ would be the first choice to compensate lift off changing and materials effects of moving part. This technique is successfully utilized in LVDT sensors. However, verification of such compensation is out of the scope of the present

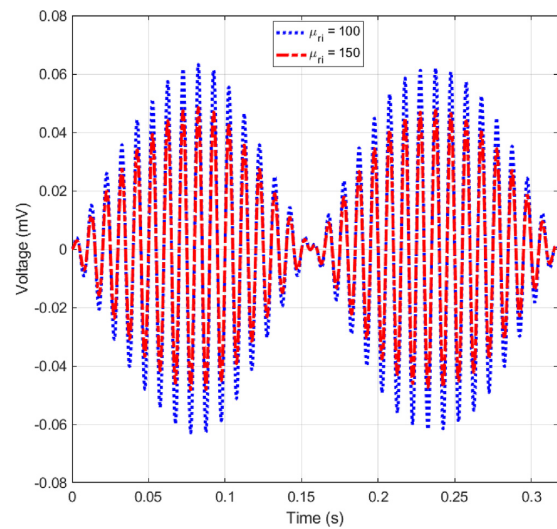


Fig. 24. Analytically calculated differential voltage versus time for an iron moving part - 100 Hz.

paper and will be a subject of the future study

Second potential approach to compensate the lift off changing and materials effects is using multi-frequency sensor technique, which is well proved in [22]; we also plan to examine this method in our future work.

Time stepping 3D FEM with motion consideration was implemented to analyze eddy current speed sensor, where sliding mesh is utilized to model moving part motion. Two fixed meshes are considered for stationary part and moving part and they are linked to each other by sliding mesh technique. Analysis of eddy current speed sensor using time stepping 3D FEM with motion is especially time consuming and complicated process and also with high probability of numerical errors, which could be mitigated using presented precise analytical method.

The methodology utilized in this paper to evaluate speed effect is also used, for example, for non-destructive testing (NDT) of metallic bodies [23–25]. Motion-induced eddy current thermography for high-speed inspection has been presented in [23] using equivalent rotating (travelling) magnetic field generated by three phase windings. The evaluation of effects of speed component of eddy current on the magnetic flux leakage inspection for non destructive testing of thick-wall steel pipe has been published in [24]. Utilizing speed effects on the induced eddy current in the conductive moving bodies with perpendicular configuration of coils relative to the moving body for non-destructive testing was presented in [25].

The presented contactless speed sensor shows better fittingness in terms for robustness and structure simplicity for practical applications in comparison with other contactless speed sensor [26].

5. Conclusion

The core of this paper is precise analysis method allowing fast design and suitability evaluations of eddy current speed sensors with both non-ferromagnetic and ferromagnetic materials for moving parts, which were overlooked in the literatures.

The performance and the design of a flat type eddy current speed sensor with air coils have been analyzed. Analytical models and 3D FEM calculations have been presented. The use of a fast and precise 3D analytical method is essential for the fast design and optimization of an air coil eddy current speed sensor. The linearity of the proposed speed sensor is excellent, despite its simple configuration. The calculated and

measured speed range has been considered up to 2 m/s, but it can be extended for higher translational speed. The proposed eddy current speed sensor could be used for all types of linear machines, as it has a simple structure and precise performance. The air coil configuration enables the proposed eddy current speed sensor to be very compact and cost-effective.

The effects of the material of the conductive moving parts have been evaluated. They have been shown to have a very critical influence on the design and analysis of eddy current speed sensors, and they must be taken into account. The output results and the performance of an eddy current speed sensor with a ferromagnetic moving part differ greatly from the results and the performance with a non-magnetic moving part. It is critical to compensate the magnetic permeability and also the conductivity of the moving part in the design of an eddy current speed sensor. Temperature stability and the effects on the conductive moving part must also be taken into consideration for an eddy current speed sensor. The conductivity and even the magnetic permeability of the moving part are affected by temperature.

The proposed configuration is without the use of a magnetic yoke for the coils, and without magnetic shielding. Adding a magnetic yoke to the sensor configuration could increase the output and the sensitivity of the sensor, and would shield the sensor from magnetic parasitic effects. Perpendicular configurations of the pick-up coils are alternatives to the flat type configuration aimed at reducing the longitudinal length of the sensor. However, perpendicular configurations would reduce the sensitivity of the sensor, and would decrease the magnetic coupling between the excitation coil and the pick-up coils.

Declaration of Competing Interest

No conflict of interest.

References

- [1] C.-T. Liu, S.-Y. Lin, Y.-Y. Yang, Flux modeling and analysis of a linear induction motor for steel mill non-contacting conveyance system application, *J. Magn. Magn. Mater.* 290–291 (2005) 1359–1362.
- [2] C.-T. Liu, S.-Y. Lin, Y.-Y. Yang, C.-C. Hwang, Analytical model development of an eddy-current-based non-contacting steel plate conveyance system, *J. Magn. Magn. Mater.* 320 (2008) 291–295.
- [3] Z. Zhang, C. Xi, Y. Yan, Q. Geng, T. Shi, A hybrid analytical model for open-circuit field calculation of multilayer interior permanent magnet machines, *J. Magn. Magn. Mater.* 435 (2017) 136–145.
- [4] D. Zeng, G. Lv, T. Zhou, Equivalent circuits for single-sided linear induction motors with asymmetric cap secondary for linear transit, *IEEE Trans. Ener. Conv.* 33 (4) (2018) 1729–1738.
- [5] N. Fernando, P. Arumugam, C. Gerada, Design of a stator for a high-speed turbo-generator with fixed permanent magnet rotor radius and volt-ampere constraints, *IEEE Trans. Ener. Conv.* 33 (3) (2018) 1311–1320.
- [6] P. Ripka, *Magnetic Sensors and Magnetometers*, Artech House, Jan 1, 2001 – Technology & Engineering.
- [7] X. Ge, Z.Q. Zhu, R. Ren, J.T. Chen, A novel variable reluctance resolver with non-overlapping tooth-coil windings, *IEEE Trans. Ener. Conv.* 30 (2) (2015) 784–794.
- [8] X. Ge, Z.Q. Zhu, A novel design of rotor contour for variable reluctance resolver by injecting auxiliary air-gap permeance harmonics, *IEEE Trans. Ener. Conv.* 31 (1) (2016) 345–353.
- [9] N. Takehira, A. Tanaka, Analysis of a perpendicular-type eddy-current speed meter, *IEE Proc. A – Phys. Science, Meas. Instr., Manag. Educ. Rev.* 135 (2) (1988) 89–94.
- [10] T. Itaya, K. Ishida, A. Tanaka, N. Takehira, T. Miki, Eddy current distribution for a rectangular coil arranged parallel to a moving conductor slab, *IET Science, Meas. Tech.* 6 (2) (2012) 43–51.
- [11] T. Itaya, K. Ishida, A. Tanaka, N. Takehira, Analysis of a fork-shaped rectangular coil facing moving sheet conductors, *IET Sci., Meas. Tech.* 3 (4) (2009) 279–285.
- [12] A. Tuysuz, M. Flankl, J.W. Kolar, A. Mutze, Eddy-current-based contactless speed sensing of conductive surfaces, *IEEE 2nd Annual Southern Power Electronics Conference (SPEEC)*, pp. 1–6, Dec. 2016.
- [13] M. Mirzaei, P. Ripka, A. Chirtsov, J. Vyhnanek, Eddy current linear speed sensor, *IEEE Trans. Mag.* 55 (1) (2019) 1–4.
- [14] H.H. Woodson, J.R. Melcher, *Electromechanical Dynamics, Part II*, John Wiley & Sons, Inc., 1968.
- [15] J.A. Shercliff, *The Theory of Electromagnetic Flow Measurement*, Cambridge University Press, 1962.
- [16] K. Yoshida, New transfer-matrix theory of linear induction machines, taking into account longitudinal and transverse ferromagnetic end effects, *IEE Proc. B – Elect. Power Appl.* 128 (5) (1981) 225–236.
- [17] S. Yamamura, *Theory of Linear Induction Motors*, second ed., John Wiley & Sons, 1979.
- [18] M. Poloujadoff, *The Theory of Linear Induction Machinery*, Clarendon Press, 1980.
- [19] D. Schieber, *Electromagnetic Induction Phenomena*, Springer-Verlag, 1986 Science.
- [20] K. Davey, Analytic analysis of single- and three-phase induction motors, *IEEE Trans. Mag.* 34 (5) (1998) 3721–3727.
- [21] S. Salon, *Finite Element Analysis of Electrical Machines*, Springer US, 1995.
- [22] M. Lu, Y. Xie, W. Zhu, A. Peyton, W. Yin, Determination of the magnetic permeability, electrical conductivity, and thickness of ferrite metallic plates using a multifrequency electromagnetic sensing system, *IEEE Trans. Ind. Inf.* 15 (7) (2019) 4111–4119.
- [23] G. Piao, J. Guo, T. Hu, H. Leung, The effect of motion-induced eddy current on high-speed magnetic flux leakage (MFL) inspection for thick-wall steel pipe, *Res. Nondest. Eval.* (2019) 1–20.
- [24] J. Wu, K. Li, G. Tian, J. Zhu, Y. Gao, C. Tang, X. Chen, Motion-induced eddy current thermography for high-speed inspection, *AIP Adv.* 7 (2017) 085105.
- [25] T. Itaya, K. Ishida, A. Tanaka, N. Takehira, T. Miki, Analysis of a fork-shaped rectangular coil oriented perpendicular to moving conductor slabs, *NDT E Int.* 44 (5) (2011) 413–420.
- [26] C. Moron, E. Suarez, Non-contact digital speed sensor, *J. Magn. Magn. Mater.* 133 (1994) 610–612.

5.2 A Position Sensor with Novel Configuration of Linear Variable Differential Transformer

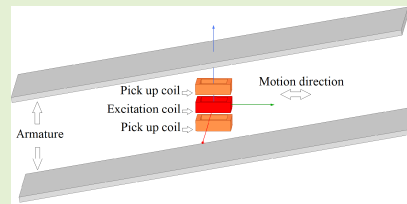
A variant of the classic LVDT is presented in this paper. Its distinguishing point is the perpendicular orientation between the coils attached to a movable plunger, and the stationary frame containing strips of high-permeability steel (referred to as *armatures* in the manuscript). There is one central excitation winding and two antiseriably connected pickup windings mounted to the plunger, without any magnetic components. Because the armatures are attached at an angle relative to the frame, the total airgap is constant along the stroke, but the ratio of airgap lengths for each of the pickup windings is continuously changing according to the plunger position. My personal contribution to this paper was mechanical design and measurements.

A Position Sensor With Novel Configuration of Linear Variable Differential Transformer

Mehran Mirzaei¹, Member, IEEE, Pavel Ripka², Member, IEEE,
and Vaclav Grim³, Graduate Student Member, IEEE

Abstract—This paper presents a position sensor based on a novel configuration of linear variable differential transformer. Design and optimization of the position sensor using finite element method are presented. The measurements are also conducted to validate experimentally the sensor performance. The sensor has short air core coils and long magnetic armatures. The axis of the rectangular excitation coil and two antiseriably connected rectangular pick up coils is perpendicular to the motion direction of the position sensor. The coils are located between two parallel silicon steel laminations serving as the armatures. The position sensor is optimized with compromise between minimization of nonlinearity error and maximum sensitivity. The main advantage of the proposed position sensor is the small ratio of coils dimensions to the working range. The position sensor is operated for excitation frequencies of 500 Hz, 1000 Hz, and 2000 Hz. The maximum nonlinearity error is less than 1.5% for the theoretical results and it is less than 2% for the measured results in ± 90 mm position range.

Index Terms—Position sensor, linear variable differential transformer, design and optimization, finite element method.



I. INTRODUCTION

THE position sensing and position sensors have a key role in various industrial applications and machineries with translational and rotational moving components [1]–[8]. The common types of position sensors are potentiometric, linear variable differential transformer (LVDT), optical, magnetostrictive, and magnetometer based, for example, magnetic Hall sensor.

Potentiometric position sensors are inexpensive, they have high accuracy, and simple signal processing [9], [10]. However, they are sensitive to the wear, dust, and vibrations. LVDT position sensors have high accuracy with lower sensitivity to the working environment [1], [11]–[15]. They could be quite expensive and bulky because of the coils. Optical position sensors are sensitive to the dust despite their high accuracy and excellent resolution. Magnetometer based position sensors are sensitive to the magnetic objects and external fields,

which affect their accuracy [2], [7]. Magnetostrictive position sensors [16] with high accuracy for long distance are sensitive to temperature, not cost effective and with less accuracy for short distance operation.

Position sensor based on variable inductance or impedance were presented in [17]–[19]. These sensors have bulky windings and heavy weight for long length measurements. Position sensors using magnetically coupled coils and short-circuited moving coil and air coil structure were designed and measured in [20] and [21]. However, these sensors suffer from low sensor output sensitivity and low immunity to the external magnetic objects. A variable reluctance differential solenoid transducer for position sensing was validated for high precision in [22], which is only shown for short lengths and it could be very bulky and heavy for large distance measuring. A permanent magnet linear resolver was used for position sensing for long distance in [23]. However, it needs salient secondary magnetic part with high precision punched or machine tooled and NdFeB permanent magnets which are less appropriate for harsh environments. The authors developed and presented long position sensor for 500 mm working range for pneumatic cylinders and hydraulic cylinders applications with small size coils and a long conical solid iron rod [24].

A novel configuration of LVDT is utilized for position sensing in this paper with short coils and long armatures for long distance position measurements. The sensor can detect positive and negative movements as conventional LVDTs. The

Manuscript received July 15, 2021; revised August 15, 2021; accepted August 15, 2021. Date of publication August 18, 2021; date of current version October 18, 2021. This work was supported in part by Czech Technical University in Prague under Grant SGS18/187/OHK3/3T/1. The associate editor coordinating the review of this article and approving it for publication was Prof. Rosario Morello. (Corresponding author: Mehran Mirzaei.)

The authors are with the Faculty of Electrical Engineering, Czech Technical University in Prague, 16627 Prague, Czech Republic (e-mail: mirzameh@fel.cvut.cz; ripka@fel.cvut.cz; vaclav.grim@fel.cvut.cz).
Digital Object Identifier 10.1109/JSEN.2021.3105879

1558-1748 © 2021 IEEE. Personal use is permitted, but republication/redistribution requires IEEE permission.
See <https://www.ieee.org/publications/rights/index.html> for more information.

Authorized licensed use limited to: CZECH TECHNICAL UNIVERSITY. Downloaded on July 30, 2022 at 16:53:59 UTC from IEEE Xplore. Restrictions apply.

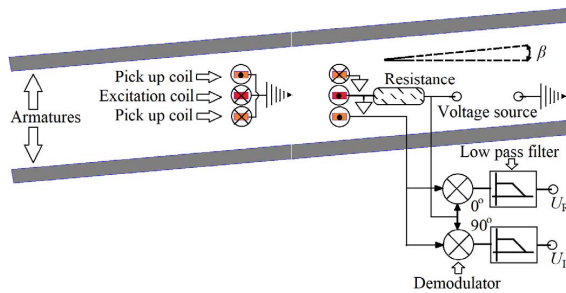


Fig. 1. Schematic model of position sensor using two parallel armatures with LVDT configuration and sensor measurement system using a lock in amplifier.

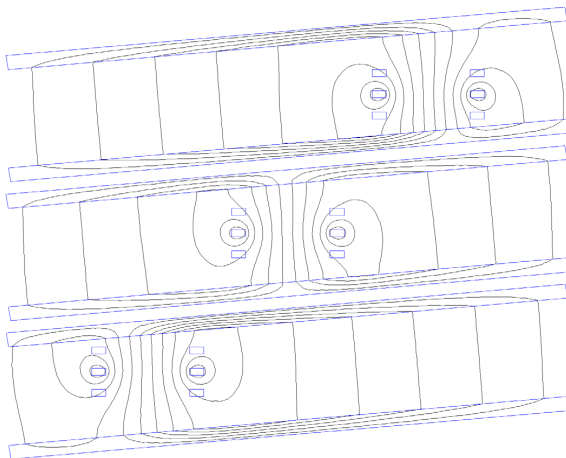


Fig. 2. Schematic magnetic flux distribution in the sensor at different relative positions of the coils relative to the armatures.

goal was to design a position sensor with simple structure and performance, which would be cost effective. Armatures are made of only two parallel silicon steel laminations with 0.5 mm thickness, which have been slightly angularly rotated from the direction perpendicular to the coil axis. Unlike the conventional LVDT sensor, the sizes of excitation and pick up coils are unchanged in this sensor to measure longer distance positions. 2D and 3D finite element method (FEM) is used for the performance analysis and design. The position sensor is designed and optimized to have high output sensitivity and low nonlinearity error.

II. BASIC STUDY AND STRUCTURE

Fig. 1 shows schematic 2D model of the position sensor, which consists of two armatures, one excitation coil and two antiserially connected pick up coils. The two armatures are in parallel and they are angularly shifted with angle, β relative to the coils in the horizontal plane (Fig. 1). Fig. 2 depicts schematic magnetic flux distributions at different relative positions of the coils and the armatures.

Equation (1) presents relationship between differential voltage, U_d and each pick up coil voltage, U_1 and U_2 .

$$\begin{aligned} U_1 &= -j\omega \cdot \Psi_1 \\ U_2 &= -j\omega \cdot \Psi_2 \end{aligned}$$

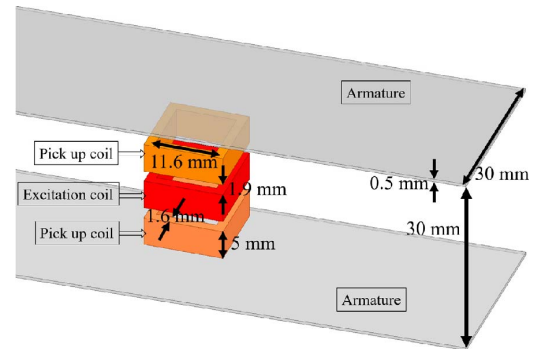


Fig. 3. 3D model of the position sensor and its dimensions – one excitation coil, two pick up coils and two armatures using 0.5 mm thickness steel laminations.

$$\omega = 2\pi \cdot f$$

$$U_d = U_2 - U_1 = -j\omega \cdot \Psi_d, \quad \Psi_d = \Psi_2 - \Psi_1 \quad (1)$$

where, the differential flux linkage, Ψ_d is $\Psi_2 - \Psi_1$. Ψ_2 and Ψ_1 are the flux linkage of each pick up coils. f is the excitation frequency.

The upper and lower pick up coils have same flux linkage ($\Psi_2 = \Psi_1$) when they are located in the center position of armatures and their differential voltage is zero. However, the differential voltage value becomes negative or positive when the relative positions of the coils to the armatures are moved to the left or right directions. Because the flux linkages in pick up coil are different ($\Psi_2 \neq \Psi_1$) as distance between them, and the armatures are not the same as shown in Fig. 2.

3D model and dimensions of the position sensor are shown in Fig. 3. The number of turns in all coils is considered identical and it is equal to 500. The longitudinal length and transversal width of armatures are 300 mm and 30 mm, respectively. The mean width, w_m and height, h of each coil are 11.6 mm and 5 mm as shown in Fig. 3. The position sensor performance is studied and measured at excitation frequencies, 500 Hz, 1000 Hz and 2000 Hz with corresponding measured current amplitudes, I_m , 84.7 mA, 83.0 mA and 79.4 mA, respectively.

III. FEM STUDY

2D and 3D time harmonic FEM [25] are used for the steady state performance analysis of the position sensor. The magnetic flux density is very low in the steel lamination of armatures as shown Fig. 4. Therefore, linear magnetic modeling is performed in the FEM simulations. And initial relative magnetic permeability, $\mu_r = 1000$ for the steel lamination is estimated and considered for the FEM analysis [13], [26]. The conductivity of steel lamination was measured, which is $\sigma = 3.14$ MS/m. The induced eddy current in the steel laminations is considered (Fig. 5) in the FEM analysis.

The following differential equations extracted from Maxwell equations are used in time harmonic magnetic field analysis:

$$\begin{aligned} \nabla \times H &= J \\ \nabla \cdot B &= 0 \rightarrow B = \nabla \times A \\ \nabla \times J &= -j\omega\sigma \cdot B \end{aligned} \quad (2)$$

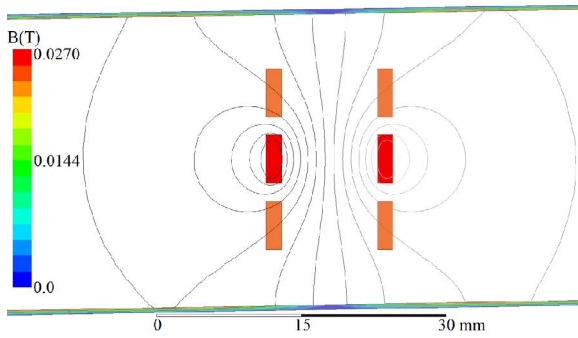


Fig. 4. Magnetic flux distribution at zero position, $I_m = 83$ mA and $\beta = 1$ deg., and $d = 0$ mm – 2D FEM.

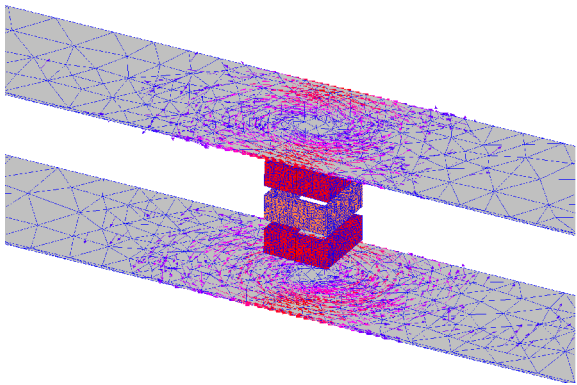


Fig. 5. 3D FEM meshed model of position sensor and induced eddy current in conductive silicon steel lamination with 0.5 mm thickness.

where, H , J , B , and A are magnetic field strength, current density, magnetic flux density, and magnetic vector potential, respectively. Magnetic vector potential has only one unknown component, A_z in 2D analysis, but it has three unknowns, A_x , A_y and A_z in general 3D case. Therefore, 3D analysis is more time consuming and it needs more memory.

The FEM analyses of the position sensor are performed in ± 100 mm range. Fig. 6 shows the voltages of each pick up coil and their differential voltage versus position, d with $\beta = 1$ deg. Real and imaginary components of voltages are calculated relative to the current of the excitation coil as a reference signal. Real component of voltage is caused by induced eddy currents in the conductive steel lamination of armatures. 3D FEM results shows less value in comparison with 2D FEM because of 3rd dimension effects (transverse effects), which is not considered in the 2D FEM. The model depth in transverse direction is considered 11.6 mm in 2D FEM, which is equal to the mean width of coil, w_m in Fig. 3. The differential voltages show linear curve versus position, d in Fig. 6, which could be utilized as a position indicator.

The differential voltage to frequency ratio is depicted in Fig. 7 up to 10 kHz with $\beta = 1$ deg., which is equivalent to differential flux linkage, $\Psi_2 - \Psi_1$ in (1). It shows that the imaginary component of voltage is considerable higher than

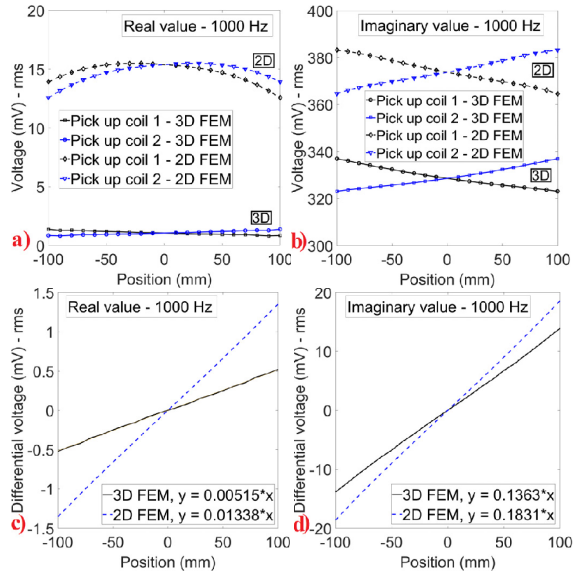


Fig. 6. The real and imaginary values of voltages of each pick up coils, U_1 and U_2 (upper, a) and b)) and their differential voltage, $U_d = U_2 - U_1$ (bottom, c) and d)) at 1000 Hz, $I_m = 83$ mA and $\beta = 1.0$ deg. – 2D FEM vs 3D FEM.

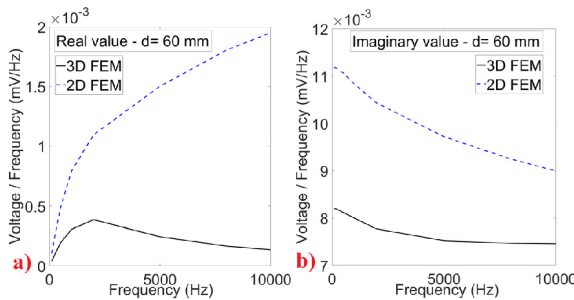


Fig. 7. The differential voltages normalized by frequency versus frequency, $I_m = 83$ mA, $\beta = 1$ deg., and $d = 60$ mm – 2D FEM vs 3D FEM.

real component of voltage similar to the results in Fig. 6. The voltage to frequency ratio is decreasing with increasing frequency because of skin effects in the conductive steel laminations. Using nonconductive ferromagnetic armatures, such as ferrite, would cancel frequency dependency of voltage to frequency ratio and diminish real component of voltage.

Absolute value of voltage, U_A can be also utilized for position sensing as both real, U_R and imaginary, U_I components have linear dependence on position.

$$U_A = \sqrt{U_R^2 + U_I^2} \quad (3)$$

Absolute value of voltage is almost equal to the imaginary component of voltage as real component voltage is much smaller especially at operating frequency, 1000 Hz.

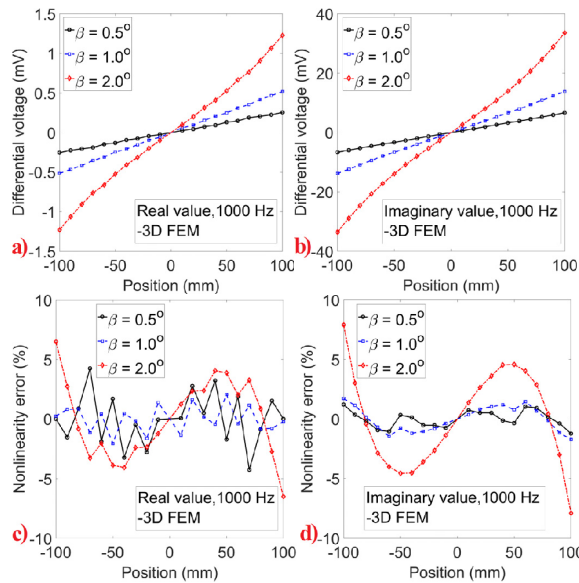


Fig. 8. The differential voltage and nonlinearity error at 1000 Hz, and $I_m = 83$ mA versus armatures angles, β .

The differential voltages and nonlinearity full scale errors for different armatures shifting angles, β are presented in Fig. 8. The differential voltage is higher for bigger shifting angles, β . However, maximum nonlinearity full scale error is also increasing with β . The calculated imaginary component of differential voltage has lower nonlinearity error, which makes it more suitable for position indicating at $\beta = 0.5$ deg. and 1.0 deg. Shifting angles, $\beta = 1.0$ deg. is preferred as it is a compromise between maximum sensitivity and minimum nonlinearity error. Voltage difference between upper and lower pick up coils versus position has less linear shape at higher armature angle as the distance between the coils and the armature is changing in larger range. The reason of the nonlinearity is the fact, that the coil coupling is always nonlinear function of armature distance. Linearity error is kept small only if the distance between the coils and armature is changing in a small range.

Increasing the gap between the excitation coil and the pick-up coils g_c increases the differential voltage with the expense of increasing the nonlinearity full scale error as shown in Fig. 9. Selecting gap distance, $g_c = 1.9$ mm and armatures shifting angles, $\beta = 1.0$ deg. is a compromise between sensitivity and nonlinearity.

Table I shows sensitivity coefficients, K_R and K_I of real and imaginary components of the differential voltage for different relative magnetic permeability, μ_r of silicon steel lamination of armatures. They are calculated based on linear curve fitting:

$$\begin{aligned} U_R &= K_R \cdot X \\ U_I &= K_I \cdot X \end{aligned} \quad (4)$$

where, X is relative position of the coils and the armatures. Increasing or decreasing relative magnetic permeability, μ_r about 25% causes about 10% change in real component

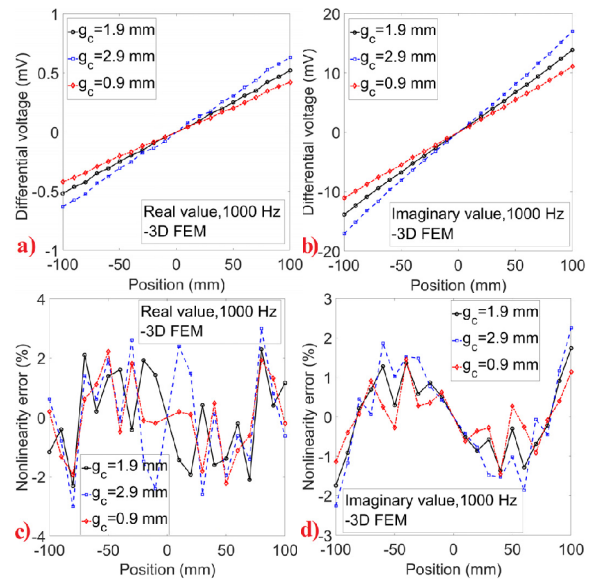


Fig. 9. The differential voltage and nonlinearity error at $\beta = 1.0$ deg., and $I_m = 83$ mA versus gap between excitation coil and pick up coils, g_c .

TABLE I
SENSITIVITY COEFFICIENTS FOR DIFFERENT
PERMEABILITY – 3D FEM

μ_r	K_R (mV/mm)	K_I (mV/mm)
750	0.005654 (109.7%)	0.1348 (99.3%)
1000	0.005154 (100.0%)	0.1358 (100.0%)
1250	0.004623 (89.7%)	0.1366 (100.6%)

sensitivity, K_R and only 0.6% to 0.7% in imaginary component sensitivity, K_I .

IV. EXPERIMENTAL RESULTS

The position sensors and experimental elements are shown in Fig. 10. Lock in amplifier is used for the voltage measurements of antiseriially pick up coils. A signal generator with internal resistance 50Ω is connected in series with excitation coil as a source voltage. Also, an external 5.85Ω resistance is connected in series with the excitation coil and signal generator. It is utilized to measure the current of the excitation coil as a reference signal for the lock in amplifier, which real and imaginary components of pick coil voltage are finally measured relative to the reference signal. The schematic model of voltage measurement using lock in amplifier is also illustrated in Fig. 1. The reference sensor is a Senpos MRTM500 type potentiometric linear position sensor with a measurement range of 500 mm and a linearity error of 0.05%.

Firstly, measured inductances of excitation coil and antiseriially connected pick up coils and 3D time harmonic FEM calculations for the coils inductances were evaluated with and without silicon steel laminations of the armatures for the initial assessment of modeling. The results are presented in Table II and Table III at 500 Hz, 1000 Hz and 2000 Hz. The 3D FEM results match better with measurements for pick up

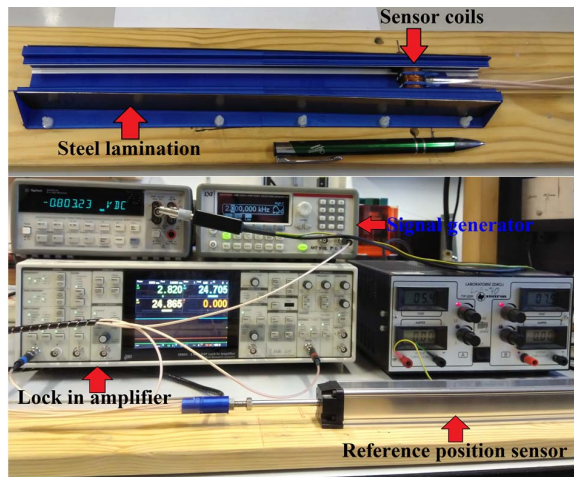


Fig. 10. The position sensor – Excitation coil, pick up coils and steel laminations(up) and experimental elements – lock in amplifier, signal generator, and reference position sensor (bottom).

TABLE II
COMPARISON BETWEEN EXPERIMENTAL AND 3D FEM – INDUCTANCES WITHOUT ARMATURES

	L_{EC} (mH)	L_{PK} (mH)
Exp.	3.470	6.2285
3D FEM	3.3279	6.2220

TABLE III
COMPARISON BETWEEN EXPERIMENTAL AND 3D FEM – INDUCTANCES WITH ARMATURES

f (Hz)	$d=0$ mm		$d=\pm 100$ mm	
	L_{EC} (mH)	L_{PK} (mH)	L_{EC} (mH)	L_{PK} (mH)
500	Exp./	Exp./	Exp./	Exp./
	3.5190/	6.3910/	3.5195/	6.4170/
1000	Exp./	Exp./	Exp./	Exp./
	3.5187/	6.390/	3.5187/	6.4158/
2000	Exp./	Exp./	Exp./	Exp./
	3.5169/	6.3878	3.5173/	6.4134
	3.3771	6.3890	3.3784	6.4333

coils inductances, L_{PK} , however, they are also in adequate range for excitation coil inductances, L_{EC} . The pick-up coil inductances are more sensitive to armature position, d than excitation coil inductances.

The measured real and imaginary components of differential voltage and their full-scale nonlinearity errors versus position are presented in Fig. 11 at 500 Hz, 1000 Hz and 2000 Hz. The measured real component of voltage curve is smaller and less linear in comparison with imaginary component. The imaginary component sensitivity is about 8.6 times higher than real component sensitivity at 2000 Hz and this ratio increases up to 14.0 and 23.7 at 1000 Hz and 500 Hz, respectively.

The maximum nonlinearity error is close to the 5% for real component of voltage and it is less than 4% for imaginary component for ± 100 mm operating range. However, the maximum nonlinearity error is less than 2% for ± 90 mm operating

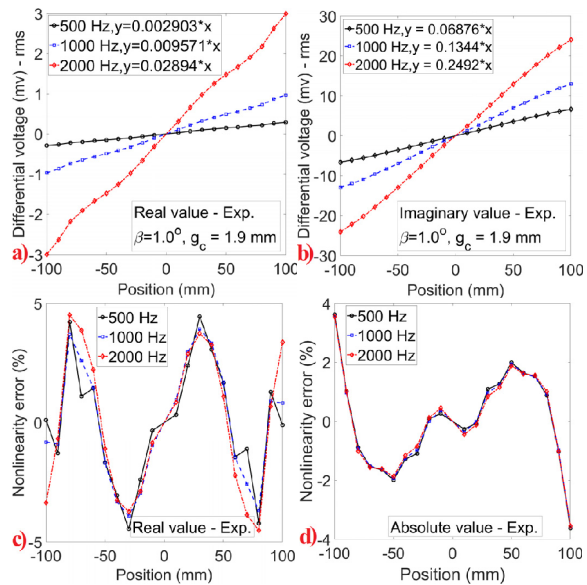


Fig. 11. The differential voltage and nonlinearity error– Experimental results for real and imaginary components.

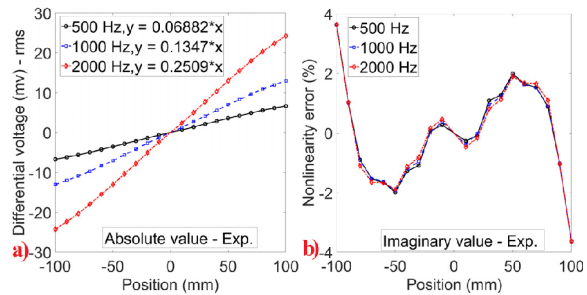


Fig. 12. The differential voltage and nonlinearity error – Experimental results for absolute value.

range. The high nonlinearity error at ± 100 mm for armatures position is mainly caused by manufacturing tolerance, as this high nonlinearity error is absent in 3D FEM at ± 100 mm in Fig. 9. The full-scale nonlinearity error is less than 1.5% for the whole ± 100 mm working range in 3D FEM results.

High nonlinearity error of real component of differential voltage has not considerable effect on the absolute value of differential voltage as shown in Fig. 12. The sensitivity coefficient of absolute value of differential voltage, K_A increases 0.7% in comparison with sensitivity coefficient of imaginary component at 2000 Hz and it increases 0.2% and 0.1% at 1000 Hz and 500 Hz, respectively.

The coils dimensions are selected quite small in comparison with armature width, 30 mm in order to shield the excitation coil and pick up coils by the armature from external fields and the influence of ferromagnetic objects. Rectangular shape coils are more appropriate than circular shape as differential voltage of pick up coils is higher with same outer diameter of the coils. Bigger dimensions of the coils can be implemented with

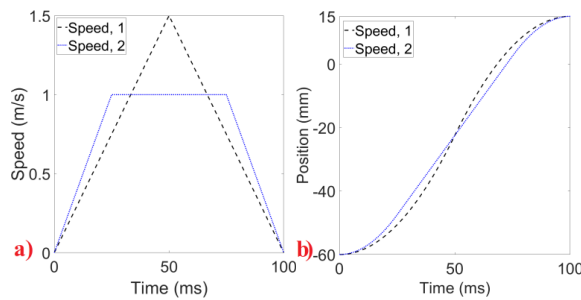


Fig. 13. Two applied time varying speed profiles and corresponding positions versus time.

same armatures, which would increase the induced voltage and thus the sensors sensitivity. However, such sensor would need additional external shielding. Standard copper wires with enough low current density are used to avoid external cooling for the sensor and increase its thermal stability. Increasing vertical distance between coils increases sensor output with expense of increasing nonlinearity error as shown in Fig. 9. Therefore, a compromise between maximum sensitivity and minimum nonlinearity error is necessary. Sensor sensitivity can be increased by increasing the number of turns of the coils. For the excitation coil the limit is the maximum flux density in the armature for linear operation, for the pickup coils the limit is the first coil resonance frequency (caused by the parasitic capacitance).

We have also tested the susceptibility to the vertical misalignment of the armature, i.e., when one of the armatures is shifted to left or right perpendicularly to the sensors motion direction. The maximum error was 0.23% for 2 mm perpendicular misalignment.

V. DYNAMIC ANALYSIS

The performance of the position sensors is important in the dynamic conditions, especially, when the sensors have conductive components. The dynamic modeling using 2D time stepping FEM analysis of the position sensor at variable speeds are performed to evaluate motional induced eddy current effects on the sensor performance. The motional induced eddy current is generated when solid conducting armatures have relative speed to the excitation coil [27]–[29]. 2D time stepping FEM is used for the dynamic analysis despite its lower accuracy. The reason is that 2D FEM has less limitation for the dynamic analysis in terms of mesh complexity and memory requirements, which is not straightforwardly conceivable in 3D time stepping FEM [30] analysis with consideration of motion. Two different speed profiles, 1 and 2 are selected for the dynamic analysis for the time range of 100 ms as shown in Fig. 13. The positions of armatures, d versus time change from -60 mm to $+15$ mm in both speed profiles, but they have different shapes.

The differential voltages versus armatures position shown for speed profiles, 1 and 2 in Fig. 14 at 500 Hz and 1000 Hz, are the same for the two speed profiles. It can be confidently concluded that motional component of induced eddy current

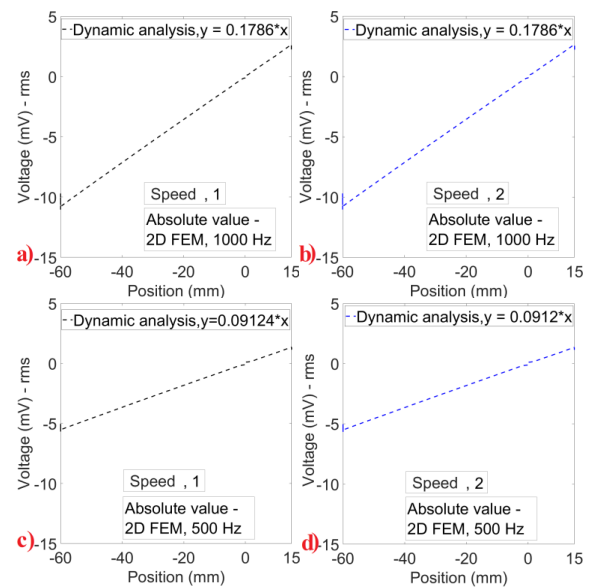


Fig. 14. The differential voltage versus position in dynamic conditions—2D FEM.

TABLE IV
SENSITIVITY COEFFICIENTS OF RATIO-METRIC FUNCTION FOR DIFFERENT PERMEABILITY – 3D FEM

μ_r	K_{R-r} (1/mm)	K_{I-r} (1/mm)
750	0.002460 (103.0%)	0.0002048 (99.4%)
1000	0.002388 (100.0%)	0.0002060 (100.0%)
1250	0.002368 (99.2%)	0.0002069 (100.4%)

in steel laminations has negligible effects on the performance of the position sensor. Fig. 15 shows measurement results for the dynamic experiments and comparison between voltages at stationary and dynamic conditions, which well coincidence between dynamic and stationary results. It approves theoretical results in Fig. 14.

VI. DISCUSSIONS

Using ratio-metric function $((U_2 - U_1)/(U_2 + U_1))$ reduces sensitivity of the position sensor to the armature material parameters, frequency and amplitude of the excitation current [11]. For example, Table IV shows sensitivity coefficients using ratio-metric function (K_{R-r} and K_{I-r}) for relative magnetic permeability change, which shows maximum 3% change for real component sensitivity, K_{R-r} and 0.4% to 0.6% in imaginary component sensitivity, K_{I-r} . These are lower sensitivities to the relative magnetic permeability change in comparison with sensitivity coefficient in Table I. Therefore, ratio-metric function could be also utilized to compensate material effects and temperature effects on the performance of the position sensor.

Real and imaginary components of differential voltage versus frequency are measured and their ratio to frequency

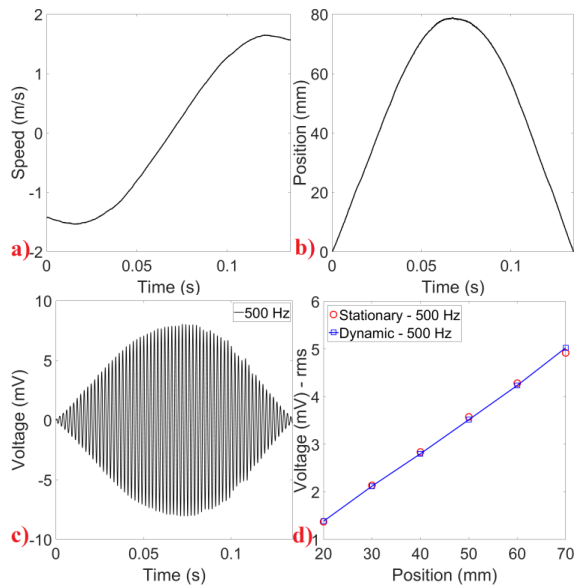


Fig. 15. Time varying speed, corresponding armature position, voltage versus time and voltage versus position – Experimental.

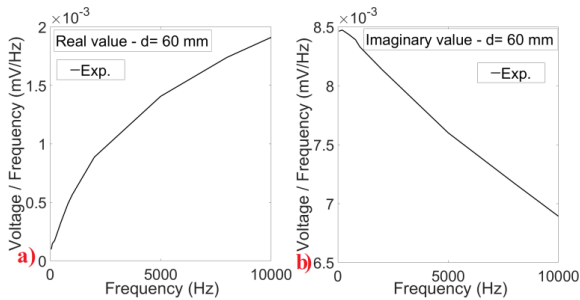


Fig. 16. The differential voltages normalized by frequency versus frequency, $I_m = 83$ mA, $\beta = 1$ deg., and $d = 60$ mm – Experimental.

are shown in Fig. 16 at armature position, $d = \pm 60$ mm. The measured imaginary component is close to the 3D FEM simulations in Fig. 7, however, real component is closer to the 2D FEM.

Fig. 17 presents the comparison between 3D FEM and experimental results for real and imaginary components of the differential voltage versus position. The real component has higher discrepancy between measurements and 3D FEM, which is similar to the 2D and 3D FEM results comparison in Fig. 6. The highest discrepancy between experimental results and 3D FEM for imaginary component of differential voltage occurs at ± 100 mm position of armature, where decrease of the experimental curve causes high nonlinearity error as shown in Fig. 11 and Fig. 12.

Non-linearity, calibration factor, repeatability, thermal stability and armatures material effects are the main sources of errors in LVDT sensors, which nonlinearity and armatures material effects are not initially controllable by manufacturing

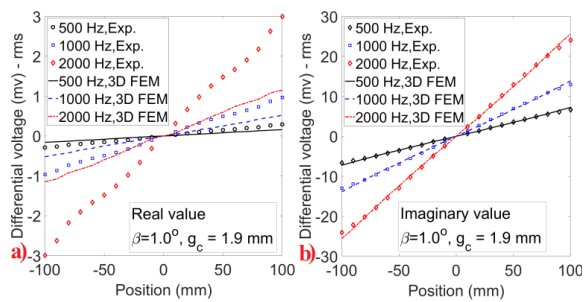


Fig. 17. The differential voltage – 3D FEM vs Experimental results.

process. Extension of linear range and nonlinearity error reduction of the LVDT position sensors using for example techniques based on the fractional order LVDT, LVDT inverse transfer characteristic and functional link artificial neural network allows sensor performance improvement for industrial applications [12], [14], [31], [32]. Multi frequency electromagnetic method and compensation technique on phase signature could be also used to compensate material effects in the position sensor [33], [34] in addition to using ratiometric function [11].

Main reason for selection of the excitation frequency until 2000 Hz is to limit the effects of induced eddy current in the silicon steel laminations on the position sensor performance. As induced eddy currents in the silicon steel lamination of armatures is stronger at higher frequencies, which attenuates excitation fields and produces eddy current losses in the laminations. Increasing to higher frequencies, 10 - 20 kHz as in conventional LVDT is feasible using, for example, Ferrite core, which is only limited by parasitic capacitance of the coils.

It is no theoretical limit for allowed speed due to the absence of friction and the sensor can have fast dynamic response, which only limited by inertia of the armatures or moving parts and mechanical constraint. The sensor performance is affected by vibration and temperature as LVDT sensor is an electromagnetic device, which it must be compensated against vibration and temperature as conventional LVDT. Temperature variation can be between -265 °C to 600 °C as conventional LVDT sensor.

Tables V and VI compare qualitatively and quantitatively the proposed LVDT sensor in this paper with conventional LVDT (CLVDT), linear potentiometer (LP), linear resolver (LR) and variable reluctance differential solenoid transducer (VRDST). The proposed LVDT sensor with compensation for output linearizing presents excellent accuracy as conventional LVDT [12], [14].

Linear magnetostrictive (LM) position sensor [16], linear optical (LP) position sensor [37], [38], linear capacitive (LC) position sensor [39] have excellent accuracy and resolution, however they would be complicated and noneconomic for long distance position sensing. They are also very sensitive to dust and dirt in harsh working environment [40]. The qualitative comparison of these sensors with the proposed LVDT sensor and conventional LVDT is presented in Table VII.

TABLE V
COMPARISON BETWEEN LVDT SENSOR IN THIS PAPER (PLVDT),
NON-COMPENSATED CONVENTIONAL LVDT (CVLDT), LINEAR
POTENTIOMETER (LP), AND LINEAR RESOLVER (LR)

	Cost	Precision	Contactless	Weight	Coils
PLVDT	Low	High	Yes	Low	Light
CLVDT	Medium	High	Yes	High	Medium
LP	Low	High	No	Low	Light
LR	High	High	Yes	Very high	Heavy

TABLE VI
COMPARISON BETWEEN LVDT SENSOR IN THIS PAPER (PLVDT),
NON-COMPENSATED CONVENTIONAL LVDT (CVLDT), VARIABLE
RELUCTANCE DIFFERENTIAL SOLENOID TRANSDUCER
(VRDST), AND LINEAR RESOLVER (LR)

	Position error	Operating range
PLVDT	1.8 mm	±90 mm
PLVDT	0.9 mm	±50 mm
CVLDT [12]	> 1.5 mm	±15 mm
CVLDT [14]	> 3 mm	±30 mm, ±95 mm
VRDST [22]	> 1 mm	0 - 7 mm
LR [35]	2.4 mm	0 - 380 mm
LR [36]	1 mm	0 - 20 mm

TABLE VII
COMPARISON BETWEEN LVDT SENSOR IN THIS PAPER (PLVDT),
NON-COMPENSATED CONVENTIONAL LVDT (CVLDT), LINEAR
CAPACITIVE (LC), LINEAR OPTICAL (LO), AND LINEAR
MAGNETOSTRICTIVE (LM)

	Range	Power	Complexity	Linearity	Accuracy
PLVDT	Long	Low	Low	Very good	High
CLVDT	Medium	High	Low	Very good	High
LO	Short	Low	High	Very good	High
LC	Short	Low	Low	Excellent	High
LM	Long	High	High	Very good	High

VII. CONCLUSION

The performance analysis and measurements of the position sensor with novel structure were presented. The sensor has simple configuration, and it is cost effective, which makes it a suitable option for industrial applications and economical mass production. The small size of the coils of the position sensor in comparison with armatures length and operating range makes it more fault tolerant in the harsh environment. Moreover, the position sensor is less bulky in comparison with its counterpart LVDT and potentiometer position sensors. The proposed LVDT sensor in this paper similarly to the conventional cylindrical counterpart can be used in industrial applications such as power turbines, hydraulics, automation, high speed railways, aircraft and satellites. The main application of the proposed position sensor is for harsh environment, submersible and high temperature cases of above-mentioned applications. As the coils are small, they can be hermetically sealed and thermally isolated easier than coils of conventional LVDT, which are longer for the same working range. Short coils are also less sensitive to external ferromagnetic objects and magnetic fields.

The conductive silicon laminations with 0.5 mm thickness were utilized for the armatures for easier manufacturing and lower material cost. These laminations limit the excitation frequency to 2000 Hz because of induced eddy current. The excitation frequency and thus the sensitivity can be increased if the lamination thickness is reduced, or if they are replaced with ferrite, iron powder or similar material with low conductivity to suppress induced eddy currents and minimize real component of differential voltage.

The measured sensitivities of the position sensor are 0.251 mV/mm, 0.135 mV/mm and 0.069 mV/mm for absolute value of differential voltage at 2000 Hz, 1000 Hz and 500 Hz, respectively. The maximum measured nonlinearity error is less than 2% in ±90 mm working range. The developed sensor has total error of 2% FS for 180 mm range without any compensation. This is acceptable only for some applications. The present analysis was limited to the proposed sensor with antiseriably connected pick-up coils. Advanced LVDTs often compensate nonlinearity error [12], [14], temperature effects and airgap variations by more complicated processing of the sensor output. The simulation procedures here can also be utilized in the analysis of such schemes. Both compensations would be necessary for the mentioned practical application.

The resolution for LVDT sensor is theoretically infinite and it is determined by the signal conditioning circuit of the sensor. The achievable resolution is 1.5 μm for the proposed sensor. Repeatability of the proposed sensor is 0.4% without compensation.

The variations of temperature, excitation current and frequency are initial sources of error in LVDT sensors, which their effects can be straightforwardly diminished using standard ratiometric function. The change of armatures magnetic permeability causes error in LVDT sensor, which standard ratiometric function decreases caused error by 15%-33% for 25% change in armatures relative permeability value. The manufacturing incorrectness is another source of the error in the position sensor. The difference in maximum nonlinearity error between theoretical calculations and experimental results is about 0.64% in this paper, which experimental maximum nonlinearity error can be reduced from 2% to about 1.36% using more precise manufacturing. Further decreasing of the nonlinearity error to below 0.1% can be made using external electronic processing unit for the LVDT sensor.

Further optimization of the position sensor in terms of increasing sensitivity with optimizing coils dimensions, reducing nonlinearity errors and extending linearity range with changing the thickness and shifting angle of the armatures in the motion direction is planned for the future works. The design of coils with magnetic cores will be also considered to increase the sensitivity.

REFERENCES

- [1] C. W. Clapp, "Use of saturable cores in linear differential transformers," *IEEE Trans. Aerosp.*, vol. 2, no. 4, pp. 1134-1142, Oct. 1964.
- [2] S. Taghvaceyan, R. Rajamani, and Z. Sun, "Non-intrusive piston position measurement system using magnetic field measurements," *IEEE Sensors J.*, vol. 13, no. 8, pp. 3106-3114, Aug. 2013.
- [3] M. Mirzaei, P. Ripka, A. Chirtsov, and V. Grim, "Temperature stability of the transformer position transducer for pneumatic cylinder," *J. Magn. Mater.*, vol. 503, Jun. 2020, Art. no. 166636.

- [4] P. Ripka, and A. Tipek, *Modern Sensors Handbook*. Wiltshire, U.K.: Wiley, 2007, pp. 305–314.
- [5] X. Ge, Z. Q. Zhu, R. Ren, and J. T. Chen, “A novel variable reluctance resolver for HEV/EV applications,” *IEEE Trans. Ind. Appl.*, vol. 52, no. 4, pp. 2872–2880, Jul/Aug. 2016.
- [6] A. S. A. Kumar, B. George, and S. C. Mukhopadhyay, “Technologies and applications of angle sensors: A review,” *IEEE Sensors J.*, vol. 21, no. 6, pp. 7195–7206, Mar. 2021.
- [7] J. O. Manyala, T. Fritz, and M. Z. Atashbar, “Integration of triaxial Hall-effect sensor technology for gear position sensing in commercial vehicle transmissions,” *IEEE Trans. Instrum. Meas.*, vol. 61, no. 3, pp. 664–672, Mar. 2012.
- [8] J. Včelák, P. Ripka, and A. Zikmund, “Long-range magnetic tracking system,” *IEEE Sensors J.*, vol. 15, no. 1, pp. 491–496, Jan. 2015.
- [9] Y. Kim, H. Y. Choi, and Y. C. Lee, “Design and preliminary evaluation of high-temperature position sensors for aerospace applications,” *IEEE Sensors J.*, vol. 14, no. 11, pp. 4018–4025, Nov. 2014.
- [10] Y. Kim and H. Y. Choi, “A geometric design study of high-temperature position sensors,” *IEEE Sensors J.*, vol. 16, no. 19, pp. 7065–7072, Oct. 2016.
- [11] S. C. Saxena and S. B. L. Seksen, “A self-compensated smart LVDT transducer,” *IEEE Trans. Instrum. Meas.*, vol. 38, no. 3, pp. 748–753, Jun. 1989.
- [12] W. Petchmaneeelumka, W. Koodtalang, and V. Riewruja, “Simple technique for linear-range extension of linear variable differential transformer,” *IEEE Sensors J.*, vol. 19, no. 13, pp. 5045–5052, Jul. 2019.
- [13] M. Mirzaei, J. Machac, P. Ripka, A. Chirtsov, J. Vyhnanek, and V. Grim, “Design of a flat-type magnetic position sensor using a finite-difference method,” *IET Sci., Meas. Technol.*, vol. 14, no. 5, pp. 514–524, Jul. 2020.
- [14] S. K. Mishra, G. Panda, and D. P. Das, “A novel method of extending the linearity range of linear variable differential transformer using artificial neural network,” *IEEE Trans. Instrum. Meas.*, vol. 59, no. 4, pp. 947–953, Apr. 2010.
- [15] G. Chen, B. Zhang, P. Liu, and H. Ding, “An adaptive analog circuit for LVDT’s nanometer measurement without losing sensitivity and range,” *IEEE Sensors J.*, vol. 15, no. 4, pp. 2248–2254, Apr. 2015.
- [16] F. Seco, J. M. Martín, and A. R. Jiménez, “Improving the accuracy of magnetostrictive linear position sensors,” *IEEE Trans. Instrum. Meas.*, vol. 58, no. 3, pp. 722–729, Mar. 2009.
- [17] H. Sumali, E. P. Bystrom, and G. W. Krutz, “A displacement sensor for nonmetallic hydraulic cylinders,” *IEEE Sensors J.*, vol. 3, no. 6, pp. 818–826, Dec. 2003.
- [18] E. G. Bakhom and M. H. M. Cheng, “High-sensitivity inductive pressure sensor,” *IEEE Trans. Instrum. Meas.*, vol. 60, no. 8, pp. 2960–2966, Aug. 2011.
- [19] S.-H. Yang, K. Hirata, T. Ota, and Y. Kawase, “Impedance linearity of contactless magnetic-type position sensor,” *IEEE Trans. Magn.*, vol. 53, no. 6, Jun. 2017, Art. no. 8001204.
- [20] K. R. Sandra, B. George, and V. J. Kumar, “A nonintrusive magnetically coupled sensor for measuring liquid level,” *IEEE Trans. Instrum. Meas.*, vol. 69, no. 10, pp. 7716–7724, Oct. 2020.
- [21] A. Grima, M. Di Castro, A. Masi, and N. Sammut, “Design enhancements of an ironless inductive position sensor,” *IEEE Trans. Instrum. Meas.*, vol. 69, no. 4, pp. 1362–1369, Apr. 2020.
- [22] B. A. Reinholz and R. J. Seethaler, “Design and validation of a variable reluctance differential solenoid transducer,” *IEEE Sensors J.*, vol. 19, no. 23, pp. 11063–11071, Dec. 2019.
- [23] L. Sun, J. Taylor, X. Guo, M. Cheng, and A. Emadi, “A linear position measurement scheme for long-distance and high-speed applications,” *IEEE Trans. Ind. Electron.*, vol. 68, no. 5, pp. 4435–4447, May 2021.
- [24] M. Mirzaei, P. Ripka, and V. Grim, “A novel position sensor with a conical iron core,” *IEEE Trans. Instrum. Meas.*, vol. 69, no. 11, pp. 9178–9189, Nov. 2020.
- [25] *Maxwell/Ansys*. Accessed: Apr. 6, 2021. [Online]. Available: <https://www.ansys.com/products/electronics/ansys-maxwell>
- [26] E. Both, “The permeability of silicon-iron at very low flux densities,” *Trans. Amer. Inst. Elect. Eng., I, Commun. Electron.*, vol. 72, no. 5, pp. 656–664, Nov. 1953.
- [27] Z. Liu, A. R. Eastham, and G. E. Dawson, “Further studies on an improved finite element method for moving conductor eddy current problems,” *IEEE Trans. Magn.*, vol. 30, no. 5, pp. 2984–2987, Sep. 1994.
- [28] N. Allen, D. Rodger, P. C. Coles, S. Stret, and P. J. Leonard, “Towards increased speed computations in 3D moving eddy current finite element modelling,” *IEEE Trans. Magn.*, vol. 31, no. 6, pp. 3524–3526, Nov. 1995.
- [29] M. Mirzaei, P. Ripka, A. Chirtsov, and J. Vyhnanek, “Eddy current linear speed sensor,” *IEEE Trans. Magn.*, vol. 55, no. 1, Jan. 2019, Art. no. 4000304.
- [30] D. Rodger, “Modeling movement in electrical machines,” *IEEE Trans. Magn.*, vol. 57, no. 6, Jun. 2021, Art. no. 8105504.
- [31] P. Veeraiyan, U. Gandhi, and U. Mangalanathan, “Fractional order linear variable differential transformer: Design and analysis,” *AEU Int. J. Electron. Commun.*, vol. 79, pp. 141–150, Sep. 2017.
- [32] V. Gunasekaran, B. George, S. Aniruddhan, D. D. Janardhanan, and R. V. Palur, “Performance analysis of oscillator-based read-out circuit for LVDT,” *IEEE Trans. Instrum. Meas.*, vol. 68, no. 4, pp. 1080–1088, Apr. 2019.
- [33] M. Lu, Y. Xie, W. Zhu, A. J. Peyton, and W. Yin, “Determination of the magnetic permeability, electrical conductivity, and thickness of ferrite metallic plates using a multifrequency electromagnetic sensing system,” *IEEE Trans. Ind. Informat.*, vol. 15, no. 7, pp. 4111–4119, Jul. 2019.
- [34] M. Lu, R. Huang, W. Yin, Q. Zhao, and A. Peyton, “Measurement of permeability for ferrous metallic plates using a novel lift-off compensation technique on phase signature,” *IEEE Sensors J.*, vol. 19, no. 17, pp. 7440–7446, Sep. 2019.
- [35] A. Paymozd, H. Saneie, A. Daniar, and Z. Nasiri-Gheidari, “Accurate and fast subdomain model for electromagnetic design purpose of wound-field linear resolver,” *IEEE Trans. Instrum. Meas.*, vol. 70, 2021, Art. no. 9003408.
- [36] P. Naderi, A. Ramezannezhad, and L. Vandeveld, “Performance analysis of variable reluctance linear resolver by parametric magnetic equivalent circuit in healthy and faulty cases,” *IEEE Sensors J.*, early access, Jul. 5, 2021, doi: [10.1109/JSEN.2021.3094798](https://doi.org/10.1109/JSEN.2021.3094798).
- [37] S. Das and B. Chakraborty, “Design of an absolute shaft encoder using optically modulated binary code,” *IEEE Sensors J.*, vol. 18, no. 12, pp. 4902–4910, Jun. 2018.
- [38] S. Paul, J. Chang, J. E. Fletcher, and S. Mukhopadhyay, “A novel high-resolution optical encoder with axially stacked coded disk for modular joints: Physical modeling and experimental validation,” *IEEE Sensors J.*, vol. 18, no. 14, pp. 6001–6008, Jul. 2018.
- [39] L.-M. Faller and H. Zangl, “Feasibility considerations on an inkjet-printed capacitive position sensor for electrostatically actuated resonant MEMS-mirror systems,” *J. Microelectromech. Syst.*, vol. 26, no. 3, pp. 559–568, Jun. 2017.
- [40] S. Paul, J. Chang, A. Rajan, and S. Mukhopadhyay, “Design of linear magnetic position sensor used in permanent magnet linear machine with consideration of manufacturing tolerances,” *IEEE Sensors J.*, vol. 19, no. 13, pp. 5239–5248, Jul. 2019.

Mehran Mirzaei (Member, IEEE) is a Ph.D. Researcher with the Department of Measurement, Faculty of Electrical Engineering, Czech Technical University in Prague, Prague, Czech Republic. He analyzes and optimizes magnetic position sensors and eddy current speed sensors. His research topic is magnetic material modeling in magnetic sensors and transducers.

Pavel Ripka (Member, IEEE) received the Ing. degree in electrical engineering and the C.Sc. degree (equivalent to Ph.D.) in 1984 and 1989, respectively, and the Docent degree in 1996. Since 2001, he has been a Full Professor with Czech Technical University in Prague. He is the coauthor of three books and 150 journal articles. His main research interests are magnetic measurements and magnetic sensors, especially fluxgate.

Vaclav Grim (Graduate Student Member, IEEE) is currently pursuing the Ph.D. degree with the Department of Measurement, Faculty of Electrical Engineering, Czech Technical University in Prague, Prague, Czech Republic. He works on applications of magnetic sensors, characterization, and optimization. His research topic is optimization of magnetic sensors.

5.3 An Axial Airgap Eddy Current Speed Sensor

Another paper working with the motion-dependent mutual inductance between one excitation winding and two pickup winding, this time focusing on rotational speed instead of linear. The circular sector-shaped windings are placed axially at the end of the rotating steel shaft. This is an advantage over radially mounted sensor, because the sensor can be integrated into standard bearing unit, where it is protected from damage. The induced eddy currents are present only on the shaft's surface under the coils, and it is shown that by applying a thin layer of copper improves the performance by increasing the decay time of the eddy currents.

My responsibility was to design and build the test platform with DC motor, non-magnetic shaft bearings and a reference speed sensor, and the manufacturing of the sensor including winding the self-supporting winding segments with a newly developed prototyping method based on disposable, 3D printed coil formers made of water soluble material.

An Axial Airgap Eddy Current Speed Sensor

Mehran Mirzaei ¹, Member, IEEE, Pavel Ripka ², Member, IEEE,
and Vaclav Grim ³, Graduate Student Member, IEEE

Abstract—This article presents a novel configuration of the eddy current speed sensor to measure the rotating speed of iron rods and shafts up to 3000 r/min. The proposed eddy current speed sensor has an axial airgap structure with one excitation coil and two antiseriably connected pick up coils. The speed sensor is mounted in the end shaft part region. Different solid iron materials for rotating shaft are considered in the measurements and calculations to evaluate solid iron material effect on the eddy current speed sensor performance. Two-dimensional (2-D) and 3-D finite element method is utilized for the performance analysis of the speed sensor. Also, a 2-D analytical method is developed for parametric analysis. A copper rod is also used to compare the speed sensor with the rotating iron shaft and copper shaft. Finally, two thin copper discs with different diameters are mounted on the solid iron shaft and their influences on the eddy current speed sensor were evaluated and measured to increase sensitivity and decrease sensor dependency on the permeability of the solid iron shaft. The achieved nonlinearity errors are about $\pm 0.2\%$.

Index Terms—2-D and 3-D finite element method (FEM), analytical, axial airgap, eddy current, material effects, speed sensor.

I. INTRODUCTION

SPEED measurement is a key theme in the control, protection, and maintenance of rotating machinery. As industry electrification for rotating machinery is growing, fast and robust measurements of rotating speed are vital. The compactness of the sensor and system for speed measurement is also essential, especially for short axial length electrical machines [1]–[5] as the speed sensor is mounted on the nondrive end of machines. Many speed sensors are based on optical principles. Nonintrusive reflective sensor for the ultrahigh-speed switched reluctance machines is described in [6]. Optical sensors are susceptible to dust and grease so that they are not ideal for a harsh environment. The triboelectric effect was utilized in [7] to measure speed, which is sensitive to dust and dirt because of electrostatic phenomena. The sensorless method was investigated and used for speed estimation [8], however, it is less reliable in faulty conditions.

Manuscript received June 8, 2021; revised August 10, 2021; accepted September 4, 2021. Date of publication September 22, 2021; date of current version April 1, 2022. (Corresponding author: Mehran Mirzaei.)

The authors are with the Faculty of Electrical Engineering, Czech Technical University, 16627 Prague, Czech Republic (e-mail: mirza-meh@fel.cvut.cz; ripka@fel.cvut.cz; vaclav.grim@fel.cvut.cz).

Color versions of one or more figures in this article are available at <https://doi.org/10.1109/TIE.2021.3113001>.

Digital Object Identifier 10.1109/TIE.2021.3113001

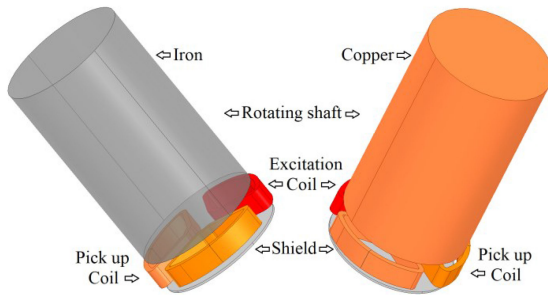
Magnetic speed sensors are robust, cheap, and reliable. An absolute magnetic rotary sensor suitable for the measurement of the angular position of motors was proposed in [9]. The sensor consists of five flat coils: the large excitation coil and four symmetrical receiving coils. The field in the receiving coils depends on the position of the conducting strip. The sensor is only 4.5 mm thick. However, this principle requires a shaft with salient conductivity.

A resolver is a long-established analog transducer for the position and speed measurement without electronics processing [10]–[12]. The conventional model of resolver has rotor winding and two stationary perpendicular windings on the stator creating a rotating field. Resolver has a similar performance as a rotating transformer. The rotor winding needs moving contacts, which makes it less reliable at higher speeds. Rotor winding can be replaced with a salient shape iron rotor as an alternative. This is a kind of variable reluctance sensor [13] and [14]. Rotating encoder or digital resolver for speed measurement is a transducer with digital outputs. The disadvantage of the resolvers is that they occupy considerable space at the nondrive part of the housing. Also, resolvers can be less practical at higher speeds as a sensitive rotating part is on the shaft. A contactless speed sensor using moving permanent magnets was presented in [15], which is based on eddy current coupling [16], has the drawback of having a mechanical moving part. Liu *et al.* [17] and Petrucha and Ripka [18] presented speed measurements utilizing stray flux in electrical machines inside the housing and end winding or on the external surface of the housing, which are not enough fault tolerant especially to overheating and mechanical fault.

Utilizing the motional component of induced eddy current in smooth conductive objects has been presented in numerous papers. As an example, the early works on speed measurement of fluids or flowmeters were presented in [19] and [20] using contact electrode or pick up coils to measure the voltage, which is proportional to the fluid speed. Later linear eddy current speed measurements for solid moving objects were developed and presented in [21]–[24] for nonmagnetic materials, which speed estimation was performed using induced voltage in the pick up coils or measured magnetic fields using, for example, Hall sensor. Eddy current speed sensors for rotating speed measurement were presented by Mirzaei *et al.* [25], [26] with pick up coils for voltage measurement and cylindrical structure, which could be less efficient to utilize in the disc shape and axial airgap machines [27]. These types of machines are designed to have very short axial length (such as Pancake shape with large diameter to axial length ratio) for industrial applications with

TABLE I
 PARAMETERS OF EDDY CURRENT SPEED SENSOR

Parameter	Definition	Value
N_c	Number of turns in the excitation coil	1000
N_p	Number of turns in the pick up coils	1000
r_o	The outer radius of the rotating shaft	15 mm
r_d	The outer radius of the copper disc	15 and 25 mm
r_m	Mean radius of coils	10 mm
g_m	The gap between coils and shaft	1.6 and 2.6 mm
g_s	The gap between coils and shield	1.6 mm
h_c	Coil height in the axial direction	5 mm
h_d	Copper disc thickness	0.6 mm
h_s	Shield thickness	0.5 mm
t_c	Coil thickness in azimuthal direction	1.2 mm
w_c	Coil sides distance	13.8 mm
L_c	Length of the straight part of the coil	10 mm


Fig. 1. Axial airgap eddy current speed sensor with shield and magnetic yoke with rotating iron shaft and with rotating copper shaft.

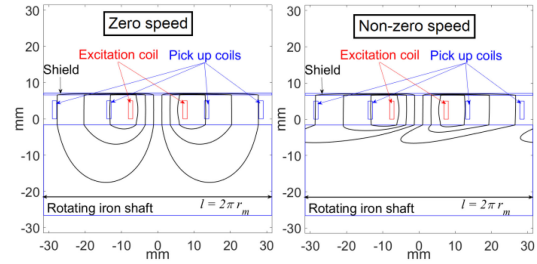
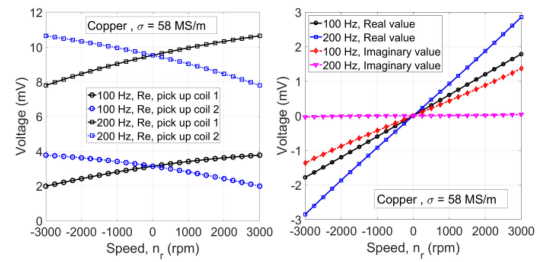
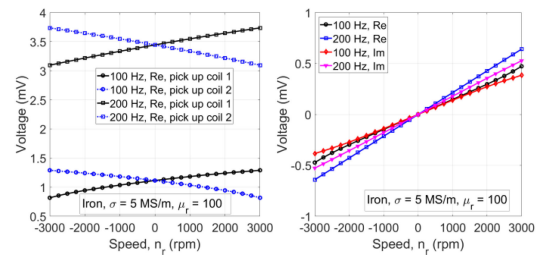
axial length constraint [28]. Therefore, axial airgap eddy current speed sensor is preferable as it has shorter axial length.

In this article, a disc shape configuration of eddy current speed sensor with axial airgap and compact axial length is measured up to 3000 r/min and analyzed using approximate Tow-dimensional (2-D) analytical method and 2-D and 3-D time stepping finite element method (FEM). The sensor comprises one excitation coil and two antiseriably connected pick up coils, which are shielded by thin disc steel lamination. The sensor can be installed in the nondrive end part of a machine shaft. The measurements and analyses are performed at various constant speeds and different excitation frequencies. The sensitivity and linearity characteristics of the sensor and the material effect of the solid iron shaft on the sensor performance are investigated.

II. MODEL

Table I and **Fig. 1** present an axial air gap sensor with a rotating conductive shaft and its dimensional parameters. The sensor has one excitation coil and two antiseriably connected pick up coils. It has a magnetic shield or yoke, which is a disc shape silicon steel lamination in this article. The outer diameter of the magnetic shield is the same outer diameter of a rotating copper or iron shaft.

The eddy current speed sensor utilizes a motional component of induced eddy current caused by a rotating conductive shaft. The motional component of induced eddy current makes asymmetrical magnetic flux distribution in double sides of the


Fig. 2. Schematic flux distribution in the linearized model of axial airgap eddy current speed sensor at zero speed (magnetic flux is symmetric) and nonzero speed (magnetic flux is asymmetric).

Fig. 3. Real (Re) component of Induced voltage of individual pick up coils (left) and antiseriably connected pick up coils (right) versus speed for rotating copper shaft-analytical method in Appendix.

Fig. 4. Real (Re) component of Induced voltage of individual pick up coils (left) and antiseriably connected pick up coils (right) versus speed for rotating iron shaft-analytical method in Appendix.

excitation coil, as shown in **Fig. 2**. The asymmetrical flux distribution induces a nonzero voltage on antiseriably connected pick up coils. **Figs. 3** and **4** present induced voltages of each pick up coil and resultant differential voltage of antiseriably connected pick up coils versus speed at 1.6 mm magnetic gap between coils and rotating shaft using the analytical method in Appendix.

RMS value of excitation current is considered 15.5 mA in the analytical calculations. Induced voltages of each pick up coil decrease or increase versus speed depending on the speed direction of the shaft, as shown in **Figs. 3** and **4**. Therefore, the differential voltage of antiseriably connected pick up coils 1 and 2 is proportional to the speed value and direction.

The real component (Re) and imaginary component (Im) of induced voltages are considered relative to excitation coil current as a reference signal. The real component of the voltage induced

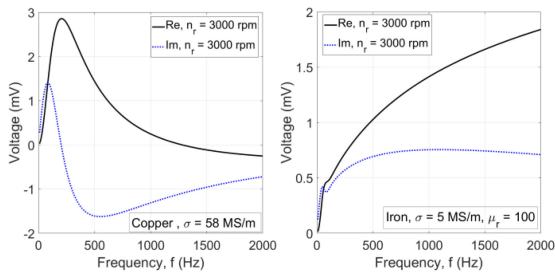


Fig. 5. Real (Re) and imaginary (Im) components of the resultant induced voltage of antiseriably connected pick up coils for the copper shaft (left) and for the iron shaft (right) versus frequency-analytical method in Appendix.

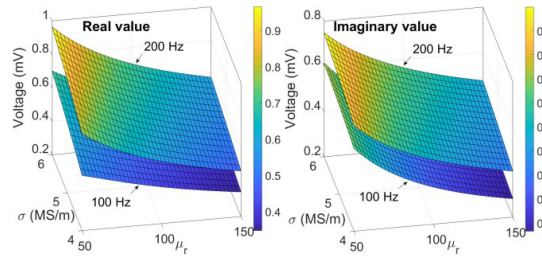


Fig. 7. Real (Re) and imaginary (Im) components of the induced voltage of antiseriably connected pick up coils for an only rotating iron shaft versus electrical conductivity and relative magnetic permeability-analytical method in Appendix.

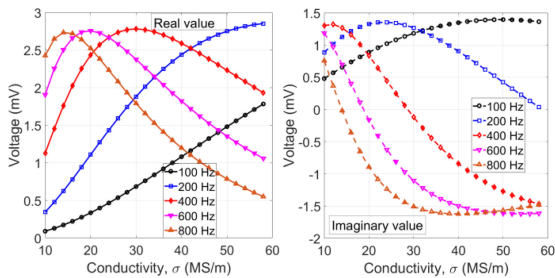


Fig. 6. Real (Re) and imaginary (Im) components of Induced voltage of antiseriably connected pick up coils versus electrical conductivity for rotating nonmagnetic shaft-analytical method in Appendix.

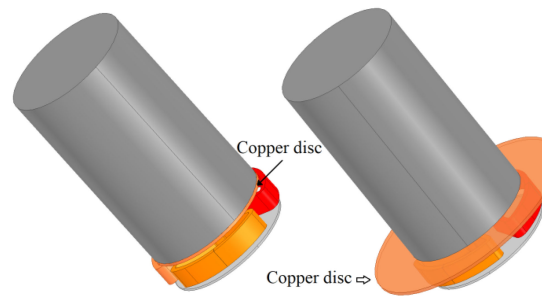


Fig. 8. Axial airgap eddy current speed sensor with shield and magnetic yoke with rotating iron shaft with 3 cm and 5 cm copper disc.

into the pick up coils voltage (1 and 2) is smaller than the imaginary component of voltage at 100 Hz and 200 Hz but it increases or decreases with higher slope versus speed (see Figs. 3 and 4).

III. PARAMETRIC ANALYSIS

Induced voltages of antiseriably connected pick up coils versus frequency show different trends for copper and iron rotating shafts, as shown in Fig. 5. For example, the real component of voltage versus frequency increases according to the induction law and then decreases for copper shaft, but it increases monotonically for iron shaft due to its lower conductivity and higher relative magnetic permeability, μ_r .

The material of the magnetic and nonmagnetic rotating shaft could be changed for various applications or its properties varies by temperature. Shaft Material effects are evaluated in Figs. 6 and 7. The conductivities corresponding to the maximum value of induced voltage for nonmagnetic shaft (copper, aluminum, or brass with $\mu_r = 1$) shifts to lower values at higher frequencies (see Fig. 6). Because the skin depth and flux penetration are higher with lower conductivity, which induced voltage becomes higher for nonmagnetic shaft.

The real and imaginary components of induced voltages shown in Fig. 7 increase with increasing conductivity and decreasing relative magnetic permeability at 100 Hz and 200 Hz for magnetic iron shaft, which shows different phenomena than nonmagnetic shaft because of relative magnetic permeability

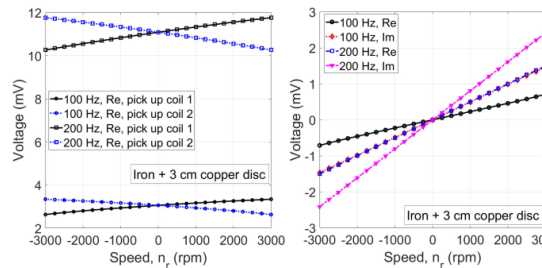


Fig. 9. Real (Re) component of Induced voltage of individual pick up coils (left) and antiseriably connected pick up coils (right) for rotating iron shaft with 3 cm diameter copper disc-analytical method in Appendix.

for magnetic iron shaft, $\mu_r > 1$. Adding copper disc on shaft end surface, as shown in Fig. 8, increases differential voltage and sensitivity of the eddy current speed sensor in comparison with an only iron rotating shaft (see Fig. 9).

Influences of copper disc thickness on the induced voltage in Fig. 10(a) with copper disc diameter, 3 cm, show that the optimum selection of copper thickness can considerably increase the induced voltage. Copper disc minimizes the effect of relative magnetic permeability variations of the iron shaft on the induced voltage of the speed sensor, as shown in Fig. 10(b), which an advantage to compensate rotating shaft materials effects on the speed sensor performance.

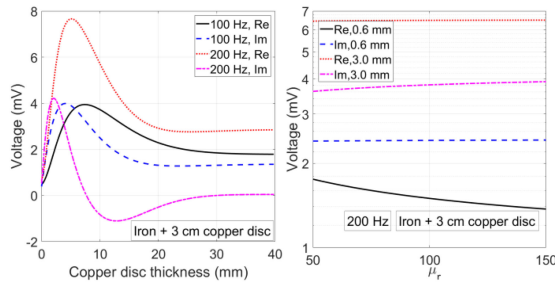


Fig. 10. Real (Re) and imaginary (Im) components of the induced voltage of antiseriably connected the pick up coils for rotating iron shaft with 3 cm diameter copper disc (a) versus copper disc thickness (left) and (b) versus relative magnetic permeability of rotating iron for different copper disc thickness, 0.6 mm and 3.0 mm (right) - analytical method in Appendix.



Fig. 11. Experimental elements with dc motor as a prime mover– with rotating iron shaft and copper disc and axial airgap eddy current speed sensor.

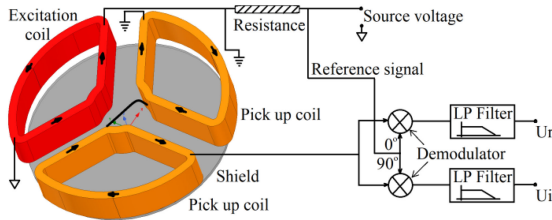


Fig. 12. Schematic block diagram of the lock-in amplifier.

IV. EXPERIMENTAL RESULTS

Fig. 11 shows the rotating shaft and eddy current sensor. The voltage of pick up coils is measured using a lock-in amplifier. Fig. 12 presents a schematic block diagram of a lock-in amplifier. Real and imaginary components of the voltage are measured relative to the excitation coil current as a reference signal. Three different solid irons are used for the rotating iron shafts with different conductivities and relative magnetic permeabilities (see Table II). The conductivities were measured and the relative magnetic permeabilities were estimated using FEM and measurements. The measurements are performed with a magnetic gap of 1.6 and 2.6 mm at 100, 200, 400, 600, and 800 Hz.

The real and imaginary components of the measured voltage for the copper shaft in Fig. 13 are satisfactory linear curves, however, only the real component of measured voltage for the

TABLE II
MATERIAL PROPERTIES OF ROTATING SHAFT

Material	Magnetic relative permeability, μ_r	Conductivity, σ_1 (MS/m)
Iron 1	86.57	5.39
Iron 2	88.83	5.24
Iron 3	78.35	4.29
Copper	1	58

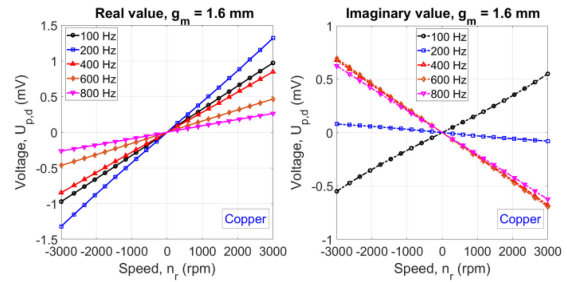


Fig. 13. Real (Re) and imaginary (Im) components of the induced voltage of antiseriably connected pick up coils for rotating copper shaft-Experimental.

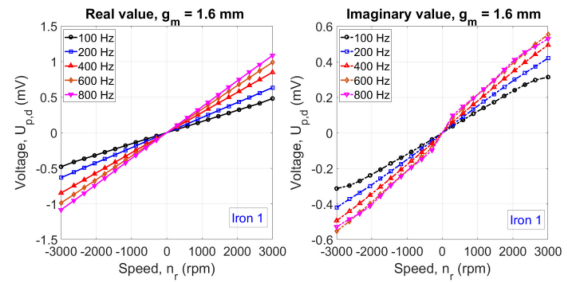


Fig. 14. Real (Re) and imaginary (Im) components of the induced voltage of antiseriably connected pick up coils for only rotating iron shaft-Experimental.

iron shaft is an acceptable linear curve, as shown in Fig. 14. The real component of induced voltage or sensitivity of speed sensor increases with increasing frequency in the iron shaft; however, it decreases for copper shaft at higher frequencies above 200 Hz.

The experimental structures of rotating iron shafts with the copper disc are shown in Fig. 11. Copper discs with a thickness of 0.6 mm and diameters of 3 and 5 cm are used for the measurements (see Fig. 8). Adding copper disc to the rotating iron shaft increases the sensitivity of eddy current speed sensor in Fig. 15. The induced voltages are considerably higher with a 5 cm diameter copper disc in comparison with a 3 cm diameter copper disc because a larger-diameter disc has higher effective conductivity and lower resistance to the induced eddy currents.

The sensor voltage is linearly proportional to the excitation coil current and, therefore, the sensor accuracy depends on the excitation current. The excitation coil is connected to a constant voltage source with 10 V amplitude and internal resistance 50 Ω . A 10 Ω resistance is used in series with the excitation

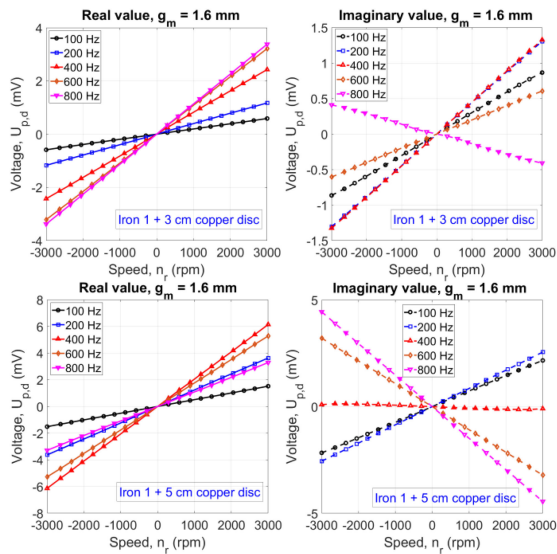


Fig. 15. Real (Re) and imaginary (Im) components of the induced voltage of antiseriably connected pick up coils for rotating iron shaft with 0.6 mm thick and 3 cm (up) and 5 cm (bottom) diameter copper disc - Experimental.

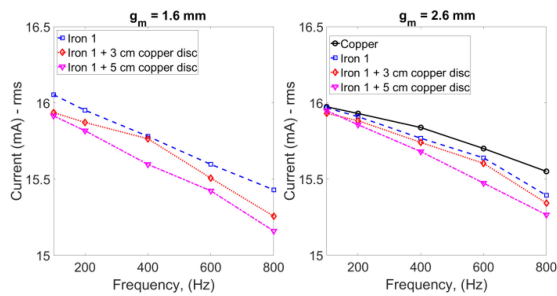


Fig. 16. Excitation coil current versus frequency for $g_m = 1.6$ mm (left) and $g_m = 2.6$ mm (right) – Experimental results.

coil to measure the excitation current, as shown in Fig. 12. The measured currents decrease with frequency, as shown in Fig. 16. It decreases by about 5% from 100 to 800 Hz because of increasing excitation coil reactance.

Tables III and IV present sensitivity coefficients, K_R and K_I (mV/r/min) of real and imaginary components of differential voltage ($U_{p,d-R}$ and $U_{p,d-I}$) of antiseriably connected pick up coils at 100, 200, 400, 600, and 800 Hz versus rotational speed, n_r in r/min

$$U_{p,d-R} = K_R \cdot n_r, \quad U_{p,d-I} = K_I \cdot n_r. \quad (1)$$

Increasing magnetic gap, g_m about 63% in percentage from 1.6 to 2.6 mm has less change in induced voltage than 63% in percentage, for example, less than 25% in the iron shaft with and without copper disc. Higher airgap has a mechanical advantage in terms of less mechanical tolerance and complexity

TABLE III
SENSITIVITY COEFFICIENT, K_R FOR REAL COMPONENT OF VOLTAGE

Frequency (Hz)	100	200	400	600	800	
Iron 1+	$g_m=1.6$ mm	20e-5	39e-5	81e-5	108e-5	113e-5
3 cm copper	$g_m=2.6$ mm	16e-5	32e-5	67e-5	93e-5	100e-5
Iron 1+	$g_m=1.6$ mm	51e-5	122e-5	205e-5	176e-5	109e-5
5 cm copper	$g_m=2.6$ mm	38e-5	94e-5	165e-5	153e-5	106e-5
Iron 3+	$g_m=1.6$ mm	19e-5	41e-5	85e-5	112e-5	116e-5
3 cm copper	$g_m=2.6$ mm	14e-5	30e-5	64e-5	88e-5	96e-5
Iron 3+	$g_m=1.6$ mm	50e-5	126e-5	211e-5	177e-5	105e-5
5 cm copper	$g_m=2.6$ mm	38e-5	97e-5	169e-5	166e-5	109e-5
Iron 1	$g_m=1.6$ mm	16e-5	21e-5	28e-5	33e-5	36e-5
	$g_m=2.6$ mm	12e-5	17e-5	22e-5	26e-5	29e-5
Iron 2	$g_m=1.6$ mm	14e-5	19e-5	26e-5	31e-5	34e-5
	$g_m=2.6$ mm	11e-5	15e-5	21e-5	24e-5	27e-5
Iron 3	$g_m=1.6$ mm	13e-5	18e-5	24e-5	29e-5	32e-5
	$g_m=2.6$ mm	10e-5	14e-5	20e-5	23e-5	25e-5
Copper	$g_m=1.6$ mm	32e-5	43e-5	28e-5	16e-5	8.9e-5
	$g_m=2.6$ mm	25e-5	34e-5	27e-5	19e-5	14e-5

TABLE IV
SENSITIVITY COEFFICIENT, K_I FOR IMAGINARY COMPONENT OF VOLTAGE

Frequency (Hz)	100	200	400	600	800	
Iron 1+3 cm copper	$g_m=1.6$ mm	29e-5	44e-5	44e-5	20e-5	-14e-5
	$g_m=2.6$ mm	25e-5	38e-5	42e-5	24e-5	0
Iron 1+	$g_m=1.6$ mm	73e-5	85e-5	-5.1e-5	-107e-5	-148e-5
5 cm copper	$g_m=2.6$ mm	59e-5	73e-5	9.7e-5	-67e-5	-105e-5
Iron 3+	$g_m=1.6$ mm	31e-5	46e-5	45e-5	16e-5	-18e-5
3 cm copper	$g_m=2.6$ mm	25e-5	38e-5	41e-5	24e-5	0
Iron 3+	$g_m=1.6$ mm	75e-5	88e-5	-10.4e-5	-111e-5	-153e-5
5 cm copper	$g_m=2.6$ mm	61e-5	75e-5	11e-5	-68e-5	-105e-5
Iron 1	$g_m=1.6$ mm	11e-5	14e-5	17e-5	19e-5	19e-5
	$g_m=2.6$ mm	9.2e-5	12e-5	14e-5	15e-5	15e-5
Iron 2	$g_m=1.6$ mm	11e-5	14e-5	17e-5	19e-5	20e-5
	$g_m=2.6$ mm	8.7e-5	11e-5	14e-5	15e-5	15e-5
Iron 3	$g_m=1.6$ mm	10e-5	13e-5	16e-5	17e-5	17e-5
	$g_m=2.6$ mm	8.5e-5	11e-5	13e-5	14e-5	14e-5
Copper	$g_m=1.6$ mm	18e-5	-2.8e-5	-22e-5	-23e-5	-21e-5
	$g_m=2.6$ mm	15e-5	1.9e-5	-12e-5	-15e-5	-14e-5

for mounting eddy current speed sensor, especially at higher speeds operation.

Differences between induced voltages and sensitivities in Tables III and IV for iron 1 with copper disc and iron 3 with the copper disc are lower compared to the corresponding values for iron shaft without copper disc as the induced voltages are less dependent on material conductivity and relative magnetic permeability of iron shaft, as shown in Fig. 10. The copper disc with 5 cm diameter suppresses the effects of iron shaft materials more than copper disc with 3 cm diameter due to the stronger induced eddy current and its higher reaction fields. Copper disc with 5 cm diameter has less edge effects in comparison with copper disc with 3 cm diameter and higher effective conductivity according to Russel–Northworthy factor, k_{R-N} (see (5) in Appendix). This factor for first harmonic ($n = \pm 1$) is calculated 0.157 for 3 cm diameter disc and it is 0.467 for 5 cm diameter disc.

The 3-D FEM analyses at 100 and 200 Hz for 1171.9 r/min and 3000 r/min are performed for comparison with measurements. The simulation results coincide well with the measured results concerning rotor material effects on the speed sensor performance (see Tables V–VIII). The numerical simulations are limited up to 200 Hz as higher number of mesh and computer

TABLE V
COMPARISON BETWEEN EXPERIMENTAL AND FEM RESULTS - 1

$g_m = 1.6$ mm $n_r = 1171.9$ rpm		$U_{p,d}$ (mV) at 100 Hz		$U_{p,d}$ (mV) at 200 Hz	
		3D FEM	Exp.	3D FEM	Exp.
Iron	Iron 1	0.4743	0.4185	0.7698	0.6961
+3 cm copper	Iron 3	0.4678	0.4234	0.7701	0.7225
+5cm copper	Iron 1	1.2124	1.049	1.94	1.757
	Iron 3	1.2076	1.062	1.9616	1.819
Iron 1		0.2413	0.2304	0.3048	0.3045
Iron 2		0.2338	0.2088	0.2970	0.2826
Iron 3		0.2280	0.1962	0.2899	0.2626
Copper		0.4562	0.4276	0.4976	0.5028

TABLE VI
COMPARISON BETWEEN EXPERIMENTAL AND FEM RESULTS - 2

$g_m = 1.6$ mm $n_r = 3000$ rpm		$U_{p,d}$ (mV) at 100 Hz		$U_{p,d}$ (mV) at 200 Hz	
		3D FEM	Exp.	3D FEM	Exp.
Iron	Iron 1	1.2326	1.046	1.9602	1.754
+3 cm copper	Iron 3	1.2253	1.074	1.9467	1.83
Iron +5cm copper	Iron 1	3.1057	2.644	4.9995	4.439
	Iron 3	3.1030	2.686	5.0928	4.594
Iron 1		0.6645	0.573	0.8099	0.7591
Iron 2		0.6461	0.5045	0.7842	0.7017
Iron 3		0.6380	0.4938	0.7694	0.6587
Copper		1.1915	1.116	1.3352	1.322

TABLE VII
COMPARISON BETWEEN EXPERIMENTAL AND FEM RESULTS - 3

$g_m = 2.6$ mm $n_r = 1171.9$ rpm		$U_{p,d}$ (mV) at 100 Hz		$U_{p,d}$ (mV) at 200 Hz	
		3D FEM	Exp.	3D FEM	Exp.
Iron	Iron 1	0.3733	0.3499	0.6079	0.5899
+3 cm copper	Iron 3	0.3692	0.338	0.6061	0.5673
Iron +5 cm copper	Iron 1	0.8913	0.8279	1.4905	1.409
	Iron 3	0.8901	0.8467	1.5077	1.444
Iron 1		0.1784	0.1815	0.2459	0.2408
Iron 2		0.1758	0.1669	0.2405	0.2242
Iron3		0.1708	0.1576	0.2330	0.2111
Copper		0.3552	0.3363	0.4162	0.4004

TABLE VIII
COMPARISON BETWEEN EXPERIMENTAL AND FEM RESULTS - 4

$g_m = 2.6$ mm $n_r = 3000$ rpm		$U_{p,d}$ (mV) at 100 Hz		$U_{p,d}$ (mV) at 200 Hz	
		3D FEM	Exp.	3D FEM	Exp.
Iron	Iron 1	0.9712	0.8833	1.5527	1.489
+3 cm copper	Iron 3	0.966	0.8533	1.5484	1.438
Iron +5 cm copper	Iron 1	2.3768	2.107	3.8656	3.561
	Iron 3	2.3793	2.138	3.9097	3.671
Iron 1		0.5033	0.458	0.6207	0.6044
Iron 2		0.4915	0.4104	0.6073	0.5622
Iron3		0.4826	0.4005	0.5940	0.5303
Copper		0.9401	0.8724	1.0910	1.04

memory are required in 3-D FEM for higher frequency simulations because of smaller skin depth. The mismatch between 3-D FEM and measurements is mainly caused by inexact material data especially relative magnetic permeability for the iron of shaft and a larger gap in measurements, which cause 3-D FEM results to become higher than measurements.

Time stepping FEM with consideration of movement is used for the simulation of axial airgap eddy current speed sensor to model shaft motion and induced eddy currents in the rotating conductive shaft [29]–[30]. Multiple connected conductive regions can be considered in the simulations using this method.

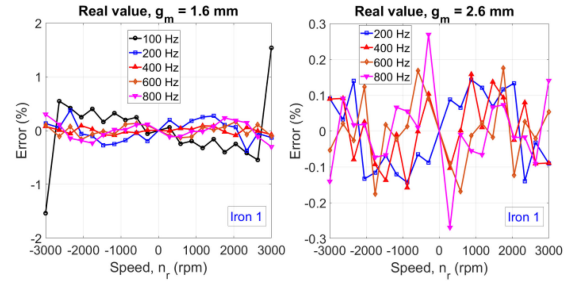


Fig. 17. Nonlinearity errors versus speed for an only rotating iron shaft at 1.6 and 2.6 mm magnetic gap between coils and rotating shaft-Experimental.

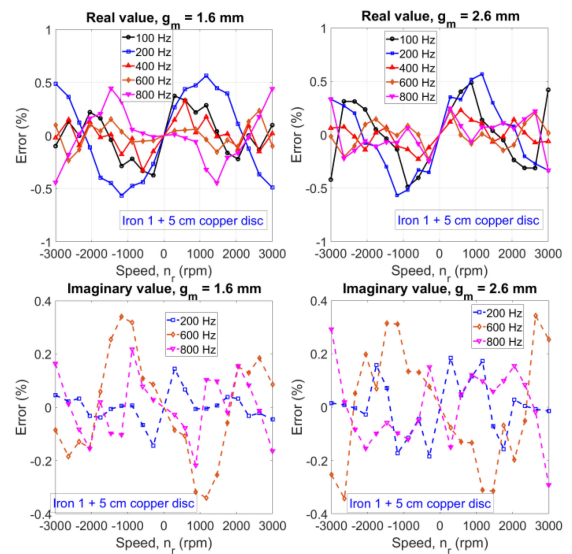


Fig. 18. Nonlinearity errors versus speed for rotating iron shaft with the copper disc at 1.6 mm and 2.6 mm magnetic gap between coils and rotating shaft and disc-Experimental.

V. NONLINEARITY ERROR ANALYSIS

The nonlinearity error is expressed in percentage of the full scale. Nonlinearity errors of the measured induced voltage of antiseriably connected pick up coils are shown in Figs. 17 and 18 for an only iron shaft and iron shaft with the copper disc at different frequencies and the magnetic gap between coils and rotating part. The nonlinearity errors are quite low as 0.2%.

The main noninherent or external reason for nonlinearity could be due to the imperfect flatness of the end shaft surface. For example, nonuniformity of the end shaft surface (see Fig. 22) was modeled using 2-D FEM with 0.5 mm saliency and the results are shown in Fig. 19 at 600 r/min and 200 Hz. The frequency spectrum of the induced voltage consists of main frequency, 200 Hz and two side frequencies, 200 ± 10 Hz, where 10 Hz is frequency corresponding to rotation speed. The parasitic signal at side frequencies cannot be efficiently suppressed by the filter in the lock in amplifier and contributes to nonlinearity errors.

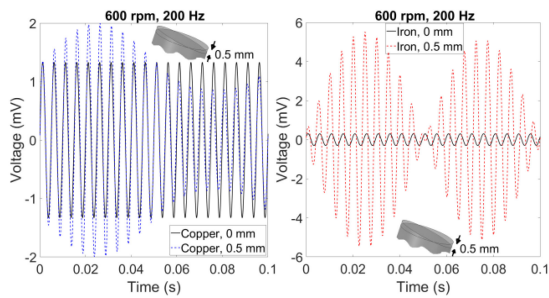


Fig. 19. Induced voltage of antiseriably connected pick up coils for rotating copper shaft and iron shaft – 2-D FEM using linearized model. Flat shaft and shaft with 0.5 mm saliency are considered.

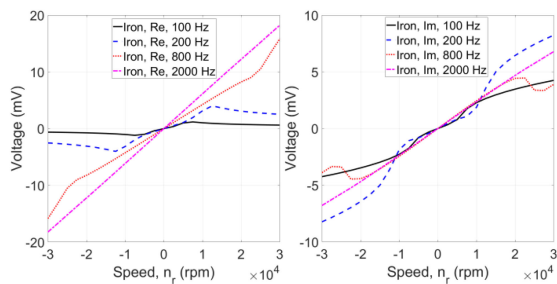


Fig. 20. Real (Re) and imaginary (Im) components of the induced voltage of antiseriably connected pick up coils for rotating iron shaft versus speed up to ± 30000 r/min - analytical method in Appendix with $I = 15.5$ mA.

VI. HIGH SPEED OPERATION

Fig. 20 shows the simulations of the axial airgap eddy current speed sensor for higher speed range, $\pm 30\,000$ r/min. The excitation frequency should be increased to obtain appropriate linearity for the sensor operation. The maximum frequency is limited by parasitic capacitance of coils and its resonance effects. For example, excitation frequency, 2000 Hz provides satisfactory results in Fig. 20 for speed range ± 30000 r/min. The sensor does not have an upper speed limitation.

VII. DISCUSSIONS

Using the fluxgate effect in an amorphous ring core to measure the field of motional component of induced eddy currents was presented in [31] for a speed sensor. This sensor has a high nonlinearity error of approximately 5% and complicated structure. A Hall sensor for speed measurement using permanent magnet excitation and utilizing motional component of induced eddy currents was presented in [32] with poor offset stability and high nonlinearity error. The proposed axial airgap eddy current speed sensor in this article has 0.2% nonlinearity error, which is better than industrial tachometer with 1.0% nonlinearity error [33]. The proposed eddy current sensor in this article has significant advantages: it has low nonlinearity error; it is cost effective and compact.

A commercial lock-in amplifier chip could be used if a real or imaginary component of induced voltage is desired for the speed meter depending on their superiority in terms of higher linearity

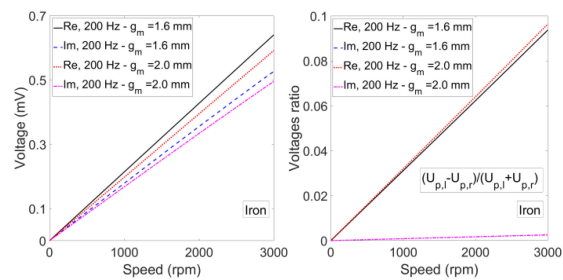


Fig. 21. Real (Re) and imaginary (Im) components of Induced voltage of antiseriably connected pick up coils versus speed for rotating iron shaft (left) and ratiometric outputs (right) - analytical method in Appendix.

and sensitivity. However, a simple rms reader can be used for speed measurement when real and imaginary components of induced voltage curve versus speed are a satisfactory straight line.

Compensating effects of shaft material, temperature, and varying mechanical and magnetic gaps between sensor and rotating shaft are important for industrial speed sensor design. Pulsed eddy current method and multifrequency method [34] are well known contactless and nondestructive approaches to compensate gap variation or liftoff, which can be utilized also for the eddy current speed sensor. Using signal with square, triangle, and sawtooth waveforms is another option. The amplitude and phase of the harmonic components in the induced voltage could be used for the compensation too. Another advantage of measuring real and imaginary components of voltage is that one can be used for speed meter and another one can be considered for compensation purpose if both components are adequate straight line versus speed. Another possible compensation method is ratiometric processing, $(U_{p,l}-U_{p,r})/(U_{p,l}+U_{p,r})$ of the pickup voltages, which is successfully utilized in LVDT sensors. For example, Fig. 21 shows the effect of increasing of gap between coils and rotating part, g about 25% (1.6 to 2 mm). Real component of induced voltage decreases 7.65%. However, corresponding ratiometric value changes by only 2.8%.

The proposed eddy current speed sensor can be utilized for speed range ± 3000 r/min in all industrial applications using standard rotating electrical and mechanical machines, for examples, squirrel cage induction machines. Therefore, this sensor is suitable for most standard applications, include fans, pumps, grinders, conveyors, mills, crushers, agitators, positioners, roller, and gate drives, and other applications.

Decreasing diameter of shaft reduces output voltage and sensitivity of the sensor as the sensitivity is dependent on the shaft diameter. Attaching larger magnetic (iron) or nonmagnetic (brass, aluminum or copper) diameter disc to the shaft, as shown in Fig. 8, or increasing excitation frequency are techniques to keep sensitivity at proper value for smaller shafts.

VIII. CONCLUSION

A novel axial airgap eddy current sensor was presented, and its performance was measured and analyzed with consideration of electrical and magnetic properties and mechanical parameters.

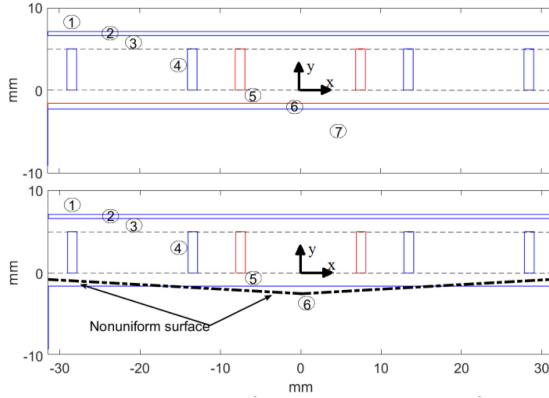


Fig. 22. Two-dimensional linearized model of axial airgap speed sensor for the 2-D analysis – Iron with copper disc (up) and only iron or copper (bottom).

The proposed eddy current speed sensor is simple, cost-effective, and compact with excellent linearity, which shows its high potentiality for industrial applications. The measured nonlinearity error is as low as $\pm 0.2\%$. Using a copper disc with an iron rotating shaft causes higher sensitivity and lower nonlinearity error in the imaginary component of the induced voltage. The effects of rotating shaft materials and the magnetic gap between coils and the rotating part on eddy current speed sensor were investigated, which are important factors on sensor accuracy and sensitivity. Using copper disc also suppresses the effect of the shaft material. A 2-D approximate analytical method was utilized for fast parametric analysis of the eddy current sensor. The 2-D and 3-D time-stepping FEM with taking into account shaft rotating speed were used for detailed and more precise analysis of the sensor performance and comparison with measurements. The real component of induced voltage in the antiseriably connected pick up coils is correlated to the eddy current losses in the moving part and the imaginary component of voltage represents the inductive coupling between the excitation coil and pick up coils.

Optimizations of axial airgap eddy current speed sensors are planned for future works in terms of increasing sensitivity and improving nonlinearity errors using optimum shape and dimensions for copper disc and choosing best nonmagnetic materials, for example, between aluminum with different conductivities, brass or stainless steel, for it. We will also concentrate on the compensation of temperature effects on material properties and airgap. Operating and evaluating axial airgap eddy current speed sensor at higher speeds are also considered for further developments.

APPENDIX

The 3-D model of the eddy current sensor is simplified to a linearized 2-D model as it is a common method to analyze axial airgap induction machines [35]–[36]. Equation (2) presents differential equations for 7 regions, as shown in Fig. 22. A_z is a magnetic vector potential.

Regions 1, 2, 3, 4, 5, 6, and 7 correspond to parts above shield, shield, air gap between shield and coils, coils, the air gap between coils and shaft, copper disc, and solid iron shaft, respectively. In the case of no copper disc, it will be only 6 regions and region 6 is an only copper or an only iron shaft

$$\begin{aligned} \frac{\partial^2 A_{z,1}}{\partial x^2} + \frac{\partial^2 A_{z,1}}{\partial y^2} &= 0 \\ \frac{\partial^2 A_{z,2}}{\partial x^2} + \frac{\partial^2 A_{z,2}}{\partial y^2} &= j\omega\sigma_s\mu_0\mu_{r,s}A_{z,2} \\ \frac{\partial^2 A_{z,3}}{\partial x^2} + \frac{\partial^2 A_{z,3}}{\partial y^2} &= 0 \\ \frac{\partial^2 A_{z,4}}{\partial x^2} + \frac{\partial^2 A_{z,4}}{\partial y^2} &= -\mu_0 J_s, \quad J_s = \frac{N_e I}{h_c t_c} \\ \frac{\partial^2 A_{z,5}}{\partial x^2} + \frac{\partial^2 A_{z,5}}{\partial y^2} &= 0 \\ \frac{\partial^2 A_{z,6}}{\partial x^2} + \frac{\partial^2 A_{z,6}}{\partial y^2} &= \sigma'_c \mu_0 \left(j\omega A_{z,6} + V \frac{\partial A_{z,6}}{\partial x} \right) \\ \frac{\partial^2 A_{z,7}}{\partial x^2} + \frac{\partial^2 A_{z,7}}{\partial y^2} &= \sigma'_i \mu_0 \mu_{r,i} \left(j\omega A_{z,7} + V \frac{\partial A_{z,7}}{\partial x} \right). \end{aligned} \quad (2)$$

The solutions of (2) are obtained using the separation of variables (Fourier method) [37]

$$\begin{aligned} A_{z,1} &= \sum_{n=\pm 1, \pm 2, \dots} (C_{1,1} e^{\gamma y} + C_{2,1} e^{-\gamma y}) e^{j(\omega t - mx)} \\ m &= \frac{2\pi n}{l}, \quad l = 2\pi r_m, \quad \gamma = |m| \\ A_{z,2} &= \sum_{n=\pm 1, \pm 2, \dots} (C_{1,2} e^{\lambda_s y} + C_{2,2} e^{-\lambda_s y}) e^{j(\omega t - mx)} \\ \lambda_s &= \sqrt{m^2 + j\omega\sigma_s\mu_0\mu_{r,s}} \\ A_{z,3} &= \sum_{n=\pm 1, \pm 2, \dots} (C_{1,3} e^{\gamma y} + C_{2,3} e^{-\gamma y}) e^{j(\omega t - mx)} \\ A_{z,4} &= \sum_{n=\pm 1, \pm 2, \dots} \left(C_{1,4} e^{\gamma y} + C_{2,4} e^{-\gamma y} + \frac{\mu_0 J_{s,n}}{m^2} \right) e^{j(\omega t - mx)} \\ J_{s,n} &= \frac{J_s}{jn\pi} (\cos(m(0.5w_c + t_c)) - \cos(m0.5w_c)) \\ A_{z,5} &= \sum_{n=\pm 1, \pm 2, \dots} (C_{1,5} e^{\gamma y} + C_{2,5} e^{-\gamma y}) e^{j(\omega t - mx)} \\ A_{z,6} &= \sum_{n=\pm 1, \pm 2, \dots} (C_{1,6} e^{\lambda_c y} + C_{2,6} e^{-\lambda_c y}) e^{j(\omega t - mx)} \\ \gamma_c &= \sqrt{m^2 + j\sigma'_c \mu_0 (\omega - mV)}, \quad V = r_m \cdot 2\pi n_r / 60 \\ A_{z,7} &= \sum_{n=\pm 1, \pm 2, \dots} (C_{1,7} e^{\lambda_i y} + C_{2,7} e^{-\lambda_i y}) e^{j(\omega t - mx)} \\ \gamma_i &= \sqrt{m^2 + j\sigma'_i \mu_0 \mu_{r,i} (\omega - mV)}, \quad V = r_m \cdot \frac{2\pi n_r}{60}. \end{aligned} \quad (3)$$

To obtain constants, C_1 's and C_2 's in (3), boundary conditions between regions in (4) are applied. H_x and B_y are x -component of magnetic field strength and y -component of magnetic flux density, respectively. All dimensional parameters in (2)–(4) are explained in Table I. n_r is the shaft rotating speed. $\mu_{r,s}$ and $\mu_{r,i}$ are relative magnetic permeability of shield and solid iron shaft. σ'_c and σ'_i are modified or effective copper disc and solid iron and copper shaft conductivities with considering the third dimension (edge effect) using, respectively, Russel–Northworthy factor, k_{R-N} [38] in (5) as follows:

$$\begin{aligned}
 A_{z,1} &= 0 \mid (y = \infty) \\
 H_{x,1} &= H_{x,2} \mid (y = h_c + g_s + h_s) \\
 B_{y,1} &= B_{y,2} \mid (y = h_c + g_s + h_s) \\
 H_{x,2} &= H_{x,3} \mid (y = h_c + g_s) \\
 B_{y,2} &= B_{y,3} \mid (y = h_c + g_s) \\
 H_{x,3} &= H_{x,4} \mid (y = h_c) \\
 B_{y,3} &= B_{y,4} \mid (y = h_c) \\
 H_{x,4} &= H_{x,5} \mid (y = 0) \\
 B_{y,4} &= B_{y,5} \mid (y = 0) \\
 H_{x,5} &= H_{x,6} \mid (y = -g_m) \\
 B_{y,5} &= B_{y,6} \mid (y = -g_m) \\
 H_{x,6} &= H_{x,7} \mid (y = -g_m - h_d) \\
 B_{y,6} &= B_{y,7} \mid (y = -g_m - h_d) \\
 A_{z,7} &= 0 \mid (y = -\infty) \\
 \sigma'_i &= k_{R-N} \sigma_i, \quad \sigma'_c = k_{R-N} \sigma_c \\
 k_{R-N} &= 1 - \frac{\tanh\left(\frac{\pi L_r}{\tau}\right)}{\left(\frac{\pi L_r}{\tau}\right) \left(1 + \tanh\left(\frac{\pi L_r}{\tau}\right) \tanh\left(\frac{\pi w_o}{\tau}\right)\right)}, \tau \\
 &= \frac{l}{3|n|}
 \end{aligned} \quad (4)$$

where, w_o (copper disc overhang) in (5) is $r_d - r_o$ (see Table I) to calculate k_{R-N} for copper disc according to Table I. It is zero for only iron or copper shaft or when copper disc has the same diameter as the rotating shaft.

Fig. 23 shows the 2-D view of coils and magnetic flux distribution with an only solid iron shaft. Equation (6) presents differential induced voltage, $U_{p,d}$ in antiseriably connected pick up coils [37]

$$\begin{aligned}
 U_{p,r} &= -2\omega N_p L_r \sum_{n=\pm 1, \pm 2, \dots} C_{U,1} \cdot C_{U,2} e^{-j\frac{2n\pi}{3}} e^{j\omega t} \\
 C_{U,1} &= \frac{\cos(m \cdot (0.5w_c + t_c)) - \cos(m \cdot 0.5w_c)}{m h_c t_c} \\
 C_{U,2} &= \left(C_{1,4} \frac{(e^{\gamma h_c} - 1)}{\gamma} - C_{2,4} \frac{(e^{-\gamma h_c} - 1)}{\gamma} + \frac{\mu_0 J_{s,n}}{m^2} h_c \right) \\
 U_{p,l} &= -2\omega N_p L_r \sum_{n=\pm 1, \pm 2, \dots} C_{U,1} \cdot C_{U,2} e^{j\frac{2n\pi}{3}} e^{j\omega t}
 \end{aligned}$$

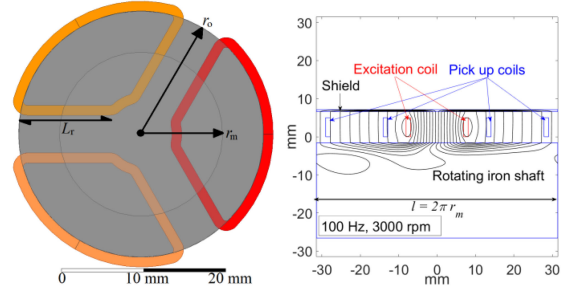


Fig. 23. Two-dimensional in-plane view of coils and rotating shaft and magnetic flux distribution with rotating iron shaft.

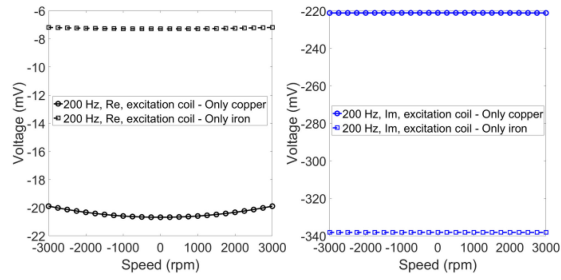


Fig. 24. Real (Re) and imaginary (Im) components of emf of the excitation coil.

$$\begin{aligned}
 U_{p,d} &= U_{p,l} - U_{p,r} \\
 &= -j4\omega N_p L_r \sum_{n=\pm 1, \pm 2, \dots} C_{U,1} \cdot C_{U,2} \sin\left(\frac{2n\pi}{3}\right) e^{j\omega t}.
 \end{aligned} \quad (6)$$

The emf of the excitation coil in (7) could be calculated as (6) and the results are shown in Fig. 24 for the real and imaginary components. The speed has small effect on the excitation coil emf, especially for the imaginary component

$$U_e = -2\omega N_e L_r \sum_{n=\pm 1, \pm 3, \dots} C_{U,1} \cdot C_{U,2} e^{j\omega t}. \quad (7)$$

REFERENCES

- [1] I. Boldea, A. Rahman, and S. A. Nasar, "Finite-width, finite-thickness, and saturation effects in solid-rotor induction machines," *IEEE Trans. Power Appl. Syst.*, vol. 94, no. 5, pp. 1500–1507, Sep/Oct. 1975.
- [2] P. D. Evans and J. F. Eastham, "Segmented-rotor disc motor," *IEE J. Electric Power Appl.*, vol. 1, no. 1, pp. 7–16, Feb. 1978.
- [3] P. D. Evans and J. F. Eastham, "Disc-geometry homopolar synchronous machine," *IEE Proc. B - Electric Power Appl.*, vol. 127, no. 5, pp. 299–307, Sep. 1980.
- [4] Z. Zhang, C. Wang, and W. Geng, "Design and optimization of halfbach-array PM rotor for high-speed axial-flux permanent magnet machine with ironless stator," *IEEE Trans. Ind. Electron.*, vol. 67, no. 9, pp. 7269–7279, Sep. 2020.
- [5] M. Noh and D. L. Trumper, "Homopolar bearingless slice motor with flux-biasing Halbach arrays," *IEEE Trans. Ind. Electron.*, vol. 67, no. 9, pp. 7757–7766, Sep. 2020.
- [6] C. Gong, S. Li, T. Habetler, J. A. Restrepo, and B. Soderholm, "Direct position control for ultrahigh-speed switched-reluctance machines based

- on low-cost nonintrusive reflective sensors," *IEEE Trans. Ind. Appl.*, vol. 55, no. 1, pp. 480–489, Jan./Feb. 2019.
- [7] Y. Wang, C. Wu, and S. Yang, "A self-powered rotating speed sensor for downhole motor based on triboelectric nanogenerator," *IEEE Sens. J.*, vol. 21, no. 4, pp. 4310–4316, Feb. 2021.
- [8] J. Guzinski and H. Abu-Rub, "Speed sensorless induction motor drive with predictive current controller," *IEEE Trans. Ind. Electron.*, vol. 60, no. 2, pp. 699–709, Feb. 2013.
- [9] Z. Zhang, F. Ni, Y. Dong, C. Guo, M. Jin, and H. Liu, "A novel absolute magnetic rotary sensor," *IEEE Trans. Ind. Electron.*, vol. 62, no. 7, pp. 4408–4419, Jul. 2015.
- [10] L. Sun, J. Taylor, A. D. Callegaro, and A. Emadi, "Stator-PM-based variable reluctance resolver with advantage of motional back-EMF," *IEEE Trans. Ind. Electron.*, vol. 67, no. 11, pp. 9790–9801, Nov. 2020.
- [11] S. Chen, Y. Zhao, H. Qiu, and X. Ren, "High-precision rotor position correction strategy for high-speed permanent magnet synchronous motor based on resolver," *IEEE Trans. Power Electron.*, vol. 35, no. 9, pp. 9716–9726, Sep. 2020.
- [12] L. Sun, Z. Luo, K. Wang, R. Cao, and S. Ding, "A stator-PM resolver with field modulation principle," *IEEE Trans. Energ. Conv.*, vol. 36, no. 1, pp. 159–172, Mar. 2021.
- [13] T. Addabbo *et al.*, "Instantaneous rotation speed measurement system based on variable reluctance sensors for torsional vibration monitoring," *IEEE Trans. Instrum. Meas.*, vol. 68, no. 7, pp. 2363–2373, Jul. 2019.
- [14] H. Saneie, Z. Nasiri-Gheidari, and F. Tootoonchian, "Design-oriented modelling of axial-flux variable-reluctance resolver based on magnetic equivalent circuits and Schwarz–Christoffel mapping," *IEEE Trans. Ind. Electron.*, vol. 65, no. 5, pp. 4322–4330, May 2018.
- [15] C. Gong, A. Tuysuz, M. Flankl, T. Stolz, J. Kolar, and T. Habetler, "Experimental analysis and optimization of a contactless eddy-current-based speed sensor for smooth conductive surfaces," *IEEE Trans. Ind. Electron.*, vol. 67, no. 10, pp. 8817–8828, Oct. 2020.
- [16] J. Wang and J. Zhu, "A simple method for performance prediction of permanent magnet eddy current couplings using a new magnetic equivalent circuit model," *IEEE Trans. Ind. Electron.*, vol. 65, no. 3, pp. 2487–2495, Mar. 2018.
- [17] X. Liu, C. Liu, and P. W. T. Pong, "Velocity measurement technique for permanent magnet synchronous motors through external stray magnetic field sensing," *IEEE Sensors J.*, vol. 18, no. 10, pp. 4013–4021, May 2018.
- [18] V. Petrucha and P. Ripka, "Rotational speed measurement and angular position reference for a cryogenic propellant electric pump," *J. Electron. Eng.*, vol. 66, no. 7/s, pp. 199–202, 2015.
- [19] J. A. Shercliff, *The Theory of Electromagnetic Flow Measurement*. Cambridge, U.K.: Cambridge Univ. Press, 1962.
- [20] C. C. Feng, W. E. Deeds, and C. V. Dodd, "Analysis of eddy-current flowmeters," *J. Appl. Phys.*, vol. 46, no. 7, pp. 2935–2940, 1975.
- [21] N. Takehira, A. Tanaka, and K. Toda, "Analysis of a speed-meter utilizing eddy current effect," *Trans. Inst. Electron. Eng. Jpn. A*, vol. 97, no. 9, pp. 457–464, Sep. 1977.
- [22] N. Takehira and A. Tanaka, "Analysis of a transmitted type speed-meter utilizing eddy current effect," *Trans. Inst. Electron. Eng. Jpn. A*, vol. 100, no. 9, pp. 483–490, Sep. 1980.
- [23] A. Tanaka and N. Takehira, "Eddy-current speed meter using galvanomagnetic devices," *Trans. Inst. Electron. Eng. Jpn. A*, vol. 106, no. 6, pp. 267–274, Jun. 1986.
- [24] K. Ishida, T. Itaya T, A. Tanaka A, and N. Takehira, "Exact analysis of a linear velocity sensor," *IEEE Trans. Inst. Meas.*, vol. 70, Oct. 2021, Art. no. 6002106.
- [25] M. Mirzaei, P. Ripka, J. Vyhnanek, A. Chirtsov, and V. Grim, "Rotational eddy current speed sensor," *IEEE Trans. Mag.*, vol. 55, no. 9, Sep. 2019, Art. no. 4003710.
- [26] M. Mirzaei, P. Ripka, V. Grim, and A. Chirtsov, "Design and optimization of an eddy current speed sensor for rotating rods," *IEEE Sens. J.*, vol. 20, no. 20, pp. 12241–12251, Jun. 2020.
- [27] Axial airgap motors, Accessed: Jun. 2021. [Online]. Available: http://www.atb_motors.com/uploads/03_PRODUKTE_Axialsplattmotoren_182_DE.pdf
- [28] J. Mei, Y. Zuo, C. H. T. Lee, and J. L. Kirtley, "Modeling and optimizing method for axial flux induction motor of electric vehicles," *IEEE Trans. Veh. Tech.*, vol. 69, no. 11, pp. 12822–12831, Nov. 2020.
- [29] P. Zhou, Z. Badics, D. Lin, and Z. J. Cendes, "Nonlinear t- ω formulation including motion for multiply connected 3-D problems," *IEEE Trans. Mag.*, vol. 44, no. 6, pp. 718–721, Jun. 2008.
- [30] Ansys/maxwell (Ansoft). Accessed: Jun. 2021. [Online]. Available: <https://www.ansys.com/products/electronics/ansys-maxwell>
- [31] E. Cardelli, A. Faba, and F. Tissi, "Contact-less speed probe based on eddy currents," *IEEE Trans. Magn.*, vol. 49, no. 7, pp. 3897–3900, Jul. 2013.
- [32] T. Sonoda, R. Ueda, K. Fujitani, T. Irisa, and S. Tatata, "DC magnetic field type eddy current speed sensor detecting cross magnetization field with amorphous core," *IEEE Trans. Magn.*, vol. MAG-21, no. 5, pp. 1732–1734, Sep. 1985.
- [33] Handheld Tachometer. Accessed: Jun. 2021. [Online]. Available: https://www.onosokki.co.jp/English/hp_e/whats_new/Catalog/PDF/ht5500e.pdf
- [34] M. Lu, W. Zhu, L. Yin, A. J. Peyton, W. Yin, and Z. Qu, "Reducing the lift-off effect on permeability measurement for magnetic plates from multifrequency induction data," *IEEE Trans. Instr. Meas.*, vol. 67, no. 1, pp. 167–174, Jan. 2018.
- [35] E. Mendrela, J. Fleszar, and E. Gierczak, *Modeling of Induction Motors With One and Two Degrees of Mechanical Freedom*. New York, NY, USA: Springer, 2003.
- [36] C. Hong, W. Huang, and Z. Hu, "Performance calculation of a dual stator solid rotor axial flux induction motor using the multi-slice and multi-layer method," *IEEE Trans. Mag.*, vol. 55, no. 2, Feb. 2019, Art. no. 8100709.
- [37] M. Mirzaei, P. Ripka, A. Chirtsov, J. Vyhnanek, and V. Grim, "Design and modeling of a linear speed sensor with a flat type structure and air coils," *J. Magnetism Magn. Mater.*, vol. 495, 2020, Art. no. 165834.
- [38] J. F. Gieras and J. Saari, "Performance calculation for a high-speed solid-rotor induction motor," *IEEE Trans. Ind. Electron.*, vol. 59, no. 6, pp. 2689–2700, Jun. 2012.



Mehran Mirzaei (Member, IEEE) is currently working toward the Ph.D. degree with the Department of Measurement, Faculty of Electrical Engineering, Czech Technical University, Prague, Czech Republic.

He analyzes and optimizes magnetic position sensors and eddy current speed sensors. His research interest includes magnetic material modeling in magnetic sensors and transducers.



Pavel Ripka (Member, IEEE) received the Ing. degree in electrical engineering in 1984, the C.Sc. degree (equivalent to Ph.D.) in 1989, and the Docent degree in electrical engineering in 1996 from Czech Technical University, Prague, Czech Republic.

Since 2001, he has been a Full Professor with Czech Technical University. He has coauthored three books and 150 journal articles. His main research interests include magnetic measurements and magnetic sensors, especially fluxgate.



Vaclav Grim (Graduate Student Member, IEEE) is currently working toward the Ph.D. degree in electrical engineering with the Department of Measurement, Faculty of Electrical Engineering, Czech Technical University, Prague, Czech Republic.

He works on applications of magnetic sensors, characterization, and optimization. His research focuses on optimization of magnetic sensors.

6 Current Sensors

This chapter summarizes all works regarding electric current sensors, specifically contactless sensors based on indirect measurement through magnetic field generated around conductors. This include yokeless circular sensors, yokeless busbar sensors, fluxgate current sensors and Rogowski coils.

Works concerning circular yokeless sensor arrays began with my bachelor thesis, which was dealing with applications of integrated AMRs. This topic was developed further with more theoretical analysis and have led to two conference posters (EMSA 2018 without proceedings and SAS 2019 with proceedings [P1]).

Papers on busbar current sensors were a continuation of the department's earlier attempts (by Mr. Přebil) on application of Texas Instrument's new chip-scale fluxgate sensors [J8]. I worked on FEM simulations and measurements with the primary objective of finding the best busbar geometry and sensor placement with respect to the frequency response [J9].

Experiments with Rogowski coils were mostly dealing with preparation of unconventional core materials and analyzing the tradeoffs between sensitivity and frequency response for different geometries and winding styles. Properties of coils based on commercial powder cores were the central point of a virtual conference poster at Intermag 2021 [P2]. The research then continued with in-house manufactured composites and resulted in a paper published in *Magnetics Letters* [J10].

6.1 Rogowski Coil with Ferromagnetic Powder Core

This paper summarizes a long series of experiments regarding powder cores. Apart from the nanocrystalline flakes mentioned in the paper, other materials were tested, including ferrite nanoparticulate with mean size of 30 nm, and micrometer-scale ferrite powder. The main issue of powder cores is their limited permeability, which for practical purposes can be regarded as inversely proportional to the amount of binder in the composite ($\lim_{n \rightarrow 1} \mu_r = \frac{3}{1-n}$ in theory, n being the volume concentration of the powder in the finished material).

Without specialized equipment the maximum achievable permeability was around 20 regardless of the material used. This is enough for application in Rogowski coils, where the main feature is the linearity allowing operation under very high field values. With low-permeability ferromagnetic core, the saturation current of such sensor is in the kiloampere region, while the sensitivity and noise performance is greatly improved in comparison to regular air-cored coils.

Magnetic Instruments

Rogowski Coil With Ferromagnetic Powder Core

Václav Grim^{1,2*} and Pavel Ripka^{1**}¹Faculty of Electrical Engineering, Czech Technical University, 160 00 Praha, Czechia²STMicroelectronics Design, Application S.R.O., 160 00 Praha, Czechia

* Graduate Student Member, IEEE

** Member, IEEE

Received 23 Nov 2021, revised 29 Dec 2021, accepted 7 Jan 2022, published 14 Jan 2022, current version 17 Feb 2022.

Abstract—We have used nanocrystalline powder to build a core for Rogowski coils suitable for application in energy meters. The sensor linearity error is 0.32% of full scale (FS) of its 20 A range, which is acceptable for this application. The main advantages of the new core are 15-fold increase in sensitivity, which results in lower noise, and high rejection of direct current. It operates at up to 1000 A dc with 20% change in sensitivity. Resulting accuracy of power measurement using a single-chip digital power meter is 0.22% FS.

Index Terms—Magnetic instruments, current measurement, energy distribution, Rogowski coils, soft magnetic materials.

I. INTRODUCTION

Rogowski coils (RCs) measure magnetomotive force, which depends on the integral of the induced electrical voltage. If the coil ends are put together, the magnetic voltage is equal to the current flowing through the coil opening [Tumanski 2011]. The main application of RC is therefore measurement of ac currents [Samimi 2015]. In order to obtain the waveform of the measured current, the voltage should be integrated by an analog or digital integrator.

Classical RCs are made of nonmagnetic materials, and they theoretically have zero nonlinearity. Therefore, they are an ideal sensor for the measurement of transient currents, e.g., during welding processes, during testing of power components, such as circuit breakers, fault current detectors [Kojovic 2013], and in particle accelerators [Cataliotti 2015, Eydan 2020]. Practical linearity is typically limited to 0.1% over three decades of current amplitude [Ramboz 2002] by the following factors:

- 1) ferromagnetic impurities in the used materials;
- 2) ferromagnetic objects in the sensor vicinity;
- 3) external stray fields such as leakage from nearby transformers.

The system linearity is also affected by the following amplifier, analog integrator (if present), and analog-to-digital converter (ADC) [Ramboz 1996].

High linearity makes RCs resistant to the dc current component or external magnetic fields, which can saturate the current transformer [Mlejnek 2009]. Therefore, an attractive application of RCs is in the electric power and energy meters, making them resistant to tampering [Zhang 2014]. Single-chip energy meters containing a digital integrator for RCs are available from several manufacturers. RCs for power line frequency may achieve 0.05% accuracy, and their temperature coefficient of sensitivity can be compensated to 2 ppm/K [Suomalainen 2009, Luo 2013].

On the other hand, low-cost RCs are made on flexible openable plastic core, which allows them to be closed around the uninterrupted

conductor [Abdi-Jalebi 2007]. Flexible RC with ferromagnetic core was described by Wei [2020]. The relative permeability of its composite core is 18. However, no functional parameters of this sensor have been reported. RCs can also be made in printed circuit board technology [Kuwabara 2018].

The typical example of the RC used for electric power meters is PA3202NL manufactured by Pulse Electronics [Roemer 2012]. The sensor with 7.5 mm inner diameter has an accuracy class of 0.2 and sensitivity of 8.33 $\mu\text{V}/\text{A}/\text{Hz}$. The winding inductance is 1.75 mH, and its resistance is 57 Ω . The current noise heavily depends on the used electronics. The discrimination of external currents is not specified by the manufacturer. We measured these parameters and describe them in Section III in order to compare our new sensor to this off-the-shelf product.

The influence of the position of the primary conductor was analyzed by Ferkovic [2009]. For perfectly homogeneous RC, this dependence is zero; however, for commercial coils, it may cause 1% error. For single-layer rigid coils with precisely machined core, this dependence is mainly caused by discontinuity between the first and last turns and may be compensated to below 0.1%.

We, therefore, concentrated on the influence of external electric currents, which is a more serious problem for practical applications. In Grim [2021], we made a theoretical analysis of this effect for the case of one missing turn, which is the worst case that may occur between the first and last turn. This maximum error is 0.6% for the distance of 75 mm, and by using a ferromagnetic core it can be reduced to 0.18%. The real measured error was 0.08% (i.e., the actual gap was smaller than one turn). The alternative way how to increase resistance against external fields is magnetic shielding [Draxler 2017]. Electrical shielding and winding pitch compensating turn are essential for every RC [Ripka 2021].

The resolution of RC for small currents is limited by its low sensitivity resulting in high noise. In this case, the total noise strongly depends on the input voltage and current noise of the attached amplifier or integrator. Noise can be reduced by increasing of the coil sensitivity by increasing of the number of turns, but this has side effects: multilayer

Corresponding author: Václav Grim (e-mail: vaclav.grim@fel.cvut.cz).
Digital Object Identifier 10.1109/LMAG.2022.3143470

1949-307X © 2022 IEEE. Personal use is permitted, but republication/redistribution requires IEEE permission.
See <https://www.ieee.org/publications/rights/index.html> for more information.

coils are less homogeneous, which increases their sensitivity to external fields and currents, and they have larger parasitic self-capacitance, which is detrimental to their frequency response.

For this reason, we use a weakly ferromagnetic core, which can increase sensitivity while keeping its linearity error low. This idea was already used in self-integrating RCs for high-frequency currents or short pulses, which use self-capacitance of the coil for integration [Ray 2000, Zhu 2006].

In this letter, we concentrate on applications at power line frequency, which is too low for self-integrating RCs. We also believe that self-capacitance of an RC is not stable enough to be relied upon in high-precision measurements. In our previous paper [Grim 2021], we have elaborated upon RC with a core made of powder cores of Sendust type. The 75 mm diameter sensor had $\pm 0.2\%$ linearity in the 500 A range and amplitude error below 0.5% up to 1 kHz frequency. In this letter, we use nanocrystalline powder core of decreased diameter, aiming the application as current sensor for energy meters. Compared to Grim [2021], we analyze more parameters relevant to this application, such as sensor noise, phase error, and total error for the digital energy meter with such RC as a current sensor.

II. SENSOR DESIGN

We used nanocrystalline alloy flakes that were produced from Fe₈₁Si_{9.7}B_{2.5}Nb_{5.5}Cu_{1.3} nanocrystalline tape with a mean particle size of 200 μm [Mazaleyrat 2002, Grybos 2018]. The annealed tape was processed in a crushing machine and vibratory disk mill [Grybos 2018]. The relative permeability measured on the uncured powder sample was 8.4. The powder was mixed with epoxy resin at 90:10 weight ratio and molded into a soluble (BVOH) 3-D-printed toroidal shell. We have experimented with curing the core in a radial magnetic field of 7 kA/m, which was created by 1 kA axial dc current; however, we did not observe any significant anisotropy similar to reported by Zheng [2015]. The core and winding parameters are as follows:

Inner diameter R_1 (mm)	40
Outer diameter R_2 (mm)	50
Height (mm)	5
Powder mass (g)	14
Mean grain size (μm)	200
Relative permeability	15
Number of turns	524
Wire diameter (mm)	0.2 (nominal)
Inductance at 1 kHz (μH)	1034
Resistance at 1 kHz (Ω)	6.023
Sensitivity ($\mu\text{V}/\text{A}/\text{Hz}$)	12.52

The results were compared with a reference specimen wound with 622 turns (0.17 mm nominal diameter) and containing no magnetic material. The difference in number of turns is caused by using wire from different manufacturer for each winding. The inductance and resistance of the nonmagnetic coil are 93.7 μH and 9.620 Ω , respectively.

III. TESTING RESULTS

A. Linearity

Linearity across the rated operational range was measured with a sine wave current source and lock-in amplifier. In the 20 A range, the

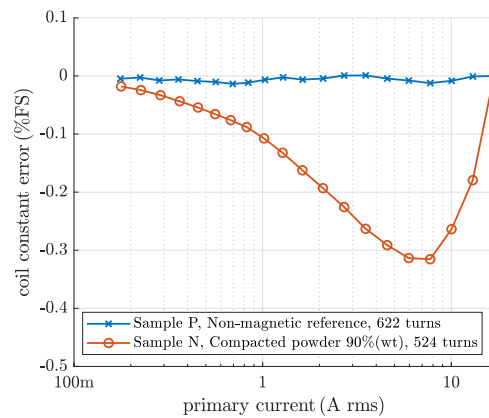


Fig. 1. Measured linearity error of the developed sensor with a ferromagnetic core compared to the reference sensor based on an air core.

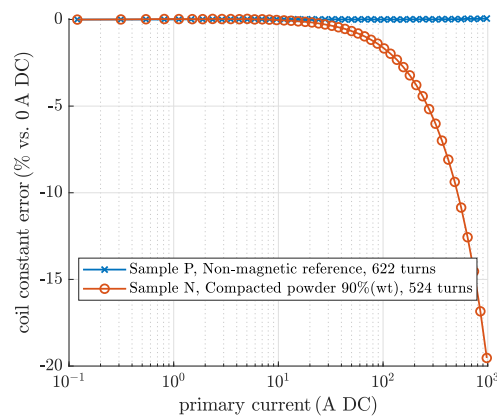


Fig. 2. Measured differential linearity error of the developed sensor compared to the air core reference sensor.

linearity error is 0.32% of full scale (FS) (see Fig. 1). The sensor's resistance to overload was tested by the incremental sensitivity method; a large direct current together with a smaller alternating current was passed through the sensor. At 1000 A, the error in sensitivity is below 20% (see Fig. 2).

B. Frequency Dependence

The frequency response was measured with a lock-in amplifier (HF2LI) against an LEM Ultrastab reference current sensor. Results are summarized in Fig. 3. The samples were measured without their electrostatic shielding. Adding a shield results in peaking, which can be adjusted by changing the winding-to-shield distance. From this perspective, the ferromagnetic sample is more favorable, because it allows for correction by the shield capacitance without the need for damping resistors.

C. Cross-Sensitivity to External Currents

External current rejection was tested with current $I_{\text{ext}} = 20$ A at 1 kHz. The output voltage was measured with a lock-in amplifier (HF2LI). External current was placed at a distance corresponding to

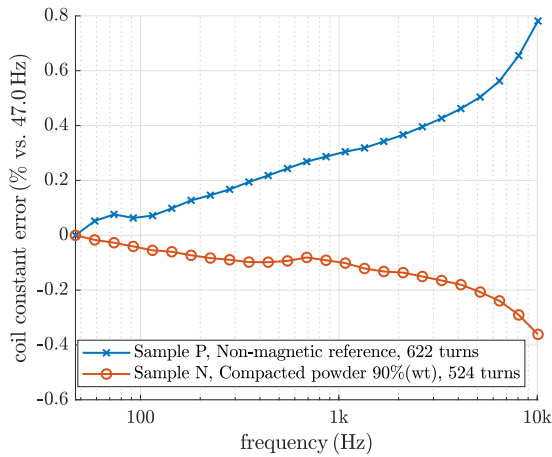


Fig. 3. Measured frequency response of the developed sensor compared to the air core reference.

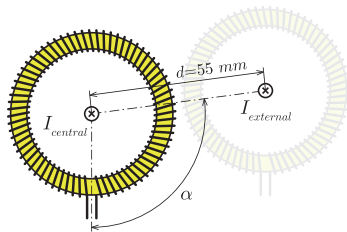


Fig. 4. Two sensors in minimum distance. This geometry was used for the testing of external current rejection.

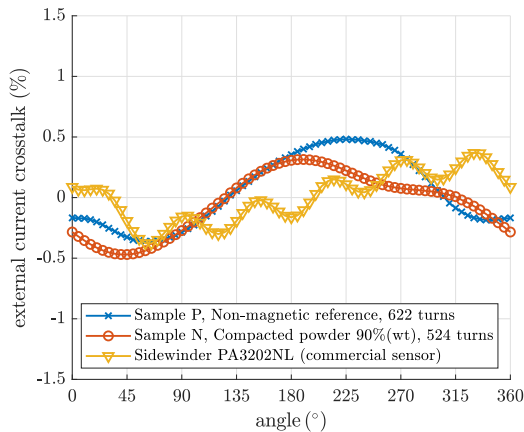


Fig. 5. Measured external current suppression. Coil terminals are coincident with 0° position. The performance of samples N and P is very similar.

sensors placed side by side (see Fig. 4, 55 mm for samples N and P, 40 mm for PA3202NL), at different angles α .

The resulting cross-sensitivity (see Fig. 5) of the ferromagnetic core is comparable to a nonmagnetic control sample. The rejection

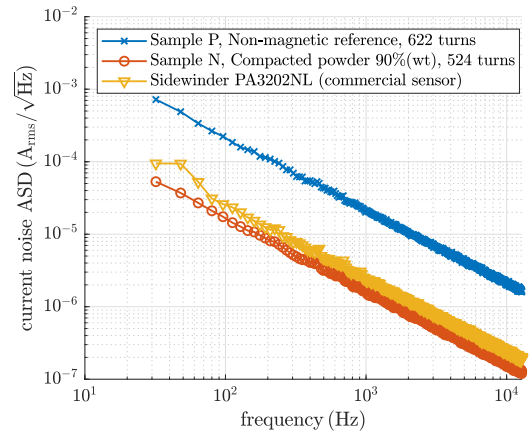


Fig. 6. Measured equivalent current spectral density of the new sensor is one order of magnitude lower than that of the reference air-core sensor.

of external current is given mostly by the uniformity of the core cross-section and winding pitch. In the case of multiphase power meters, the relative position of each phase is constant, and this cross-sensitivity can be corrected during data postprocessing. The ripples visible in the measurement of the commercial sensor PA3202NL are caused by the internal construction of the coil, which consists of six solenoidal segments in a circular arrangement.

D. Noise

Sensor noise was measured with an Agilent 35670 A fast Fourier transform (FFT) spectrum analyzer from 0 Hz to 12.8 kHz at zero current inside a three-layer magnetic shielding. The resulting noise voltage spectral density was divided by the sensor's approximate transfer function

$$H(s) = s \cdot \frac{V_{\text{out}, I=I_{\text{rated}}}}{2\pi f I_{\text{rated}}}$$

to obtain the equivalent current noise spectral density (see Fig. 6).

The noise of the sensor itself is too low to be measured; the result consists solely of the noise floor of the measuring instrument. The thermal noise of the winding is around 30 dB below the instrument noise. Therefore, in practical applications, the parameters of the ADC and integrator determine the overall noise performance of the system.

E. Accuracy of the Power Measurement

In this section, we demonstrate the performance of the new sensors in conjunction with a single-chip power meter containing a digital integrator STPM34, manufactured by ST Microelectronics.

The block diagram of the measurement setup is shown in Fig. 7. A 2.35Ω power resistor was used as a load. A Tektronix PA1000 power analyzer with internal shunt was used as a reference instrument. Power was sourced from a Techtron 7548 power amplifier at 50 Hz.

A full-scale current of 20 A was chosen to match the maximum range of the reference instrument. The results are summarized in Fig. 8. The suggested sensor creates additional linearity error of 0.22% FS.

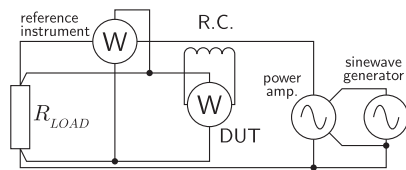


Fig. 7. Schematic diagram of power measurement. Two wattmeters (W) are used: a single-chip electronic power/energy meter with digital integrator with RC as a current sensor (labeled DUT = device under test), and a reference wattmeter Tektronix PA1000 with internal shunt resistor (labeled *reference instrument*).

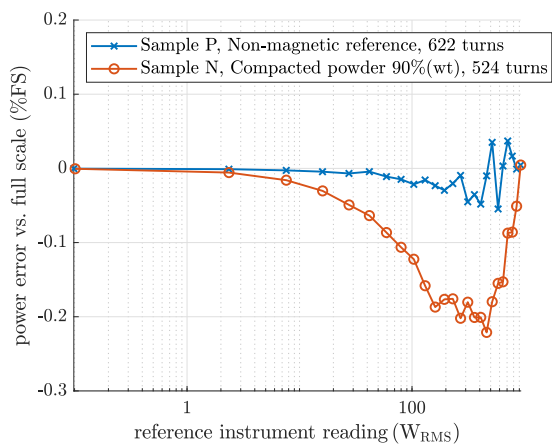


Fig. 8. Power measurement with resistive load. The nonlinearity of the ferromagnetic core material causes increased error of -0.22% FS, which is acceptable for domestic energy meters.

Maximum phase error (without applying the phase compensation available in the STPM34) is below 0.3° .

IV. CONCLUSION

A small-size RC with a nanocrystalline powder core is suitable as an ac current sensor for energy meters. The achieved linearity error is 0.32% for the 20 A range. The new sensor is also highly resistant to the dc component in the measured current: 100 A dc only causes 1.6% error, and remains operational even for overcurrent of 1000 A dc with a 20% error. Compared to the air core, the nanocrystalline sensor noise was reduced 15-fold to $36 \mu\text{A}/\sqrt{\text{Hz}}$ at 50 Hz. The sensor was tested together with a single-chip power meter containing a digital integrator. The resulting error for the measurement of power was 0.22% FS. Compared to a commercially available air-cored sensor of comparable size, we achieved 50% increase in sensitivity, and noise reduced by 3.5 dB. The suppression of the external current is comparable. The main factor limiting the latter parameter is the mechanical precision of the core. Composite cores of this type can be manufactured in arbitrary shapes for specific applications.

ACKNOWLEDGMENT

This work was supported by the Grant Agency of the Czech Republic within the Nanofluxgate Project under Grant GACR GA20-27150S.

REFERENCES

- Abdi-Jalebi E, McMahon R (2007), "High-performance low-cost Rogowski transducers and accompanying circuitry," *IEEE Trans. Instrum. Meas.*, vol. 56, pp. 753–759, doi: [10.1109/TIM.2007.894801](https://doi.org/10.1109/TIM.2007.894801).
- Cataliotti A, Cosentino V, Cara D D, Nuccio S, Tinè G (2015), "Rogowski coil current transducer compensation method for harmonic active power error," *Measurement*, vol. 63, pp. 240–251, doi: [10.1016/j.measurement.2014.12.005](https://doi.org/10.1016/j.measurement.2014.12.005).
- Draxler K, Styblikova R (2017), "Magnetic shielding of Rogowski coils," in *Proc. IEEE Int. Instrum. Meas. Technol. Conf.*, pp. 1–5, doi: [10.1109/IMTC.2017.7969952](https://doi.org/10.1109/IMTC.2017.7969952).
- Eydan A, Shirani B, Sadeghi Y, Asgarian M A, Noori E (2020), "Design and fabrication of an optimized Rogowski coil for plasma current sensing and the operation confidence of Alvand tokamak," *Nucl. Eng. Technol.*, vol. 52, pp. 2535–2542, doi: [10.1016/j.net.2020.04.011](https://doi.org/10.1016/j.net.2020.04.011).
- Ferkovic L, Ilic D, Malaric R (2009), "Mutual inductance of a precise Rogowski coil in dependence of the position of primary conductor," *IEEE Trans. Instrum. Meas.*, vol. 58, pp. 122–128, doi: [10.1109/TIM.2008.928412](https://doi.org/10.1109/TIM.2008.928412).
- Grim V, Ripka P, Draxler K, Mirzaei M (2021), "Rogowski coil with ferromagnetic core for precise monitoring of low-frequency currents," in *Proc. IEEE Int. Magn. Conf.*, 2100009, doi: [10.1109/INTERMAG42984.2021.9579562](https://doi.org/10.1109/INTERMAG42984.2021.9579562).
- Grybos D, Leszczynski J S, Kwiecień M, Swieboda C, Lasak P, Pluta W, Rygal R, Soinski M (2018), "Properties of Fe-based nanocrystalline magnetic powder cores (MPC) and structure of particle size distribution (PSD)," *J. Electron. Eng.*, vol. 69, pp. 163–169, doi: [10.2478/jee-2018-0020](https://doi.org/10.2478/jee-2018-0020).
- Kojovic L A, Bishop M T, Sharma D (2013), "Innovative differential protection of power transformers using low-energy current sensors," *IEEE Trans. Ind. Appl.*, vol. 49, pp. 1971–1978, doi: [10.1109/TIA.2013.2264792](https://doi.org/10.1109/TIA.2013.2264792).
- Kuwabara Y, Wada K, Guichon J M, Schanen J L, Roudet J (2018), "Implementation and performance of a current sensor for a laminated bus bar," *IEEE Trans. Ind. Appl.*, vol. 54, pp. 2579–2587, doi: [10.1109/TIA.2018.2796538](https://doi.org/10.1109/TIA.2018.2796538).
- Luo P, Li Z, Li H, Li H (2013), "A high-current calibration system based on indirect comparison of current transformer and Rogowski coil," *Meas. Sci. Technol.*, vol. 24, pp. 125005–125015, doi: [10.1088/0957-0233/24/12/125005](https://doi.org/10.1088/0957-0233/24/12/125005).
- Mazaleyrat F, Léger V, Lebourgeois R, Barrué R (2002), "Permeability of soft magnetic composites from flakes of nanocrystalline ribbon," *IEEE Trans. Magn.*, vol. 38, pp. 3132–3134, doi: [10.1109/TMAG.2002.802419](https://doi.org/10.1109/TMAG.2002.802419).
- Mlejnek P, Kašpar P (2009), "Detection of disturbance of working conditions of current transformer in energy meters for reduction of unauthorized current consumption," in *Proc. Int. Conf. Power Electron. Drive Syst.*, pp. 1504–1507, doi: [10.1109/PEDS.2009.5385665](https://doi.org/10.1109/PEDS.2009.5385665).
- Ramboz J D (1996), "Machinable Rogowski coil, design, and calibration," *IEEE Trans. Instrum. Meas.*, vol. 45, pp. 511–515, doi: [10.1109/19.492777](https://doi.org/10.1109/19.492777).
- Ramboz J, Destefan D, Stant R S (2002), "The verification of Rogowski coil linearity from 200 A to greater than 100 kA using ratio methods," in *Proc. 19th IEEE Instrum. Meas. Technol. Conf.*, pp. 687–692, doi: [10.1109/IMTC.2002.100692](https://doi.org/10.1109/IMTC.2002.100692).
- Ray W F, Hewson C R (2000), "High performance Rogowski current transducers," in *Proc. Conf. Rec.-IAS Annu. Meet. IEEE Ind. Appl. Soc.*, vol. 5, pp. 3083–3090, doi: [10.1109/IAS.2000.882606](https://doi.org/10.1109/IAS.2000.882606).
- Ripka P, Ed. (2021), *Magnetic Sensors and Magnetometers*, 2nd ed. Norwood, MA, USA: Artech House.
- Roemer G (2012), "Using the pulse sidewinder Rogowski coil to measure AC current," *Pulse Eng.*, Tech. Rep. [Online]. Available: https://www.allaboutcircuits.com/uploads/articles/Kemet_Pulse-Power-BU-Measure-AC-Current-Using-Sidewinder-Rogowski.pdf
- Samimi M H, Mahari A, Farahnakian M A, Mohseni H (2015), "The Rogowski coil principles and applications: A review," *IEEE Sens. J.*, vol. 15, pp. 651–658, doi: [10.1109/JSEN.2014.2362940](https://doi.org/10.1109/JSEN.2014.2362940).
- Suomalainen E P, Hallström J K (2009), "Onsite calibration of a current transformer using a Rogowski coil," *IEEE Trans. Instrum. Meas.*, vol. 58, pp. 1054–1058, doi: [10.1109/TIM.2008.2007031](https://doi.org/10.1109/TIM.2008.2007031).
- Tumanski S (2011), *Handbook of Magnetic Measurements*. Boca Raton, FL, USA: CRC Press.
- Wei C, Lin C, Boyang M, Yuntao G, Shi Y (2020), "Development of magnetic core framework for flexible Rogowski coil current transducer," in *Proc. Ind. Electron. Conf.*, pp. 3493–3497, doi: [10.1109/IECON43393.2020.9254471](https://doi.org/10.1109/IECON43393.2020.9254471).
- Zhang M, Li K, He S, Wang J (2014), "Design and test of a new high-current electronic current transformer with a Rogowski coil," *Metro. Meas. Syst.*, vol. 21, pp. 121–132, doi: [10.2478/mms-2014-0012](https://doi.org/10.2478/mms-2014-0012).
- Zheng Y Y, Wang Y G, Xia G T (2015), "Amorphous soft magnetic composite-cores with various orientations of the powder-flakes," *J. Magn. Magn. Mater.*, vol. 396, pp. 97–101, doi: [10.1016/j.jmmm.2015.08.036](https://doi.org/10.1016/j.jmmm.2015.08.036).
- Zhu J, Zhang Q, Jia J, Tao F, Yang L, Yang L (2006), "Design of a Rogowski coil with a magnetic core used for measurements of nanosecond current pulses," *Plasma Sci. Technol.*, vol. 8, pp. 457–460, doi: [10.1088/1009-0630/8/4/19](https://doi.org/10.1088/1009-0630/8/4/19).

6.2 Self-oscillating DC Current Transformer with Nanocrystalline Core

This is a conference proceedings paper from IEEE Sensors 2021 virtual conference, where it was presented as a poster.

The key idea is that all functions of a closed-loop fluxgate sensor i.e. excitation, sensing and compensation may be covered by a single winding on a single core. The excitation and compensation sources are merged into one H-bridge. The presence of the bridge allows for the compensation current to be recirculated with low losses, in theory given only by the winding thickness and $R_{DS(ON)}$ of the transistors. With this improvement it is possible to reach compensation currents much larger than the excitation current peaks and thus reach very wide measurement range (± 100 A in this particular design) with low power consumption.

The paper provides a theoretical elaboration of the relations between number of turns, winding cross-sectional area, switching frequency and conduction losses. I personally did everything except literature review and the presentation at the virtual conference.

Self-oscillating DC Current Transformer with Nanocrystalline Core

Václav Grim
Department of Measurement
Czech Technical University
Praha, Czechia
0000-0003-1685-5321

Pavel Ripka
Department of Measurement
Czech Technical University
Praha, Czechia
0000-0003-1115-6265

Abstract—A simple and robust circuit for contactless current measurement, based on a free-running relaxation oscillator with variable threshold values, is presented. Its performance was evaluated and compared with other methods, in particular the traditional second harmonic detection. Linearity error below 0.1% was achieved across the range of ± 100 A.

Index Terms—current measurement, fluxgate, soft magnetic materials, metrology

I. INTRODUCTION

Contactless current measurement is possible with several different methods, all of them are based on measuring the magnetic field around the conductor [1]. For large currents (hundreds of Amperes and more), magneto-optical transducers are the most modern, although expensive, approach [2]. For smaller currents or for lower cost applications that need to sense DC current as well, closed-loop Hall sensors or fluxgate sensors are used [3].

Self-oscillating transducers were previously presented e.g. in [4] or [5]. The proposed design uses a different feedback mechanism and offers a reduced current consumption, because no power is being dissipated in a linear amplifier.

Efforts in lowering the power consumption using switched amplifiers were presented e.g. in [6] or in [7].

II. THEORY OF OPERATION

The sensor utilizes the non-linear B-H characteristic of a toroidal ferromagnetic core. It has only one core with one secondary winding, the primary winding comprises of one pass through the transducer. The block diagram of the circuit is shown in Fig. 1. It is a free-running relaxation oscillator with variable threshold values. The circuit does not have a fixed oscillation frequency, the switching is controlled by cycle-by-cycle current limiter. The closed-loop operation allows for greatly increased measurement range.

Modeling of circuits with nonlinear inductances is described in great detail in [8]. However, for illustration of the working principle, the nonlinear B-H curve of the ferromagnetic core can be simplified to a piecewise linear function with two constant incremental permeabilities: μ_{sat} for saturated state and μ_{unsat} for unsaturated state, corresponding to inductances

This study was supported by the Grant Agency of the Czech Republic within the Nanofluxgate project (GACR GA20-27150S).

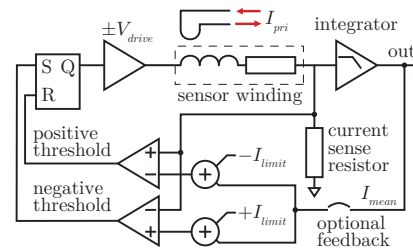


Fig. 1. Block diagram of the proposed circuit

L_{unsat} and L_{sat} . When current is applied to the primary winding, the observed B-H curve is shifted left or right.

The working principle is described by Fig. 2. Excitation is provided by a constant voltage square wave source. When there is no current in the primary, the oscillation is completely symmetric and the duty cycle is 50% (Fig. 2a). The blue voltage waveform is shown across the winding inductance only, excluding the wire resistance. The winding current of each piecewise segment is expressed as

$$I(t) = e^{-\frac{R}{L}t} (I(t_0) - \frac{V_{drive}}{R}) + \frac{V_{drive}}{R} \quad (1)$$

where $I(t_0)$ is the initial current and R is the sum of winding resistance, the current sense resistor and the internal resistance of the voltage source V_{drive} . The resistance R (together with hysteretic losses) is the cause for the change in duty cycle when a primary current is applied.

In open loop mode (Fig. 2b) the current threshold I_{limit} remains the same for both polarities, but the current peaks become asymmetric. The saturation current is shifted by the primary current divided by the turns ratio.

In feedback mode (Fig. 2c) the threshold values are controlled, so that the current peaks are centered around the mean excitation current. The DC current I_{mean} may be much larger than the ripple current $\pm I_{limit}$.

III. CORE AND WINDING SELECTION

Nanocrystalline tape wound toroidal core was used for construction of the transducer. Vitroperm 500F was used for its low coercivity and large saturation induction. Nanocrystalline

6.2 Self-oscillating DC Current Transformer with Nanocrystalline Core

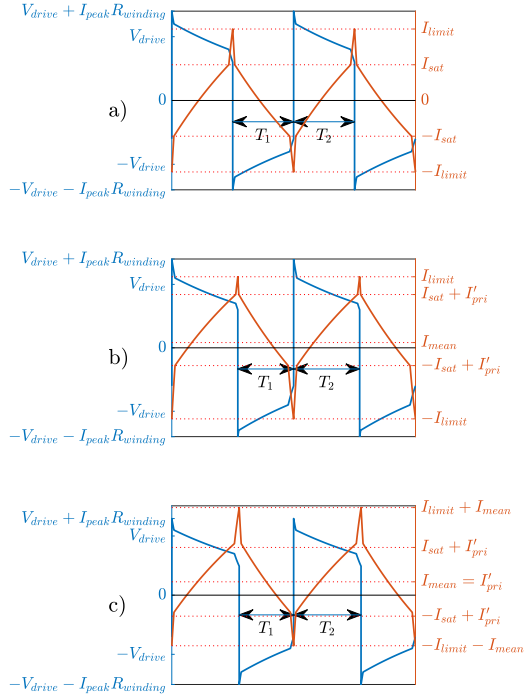


Fig. 2. Voltage (blue) and current (red) waveforms with zero primary current (a), in open-loop mode (b) and in feedback mode (c)

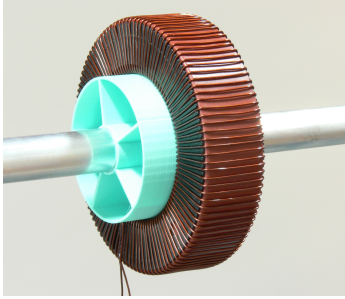


Fig. 3. The transducer placed on a test conductor

materials are favored in the construction of current transformers for their narrow and linear B-H loop [9].

For the sensor to achieve low overall power consumption, it is important to keep resistive losses in the winding at minimum. The ratio X_L/R will be referred to as Ω to distinguish it from Q , which is defined only for second-order LTI systems. Only the steady-state compensation current $I_{mean} = I_{pri}/N$ is considered in the following calculations. In ideal case without iron losses, a winding with a given Ω dissipates only $1/\sqrt{\Omega^2 + 1} \approx 1/\Omega$ of the compensation power.

If the core spends most of the time in unsaturated state, the

frequency can be estimated as

$$f = \frac{V_{drive}}{4N \cdot L_{1T} \cdot I_{sat,1T}} \quad (2)$$

where L_{1T} and $I_{sat,1T}$ are the inductance and saturation current of a single-turn excitation winding. The maximum current which satisfies a chosen Ω is

$$I_{mean} = \frac{1}{\Omega} \frac{V_{drive}}{N^2 R_{1T}} = \frac{1}{\Omega} \frac{V_{drive} \cdot A_{Cu}}{N^2 \cdot \rho_{Cu} \cdot l_{1T}} \quad (3)$$

where A_{Cu} is the total cross-sectional area of the winding, ρ_{Cu} is the resistivity of copper ($17 \times 10^{-9} \Omega \text{m}$) and l_{1T} is the turn length.

Another constraint is imposed by the maximum current density J_{max} allowed in the winding

$$J_{max} = \frac{N \cdot I_{mean}}{A_{Cu}} \quad (4)$$

Combining expressions 2, 3 and 4, the optimum number oscillation frequency and its associated number of turns are found as

$$f = \frac{\Omega \cdot J_{max} \cdot \rho_{Cu} \cdot l_{1T}}{4 \cdot L_{1T} \cdot I_{sat,1T}} \quad (5)$$

$$N = \frac{V_{drive}}{4f \cdot L_{1T} \cdot I_{sat,1T}} \quad (6)$$

The product $L_{1T} \cdot I_{sat,1T}$ in equation 5 is largely independent on the material permeability. Frequency can be adjusted by changing the core dimensions; inductance is proportional to the core cross sectional area A_{fe} .

The required thickness of the wire is given simply by the maximum primary current that is to be measured.

$$d_{wire} = \sqrt{\frac{4}{\pi} \frac{I_{pri}}{N \cdot J_{max}}} \quad (7)$$

For the particular sample with $L_{1T} = 96 \mu\text{H}$, $I_{sat,1T} = 2.5 \text{ A}$ and $l_{1T} = 90 \text{ mm}$, we chose $\Omega = 20$, $J_{max} = 3 \text{ A/mm}$, $V_{drive} = 10 \text{ V}$ and $I_{pri} = 100 \text{ A}$. The calculated parameters are $f = 96 \text{ Hz}$, $N = 109$ and $d_{wire} = 0.62 \text{ mm}$. Closest available diameter of 0.71 mm was used, which in theory should further reduce the resistive losses by 19%.

IV. CIRCUIT DESIGN

Detailed schematic diagram is provided in Fig. 4. The circuit is based on full bridge topology. It uses a gate driver (HIP4080A) and four N-MOSFETs to provide low-impedance square wave voltage across the winding. There are no other switching nodes or inductors in the circuit. A key element is the bulk capacitor across the H-bridge. It provides and absorbs all of the inductive current in the winding, both the saturation peaks and the compensation current I_{mean} .

The value of the current sense resistors has to be low compared to the winding resistance, in order to not degrade the Ω -factor. The winding resistance is $420 \text{ m}\Omega$, an R_{sense} of $100 \text{ m}\Omega$ is a suitable compromise between power efficiency and precise operation of the current limiting comparators.

There are two feedback paths in the circuit. The inner loop controls the bridge switching based on the instantaneous

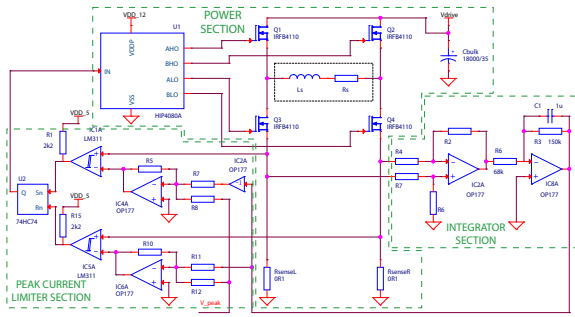


Fig. 4. Schematic diagram of the circuit

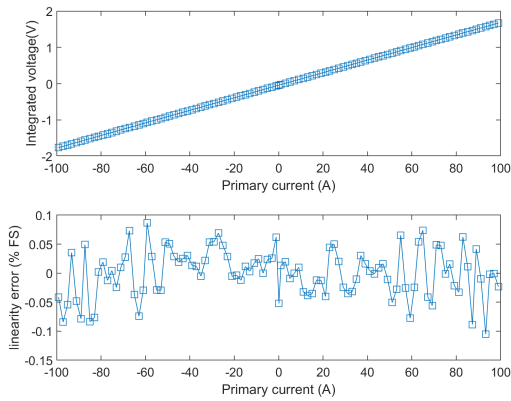


Fig. 5. Measured linearity error

currents flowing through R_{senseL} and R_{senseR} . The outer loop adjusts the threshold values for the inner loop. It is implemented as a simple first-order active RC network with cutoff frequency of 1 Hz.

V. MEASUREMENTS

A straight, 2m long aluminum bar was used as a test conductor. The current was provided by a Sorensen SGX power supply. Reference current readings were taken by a LEM IT 200-S transducer. Voltages were measured by Agilent 34401A and 34410A digital multimeters.

A. Linearity measurement

Linearity was calculated from 101 points between -100 A and $+100$ A. The output signal was taken from the integrator (IC8A in Fig. 4). The resulting Fig. 5 shows linearity error of 0.1 % FS.

B. Noise measurement

Noise was measured from 1000 samples obtained by DMM with sampling period 500 ms. Higher sampling rate is not required, because the noise spectrum is meaningful only up to

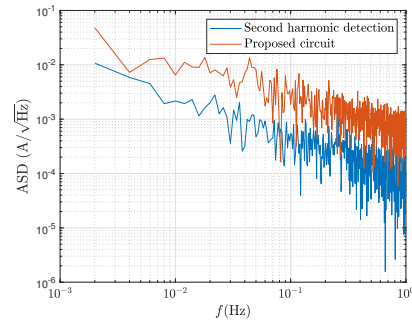


Fig. 6. Measured noise spectral density

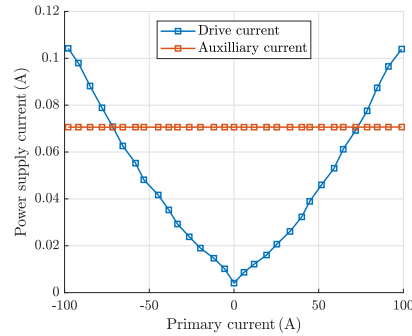


Fig. 7. Current consumption from individual power supplies

the cutoff frequency of the lowpass filter. The primary current was zero during the whole measurement.

For the purpose of comparison, another measurement was done, in which a constant frequency sinewave voltage source was connected to the coil instead of the self-oscillating excitation circuit. The magnitude of the second harmonic component of the current was measured with a current sense resistor and a lock-in amplifier (SR830). The noise in this mode is somewhat lower, as shown in Fig. 6.

C. Power consumption measurement

The power consumption was measured across the whole measurement range (-100 A to $+100$ A). The quiescent current drawn from $V_{DD,+12}$ and $V_{EE,-12}$, which is largely independent on measured current, is shown separately from the switching current drawn from V_{drive} . Three Agilent DMMs in DC mode with long integration time (100 NPLC) were used for this measurement. The results are shown in Fig. 7.

VI. CONCLUSION

A novel approach to self-oscillating DC current transformer with full-bridge driver is presented. The switching topology reduces the power consumption by a factor of 8 compared to the case where the compensation current is provided by a linear amplifier (110 mA vs. $I_P/N_S = 920$ mA for the measured current of 100 A). For the 100 A FS range the device has 0.1 % linearity and noise of only $1 \text{ mA}/\sqrt{\text{Hz}}$ at 1 Hz.

REFERENCES

- [1] S. Ziegler, R. C. Woodward, H. H. C. Iu, and L. J. Borle, "Current sensing techniques: A review," *IEEE Sens. J.*, vol. 9, no. 4, pp. 354–376, 2009, ISSN: 1530437X. DOI: 10.1109/JSEN.2009.2013914.
- [2] A. Frank, G. M. Mueller, L. Yang, *et al.*, "Fiber optic current and voltage sensors for electric power transmission systems," in *Fiber Opt. Sensors Appl. XV*, H. H. Du, A. Mendez, and C. S. Baldwin, Eds., vol. 10654, SPIE, May 2018, p. 1, ISBN: 9781510618190. DOI: 10.1117/12.2303945.
- [3] P. Ripka, Ed., *Magnetic Sensors and Magnetometers*. Artech, 2001, ISBN: 1580530575.
- [4] P. Pejovic, "A simple circuit for direct current measurement using a transformer," *IEEE Trans. Circuits Syst. I Fundam. Theory Appl.*, vol. 45, no. 8, pp. 830–837, 1998, ISSN: 10577122. DOI: 10.1109/81.704822.
- [5] J. Cao, J. Zhao, and S. Cheng, "Research on the simplified direct-current fluxgate sensor and its demodulation," *Meas. Sci. Technol.*, vol. 30, no. 7, p. 075 101, May 2019, ISSN: 13616501. DOI: 10.1088/1361-6501/ab09bf.
- [6] G. Velasco-Quesada, M. Román-Lumbreras, R. Pérez-Delgado, and A. Conesa-Roca, "Class H power amplifier for power saving in fluxgate current transducers," *IEEE Sens. J.*, vol. 16, no. 8, pp. 2322–2330, 2016, ISSN: 1530437X. DOI: 10.1109/JSEN.2016.2516399.
- [7] S. Veinovic, M. Ponjavic, S. Milic, and R. Djuric, "Low-power design for DC current transformer using class-D compensating amplifier," *IET Circuits, Devices Syst.*, vol. 12, no. 3, pp. 215–220, May 2018, ISSN: 1751858X. DOI: 10.1049/iet-cds.2017.0324.
- [8] M. M. Ponjavić and R. M. Durić, "Nonlinear modeling of the self-oscillating fluxgate current sensor," *IEEE Sens. J.*, vol. 7, no. 11, pp. 1546–1553, 2007, ISSN: 15581748. DOI: 10.1109/JSEN.2007.908234.
- [9] K. Draxler and R. Styblíková, "Use of nanocrystalline materials for current transformer construction," *J. Magn. Magn. Mater.*, vol. 157-158, pp. 447–448, 1996, ISSN: 03048853. DOI: 10.1016/0304-8853(95)01055-6.

6.3 DC Current Sensor Using Switching-Mode Excited In-situ Current Transformer

This paper presents a way of repurposing an ordinary current transformer into a DC fluxgate current sensor, with the possibility to switch between these two modes during operation as needed. This is an advantage for applications in power distribution, where there is a need for precise AC measurement with low power consumption, with an occasional check on the DC offset. The circuit is based on a type D amplifier, and therefore the current through the winding is recovered back into the bulk capacitor on each switching of excitation voltage polarity.

I was the first author of this paper. The hardware design, most measurements and writing was done by me personally.



Research articles

DC current sensor using switching-mode excited in-situ current transformer

Václav Grim, Pavel Ripka*, Jan Bauer

Faculty of Electrical Engineering, Czech Technical University, Prague 16627, Czech Republic



ARTICLE INFO

Keywords:

Current sensor
Current transformer
Ferroresonance

ABSTRACT

DC current component in the power grid may cause gross measurement errors and lead to overheating of power transformers. We have previously developed method how to measure DC current using fluxgate effect in existing current transformers. In this paper we show that using ferroresonance the power consumption of such device can be drastically reduced. The microprocessor can both control the H-bridge excitation unit and perform signal processing, avoiding the need of external instruments.

1. Introduction

DC currents in the grid may be caused by geomagnetic induction: DC current spikes up to 200 A with 3 min duration are observed during geomagnetic storms [1]. Another sources of DC current component are switching transients and uncompensated transformerless inverters, which are now standard in solar and wind power plants [2]. Novel source of “DC induction” through ground potentials are DC power transmission lines [3]. There is also a possibility of deliberate usage of half wave rectifiers for large loads, for the purpose of lowering the measured energy consumption: the half-way rectified current contains large DC current component, which partly saturates current transformer in the energy meter. The resulting error is always negative.

The current transformer (CT) are still the most popular devices for industrial applications [4]. CTs are susceptible to measurement errors caused by DC component in the measured (primary) current [5] and remanence [6] and also by magnetization from external fields. In order to avoid these gross errors, 2 types of DC tolerant current transformers has been developed: linear dc tolerant current transformers and dual-core current transformers.

Dual-core CTs have one core with high permeability for achieving low error and second core with low permeability and high DC immunity. While this combination works well for resistive loads, it fails for loads with inductive or capacitive character. The reason is rapid change of phase error when the high-permeability core is saturated. This leads to the gross error of measured power for loads with lower power factor [7].

Linear dc tolerant current transformers are usually made of nanocrystalline material with perpendicular anisotropy induced by field annealing [8] or by stress annealing [9]. Due to the perpendicular anisotropy the B-H characteristics is flat, with decreased permeability and

high linearity, and with increased saturation field. Thanks to high saturation field the core is more resistant to saturation. Thanks to linear characteristics, the phase error is small; the amplitude error caused by decreased permeability can be easily compensated [4].

However, most of the precise CTs installed in the grid are based on permalloy, with very low DC current immunity. Replacing them would be extremely expensive. Methods of improvement of accuracy of these transformers in the presence of DC current and means to measure this DC current component are therefore highly desired by the industry.

We have shown that DC currents can be measured with 5% accuracy by existing CTs using additional AC excitation and detection of the second harmonic of the excitation frequency using the fluxgate principle [10].

There are three main reasons why it is important to measure DC current component in the grid:

1. To detect excessive level of DC current component which cause gross measurement errors or may cause saturation of power transformers and overheating
2. To act as zero indicator for the DC compensation scheme for transformerless power inverters
3. To feedback-compensate primary DC current component of current transformer to restore its accuracy for measuring of AC currents.

DC current comparators work on the similar principle as our device, but they require three windings: excitation, detection and feedback. DC current comparators also have two toroidal cores excited in opposite direction, so that the net AC flux is ideally zero and no current on excitation frequency is injected into the primary circuit [11]. Our simple device has many disadvantages which will be discussed later, but one very important advantage: it requires only single winding and single

* Corresponding author.

E-mail addresses: vaclav.grim@fel.cvut.cz (V. Grim), ripka@fel.cvut.cz (P. Ripka).<https://doi.org/10.1016/j.jmmm.2019.166370>

Received 13 August 2019; Received in revised form 18 December 2019; Accepted 28 December 2019

Available online 30 December 2019

0304-8853/ © 2019 Elsevier B.V. All rights reserved.

core so that it can use current transformers already installed in million volumes within the power grid. We cannot use autooscillation circuit such as described in [12] because we have to keep the secondary burden constant in order to maintain the AC operation of the CT.

First disadvantage of active DC current transformer which we developed and described in [10] is its complicated electronics and large power consumption of 391 W from 230 V grid (324 W for the power amplifier, 23 W for the generator and 44 W for the lock-in amplifier). The CTs can be demagnetized by momentarily increasing its burden by using pulse width modulation (PWM) switchable resistor [13]. PWM (Class D amplifier) has been also used for feedback compensation of current transducer [14]. This type of amplifier has very high efficiency, but suffer of the large ripple. Class H amplifier is a more complicated solution, but without the problem of ripple [15].

Similar technique was used in [16] for measuring and compensation of the DC bias in AC grid voltage. Measuring DC voltage instead of current is complementary approach which is very challenging: DC bias of 1 mV in 400 V grid may already cause serious saturation of the distribution transformer. Such small DC component can be measured by using all-even harmonics detection of the magnetization current of the saturable reactor [16].

In this paper we use excitation circuit to inject AC into the CT's secondary winding. Then we are able to measure DC component of the primary current by monitoring the second harmonic current in the secondary winding. The advantage of our method is that in can be used in-situ on current transformers already installed in the grid.

2. Current transformer with simulated sinewave excitation

In this mode we use sine wave excitation voltage in a way similar to [10], but in order to lower the energy consumption, we replaced the analog power amplifier by a hard-switched H-bridge. Sigma-delta bit-stream controls the switching of one half of the bridge (Q3 and Q4), the other half (Q1 and Q2) is toggled only once per half-period based on polarity of the generated sine wave. This is done in order to reduce switching losses and switching noise.

2.1. Circuit description

Simplified schematic diagram of the proposed circuit is shown in Fig. 1. The current transformer elaborated in this paper is Norma 179, rated at 400A primary and 5A secondary current with nominal burden of 0.2 Ω . On-state resistance of the switches must not significantly affect the total burden resistance defined by R_{burden} , therefore we chose IRFB4110 N-channel MOSFETs with $R_{DS(ON)} = 4.5$ m Ω . Gate currents

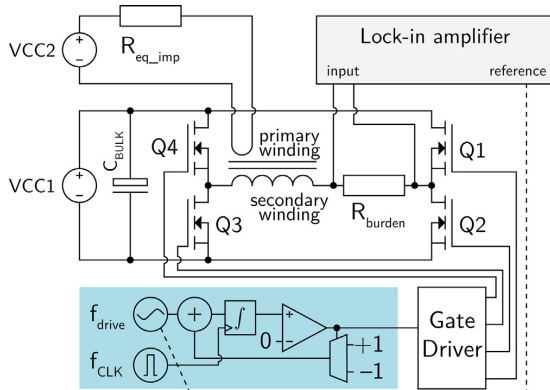


Fig. 1. Switched DC current transformer. Shaded rectangle denotes software-emulated digital circuitry.

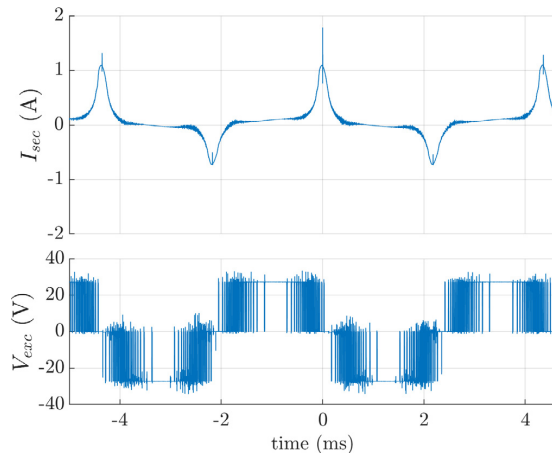


Fig. 2. Excitation voltage for unipolar switching (lower trace) simulating 43 Hz sinewave and corresponding excitation current (upper trace).

were provided by HIP4081A gate driver. All control and synchronization signals were generated by a Cortex-M4 MCU (NXP MK20) running at 72 MHz. Software-based delta-sigma modulator was used to generate a 43 Hz sine wave with a modulation frequency of 100 kHz. The H-bridge together with a digital delta-sigma modulator form a high power DAC. The amplitude and waveform of the AC component is controlled by a numerically controlled oscillator (f_{drive} in Fig. 1).

2.2. Measurement methodology and results

Measured signal is extracted from voltage drop across the 0.1 Ω burden resistor using a HF2LI benchtop lock-in amplifier. The circuit can be operated in two modes. In passive mode Q1, Q4 are permanently on and Q2, Q3 off. This corresponds to conventional operation of a CT. Active mode is used for the measurement of DC primary current. In this case the H bridge is switched to add AC component into the CT secondary winding.

The DC component of the current I_{PRI} can be measured from 2nd harmonics of the injected current. Fig. 2 shows the generated sine wave and resulting excitation current waveform.

While 43 Hz excitation frequency is sufficient for detection of DC current component, measuring 50 Hz current requires to increase excitation frequency - we have selected 237 Hz excitation for this purpose.

2.3. Power consumption

The advantage of this solution is that the power consumption is only 30 W from 230 V grid (VCC1 + microprocessor + gate driver).

Net current consumption for 43 Hz is 20 mA from 5 V for bridge voltage, 18 mA from 5 V for MCU and current sense amplifier, 33 mA from 12 V for gate driver.

However, net current consumption for 237 Hz excitation frequency is dramatically increased: 236 mA from 26 V for bridge voltage, 18 mA from 5 V for MCU and current sense amplifier, 33 mA from 12 V for gate driver. Additional issues include non-linearity of its transfer characteristics and rather complicated control. We therefore decided to use the ferroresonant mode.

3. Current transformer with series resonant excitation

The nonlinear LC excitation tank was described for fluxgate sensors and sinewave excitation in [17], for squarewave excitation by [18] and [19]. We have used the same ferroresonant circuit to achieve large

6.3 DC Current Sensor Using Switching-Mode Excited In-situ Current Transformer

V. Grim, et al.

Journal of Magnetism and Magnetic Materials 500 (2020) 166370

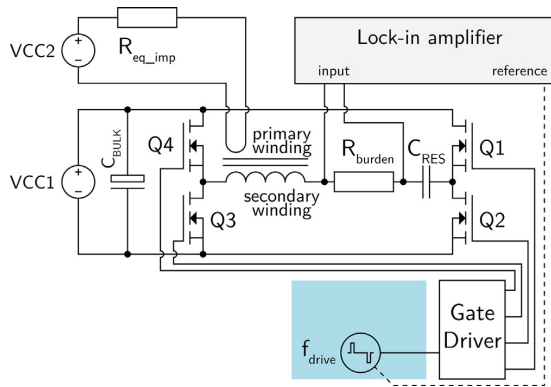


Fig. 3. Serial excitation resonant circuit. Shaded rectangle denotes internal operation of the controlling MCU.

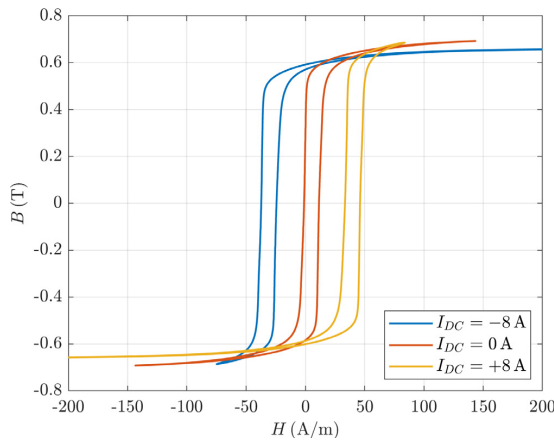


Fig. 4. Working hysteresis loop.

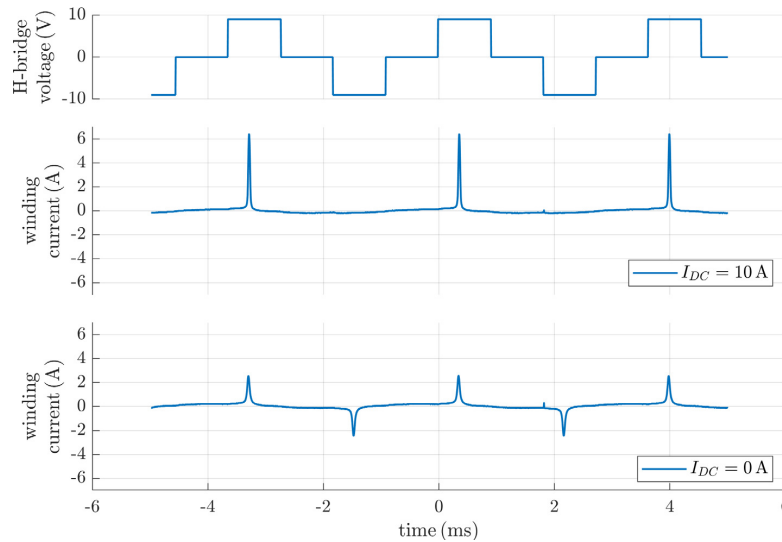


Fig. 5. Excitation current for different values of DC primary current.

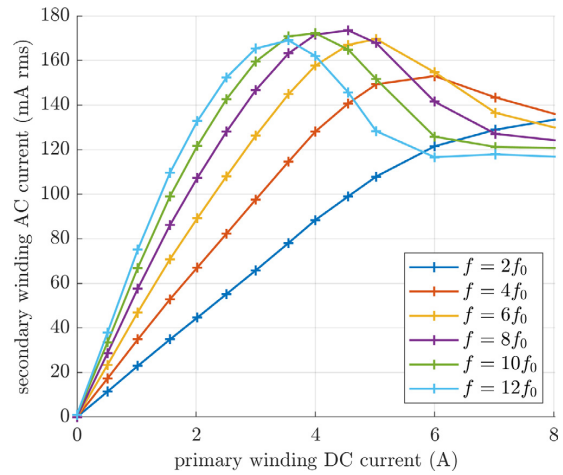


Fig. 6. Even harmonic response of the excitation current to the DC primary current.

excitation current peaks into the secondary or the CT while keeping the excitation power low. The circuit behavior is complex due to large nonlinearities, and the resonant mode is self-sustaining only over a certain range of supply voltage VCC_1 .

3.1. Principle of operation

This resonant method uses the same hardware setup as the sine wave method with the exception of added 10 μF capacitor C_{RES} (Fig. 3). The H-bridge creates a rectangular voltage waveform, which causes large resonant peaks of current through the secondary winding (Fig. 5).

The DC primary current causes large unbalance of the excitation current as shown in Fig. 5. Current unbalance can be observed at all even harmonics. The response for first six even harmonics is shown in Fig. 6. Even though its relatively low sensitivity, 2nd harmonic was selected for our implementation as it has the best linearity, which is important for open-loop operation. In case of feedback compensated

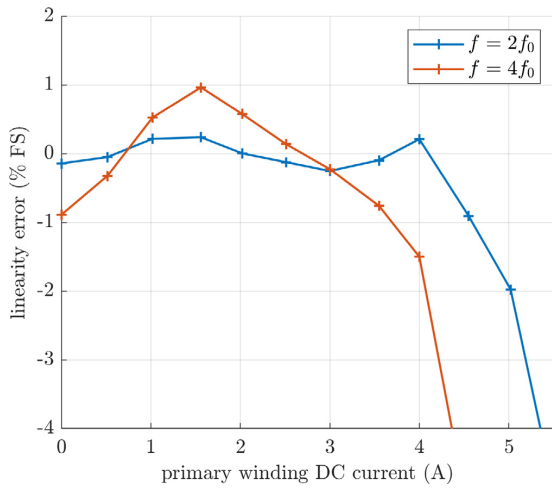


Fig. 7. Measured non-linearity for second and fourth harmonics.

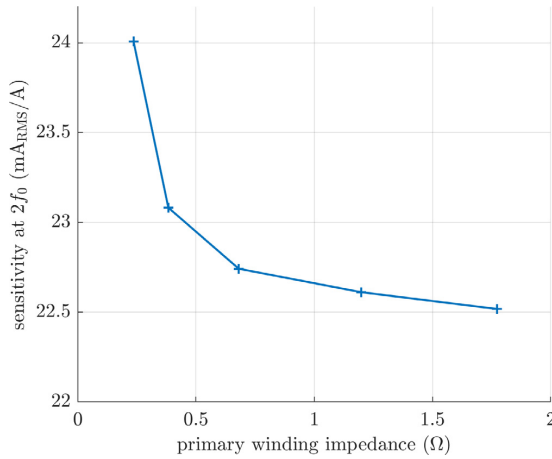


Fig. 8. Second harmonic sensitivity as a function of the impedance in primary circuit.

mode the linearity is not critical and all-even harmonics approach can be used similarly as in [15b].

The disadvantage is that this mode does not allow feedback compensation by using the same switching transistors, as the serial capacitor blocks DC current component in the secondary winding. However, the sensor characteristics is linear even without compensation (linearity error is only 0.4% for current up to 6 A) as shown in Fig. 7. The DC current range is limited to 16 A, for larger current the resonant mode is extinguished.

3.2. Iron losses estimation

The power consumption in the resonance mode is expected to be reduced. However, the power consumed from 230 V grid is the same 30 W as in the simulated sinewave mode. The main advantage of the resonant mode is reduced supply voltage which allows to increase the excitation frequency without significant increase of net power consumption. The bridge supply current from 9 V source was 180 mA (compare with 236 mA from 26 V for simulated sinewave).

The dynamic hysteresis loop (Fig. 4) shows that the excitation peaks

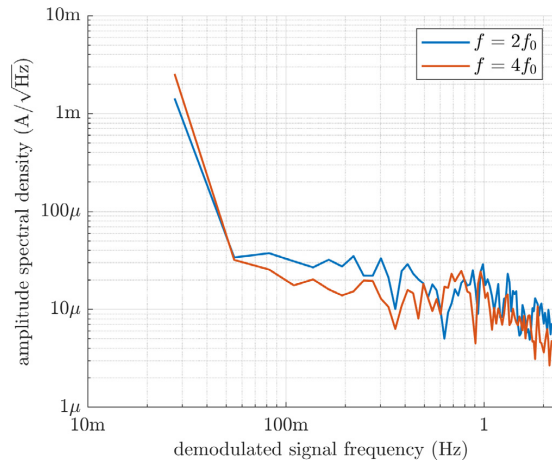


Fig. 9. Spectrum of demodulated signal, second and fourth harmonics.

guarantee deep saturation of the core material, which is vital to achieve low remanence and wide range. The hysteresis loop was measured by sampling H and B. H was derived from the 50 Hz current flowing through the 40-turn auxiliary primary winding and B was calculated from the integrated induced voltage at 80-turn secondary winding. The main single-turn primary winding was connected to Kepco BOP power supply in constant voltage mode through a 0.7 Ω resistor to provide DC bias current. Sampling was made by Agilent MSO3012 oscilloscope in high resolution mode. Integration and averaging of 10 periods was done during post-processing.

In order to find the axis scale we have measured the core dimension using X-ray tomography: the core internal/external diameters are $d_1 = 57.56$ mm, $d_2 = 81.42$ mm, and height $h = 30.18$ mm. Stacking factor was estimated at 0.9. The hysteresis losses for can be derived from the same hysteresis loop as

$$P_{hyst} = fV \oint HdB$$

where f the excitation frequency and V is the core volume. From Fig. 4 we can estimate that for sinewave excitation the work done during one magnetization cycle is 20 J/m^3 , which for the volume of 0.00008 m^3 and 275 Hz frequency makes hysteresis power loss of only 0,44 W.

3.3. Experimental results

The switching timing is shown in Fig. 5. The excitation current has a form of narrow peaks with repetition frequency of 237 Hz and 6 A p-p amplitude, which corresponds to $H_{max} = 80 \cdot 3 \cdot \pi / 0.22 = 3400 \text{ A/m}$ for zero DC current in primary.

Fig. 6 shows the first six even harmonics of excitation current versus the primary DC current. The 2nd harmonics has lowest sensitivity, but largest linear range: for 8 A current the linearity error is already 20%. Fig. 7 shows linearity error in 5 A range for 2nd and 4th harmonics: in the 4A range the linearity error of 2nd harmonics is only $\pm 0.2\%$, while for the 4th harmonics this error is $\pm 1.5\%$. For the open-loop operation we have selected 2nd harmonics because it has the lowest linearity error. For the feedback-compensated mode a sum of all even harmonics would give the best results in term of sensitivity.

An important feature of this mode is low dependence of the sensitivity on impedance in the primary circuit (Fig. 8).

In order to evaluate resolution we measured noise spectra of 2nd and 4th harmonics signals (Fig. 9). The noise spectrum density is $20 \mu\text{A}/\sqrt{\text{Hz}}$ at 1 Hz for 2nd harmonics and slightly lower value for 4th harmonics. The noise in the 100 mHz to 3 Hz frequency band is below

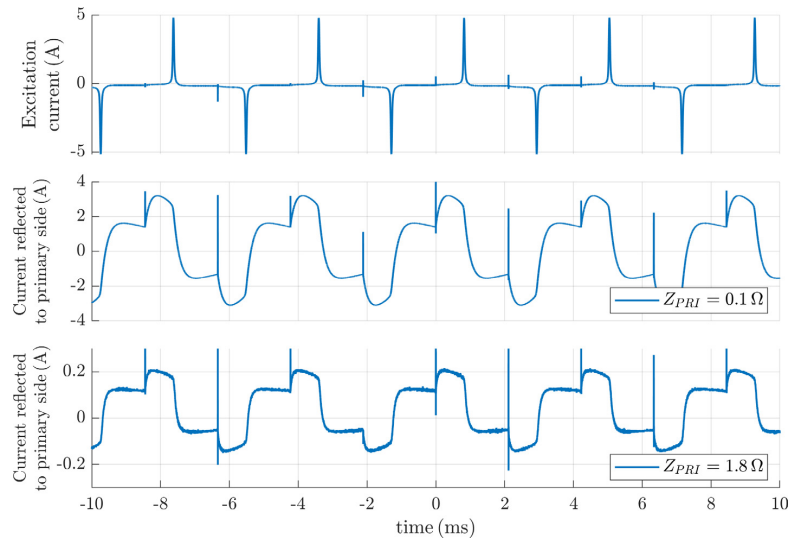


Fig. 10. Series resonance mode: excitation current (top trace), AC current injected into the primary circuit I_{1exc} for primary impedance $R_1 = 100\text{ m}\Omega$ (middle trace) and for $R_1 = 1.8\ \Omega$ (bottom trace).

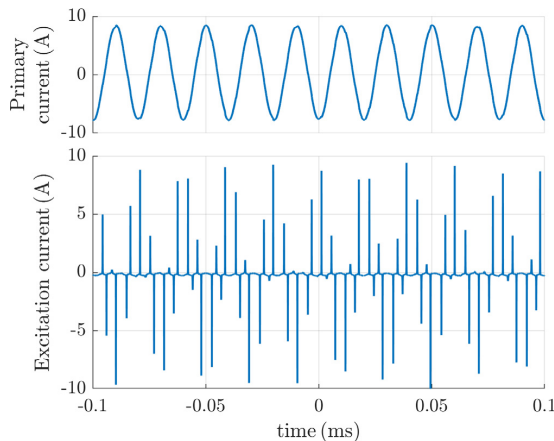


Fig. 11. Response of the secondary current to 16 A_{pp} primary current.

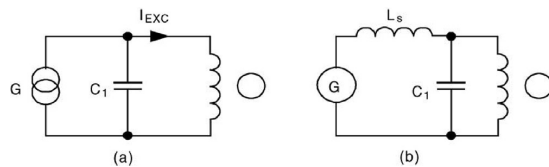


Fig. 12. Parallel excitation circuit a) idealized b) implemented by choke in series [17].

50 μA rms.

3.4. Current injected into the primary conductor

Excitation current appears also in the primary circuit due to the (current) transformer effect. This is illustrated in Fig. 9. Secondary winding was driven with 10 A_{pp} pulses. The injected current is large for short-circuited primary: for $R_1 = 100\text{ m}\Omega$ impedance in the primary

circuit the injected current is $I_{1exc} = 6.2\text{ A p-p}$. However, the injected current is acceptable for realistic grid impedance: for $R_1 = 1.8\ \Omega$ the injected current is $I_{1exc} = 350\text{ mA p-p}$.

3.5. Response to AC primary current

The secondary current I_2 response to 50 Hz primary current I_1 is shown in Fig. 10. Signal from the primary side modulates the excitation waveform. Due to large nonlinearity the frequency spectrum of I_2 is very rich, containing multiples of mains frequency (50 Hz) and excitation frequency (237 Hz) and their modulation products. The amplitude of the 50 Hz primary current can be measured from these modulation products, however the accuracy is low compared with standard CT operation. The final instrument is therefore expected to operate in active driving mode (Mode 2) only for short periods and most of the time remain in ordinary AC-only passive mode (Mode 1).

4. Parallel resonance excitation mode

The parallel excitation circuit is shown in Fig. 11. Instead of using current generator it is enough to increase the impedance of the excitation source by serial resistance or inductance (see Fig. 12).

We have tested this operation mode with serial inductance $L_s = 20\text{ mH}$ in series with $R_s = 14\ \Omega$. The achieved excitation parameters were similar as for the serial mode, however the circuit was more sensitive to impedance in the primary circuit.

5. Conclusion

We have developed compact microprocessor-controlled instrument, which can be used with existing current transformer to add the functionality of DC current measurement and compensation. The power consumption depends on the measurement mode and used CT. As the DC currents in the real grid are changing only slowly, sampling time of 1 s and measurement time of 100 ms will be sufficient. Thus the 90% of the time the transducer works in the classical CT mode, making only negligible compromise for AC accuracy.

For 400A/5A, 5VA CT we have demonstrated open-loop DC measurement range of 8 A, with (maximum) linearity error of 20%. For the

currents below 4 A the linearity error is below 0.2%. The linearity can be further improved by using feedback compensation. The current resolution is 50 μA (noise power spectrum density PSD = 20 $\mu\text{A}/\sqrt{\text{Hz}}$ at 1 Hz) The power consumption for 10% duty cycle will be below 0.5 W. Even though the instrument uses only a single core, it injects only 350 mA p-p into the primary circuit. The last advantage is that the response to the primary current is linear and does not depend on the grid impedance. Because of that the feedback compensation of the primary DC current is only necessary if high accuracy is required.

CRedit authorship contribution statement

Václav Grim: . : Data curation, Formal analysis, Validation, Visualization, Writing - review & editing. **Pavel Ripka:** Conceptualization, Funding acquisition, Investigation, Methodology, Project administration, Supervision, Writing - original draft. **Jan Bauer:** Conceptualization, Investigation, Validation.

Declaration of Competing Interest

The authors declare that they have no known competing financial interests or personal relationships that could have appeared to influence the work reported in this paper.

Acknowledgment

This study was supported by the Grant Agency of the Czech Republic within the New Methods for the Measurement of Electric Currents” project (GACR 17-19877S).

References

- [1] B. Kasztenny, N. Fischer, D. Taylor, T. Prakash, J. Jalli, Do CTs Like DC? 69th Annual Conference for Protective Relay Engineers, College Station, Texas, 2016.
- [2] G. Buticchi, E. Lorenzani, G. Franceschini, A DC offset current compensation strategy in transformerless grid-connected power converters, *IEEE Trans. Power Delivery* 26 (4) (2011) 2743–2751, <https://doi.org/10.1109/tpwrd.2011.2167160>.
- [3] S.H. Yang, G. Zhou, Z.N. Wei, Influence of high voltage DC transmission on measuring accuracy of current transformers, *IEEE Access* 6 (2018) 72629–72634.
- [4] P. Ripka, Contactless measurement of electric current using magnetic sensors, *Tech. Mess.* 89 (10) (2019) 586–598, <https://doi.org/10.1515/teme-2019-0032>.
- [5] P. Mlejnek, P. Kaspar, DC tolerance of current transformers and its measurement, *J. Electr. Eng.* 57 (8/S) (2006) 48–50.
- [6] K. Draxler, R. Styblikova, Demagnetization of instrument transformers before calibration, *J. Electr. Eng.-Elektrotechnicky Casopis* 69 (6) (2018) 426–430.
- [7] P. Mlejnek, P. Kaspar, Drawback of using double core current transformers in static watt-hour meters, *Sensor Lett.* 7 (3) (2009) 394–396.
- [8] W. Pluta, C. Swieboda, J. Leszczynski, M. Soinski, Some remarks on metrological properties and production technology of current transformers made of nanocrystalline cores, *Measurement* 97 (2017) 38–44, <https://doi.org/10.1016/j.measurement.2016.11.024>.
- [9] W. Gunther, Stress annealing process suitable for the production of low permeable nanocrystalline tape wound cores, *J. Magn. Mag. Mat.* 290 (2005) 1483–1486, <https://doi.org/10.1016/j.jmmm.2004.11.555>.
- [10] P. Ripka, K. Draxler, R. Styblikova, DC-compensated current transformer, *Sensors* 16 (2016) 114.
- [11] P. Ripka, Electric current sensors: a review, *Meas. Sci. Technol.* 21 (11) (2010) 1–23.
- [12] J.A. Cao, J. Zhao, S. Cheng, Research on the simplified direct-current fluxgate sensor and its demodulation, *Meas. Sci. Technol.* 30 (7) (2019).
- [13] J. Bauer, P. Ripka, K. Draxler, R. Styblikova, Demagnetization of current transformers using PWM burden, *IEEE Trans. Magn.* 51 (2015) Article#: 4000604.
- [14] S. Veinovic, M. Ponjavic, S. Milic, et al., Low-power design for DC current transformer using class-D compensating amplifier, *IET Circuits Devices & Systems* 12 (3) (2018) 215–220.
- [15] G. Velasco-Quesada, M. Roman-Lumbreras, R. Perez-Delgado, et al., Class H power amplifier for power saving in fluxgate current transducers, *IEEE Sensors J.* 16 (8) (2016) 2322–2330.
- [16] S.N. Vukosavic, L.S. Peric, High-precision sensing of DC bias in ac grids, *IEEE Trans. Power Del.* 30 (3) (2015) 1179–1186.
- [17] P. Ripka, W.G. Hurley, Excitation efficiency of fluxgate sensors, *Sensors and Actuators A* 129 (2006) 75–79, <https://doi.org/10.1016/j.sna.2005.09.047>.
- [18] A. Cerman, J.M.G. Merayo, P. Brauer, F. Primdahl, Self-Compensating Excitation of Fluxgate Sensors for Space Magnetometers. IMTC 2008. IEEE, 2008. doi: 10.1109/IMTC.2008.4547387.
- [19] S. Liu, D.P. Cao, C.Z. Jiang, A solution of fluxgate excitation fed by squarewave voltage, *Sens. Act. A* 163 (2010) 118–121, <https://doi.org/10.1016/j.sna.2010.08.003>.

6.4 A Busbar Current Sensor with Frequency Compensation

One of my earliest works at the department, a geometry optimization study building upon previous works with plain rectangular copper bus bars. The concept of measuring magnetic field near the center of a conductor is not new, it was even a part of the official Texas Instrument's application note. The newly added concept was the adjustment of the conductor cross section in order to compensate for skin effect, which also causes lower intensity of magnetic field in the area of interest (the central hole) as the frequency increases.

A massive number of finite element method simulations was done during the optimization phase. The overall shape (trapezoid with offset hole) was determined by trial and error. The exact dimensions were found with several iterative rounds of parametric sweeps.

My contribution consists of FEM simulations, measurements and making most of the figures.

A Busbar Current Sensor With Frequency Compensation

Pavel Ripka, Václav Grim, and Vojtěch Petrucha

Faculty of Electrical Engineering, Czech Technical University in Prague, 166 27 Praha, Czech Republic

DC/AC yokeless galvanically insulated electric current sensors are required for applications, e.g., in automotive and aerospace engineering, where size, weight, and/or price are strictly limited. A busbar current sensor with differential fluxgate in the hole has 1000 A range and 10 mA resolution. Using an asymmetric shape, we achieved a frequency error below $\pm 3\%$ up to 1 kHz, while keeping high temperature stability and low sensitivity to mechanical misalignments. The 2.5 mA/°C maximum dc drift is four times better than when using an AMR sensor and 1000 times better than when using a Hall sensor. The sensor linearity error is below 0.1%.

Index Terms—Current sensor, fluxgate, magnetic sensor.

I. INTRODUCTION

COMPACT yokeless current sensors are small, lightweight, and cheap. They are used in mobile and embedded applications, and for measuring high dc/ac currents, for which a magnetic core would be too large [1]–[3].

A. Busbar Sensor With Magnetic Sensors on the Surface

Conventional busbar sensors use a pair of Hall sensors on the conductor surface [4], [5]. Differential configuration partly suppresses the external fields. A current range of 10 kA is easily achievable [6], but the sensor has high offset drift. A current sensor based on magnetostriction has a similar problem with stability [7]. The use of an integrated fluxgate allows us to increase the range of the sensor to 600 A with a similar offset stability and noise. A disadvantage of current sensors of this type is their high sensitivity to the distance between the sensor and the conductor surface, which changes due to temperature dilatation. Our experiments have shown that a 0.1 mm shift of the sensor causes a 2% change in sensitivity. Another disadvantage of this type of current sensor is its very high frequency dependence: for a magnetic sensor directly on the surface of the busbar, the sensitivity at 1 kHz drops to 12% of the dc sensitivity.

B. Busbar Sensor With Magnetic Sensors in the Hole

A dc/ac current sensor with a differential integrated fluxgate inside the busbar is described in [8]. An advantage of this solution is that the range can easily be adjusted by changing the distance of the sensor from the busbar center, where the sensitivity is zero.

A similar busbar sensor with a range of 300 A is described in [9]. It uses an AMR sensor bridge in a semi-cylindrical slot in the busbar. Unlike the sensor described in [9], we use a differential sensor, which suppresses the influence of external currents and magnetic fields much more effectively.

Manuscript received August 9, 2016; revised October 18, 2016; accepted October 20, 2016. Date of publication October 25, 2016; date of current version March 16, 2017. Corresponding author: P. Ripka (e-mail: ripka@fel.cvut.cz).

Color versions of one or more of the figures in this paper are available online at <http://ieeexplore.ieee.org>.

Digital Object Identifier 10.1109/TMAG.2016.2620959

0018-9464 © 2016 IEEE. Personal use is permitted, but republication/redistribution requires IEEE permission. See http://www.ieee.org/publications_standards/publications/rights/index.html for more information.

The busbar sensor with a hole has the advantage over a sensor on the surface that the frequency dependence is lower. With a cylindrical hole, the frequency error is 14%, while for amphitheater geometry, the error was reduced to 9% [10]. Problems with amphitheater geometry were the large sensitivity to a geometrical mismatch, and increased manufacturing complexity.

This paper presents the new shape of the busbar and the optimization of the sensor position, which led to $\pm 3\%$ frequency error from dc to 1 kHz. Sensitivity to temperature dilatation and geometrical mismatch is also analyzed.

All electromagnetic field simulations were performed in Ansys Maxwell using a 3-D eddy current solver and adaptive meshing. The final solution uses approximately 600k tetrahedra. Effects of heating were examined by co-simulation between Maxwell 3-D (to calculate losses) and Ansys Mechanical (to get temperature distribution).

II. SENSOR DESIGN

A. Differential Fluxgate Sensor

For the current sensor, we use the integrated fluxgate DRV425, manufactured by Texas Instruments [11]. The main advantage of this sensor is its low offset drift with temperature 5 nT/°C compared with AMR (20 nT/°C) and the Hall sensor (5 μ T/°C).

Two fluxgate sensors were connected in a differential mode. Each sensor is individually feedback compensated, and we process the difference between the compensation currents. All the necessary electronics is integrated inside the sensor chips. The only external components are the sensing resistors. The compensation current flowing through the microfabricated solenoid compensation coil is in the range of 10 mA for the measured current of 1000 A. This high ratio cannot be achieved by a fluxgate-based ac/dc current transformer, due to the high parasitic capacitance of the secondary winding [12].

The two fluxgate sensors are mounted on the opposite sides of the printed circuit board. The effective distance between the sensors was 2.7 mm.

B. Busbar Geometry

Fig. 1 shows the electric current distribution inside the 60 mm \times 10 mm conductor and the magnetic field in the free air for a central cylindrical hole 19 mm in diameter. While

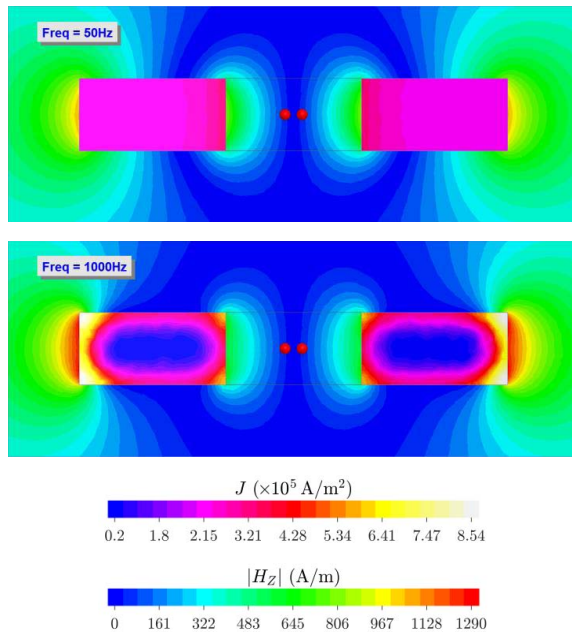


Fig. 1. Electric current distribution inside the 60 mm × 10 mm conductor and the magnetic field in the free air for a central cylindrical hole 19 mm in diameter. The FEM simulation was performed for $f = 50$ Hz and 1 kHz. Red dots: sensor positions.

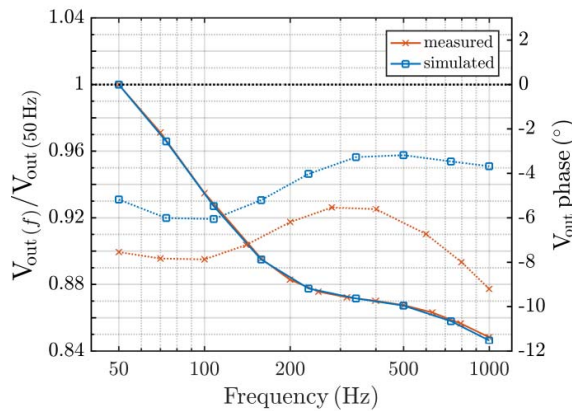


Fig. 2. Frequency dependence of the busbar current sensor with the traditional symmetrical design (measurement and 3-D simulation). Full line: amplitude characteristics. Dotted line: phase characteristics.

the current is very homogeneous for a frequency of 50 Hz, at 1 kHz, the effect of an eddy current increased the current density at the external corners by a factor of 1.5. As these regions are further away from the sensors, this results in a decreased sensitivity of the sensor.

The frequency dependence as a result of 3-D simulation and measurement is shown in Fig. 2 for a differential magnetic sensor having a gradiometric distance of 2.7 mm. The frequency error of 16% at 1 kHz should be compared with the 32% error of the transducer based on Hall sensors on the surface of the busbar [5]. The phase error at 1 kHz is 10°,

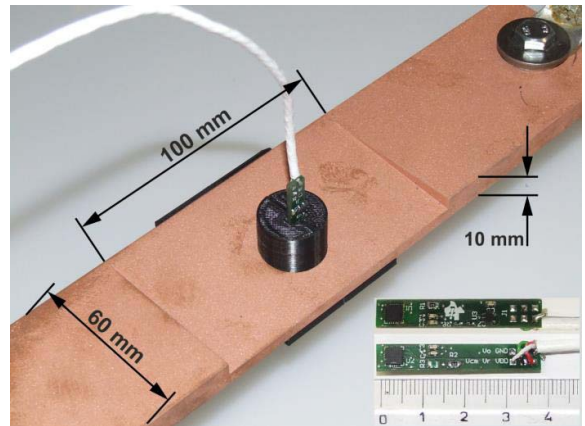


Fig. 3. New busbar sensor with a wedge-shaped profile. The circular hole is located asymmetrically and the position of the sensors in the hole is also asymmetrical.

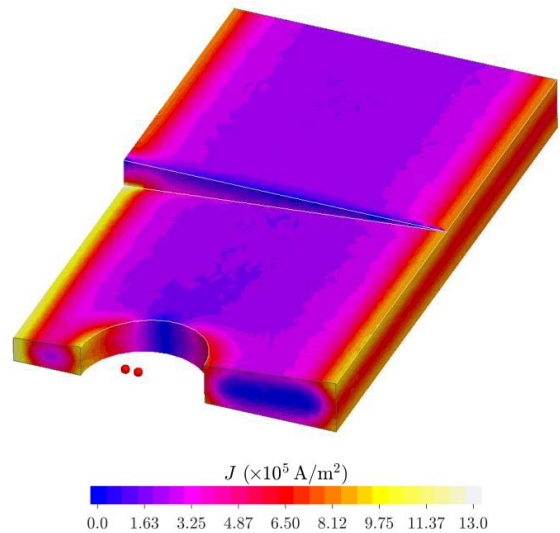


Fig. 4. Electric current distribution in the new busbar sensor at 1 kHz. Red dots: sensor positions.

which is too large for this sensor to be used for power and energy measurements. We attribute the difference between the simulated and measured phase characteristics to error in simulation, as we observed negligible phase error of the sensor itself at low frequencies.

In order to better compensate the frequency dependence, we analyzed a range of alternative geometries. Based on 3-D Finite-Element Modelling (FEM) simulations, we selected an asymmetric design with a wedge bar. The new sensor is shown in Fig. 3. The dimensions were selected, so that the sensitivity is approximately 1 mV/A. As the fluxgate sensitivity is 488 mV/mT (12.2 mA/mT with a 10 Ω sensing resistor and an instrumentation amplifier with gain of 4), the corresponding field factor is 500 A/mT.

Fig. 4 shows the 3-D FEM simulation of the current distribution of the new asymmetric design. Because of the

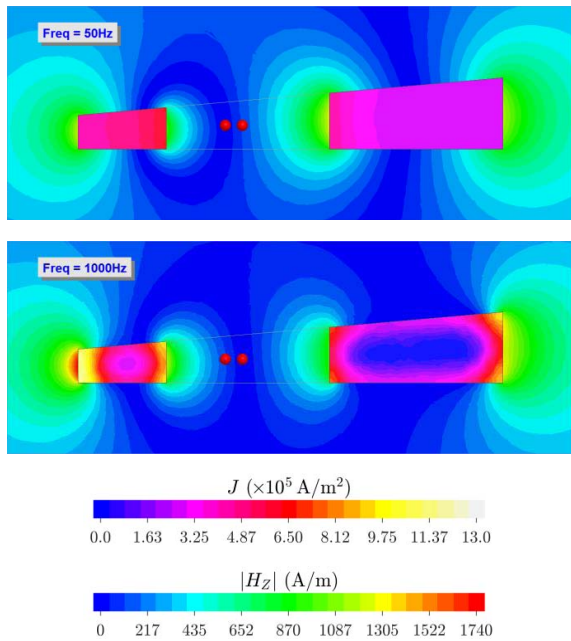


Fig. 5. Current and field distribution in the new busbar sensor with a wedge-shaped profile. 3-D FEM simulation at 50 Hz and 1 kHz. Red dots: sensor position.

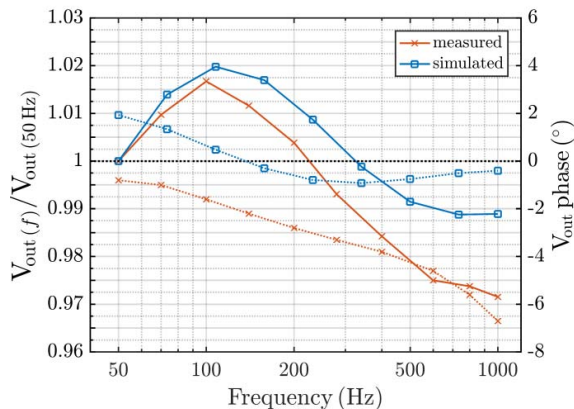


Fig. 6. Frequency dependence of the busbar current sensor with the new asymmetrical design (measurement and 3-D simulation). Full line: amplitude characteristics. Dotted line: phase characteristics.

modified shape, the current is even more redistributed due to the eddy currents. Fig. 5 shows the current and magnetic field distribution in the central plane, where both magnetic sensors are located. It is clear that the field gradient is more frequency dependent than the previous geometry. We solved the task of selecting the position of the differential sensor pair to minimize the frequency dependence while keeping a reasonable conversion factor and low sensitivity to misalignment. This optimization was made by parametric FEM simulation. The selected sensor locations are marked by red dots.

The measured frequency characteristics shown in Fig. 6 confirmed the expectations from the simulations. The measured

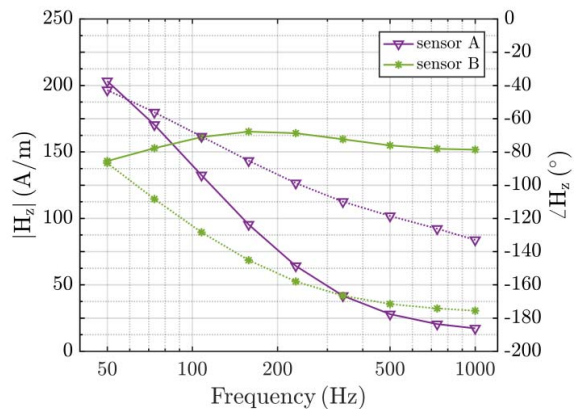


Fig. 7. Simulated frequency dependence of individual sensors.

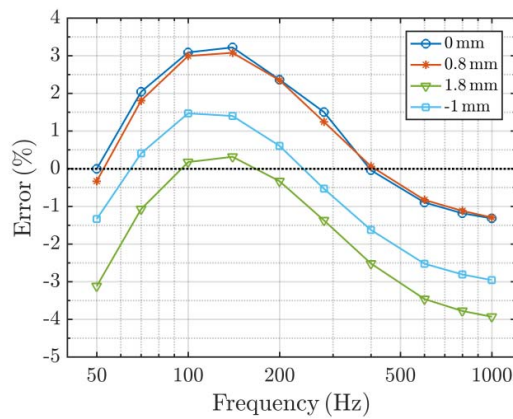


Fig. 8. Measured frequency characteristics for several values of the vertical position of the sensors in the hole. The graph shows deviation from sensitivity at 50 Hz.

frequency error up to 1 kHz is below 3%. The phase error was only slightly reduced to 8° at 1 kHz, but up to 600 Hz, the phase characteristics is linear.

Fig. 7 shows the principle of the compensation mechanism: the frequency dependence of the individual sensors is high. The differences are caused by different effect of eddy currents in each point. In this way, the frequency dependence of the differential signal is dramatically decreased. If we vectorially subtract voltages for A and B sensors, we obtain theoretical characteristics shown in Fig. 6.

The compensation technique based on the subtraction of two similar variables raises the question of the stability of this compensation in real conditions. We therefore studied the stability of the sensor with temperature and geometrical tolerances.

III. SENSOR STABILITY AND RESISTANCE TO EXTERNAL CURRENTS

Fig. 8 shows how the frequency characteristics change with vertical sensor misalignment. It is clear that the changes in the shape of the frequency characteristics are negligible, but the

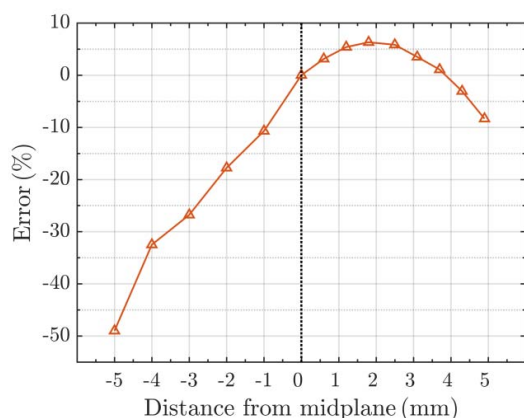


Fig. 9. Dependence of the sensitivity on the vertical position of the sensors in the hole. The graph shows deviation from sensitivity at the central point.

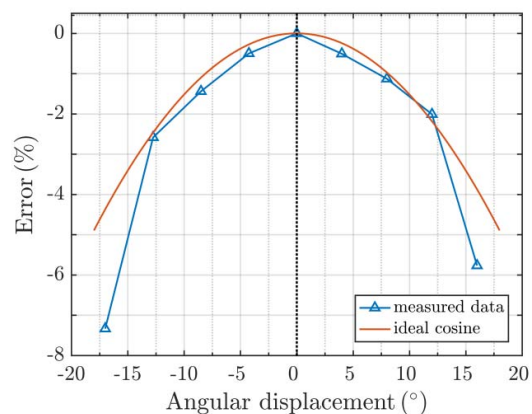


Fig. 10. Sensitivity error caused by rotational displacement of the sensor. The theoretical error caused by cosine dependence is shown for comparison.

sensitivity depends on the vertical position of the sensor, as shown in Fig. 9. The maximum sensitivity point is not in the central plane, as for a simple busbar sensor, but 2 mm above. In this optimum location, the sensitivity to position error is also minimized.

Fig. 10 shows the sensitivity to rotational displacement of the differential sensor. It is clear that the characteristics differ significantly from the cosine shape. By linear approximation, we may estimate that 0.2° angular displacement caused by temperature cycling would cause only 0.025% error, which is negligible in comparison with the 0.1% linearity error of the device.

We also examined the effect of self-heating by FEM simulations. At a maximum current of 1000 A, the temperature of the current bar is 50°C . The sensitivity change caused by temperature effects is 1%. In comparison with this, the sensitivity change with the temperature of the fluxgate sensor itself is only $7\text{ ppm}/^\circ\text{C}$.

The dc offset stability depends mainly on the parameters of the fluxgate sensor. The specified maximum drift of $5\text{ nT}/^\circ\text{C}$

would correspond to $2.5\text{ mA}/^\circ\text{C}$. The dc current resolution is limited to 10 mA, as the sensor noise power spectrum density is $2\text{ mA}/\sqrt{\text{Hz}}$ at 1 Hz.

With a sensitivity of 500 A/mT , the calculated effect of an external 1000 A current at a distance of 15 cm is $3.4\ \mu\text{T}$, so the error is only 0.17%. We measured the influence of the external current in the real busbar and found a very similar error of 0.15%.

IV. CONCLUSION

The busbar fluxgate current sensor presented here has very small ferromagnetic cores inside the two integrated feedback-compensated fluxgate sensors. This keeps the power consumption of our device below 100 mW, even for the maximum measured current of 1000 A. This is much lower than the power consumption of around 15 W, even when using very efficient electronics, for another class of feedback-compensated fluxgate current sensors with large cores around the measured current conductor [13].

In addition to the advantages of the yokeless busbar current sensor, which are its small size, lightweight, and low power consumption, we also should mention its disadvantages. The sensor needs to be inserted into the measured circuit, which is not practical for ambulatory measurements. Compared with that, the yoke can be made openable as clamps. A yoke is also believed to better suppress the influence of external fields, but we have shown that the small distance of our differential sensor pair performs similarly, as the error for an external current at a distance of 15 cm is only 0.15%.

The new shape of the busbar sensor improved the frequency characteristics: the achieved error was $\pm 3\%$ in amplitude and 8° in phase at 1 kHz. The sensor linearity is 0.1%, in comparison with 1% in [9]. With 1000 A range, the sensor has 10 mA resolution and $2.5\text{ mA}/^\circ\text{C}$ maximum dc drift. The temperature stability is, therefore, four times better than when using an AMR sensor and 1000 times better than when using Hall sensors. The external current in a 9 cm distant busbar is suppressed by a factor of 66.

ACKNOWLEDGMENT

The authors would like to thank A. Chirtsov, who performed some of the measurements. A. Chirtsov and V. Grim received student support from Texas Instruments, which also supplied the sensor boards.

REFERENCES

- [1] P. Ripka, "Electric current sensors: A review," *Meas. Sci. Technol.*, vol. 21, no. 11, pp. 1–23, Sep. 2010.
- [2] G. Velasco-Quesada, M. Roman-Lumbreras, A. Conesa-Roca, and F. Jerez, "Design of a low-consumption fluxgate transducer for high-current measurement applications," *IEEE Sensors J.*, vol. 11, no. 2, pp. 280–287, Feb. 2011.
- [3] X. Yang, Y. Li, W. Zheng, W. Guo, Y. Wang, and R. Yan, "Design and realization of a novel compact fluxgate current sensor," *IEEE Trans. Magn.*, vol. 51, no. 3, pp. 1–4, Mar. 2015.
- [4] BBM, *Current Sensors Manufactured by Senis, Catalogue*, accessed Nov. 4, 2016. [Online]. Available: <http://www.senis.ch/>
- [5] M. Blagojević, U. Jovanović, I. Jovanović, D. Mančić, and R. S. Popović, "Realization and optimization of bus bar current transducers based on Hall effect sensors," *Meas. Sci. Technol.*, vol. 27, no. 6, p. 065102, 2016.

- [6] K.-L. Chen and N. Chen, "A new method for power current measurement using a coreless Hall effect current transformer," *IEEE Trans. Instrum. Meas.*, vol. 60, no. 1, pp. 158–169, Jan. 2011.
- [7] F. Koga, T. Tadatsu, J. Inoue, and I. Sasada, "A new type of current sensor based on inverse magnetostriction for large current detection," *IEEE Trans. Magn.*, vol. 45, no. 10, pp. 4506–4509, Oct. 2009.
- [8] M. F. Snoeij, V. Schaffer, S. Udayashankar, and M. V. Ivanov, "Integrated fluxgate magnetometer for use in isolated current sensing," *IEEE J. Solid-State Circuits*, vol. 51, no. 7, pp. 1684–1694, Jul. 2016.
- [9] Z. Zhenhong, O. Syuji, A. Osamu, and K. Hideto, "Development of the highly precise magnetic current sensor module of ± 300 A utilizing AMR element with bias-magnet," *IEEE Trans. Magn.*, vol. 51, no. 1, pp. 1–5, Jan. 2015.
- [10] P. Ripka, M. Přebil, V. Petrucha, V. Grim, and K. Draxler, "A Fluxgate Current Sensor With an Amphitheater Busbar," *IEEE Trans. Magn.*, vol. 52, no. 7, Jul. 2016, Art. no. 4002004.
- [11] *DRV425 Fluxgate Magnetic-Field Sensor, Texas Instruments Datasheet*, accessed Nov. 4, 2016. [Online]. Available: <http://www.ti.com/product/DRV425/datasheet>
- [12] P. Ripka, K. Draxler, and R. Styblikova, "AC/DC current transformer with single winding," *IEEE Trans. Magn.*, vol. 50, no. 4, Apr. 2014, Art. no. 8400504.
- [13] G. Velasco-Quesada, M. Román-Lumbreras, R. Pérez-Delgado, and A. Conesa-Roca, "Class H power amplifier for power saving in fluxgate current transducers," *IEEE Sensors J.*, vol. 16, no. 8, pp. 2322–2330, Apr. 2016.

6.5 A 3-Phase Current Transducer Based on Microfluxgate Sensors

After experimenting with busbar current sensors, where there is only one conductor and an infinitely distant return path, next step was to examine the case of several conductors existing in close vicinity, as is the case with three-phase overhead power lines. A poster was presented at Eurosensors 2018 conference, which was later extended into this journal paper.

The geometry of thin, parallel wires is easily modeled analytically, without the need for finite element simulations. The solution to the inverse problem of extracting the currents and external field is found by solving a small matrix equation. The estimate of external field is found in polynomial form of arbitrarily high order, given by the number of sensors, but in practice it does not make sense to assume more than third order polynomial due to inaccuracies introduced by geometrical and electrical tolerances.

The presented method of using the whole available dataset at once is a significant improvement over using independent sensors on each phase conductor.

My responsibility was the theoretical analysis and modeling, drawing figures and performing measurements (together with Mr. Chirtsov).

Contents lists available at [ScienceDirect](https://www.sciencedirect.com)

Measurement

journal homepage: www.elsevier.com/locate/measurement

A 3-phase current transducer based on microfluxgate sensors

Pavel Ripka*, Václav Grim, Andrey Chirtsov

Czech Technical University in Prague, Faculty of Electrical Engineering, Technicka, 166 27 Praha 6, Czech Republic



ARTICLE INFO

Article history:

Received 29 April 2019
 Received in revised form 11 June 2019
 Accepted 14 June 2019
 Available online 19 June 2019

Keywords:

Current measurement
 Fluxgate
 Power distribution

ABSTRACT

Novel 3-phase DC/AC current transducer for 3-phase current lines is based on 8 integrated fluxgate sensors. Using full information from each sensor rather than gradiometric pairs, we suppress crosstalk between individual phases and external magnetic fields up to the 4th order gradients. The suppression of external currents at a distance of 1 m is 90 dB. The main advantage of the used microfluxgates is excellent temperature stability allowing operation outside the laboratory: the achieved temperature coefficient of the sensitivity is 50 ppm/K, and the offset stability is 1 mA/K. These values are 20-times better than temperature stability achievable with current transducers sensors based on Hall sensors and magnetoresistors.

© 2019 Elsevier Ltd. All rights reserved.

1. Introduction

Fast and precise control of modern electric grids requires to measure voltage and current values at multiple points [1]. This requires to deploy large number of new sensors on existing power lines and stations. The ability to measure the current DC component is required, as DC electric current may saturate current measurement transformers, leading to large measurement errors and possible failures. The DC current component is induced from geomagnetic variations and is also caused by transients, by transformerless inverters, and by induction from current changes in DC power lines [2].

In order to reduce the installation costs, ideal sensors are light so that they do not need their own supporting structure. The current sensor that is most widely used in electric grids is the current transformer. Some weight reduction can be achieved by using nanocrystalline alloys with high saturation magnetization and high permeability [3]. The cores can be cut to allow installation without breaking the measured conductor [4]. However, current transformers are still heavy, and the costs for installing them on the existing lines are high. Traditional current transformers also cannot measure the DC component, although efforts have been made to measure it using the fluxgate principle [5]. DC currents can be measured by magnetic sensors in the airgap of the ferromagnetic yoke (core) around the measured conductor [6]. This is also a heavy device with high installation costs.

Rogowski coils are lightweight and if made flexible they can be easily mounted on existing conductors, but they measure only AC or pulse currents since they are based on the induction law [7]. The B-Dot sensors work on the same principle, using flat coils made of multilayer PCB [8]. These sensors have wide bandwidth, but they are suitable only for measuring large AC currents, because the low number of coil turns limits their sensitivity at low frequency. Fiber optic current sensors based on Faraday effect are temperature sensitive and they have large noise [9].

Yokeless current transducers using magnetic sensor arrays have best potential for this application. Gradiometric sensors suppress the influence of homogeneous external fields. They can be used if the unmeasured external currents are far enough away for their gradient to be negligible [10,11]. Increasing the number of sensors inside the busbar can reduce the crosstalk from external currents [12].

Circular sensor arrays are based on Ampère's law. If the number of sensors is large, the sum of their output approximates the line integral and the reading is independent on external magnetic fields. To achieve this, 6 or 8 sensors are required for each phase [13–17]. Another advantage of these multisensor arrays is that they are immune to position changes of the measured conductor [18]. Sensors in the array may be divided into gradiometric pairs. Using three gradiometric pairs, error of 0.3% was achieved for external currents in the distance of 30 cm [19].

Hall sensors, Lorenz-force sensors, Anisotropic magnetoresistors (AMR) and Giant magnetoresistors (GMR), and also microfluxgate sensors, are magnetic sensors that are suitable for yokeless current transducers. Hall sensors are used in [10], and in [14]. Thanks to their range up to 2 T, they can measure very high currents in the kA range. However, they suffer from poor DC stability

* Corresponding author.

E-mail addresses: ripka@fel.cvut.cz (P. Ripka), vaclav.grim@fel.cvut.cz (V. Grim), chirtand@fel.cvut.cz (A. Chirtsov).

and, in addition, their sensitivity is temperature-dependent. AMR sensors were used in [16,20,21]. AMR sensors have a limited dynamic range: low-noise sensors can measure fields only up to 0.2 mT [22]. GMR sensors still suffer from limited linearity. TMR sensors were used in [19]. They may have 1% linearity and hysteresis in the linear range of 0.5 mT, and their frequency response is up to MHz range [23], but their weak point is poor DC stability. MEMS sensors based on Lorentz force sensors and also sensors based on the force effect on a permanent magnet [24] have high linearity and a very high field range, but they still have high noise [25]. High noise and poor DC stability are also attributes of magnetostriction sensors [26] and sensor based on shape memory alloy [27]. Microfluxgate sensors are used in [11,12,15]. They have 2 mT range, a dynamic range similar to that of AMR sensors, but they have excellent temperature stability of both offset and sensitivity. Other sensor types such as magnetoelectric [28] or force-based [29] have been also used for current transducers, but without achieving competitive parameters.

The application of a yokeless current transducer for measurements in a 3-phase network was suggested only recently, in [21]. The authors use 6 Anisotropic Magnetoresistance (AMR) sensors in 3 gradiometric pairs, and each pair measures the phase current from a close distance of 30 mm. Although this simple solution suppresses the external homogeneous field, it does not suppress the field gradients, which are not negligible for close external currents. The simple gradiometric configuration also suffers from crosstalk between the phases.

The first version of our improved 3-phase transducer, using 6 sensors, was described in [30]. Our application also requires the DC current component to be measured. We therefore decided to use microfluxgate sensors, which have better DC offset stability than AMR sensors. Instead of calculating 3 field gradients, we performed more complex processing of the sensor outputs. As a result, the suppression of external currents was improved 15-fold in comparison with [21].

In this paper, we present an improved version of our design, using 8 sensors. We will show both theoretically and experimentally that much better suppression can be achieved with the new hardware. However, individual sensor calibration is necessary, and also corrections for sensor mismatch.

The paper is organized as follows: In Section 2, we describe several geometrical configurations of the sensors measuring the currents in the 3-phase power line, and we define the calculation methods for evaluating the measured currents. In Section 3, we describe a model of three-phase power lines and associated instrumentation used for testing. The calibration method is described in Section 4. In Section 5, the theoretical results for crosstalk are compared with the measurements. Sensor noise and temperature stability are discussed in Section 6.

2. Description of measurement methods

We assume a simple linear three-phase overhead power line with the distance between conductors $d = 30$ cm. For the measurement we use an array of lightweight magnetic sensors mounted in plane perpendicular to the conductors.

2.1. Asymmetrical gradient method

This configuration was described in [21] and also used in [19]. It uses pairs of close sensors (Fig. 1a) to calculate the gradients (or more precisely the differences) $H_2 - H_1$, $H_4 - H_3$, and $H_6 - H_5$, which are then used to calculate the phase currents values, while the external fields are partly suppressed.

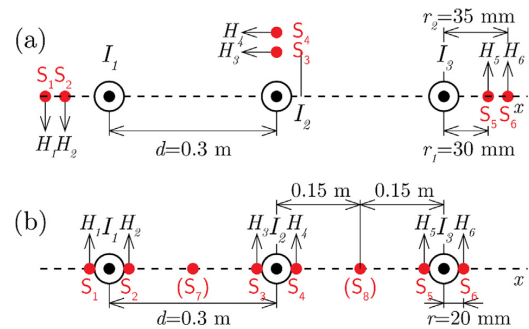


Fig. 1. Placement of the sensors (a) for the asymmetrical gradient method [21], and (b) for all other methods (dimensions not to scale).

If only I_1 current is present, then $H_1 = I_1/2\pi r_2$, $H_2 = I_1/2\pi r_1$ and we can write

$$I_{1true} = 2\pi \frac{(H_2 - H_1)}{\left(\frac{1}{r_1} - \frac{1}{r_2}\right)} \quad (1)$$

If only I_2 is present, then $H_{1false} = I_2/2\pi(r_1 + d)$ and $H_{2false} = I_2/2\pi(r_2 + d)$.

Now we can evaluate the crosstalk as

$$\frac{I_{false}}{I_{true}} = \frac{\Delta H_{false}}{\Delta H_{true}} = \frac{\frac{1}{d+r_2} - \frac{1}{d+r_1}}{\frac{1}{r_2} - \frac{1}{r_1}} \quad (2)$$

where true values are caused by current I_1 , and false field and current readings are caused by current I_2 of the same size.

For the dimensions from Fig. 1a, the crosstalk ratio is 0.95% or -40 dB. The suppression of external currents can be calculated using (2), if we replace d by the distance of the external current to the respective conductor. The results are plotted in Fig. 6.

The disadvantage of this method lies in the loss in sensitivity caused by the fact that in (2) we subtract two similar values, H_1 and H_2 .

2.2. Symmetrical gradient method

This configuration uses two sensors at each phase wire, located symmetrically at each side of the measured conductor at a distance $r = 20$ mm (as shown in Fig. 1b). Differential method again suppresses an external homogeneous field component (such as the Earth's field).

If only I_1 current is present, then

$$H_1 = I_1/2\pi r, \quad H_2 = -I_1/2\pi r, \quad I_{1true} = (H_1 - H_2) \pi r,$$

If only I_2 is present, then $H_{1false} = I_2/2\pi(d + r)$ and $H_{2false} = I_2/2\pi(d - r)$ and for the crosstalk ratio from the nearest phase we can write

$$\frac{I_{false}}{I_{true}} = \frac{r}{d+r} - \frac{r}{d-r} \quad (3)$$

For the dimensions from Fig. 1, the crosstalk ratio from the nearest phase is 0.9%, i.e. similar to that for the asymmetrical gradient method. The advantage is that the sensitivity is higher than when the first method is used, resulting in smaller error and less noise. This is due to the fact that H_1 and H_2 have opposite signs. However, the larger sensor distance results in lower immunity to field gradients.

The suppression of external currents can be calculated using (3), if we replace d by the distance of the external current from the respective conductor. The results are again plotted in Fig. 6.

2.3. Method with polynomial estimation

The last method corrects the disadvantages of both previous configurations. We use the same arrangement as is presented in Fig. 1b. Instead of calculating the field gradients, we utilize the output of all sensors in a more complex way.

From the readings of six sensors we can calculate three unknown phase currents and the position and amplitude of one external current. If the currents are DC, we have 6 independent equations, and for AC current we have 6 equations for instantaneous values, or for a sinewave waveform we have 6 equations for amplitude and 6 for phase.

However, we cannot always assume that there will be only a single external current, and we should consider the effect of external fields of other origin, such as ferromagnetic objects, which can also distort the field from an external current. We therefore decided to find a universal solution that nulls the external field in the y-direction and its gradients up to the second order. Fields in the x-direction do not affect the sensors at all. We therefore suppose that the field at each sensor consists of three contributions from the phase currents and a contribution from the external field H_{ext}

$$H_n = \frac{I_1}{2\pi(S_{nx} - W_{1x})} + \frac{I_2}{2\pi(S_{nx} - W_{2x})} + \frac{I_3}{2\pi(S_{nx} - W_{3x})} + H_{ext}(x, y, t) \quad (4)$$

where H_n is field intensity at sensor n , I_1 – I_3 are (unknown) phase currents, S_{nx} is the x-coordinate of sensor n , and W_{nx} is the x-coordinate of each phase conductor. The solution does not depend on the placement of the origin of the coordinate system; here $W_{3x} = 0$ was assumed.

External field H_{ext} may have any spatial distribution, which we approximate with a fourth degree polynomial:

$$H_{ext}(x) \approx H_{E0} + H_{E1}x + H_{E2}x^2 + H_{E3}x^3 + H_{E4}x^4 \quad (5)$$

Six sensors give suppression up to 2nd order gradient [30]. In order to null response up to 4th order gradient, the number sensors should be increased to 8. Two additional sensors, S_7 and S_8 , are placed halfway between the phase conductors (Fig. 1b).

Eight sensors produce eight different equations [30]. A linear system is formed:

$$\begin{pmatrix} H_1 \\ H_2 \\ H_3 \\ H_4 \\ H_5 \\ H_6 \\ H_7 \\ H_8 \end{pmatrix} = \begin{pmatrix} \frac{1}{2\pi(S_{1x}-W_{1x})} & \frac{1}{2\pi(S_{1x}-W_{2x})} & \frac{1}{2\pi(S_{1x}-W_{3x})} & 1 & S_{1x} & S_{1x}^2 & S_{1x}^3 & S_{1x}^4 \\ \frac{1}{2\pi(S_{2x}-W_{1x})} & \frac{1}{2\pi(S_{2x}-W_{2x})} & \frac{1}{2\pi(S_{2x}-W_{3x})} & 1 & S_{2x} & S_{2x}^2 & S_{2x}^3 & S_{2x}^4 \\ \frac{1}{2\pi(S_{3x}-W_{1x})} & \frac{1}{2\pi(S_{3x}-W_{2x})} & \frac{1}{2\pi(S_{3x}-W_{3x})} & 1 & S_{3x} & S_{3x}^2 & S_{3x}^3 & S_{3x}^4 \\ \frac{1}{2\pi(S_{4x}-W_{1x})} & \frac{1}{2\pi(S_{4x}-W_{2x})} & \frac{1}{2\pi(S_{4x}-W_{3x})} & 1 & S_{4x} & S_{4x}^2 & S_{4x}^3 & S_{4x}^4 \\ \frac{1}{2\pi(S_{5x}-W_{1x})} & \frac{1}{2\pi(S_{5x}-W_{2x})} & \frac{1}{2\pi(S_{5x}-W_{3x})} & 1 & S_{5x} & S_{5x}^2 & S_{5x}^3 & S_{5x}^4 \\ \frac{1}{2\pi(S_{6x}-W_{1x})} & \frac{1}{2\pi(S_{6x}-W_{2x})} & \frac{1}{2\pi(S_{6x}-W_{3x})} & 1 & S_{6x} & S_{6x}^2 & S_{6x}^3 & S_{6x}^4 \\ \frac{1}{2\pi(S_{7x}-W_{1x})} & \frac{1}{2\pi(S_{7x}-W_{2x})} & \frac{1}{2\pi(S_{7x}-W_{3x})} & 1 & S_{7x} & S_{7x}^2 & S_{7x}^3 & S_{7x}^4 \\ \frac{1}{2\pi(S_{8x}-W_{1x})} & \frac{1}{2\pi(S_{8x}-W_{2x})} & \frac{1}{2\pi(S_{8x}-W_{3x})} & 1 & S_{8x} & S_{8x}^2 & S_{8x}^3 & S_{8x}^4 \end{pmatrix} \cdot \begin{pmatrix} I_1 \\ I_2 \\ I_3 \\ H_{E0} \\ H_{E1} \\ H_{E2} \\ H_{E3} \\ H_{E4} \end{pmatrix} \quad (6)$$

Solving this matrix equation (using the default Matlab solver) provides all currents and a 1-D estimate of the external field (homogeneous component and first four gradients) at the same time.

Ideally, the crosstalk from the other two phases is zero.

Table 1
Sensitivity analysis of polynomial estimation method, external conductor I_4 at 100 cm.

Input quantity ξ	Sensitivity ((% I_3)/(% ξ))
Wire-to-wire distance	0.05
Wire-to-sensor distance	0.77
Sensor gain variations	0.78

The suppression of the external currents depends on the distance of the current in a complex way, and cannot be expressed analytically. We have calculated the suppression numerically for each distance, and the results are plotted in Fig. 4, together with the values calculated for the two gradiometric methods. It is clear that when using only 6 sensors the improvement over the asymmetrical gradiometric method is only slight: by a factor of 15 for very short distances and by a factor of 30 for a distance of 1 m. The reason for this is that the field from the external conductor is rich in higher-order gradients, which are not nulled. Using 8 sensors shows best theoretical suppression.

In order to test how our method is robust against uncertainty in the position of the sensors and their sensitivity, we have made sensitivity analysis using Monte Carlo method. Position or gain of each sensor was varied randomly around its nominal value. Perturbations followed a normal distribution with small amplitude ($\sigma = 0.01\%$ of nominal value). Sensor readings at corresponding locations were calculated and from them the value of I_3 was deduced. No correlation among dimensions or gains was assumed, i.e. each variable subject to perturbation is modified by a newly generated random number. Simulation was repeated 100 000 times. Sensitivity coefficients shown in the following table are ratios of normalized standard deviations.

Table 1 shows that the sensitivities calculated for I_3 (which is the measured current nearest to external current I_4) are less than 1. The sensitivity to the sensor noise is the same as to the sensor gain variation, because the measured noise spectrum is close to AWGN approximation.

3. Measurement setup

The measurements were performed with 5 A_{RMS} phase currents supplied from a 50 Hz three-phase transformer. The 4.4 m long

straight power line was terminated by resistors. Sensor boards were mounted on wooden support (Fig. 2). TI DRV425 integrated microfluxgate sensors were used as vectorial field sensors (Fig. 3). 5 A external current was supplied from another transformer. The true current values were measured using 0.05% precise

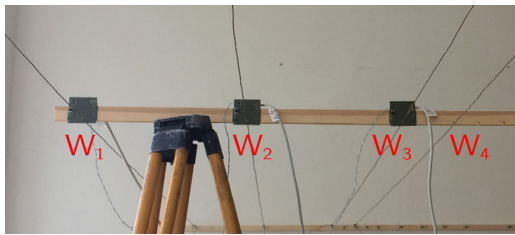


Fig. 2. A photo of the measurement setup with W_4 at a distance of 10 cm from W_3 [30].

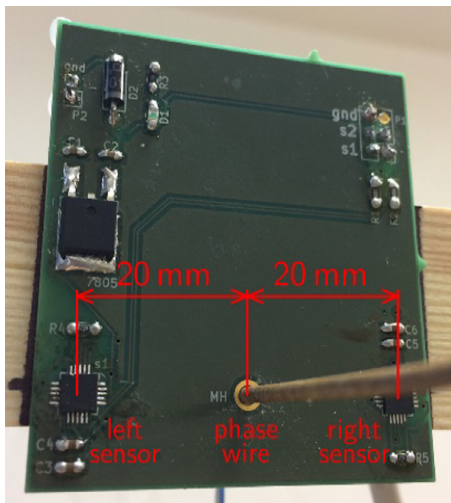


Fig. 3. Detail of sensor PCB with a pair of DRV425s [30].

shunt resistors. The voltage drops across the shunts as well as sensor outputs were measured by NI 6211 16-bit A/D converter USB module with 5000 samples/s rate. All collected data was processed offline in Matlab and averaged over 10 periods.

4. Calibration

The sensitivity of each sensor was calibrated in Helmholtz coils using a simple system controlled by LabVIEW. DC current with alternating polarity was used to eliminate the effects of the geomagnetic field. Using this procedure, we are able to separate the influence of sensitivity errors and geometrical errors. Table 2 shows the sensitivity correction coefficients that were obtained.

Sensor calibration was also performed by passing a 5 A current successively through individual phase conductors. The results were

Table 2 Results of the sensitivity calibration.

Sensor #	Correction factor	Sensitivity deviation (%)
1	0.974748	-2.52
2	0.974569	-2.54
3	0.97903	-2.09
4	0.97062	-2.94
5	1.0605	6.05
6	1.03849	3.85
7	0.98495	-1.51
8	0.988595	-1.14

very similar, indicating that the sensitivity mismatch is the dominating factor, and the geometrical errors are negligible.

5. Calculated and measured results

A comparison of the calculated results shows that our new polynomial estimation method has an advantage over both gradient methods (described in Sections 2.1 and 2.2.). Fig. 4 summarizes the calculated theoretical rejection of the external current in the x-direction. At greater distances, increasing the number of sensors from 6 to 8 significantly increases the rejection. For the external current at a distance of 1 m and using a polynomial method with 8 sensors, the crosstalk from the external currents is theoretically 0.001, compared with 0.1 which can be achieved by the asymmetrical gradient configuration suggested in [21].

We also analyzed the influence of the angular position of the external current: we observe that the maximum error is for external currents in the x- and y-directions. This is clear from Fig. 5, which shows the rejection of the external current at a distance of 50 cm, as a function of its angular position. Zero error is reached for the external current in the 45° direction.

Fig. 6 shows the measured rejection ratio of the external current as a function of distance. While for 6 sensors the measured values

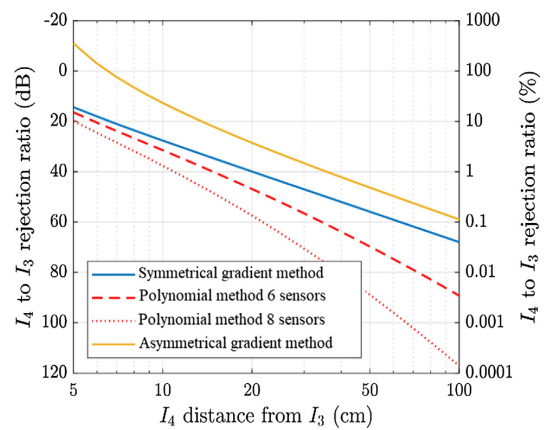


Fig. 4. Suppression of external current in the x direction as a function of its distance: A theoretical comparison of various current measurement methods.

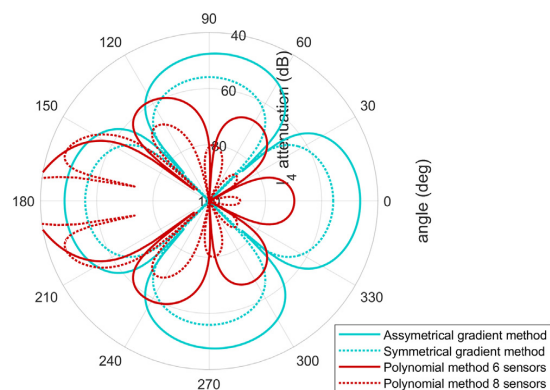


Fig. 5. Suppression of external current at a distance of 50 cm as a function of the angular position (calculated values).

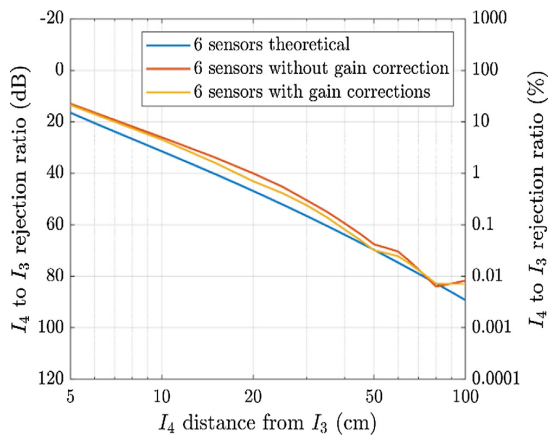


Fig. 6. Measured suppression of external current in the x direction as a function of its distance for setup with 6 sensors, with and without gain corrections.

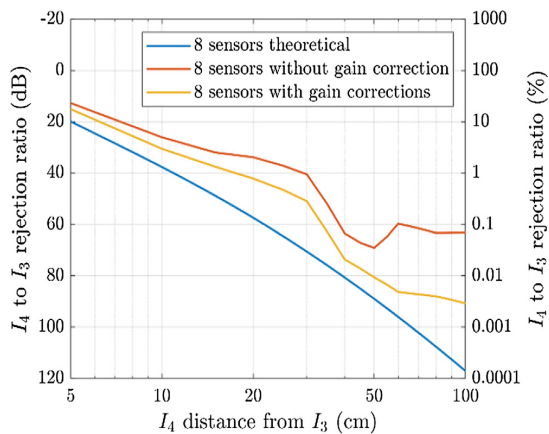


Fig. 7. Measured suppression of external current in the x direction as a function of its distance for setup with 8 sensors, with and without corrections.

correspond well with the simulations in Fig. 6, the rejection ratio of the 8-sensor transducer is smaller than expected. After a detailed analysis, we found that an 8-sensor transducer is much more sensitive to the mismatch of sensor parameters. We calibrated individual sensors, and after a correction had been made for their sensitivities, the rejection ratio improved significantly, as shown in Fig. 7. The measured rejection at a distance of 1 m was 80 dB (crosstalk 0.003%), i.e. a 300-fold improvement in comparison with [21].

6. Noise, temperature stability and linearity

The application of our sensors is the measurement of geomagnetically induced currents in long power lines. These currents are DC with rate of change in minutes. Using traditional DC current sensors in outdoor environment resulted in unacceptable temperature drifts: with AMR sensors the transducer offset drift was 50 mA/K and the sensitivity temperature coefficient was 0.3%/K. By replacing AMR by microfluxgate sensor, these values were improved to 1 mA/K and 50 ppm/K. These values were calculated from the datasheet of the manufacturer and verified by measurement at 3 temperatures.

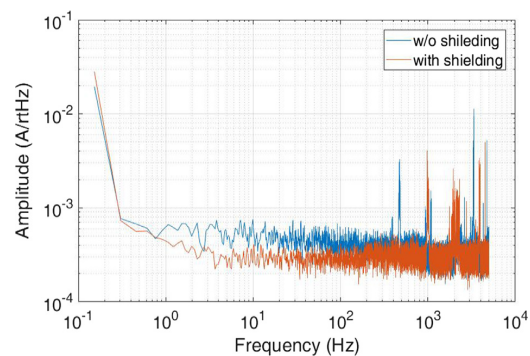


Fig. 8. Measured noise spectrum of the complete transducer inside the shielding and without shielding.

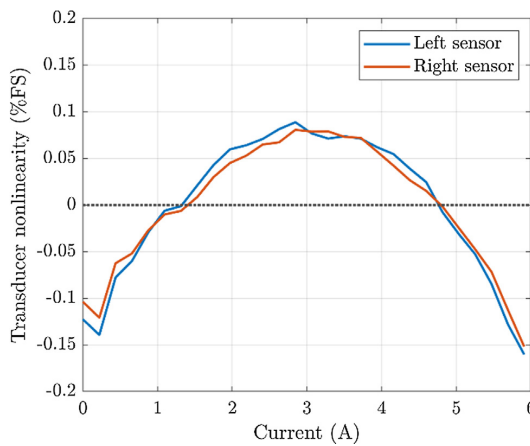


Fig. 9. Linearity of the complete transducer.

Sensor noise was measured with the use of two different methods: the noise of the individual sensor was measured using SR770 spectrum analyzer. The achieved noise power density was 2.5 nT/√Hz at 1 Hz, corresponding to ideal noise level of 0.25 mA/√Hz at 1 Hz. The noise of the complete transducer was measured using Matlab FFT calculation from sampled data (Fig. 8). Measurements were performed at room temperature (20–25 °C). In both cases, a three-layer permalloy shield was used. The noise power spectrum density of the complete transducer including the A/D converter is 0.4 mA/√Hz at 1 Hz. For frequencies higher than 1 Hz the noise spectrum is white – the RMS noise level from 1 Hz to 1 kHz is 6 mA. This is comparable to the noise level of transducer based on precise AMR sensors.

Another advantage of the proposed sensor is high linearity which is limited by 0.1% linearity error of individual feedback compensated microfabricated fluxgate sensors. The measured linearity error of the complete transducer is shown in Fig. 9.

7. Discussion

We described optimized microfluxgate current transducer suitable for monitoring geomagnetically induced currents and other DC current components in 3-phase current lines. The traditional way to process the sensor data, which we call the “gradient method”, calculated the differences of two sensors in a gradiomet-

ric pair. However, this method lost part of the information. The gradiometric method suppressed only the homogeneous component of the external field, not the field gradients. For external (non-measured) currents within a small distance the gradients are high, which results in poor suppression of these currents.

In our novel method, we utilize the output of all sensors in a more complex way by solving Eq. (4). First of all, we completely compensate the crosstalk between the phases. Using six sensors, we also suppress the first and second gradient of the external field.

By using 8 sensors we can suppress field gradients up to the 4th order. This results in even larger suppression of external currents. Sensor calibration is necessary in order to achieve the projected parameters for an 8-sensor transducer. The measured rejection at 1 m distance was 90 dB (or 0.003%), i.e. a 300-fold improvement in comparison with [21]. By Monte Carlo simulations we verified that the method is robust against uncertainty of sensor position and sensor data.

Replacing magnetoresistive sensors by integrated fluxgate sensors improved the temperature stability 50-fold: 1 mA/K offset stability and 50 ppm/K temperature coefficient of sensitivity of the developed current transducer was achieved. The transducer noise is 6 mA RMS (1 Hz–1 kHz) and linearity error is 0.15% in 6 A range.

LEM LF210, which has 20 mA RMS noise, 0.15 A offset and 75 g mass for single phase, is an example of an available DC/AC current transducer with the same 200 A range. Compared to that, our sensor is lightweight (12 g for each phase). It can therefore be mounted on existing overhead 3-phase current lines with low installation costs. It also has excellent temperature stability and low noise.

Declaration of Competing Interest

The authors declare that they have no known competing financial interests or personal relationships that could have appeared to influence the work reported in this paper.

Acknowledgements

This work was supported by the Grant Agency of the Czech Republic within the New Methods for the Measurement of Electric Currents" project (GACR 17-19877S).

References

- [1] Salman, K. Salman, Introduction to the Smart Grid, The Institution of Engineering and Technology, 2017.
- [2] A. Pulkkinen, E. Bernabeu, A. Thomson, et al., Geomagnetically induced currents: science, engineering, and applications readiness, *Space Weather-Int. J. Res. Appl.* 15 (7) (2017) 828–856.
- [3] W. Pluta, C. Swieboda, J. Leszczynski, et al., Some remarks on metrological properties and production technology of current transformers made of nanocrystalline cores, *Measurement* 97 (2017) 38–44.
- [4] C. Swieboda, J. Walak, M. Soinski, et al., Nanocrystalline oval cut cores for current instrument transformer prototypes, *Measurement* 136 (2019) 50–58.
- [5] P. Ripka, K. Draxler, R. Styblíková, DC-compensated current transformer, *Sensors* 16 (2016) 2016.
- [6] X. Cheng, Z. Sun, X. Wang, et al., Open-loop linear differential current sensor based on dual-mode Hall effect, *Measurement* 50 (2014) 29–33.
- [7] A. Cataliotti, V. Cosentino, D. Di Cara, et al., Rogowski coil current transducer compensation method for harmonic active power error, *Measurement* 63 (2015) 240–251.
- [8] J.G. Wang, D.C. Si, T. Tian, et al., Design and experimental study of a current transformer with a stacked PCB based on B-dot, *Sensors* 17 (4) (Apr 2017).
- [9] Z.P. Wang, X.Z. Wang, Theoretical analysis of the temperature characteristics of an optical current sensing element, *Measurement* 42 (2) (2009) 277–280.
- [10] M. Blagojevic, U. Jovanovic, I. Jovanovic, et al., Realization and optimization of bus bar current transducers based on Hall effect sensors, *Meas. Sci. Technol.* 27 (6) (2016).
- [11] P. Ripka, A. Chirtsov, Influence of external current on yokeless electric current transducers, *IEEE Trans. Magnetics* 53 (11) (Nov 2017) 4.
- [12] P. Ripka, A. Chirtsov, Busbar current transducer with suppression of external fields and gradients, *IEEE Trans. Magnetics* 54 (11) (2018).
- [13] L. Di Rienzo, Z. Zhang, Spatial harmonic expansion for use with magnetic sensor arrays, *IEEE Trans. Magnetics* 46 (1) (2010) 53–58.
- [14] Y.P. Tsai, K.L. Chen, Y.R. Chen, et al., Multifunctional coreless hall-effect current transformer for the protection and measurement of power systems, *IEEE Trans. Instrum. Meas.* 63 (3) (2014) 557–565.
- [15] R. Weiss, R. Makuch, A. Itzke, et al., Crosstalk in circular arrays of magnetic sensors for current measurement, *IEEE Trans. Ind. Electron.* 64 (6) (2017) 4903–4909.
- [16] P. Mlejnek, P. Ripka, AMR yokeless current sensor with improved accuracy, in: I. Barsony, Z. Zolnai, G. Battistig (Eds.), Proceedings of the 30th Anniversary Eurosensors Conference - Eurosensors 2016, Procedia Engineering, 2016, pp. 900–903.
- [17] P. Mlejnek, P. Ripka, Off-center error correction of AMR yokeless current transducer, *J. Sens.* 2017 (2017).
- [18] H. Yu, Z. Qian, H.Y. Liu, et al., Circular array of magnetic sensors for current measurement: analysis for error caused by position of conductor, *Sensors* 18 (2) (2018) 12.
- [19] Y. Chen, Q. Huang, A.H. Khawaja, et al., A novel non-invasion magnetic sensor array based measurement method of large current, *Measurement* 139 (2019) 78–84.
- [20] P. Mlejnek, P. Ripka, Off-center error correction of AMR yokeless current transducer, *J. Sens.* (2017) 7.
- [21] A. Bernieri, L. Ferrigno, M. Laracca, et al., An AMR-based three-phase current sensor for smart grid applications, *IEEE Sens. J.* 17 (23) (2017) 7704–7712.
- [22] L. Jogschies, D. Klaas, R. Kruppe, et al., Recent developments of magnetoresistive sensors for industrial applications, *Sensors* 15 (11) (2015) 28665–28689.
- [23] M. Dabek, P. Wisniowski, P. Kalabinski, et al., Tunneling magnetoresistance sensors for high fidelity current waveforms monitoring, *Sens. Actuators A-Phys.* 251 (2016) 142–147.
- [24] M. Kahr, M. Stifter, et al., Dual resonator MEMS magnetic field gradiometer, *Sensors* 19 (2019).
- [25] W. He, Y.R. Lu, C.W. Qu, et al., A non-invasive electric current sensor employing a modified shear-mode cymbal transducer, *Sens. Actuators A-Phys.* 241 (2016) 120–123.
- [26] G.F. Lou, X.J. Yu, R. Ban, A wide-range DC current sensing method based on disk-type magnetoelectric laminate composite and magnetic concentrator, *Sens. Actuators A-Phys.* 280 (2018) 535–542.
- [27] S. Pisupati, D. Kundukoori, N. Mekala, et al., Design of resonance based DC current sensor using BAW quartz resonators, *Sens. Actuators A-Phys.* 271 (2018) 104–110.
- [28] D.L. Shi, Q. Zhang, Y.M. Ye, et al., High-frequency current sensor based on lead-free multiferroic BiFeO₃-BaTiO₃-based ceramics, *Measurement* 104 (2017) 287–293.
- [29] B. Santhosh Kumar, K. Suresh, U. Varun Kumar, et al., Resonance based DC current sensor, *Measurement* 45 (3) (2012) 369–374.
- [30] P. Ripka, Václav Grim, Andrey Chirtsov, Improved 3-phase current transducer, *Proceedings MDPI* 2 (13) (2018) 1070.

6.6 Characterization of circular array current transducers

A continuation of a series of works building upon the known concept of circular sensor arrays. Posters were presented at EMSA 2018 and SAS 2019, and from the latter proceedings were published.

A distinguishing feature is the inclusion of chip-scale fluxgate sensors from Texas instruments. Most effort was given to modeling of imperfections caused by tolerances in assembly and installation of such sensors. That helped to identify the performance-critical parameters that have to be given the most attention. Calibration methods suitable for automated test equipment were developed, of which the most noteworthy is the post-assembly adjustment of sensitivity axis direction based on two-dimensional sensing elements.

I contributed with the concept, theory, transducer PCB design and assembly, measurement, making of the figures and most writing.

This full text paper was peer-reviewed at the direction of IEEE Instrumentation and Measurement Society prior to the acceptance and publication.

Characterization of circular array current transducers

Václav Grim
Department of Measurement
Czech Technical University
Praha, Czechia
vaclav.grim@fel.cvut.cz

Pavel Ripka
Department of Measurement
Czech Technical University
Praha, Czechia
ripka@fel.cvut.cz

Jan Fischer
Department of Measurement
Czech Technical University
Praha, Czechia
fischer@fel.cvut.cz

Abstract—This paper is evaluating different aspects affecting the performance of circular arrays of magnetic sensors used for contactless current transducer. Some of these error mechanisms are quantified using analytical expressions to provide designers with theoretical upper limits of achievable accuracy. Novel method of misalignment compensation using multi-axial sensors is presented. Measurements were performed with different sensor arrays to verify theoretical assumptions and determine limiting factors for real-world application of yokeless transducers.

Index Terms—current transducer, magnetometer, magnetic sensor, AMR, fluxgate, contactless measurement

I. INTRODUCTION

Circular arrays of magnetic sensors for contactless measurement of electric current have received significant attention in recent years [1]. Published works use either Hall sensors [2], Anisotropic Magnetoresistors (AMR) [3] or fluxgate integrated sensor ICs [4].

The principal advantage of circular array it much better immunity against the external currents (lower crosstalk error) compared to simple differential sensor configuration [5]. Increasing the number of sensors from 2 [6] to 4 [7] reduces this error to 6%, but optimum number of sensors is higher [8, 4]. The same advantage applies also to low sensitivity to position of the measured conductor. When using 8 uncalibrated AMR sensors the position error was $\pm 0.4\%$ and after correction the error decreases to $\pm 0.06\%$ [9].

Compared to electric current sensors with yoke, circular arrays are much lighter, have better linearity and do not suffer from the remanence which may cause perming error [1].

In this paper we analyze the errors of individual sensors and methods for their compensation to improve the accuracy of the current transducer.

Offsets and sensitivities of individual sensors in circular transducer with AMRs were analyzed in [9]. For flipped AMR sensors the offset is low compared to the Earth's field. Final compensation must be made with zero measured current and a defined direction towards the Earth's magnetic field. The observed differences in open-loop sensitivities between individual sensor from the same batch were $\pm 2\%$. This fact is not surprising as sensitivity depends on the thickness and permeability of the sputtered magnetic layer, which are extremely difficult to control.

In this paper we extend this error analysis by considering the alignment error of individual sensors. We also extend

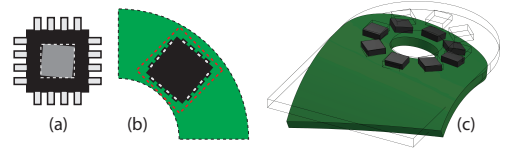


Fig. 1. Different misalignment causes: chip packaging (a), PCB assembly (b), board deformation (c)

the error analysis by the influence of the external current. The error analysis is verified by measurement, using 3-axial AMR sensors. Presented calculations provide insight into relations between transducer's geometry and its performance. By knowing the effect of individual error sources, we were able to develop a method for compensation for errors caused by assembly tolerances.

II. PRINCIPLE OF OPERATION

Yokeless sensors' working principle is Ampere's law:

$$I = \oint_l \vec{H} \cdot d\vec{l} \quad (1)$$

The theoretical continuous integration path is approximated using finite number of points, in which sensors are placed.

$$\oint_l \vec{H} \cdot d\vec{l} \rightarrow \sum_{n=1}^N \vec{H}_n \cdot \vec{l}_n \quad (2)$$

Vector \vec{H}_n denotes magnetic field intensity at point n and vector \vec{l}_n is the path between points n and $n+1$. Tangential components of field in each sensor are summed to provide the total magnitude of current enclosed by the loop. Such path discretization always has negative effect on accuracy, as elaborated in section IV.

Both AC and DC measurements are possible, bandwidth is usually limited only by sampling frequency of the sensors' ADC. The ADC has 16-bit resolution and maximum output data rate of 1000 SPS. It is integrated into the sensor package, therefore it is not possible to measure its parameters separately from the actual AMR bridge.

III. DISCUSSION OF ERROR SOURCES

A. Individual sensor errors

The particular type of AMR (LIS3MDL from *STMicroelectronics*) used in this paper is not targeted to metrological applications. Precise AMR sensor such as Honeywell HMC1001 use feedback compensation to achieve high linearity and high temperature stability of the gain. These devices are expensive and large. Another disadvantage of precise AMRs is their small range, usually limited to 200 μT (HMC1001) or 600 μT (HMC1021), while open-loop AMRs such as LIS3MDL operate to 1.6 mT. This increases the current measurement range of the 14 mm diameter current transducer from 7 A for compensated HMC1001 and 21 A for compensated HMC1021 to 56 A for uncompensated LIS3MDL. LIS3MDL is small 3-axial sensor with low power consumption of 40 μA , compared to max. 6 mA for HMC1021. It should be noted that for both open-loop and compensated sensors calibration of the sensitivity is mandatory due to uncertainty of the feedback coil factor.

Non-linearity of the open-loop sensors is significant: linearity error of LIS3MDL is $\pm 0.12\%$ but this error value is specified only for fields up to 0.6 mT in FS range of 1.2 mT. For larger fields this error rapidly increases. Measurement of fields up to 1.6 mT resulted in non-linearity of 0.4% FS (Fig. 2). Best-fit straight line method was used.

All calculations assume the AMR die to be infinitely small and centered perfectly in the package. In reality there will always be misalignment, as well as deformation of impinging flux lines caused by high permeability of the sensor's internal structures.

Crossfield error is non-linear sensitivity to the field in the direction perpendicular to the main sensing axis. Crossfield error is significant for high-sensitivity AMR sensors such as HMC1001 [10]. In our case the used sensors have high value of anisotropy field. Therefore crossfield error cannot play significant role in the error budget.

B. System Level Errors

Other types of errors are possible to reduce with careful system-level transducer design. Rejection of external field depends on sensor arrangement, as is described later in the text. Mounting misalignment and board deformation (figure 1) also creates additional errors, which may be partially canceled by scaling and rotating the axis of sensitivity of individual sensors.

IV. CALCULATION OF EXTERNAL CURRENT REJECTION

Continuous integration of \vec{H} along a closed path is by definition immune to any currents outside the loop. This is the principle of a Rogowski coil with theoretically infinite external current suppression, limited only by variations in winding uniformity. In case of a finite number of measurement points (where sensors are located) the length of path element $d\vec{l}$ increases from zero to non-zero. This introduces a systematic error and sensitivity to current-carrying conductors outside the sensor circle (cross talk) is no longer zero. Specifically

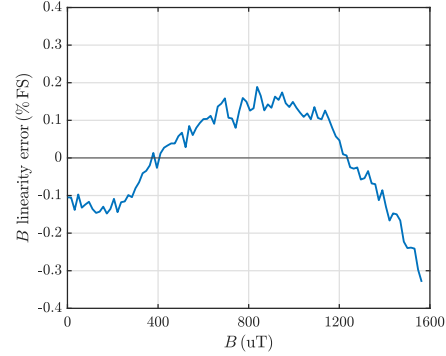


Fig. 2. Non-linearity measurement of single LIS3MDL sensor

trajectory along the outside circumference of the sensor PCB is observed, because it represents closest possible location of external conductors

Crosstalk error was already analyzed in [8] and [4]. We bring simple, but more illustrative approach which is precise enough in arrays with larger number of sensors. All following calculations assume N sensors uniformly distributed on a circle with diameter r_1 and one external conductor w swept along a circle with diameter r_2 , whose position is defined by angle φ (explanation in picture 3). Response of sensor n (located at \vec{s}_n) to current in nominal position in the center of the circle is

$$H_{n,center} = \frac{I}{2\pi r_1} \quad (3)$$

Response to external current in wire w is

$$H_{n,ext} = \frac{\left((w - \vec{s}_n) \times \begin{pmatrix} 0 \\ 0 \\ I \end{pmatrix} \right) \cdot \vec{s}_{n,tg}}{2\pi |w - \vec{s}_n|^2} \quad (4)$$

where $\vec{s}_{n,tg}$ is the normalized sensitivity direction of sensor n , tangential to the pitch circle. Combining N instances of expressions 3 and 4, each rotated by $2\pi n/N$, yields total formula for external current rejection

$$\frac{H_{ext}}{H_{center}} = \frac{\sum_{n=0}^{N-1} \frac{I}{2\pi \left| \begin{pmatrix} r_2 \cos \varphi \\ r_2 \sin \varphi \end{pmatrix} - \begin{pmatrix} r_1 \cos \frac{2\pi}{N} n \\ -r_1 \sin \frac{2\pi}{N} n \end{pmatrix} \right|} \cdot \left(\begin{pmatrix} r_1 \cos \frac{2\pi}{N} n \\ r_1 \sin \frac{2\pi}{N} n \end{pmatrix} \cdot \begin{pmatrix} -\sin \varphi \\ \cos \varphi \end{pmatrix} \right)}{N \cdot \frac{I}{2\pi r_1}} \quad (5)$$

Resulting expression, although possible to evaluate numerically, does not provide the required intuitive insight to this problem. Moreover, the actual shape of the waveform is not as important as its magnitude. When this expression is converted into asymptotic form by making $n = \infty$, it is simplified into

$$\frac{H_{ext}}{H_{center}} = \left(\frac{r_1}{r_2} \right)^n \quad (6)$$

Difference between exact and simplified forms is less than 0.05% for any $n > 8$. In Fig. 4 this difference (red and blue line) is visible only in leftmost part of the plot.

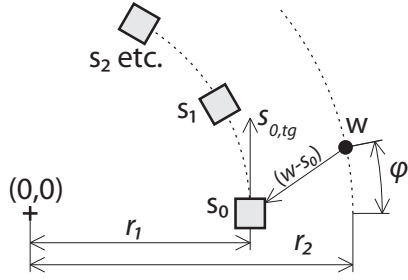


Fig. 3. Explanation of symbols used in equations 3–5

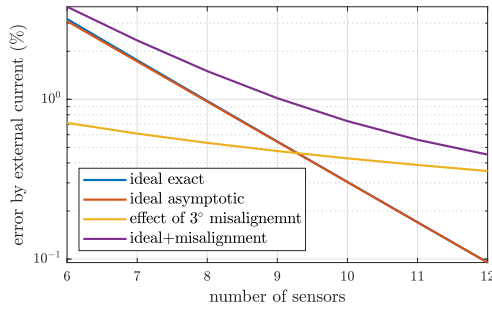


Fig. 4. Theoretical accuracy limits before and after considering the effect of misalignment

V. EFFECT OF MISALIGNMENT

A. Estimation of Misalignment Errors

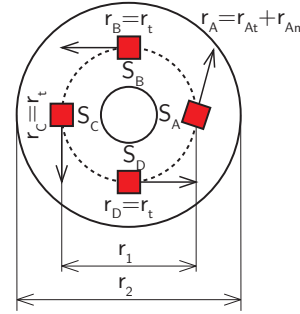
Sensor misalignment becomes a major concern after sensor count is increased beyond a point where errors due to path discretization become negligible, e.g. for $d_1 = 7$ mm and $d_2 = 12.5$ mm, 12 sensors give sensitivity to external field only 0.1% (Fig. 4). Theoretical model of misalignment assumes one sensor rotated by a small angle $\Delta\varphi$, while all others are in exact position. The total error may be expressed as

$$\frac{H_{ext}}{H_{center}} = \frac{I}{2\pi \left| \begin{matrix} r_2 \cos \varphi \\ r_2 \sin \varphi \end{matrix} \right| - (r_1)} \cdot \frac{((- \sin \Delta\varphi) \cdot (- \sin \varphi))}{N \cdot \frac{I}{2\pi r_1}} + \frac{\sum_{n=1}^{N-1} \frac{I}{2\pi \left| \begin{matrix} r_2 \cos \varphi \\ r_2 \sin \varphi \end{matrix} \right| - (r_1 \cos \frac{2\pi}{N} n)} \cdot \left(\begin{matrix} r_1 \cos \frac{2\pi}{N} n \\ r_1 \sin \frac{2\pi}{N} n \end{matrix} \right) \cdot (- \sin \varphi)}{N \cdot \frac{I}{2\pi r_1}} \quad (7)$$

When the number of sensor is high, only the normal component (r_{AN} in Fig. 5) is relevant, and the expression reduces to

$$\frac{\Delta\varphi}{N} \cdot \frac{\sin \varphi \sqrt{r_1^2 + r_2^2 - 2r_1 r_2 \cos \varphi}}{r_1} \quad (8)$$

This is illustrated by Fig. 6 a,b,c. Total value (a) is not as interesting as normal component (b), which is easily calculated and provides good approximation of the actual error value. As seen in Fig. 9, misalignment is the limiting factor when precision better than a few percent is required.


 Fig. 5. Explanation of misalignment calculation method, S_n being sensor location and r_n its axes of sensitivity

B. Method for misalignment compensation

Most designs published so far deal with single-axis sensors aligned with tangential direction around the wire. There is a possibility for improvement if two- or three-axis devices are used. In case of inaccurate mounting or board deformation the sensitivity axis will no longer be in the tangential direction to the flux line. This effect can be corrected by a rotation matrix. Calibration is made for known measured current using the reading of two perpendicular sensors, from which we calculate angular misalignment of each sensor. We use the fact that sensors in one package are orthogonal within 0.1° – this allows us to compensate angular misalignment to the same level of accuracy.

VI. MEASUREMENT ON SAMPLES

LIS3MDL integrated AMR sensors from STMicroelectronics were used in two different transducer designs: one with 8 sensors and the other with 12 sensors (Fig. 7). Overall dimensions denoted in Fig. 7 are the same for both boards. All sensors on a PCB are connected via common SPI bus, chip select inputs are used to sequentially read out results from individual sensors.

Before the actual measurement was conducted, calibration of sensors was done to closely match the gain of all sensors on the PCB. A conductor carrying 5 A was placed exactly in the centre of the hole and correction coefficients were adjusted to get readings of $142.86 \mu\text{T}$ in tangential direction and $0 \mu\text{T}$ in radial and vertical direction. Correction coefficients are shown in table I

Test fixture holding the transducer in perpendicular position relative to the wire at specific position along its circumference is used for measurement of external current rejection (Fig. 8). DC test current of 5 A was commutated to exclude the influence of geomagnetic field.

Results are in agreement with theory: in the first transducer with 8 sensors, uniform ripple of around $\pm 1\%$ is the main factor defining the sensitivity to external current. In case of second transducer consisting of 12 sensors, this ripple is barely noticeable, but other sources such as misalignment or gain

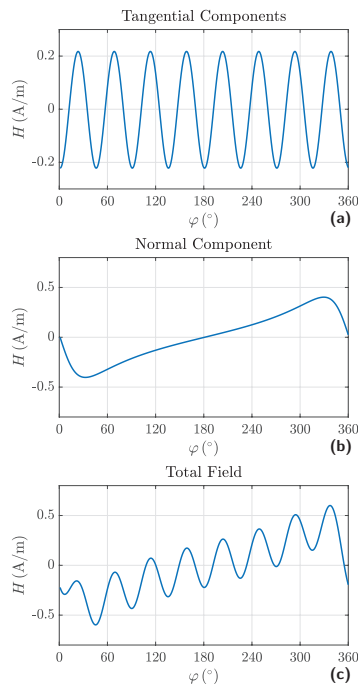


Fig. 6. Calculated response to 5 A external current. Transducer with 8 sensors, one of them rotated by 3°: a) contribution from tangential components b) contribution from normal component due to angular misalignment c) total transducer output.

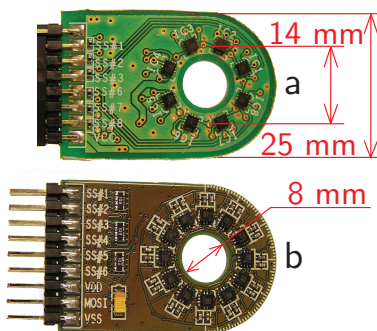


Fig. 7. Manufactured and measured sample transducers with 8 (a) and 12 (b) sensors

errors are still present and cause the nonperiodic characteristic in Fig. 9b, similar to theoretical calculation in Fig. 6b.

VII. CONCLUSION

Several methods were discussed to help with the process of designing a yokeless sensor with desired performance. Measurements have shown good agreement with theoretical

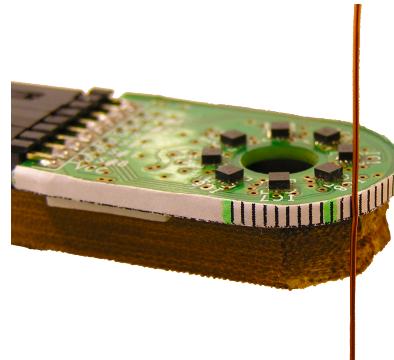


Fig. 8. Detail of angular scale on transducer board to measure the position of the conductor with the external current

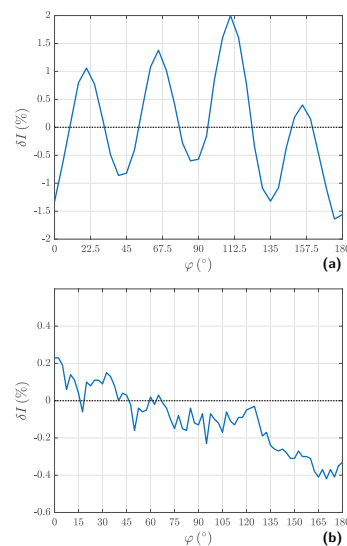


Fig. 9. Measured sensitivity to external field, in % of sensitivity to measured current in board center. Board with 8 sensors (a) and with 12 sensors (b) with correction of sensitivity variations

calculations. We have shown that when using 6 sensors as in [4] or 8 sensors as in our first transducer, sensitivity to the external currents (crosstalk error) is mainly given by finite number of sensors. For 8 sensors this type of error is 2% at 25 mm and cannot be corrected or compensated. When using 12 sensors as in our second transducer, other error sources become dominant, mainly the misalignment of sensitivities, angular misalignment and offsets. For external conductor in 25 mm distance the error was 0.4% and could be compensated to 0.2%.

Long-term stability of AMR sensors becomes an issue if zero calibration is not possible between the measurements.

n	gain difference (%)	angle difference (°)
1	-4.68	2.50
2	-13.79	2.17
3	-5.22	2.00
4	-5.76	1.48
5	-7.17	0.61
6	-8.76	4.01
7	-8.93	4.18
8	-8.77	4.00

TABLE I
CALIBRATION COEFFICIENTS FOR 8-SENSOR TRANSDUCER

ACKNOWLEDGMENT

This work was supported by the Grant agency of the Czech Republic through the project "New methods for the measurement of electric currents" (GACR 17-19877S).

REFERENCES

- [1] Pavel Ripka. "Electric current sensors: a review". In: *Meas. Sci. Technol.* 21.11 (Nov. 2010), p. 112001. ISSN: 0957-0233. DOI: 10.1088/0957-0233/21/11/112001.
- [2] Yuan-Pin Tsai et al. "Multifunctional Coreless Hall-Effect Current Transformer for the Protection and Measurement of Power Systems". In: *IEEE Trans. Instrum. Meas.* 63.3 (Mar. 2014), pp. 557–565. ISSN: 0018-9456. DOI: 10.1109/TIM.2013.2281555.
- [3] Pavel Mlejnek and Pavel Ripka. "AMR Yokeless Current Sensor with Improved Accuracy". In: *Procedia Eng.* Vol. 168. Elsevier, Jan. 2016, pp. 900–903. DOI: 10.1016/j.proeng.2016.11.301.
- [4] Roland Weiss et al. "Crosstalk in Circular Arrays of Magnetic Sensors for Current Measurement". In: *IEEE Trans. Ind. Electron.* 64.6 (June 2017), pp. 4903–4909. ISSN: 0278-0046. DOI: 10.1109/TIE.2017.2674630.
- [5] Pavel Ripka and Andrey Chirtsov. "Influence of External Current on Yokeless Electric Current Transducers". In: *IEEE Trans. Magn.* 53.11 (Nov. 2017), pp. 1–4. ISSN: 0018-9464. DOI: 10.1109/TMAG.2017.2715075.
- [6] Marjan Blagojević et al. "Realization and optimization of bus bar current transducers based on Hall effect sensors". In: *Meas. Sci. Technol.* 27.6 (June 2016), p. 065102. ISSN: 0957-0233. DOI: 10.1088/0957-0233/27/6/065102.
- [7] Kun-Long Chen and Nanming Chen. "A New Method for Power Current Measurement Using a Coreless Hall Effect Current Transformer". In: *IEEE Trans. Instrum. Meas.* 60.1 (Jan. 2011), pp. 158–169. ISSN: 0018-9456. DOI: 10.1109/TIM.2010.2049234.
- [8] L. Di Rienzo and Z. Zhang. "Spatial Harmonic Expansion for Use With Magnetic Sensor Arrays". In: *IEEE Trans. Magn.* 46.1 (Jan. 2010), pp. 53–58. ISSN: 0018-9464. DOI: 10.1109/TMAG.2009.2027899.
- [9] Pavel Mlejnek and Pavel Ripka. "Off-Center Error Correction of AMR Yokeless Current Transducer". In: *J. Sensors* 2017 (2017), pp. 1–7. ISSN: 1687-725X. DOI: 10.1155/2017/6057634.
- [10] Pavel Ripka, Jan Vyhnánek, and Andrey Chirtsov. "Crossfield response of industrial magnetic sensors". In: *Int. J. Appl. Electromagn. Mech.* 55 (Oct. 2017). Ed. by Zhiguang Cheng et al., pp. 39–47. ISSN: 13835416. DOI: 10.3233/JAE-172256.

7 List of all co-authored publications

7.1 Publications in Impacted Journals

- [J10] V. Grim and P. Ripka, “Rogowski Coil with Ferromagnetic Powder Core,” *IEEE Magn. Lett.*, vol. 13, 2022, ISSN: 19493088. DOI: 10.1109/LMAG.2022.3143470, Contribution 60%.
- [J11] V. Grim, P. Ripka, and J. Bauer, “DC Current Sensor Using Switching-Mode Excited In-situ Current Transformer,” *J. Magn. Magn. Mater.*, vol. 500, 2020, ISSN: 0304-8853. DOI: 10.1016/J.JMMM.2019.166370, Contribution 50%.
- [J1] P. Ripka, V. Grim, M. Mirzaei, *et al.*, “Modelling and Measurement of Magnetically Soft Nanowire Arrays for Sensor Applications,” *Sensors*, vol. 21, no. 3, 2021, ISSN: 1424-8220. DOI: 10.3390/s21010003, Contribution 15%.
- [J2] P. Ripka, V. Grim, and M. Mirzaei, “The apparent permeability and the amplification factor of magnetic wires and wire arrays,” *J. Magn. Magn. Mater.*, vol. 527, 2021, ISSN: 03048853. DOI: 10.1016/j.jmmm.2021.167726, Contribution 25%.
- [J3] M. Mirzaei, P. Ripka, and V. Grim, “A Simplified 2D Equivalent Model for Magnetic Wire Array,” *IEEE Trans. Magn.*, vol. 58, no. 2, 2021, ISSN: 19410069. DOI: 10.1109/TMAG.2021.3085485, Contribution 25%.
- [J4] P. Ripka, D. Hrakova, V. Grim, and M. Mirzaei, “Multiwire Parallel Fluxgate Sensors,” *IEEE Trans. Magn.*, vol. 58, no. 2, 2022, ISSN: 0018-9464. DOI: 10.1109/tmag.2021.3093017, Contribution 20%.
- [J5] M. Mirzaei, P. Ripka, A. Chirtsov, J. Vyhnánek, and V. Grim, “Design and Modeling of a Linear Speed Sensor with a Flat Type Structure and Air Coils,” *J. Magn. Magn. Mater.*, vol. 495, 2020, ISSN: 0304-8853. DOI: 10.1016/J.JMMM.2019.165834, Contribution 20%.
- [J6] M. Mirzaei, P. Ripka, and V. Grim, “A Position Sensor with Novel Configuration of Linear Variable Differential Transformer,” *IEEE Sens. J.*, vol. 21, no. 20, pp. 22 899–22 907, 2021, ISSN: 1530-437X. DOI: 10.1109/JSEN.2021.3105879, Contribution 20%.
- [J7] M. Mirzaei, P. Ripka, and V. Grim, “An Axial Airgap Eddy Current Speed Sensor,” *IEEE Trans. Ind. Electron.*, vol. 69, no. 9, pp. 9586–9595, 2022, ISSN: 15579948. DOI: 10.1109/TIE.2021.3113001, Contribution 25%.
- [J8] P. Ripka, M. Přibil, V. Petrucha, V. Grim, and K. Draxler, “A Fluxgate Current Sensor with an Amphitheater Busbar,” *IEEE Trans. Magn.*, vol. 52, no. 7, 2016, ISSN: 00189464. DOI: 10.1109/TMAG.2016.2540523, Contribution 10%.
- [J9] P. Ripka, V. Grim, and V. Petrucha, “A Busbar Current Sensor with Frequency Compensation,” *IEEE Trans. Magn.*, vol. 53, no. 4, 2017, ISSN: 00189464. DOI: 10.1109/TMAG.2016.2620959, Contribution 30%.
- [J12] P. Ripka, V. Grim, and A. Chirtsov, “A 3-Phase Current Transducer Based on Microfluxgate Sensors,” *Measurement*, vol. 146, pp. 133–138, 2019, ISSN: 0263-2241. DOI: 10.1016/J.MEASUREMENT.2019.06.028, Contribution 45%.
- [J13] M. Mirzaei, P. Ripka, and V. Grim, “A Novel Position Sensor with a Conical Iron Core,” *IEEE Trans. Instrum. Meas.*, vol. 69, no. 11, pp. 9178–9189, 2020, ISSN: 15579662. DOI: 10.1109/TIM.2020.2999691, Contribution 25%.

- [J14] M. Mirzaei, P. Ripka, V. Grim, and A. Chirtsov, “Design and Optimization of an Eddy Current Speed Sensor for Rotating Rods,” *IEEE Sens. J.*, vol. 20, no. 20, pp. 12 241–12 251, 2020, ISSN: 15581748. DOI: 10.1109/JSEN.2020.3000442, Contribution 25%.
- [J15] M. Mirzaei, P. Ripka, V. Grim, L. Jelínek, and J. Svatoš, “Thickness evaluation of hollow nonmagnetic cylinders utilizing a motional eddy current,” *Measurement*, vol. 189, 2022, ISSN: 0263-2241. DOI: 10.1016/J.MEASUREMENT.2021.110463, Contribution 15%.
- [J16] A. Chirtsov, P. Ripka, and V. Grim, “Three-Phase Busbar Current Transducer,” *IEEE Magn. Lett.*, vol. 10, 2019, ISSN: 19493088. DOI: 10.1109/LMAG.2019.2957257, Contribution 30%.
- [J17] M. Mirzaei, P. Ripka, J. Macháč, V. Grim, and J. Svatoš, “Design and modeling of an axisymmetric eddy current sensor for speed measurement of nonmagnetic rods,” *Sensors Actuators A Phys.*, vol. 344, 2022, ISSN: 0924-4247. DOI: 10.1016/J.SNA.2022.113728, Contribution 15%.
- [J18] M. Mirzaei, P. Ripka, and V. Grim, “A novel eddy current speed sensor with a ferrite E-core,” *IEEE Magn. Lett.*, vol. 11, 2020, ISSN: 19493088. DOI: 10.1109/LMAG.2020.2993501, Contribution 20%.
- [J19] P. Ripka, A. Chirtsov, and V. Grim, “Contactless Piston Position Transducer with Axial Excitation,” *IEEE Trans. Magn.*, vol. 53, no. 11, 2017, ISSN: 00189464. DOI: 10.1109/TMAG.2017.2715073, Contribution 20%.
- [J20] M. Mirzaei, P. Ripka, J. Vyhnánek, A. Chirtsov, and V. Grim, “Modeling of hysteresis loops using rational and power functions,” *J. Magn. Magn. Mater.*, vol. 522, 2021, ISSN: 03048853. DOI: 10.1016/j.jmmm.2020.167563, Contribution 5%.
- [J21] M. Mirzaei, P. Ripka, and V. Grim, “A Linear Eddy Current Speed Sensor for Speed Measurement of Conductive Objects,” *IEEE Trans. Ind. Appl.*, 2022, ISSN: 19399367. DOI: 10.1109/TIA.2022.3198625, Contribution 25%.
- [J22] M. Mirzaei, P. Ripka, A. Chirtsov, and V. Grim, “Eddy current speed sensor with magnetic shielding,” *J. Magn. Magn. Mater.*, vol. 502, 2020, ISSN: 03048853. DOI: 10.1016/j.jmmm.2020.166568, Contribution 10%.
- [J23] M. Mirzaei, P. Ripka, and V. Grim, “A Novel Structure of an Eddy Current Sensor for Speed Measurement of Rotating Shafts,” *IEEE Trans. Energy Convers.*, 2022, ISSN: 0885-8969. DOI: 10.1109/TEC.2022.3195921, Contribution 25%.
- [J24] M. Mirzaei, J. Macháč, P. Ripka, A. Chirtsov, J. Vyhnánek, and V. Grim, “Design of a flat-type magnetic position sensor using a finite-difference method,” *IET Sci. Meas. Technol.*, vol. 14, no. 5, pp. 514–524, 2020, ISSN: 1751-8830. DOI: 10.1049/iet-smt.2019.0197, Contribution 10%.
- [J25] M. Mirzaei, P. Ripka, A. Chirtsov, and V. Grim, “Temperature stability of the transformer position transducer for pneumatic cylinder,” *J. Magn. Magn. Mater.*, vol. 503, 2020, ISSN: 03048853. DOI: 10.1016/j.jmmm.2020.166636, Contribution 10%.

7.2 Publications in Conference Proceedings

- [P1] V. Grim, P. Ripka, and J. Fischer, “Characterization of circular array current transducers,” in *IEEE Sensors Appl. Symp.*, IEEE, 2019, ISBN: 9781538677131. DOI: 10.1109/SAS.2019.8706029, Contribution 40%.

- [P2] V. Grim, P. Ripka, K. Draxler, and M. Mirzaei, "Rogowski Coil with Ferromagnetic Core for Precise Monitoring of Low-frequency Currents," in *2021 IEEE Int. Magn. Conf.*, IEEE, 2021, Contribution 50%.
- [P3] V. Grim and P. Ripka, "Self-oscillating DC Current Transformer with Nanocrystalline Core," in *2021 IEEE Sensors*, IEEE, 2021, ISBN: 9781728195018. DOI: 10.1109/SENSORS47087.2021.9639745, Contribution 50%.
- [P4] M. Mirzaei, P. Ripka, and V. Grim, "A Linear Eddy Current Speed Sensor for Speed Measurement of Magnetic and Nonmagnetic Conductive Objects," in *2021 13th Int. Symp. Linear Drives Ind. Appl.*, IEEE, 2021, ISBN: 978-1-7281-7210-1. DOI: 10.1109/LDIA49489.2021.9505714, Contribution 25%.
- [P5] V. Grim, J. Pek, P. Ripka, and A. Chirtsov, "Magnetometric Localization and Measurement of Hidden AC Currents," in *2019 IEEE Sensors Conf.*, IEEE, 2019, ISBN: 9781728116341. DOI: 10.1109/SENSORS43011.2019.8956513, Contribution 30%.
- [P6] P. Ripka, V. Grim, and A. Chirtsov, "Improved 3-Phase Current Transducer," *Proceedings*, vol. 2, no. 13 (Proceedings of Eurosensors 2018), 2018, ISSN: 2504-3900. DOI: 10.3390/PROCEEDINGS2131070, Contribution 33%.
- [P7] M. Mirzaei, P. Ripka, and V. Grim, "Estimation of a Magnetization Curve of a Flux-gate Wire Core Using an Inverse Technique," in *2021 IEEE Sensors*, IEEE, 2021, ISBN: 9781728195018. DOI: 10.1109/SENSORS47087.2021.9639484, Contribution 25%.
- [P8] M. Mirzaei, P. Ripka, and V. Grim, "Conductivity Measurement of Nonferrous Plates using A Novel Sensor with Triangular Arrangements of Triple Coils," in *Jt. MMM InterMag Conf.*, IEEE, 2022, ISBN: 978-1-6654-8334-6. DOI: 10.1109/INTERMAG39746.2022.9827796, Contribution 25%.

8 Conclusion

Although the scope of my thesis is wide, FEM simulations and parametric design optimization is a common point for all the papers included in this collection. Together with novel magnetic materials, this was a key point for improvement of sensor accuracy, reducing their size and power consumption. Together with other team members, especially Dr. Mirzaei, we succeeded in integration of novel non-linear magnetic material models into industry-standard numerical field solvers.

In some cases the 3D FEM is not trivial or even impossible. This happened for large sensor arrays as well for moving eddy current problems. We found effective ways how to reduce the problem complexity by using lower-dimensional equivalent structures. All simulations were also verified by measurement and this was often my main role in the team.

There were also a lot of work dedicated to other research directions, that did not result in any publications. This was the case with cast toroidal cores made of weakly ferromagnetic composites. The methods of their manufacturing were successfully developed, but ultimately their properties proved uninteresting.

The core of the thesis are several sensor papers, where I had key contribution and I was usually the first author. Here I briefly review my main achievements:

1. **Rogowski Coil with Ferromagnetic Powder Core [J10]:** I have shown that using low-permeability core, the sensitivity of the Rogowski coil can be increased by the factor of 10, without significant degradation of linearity. This finding may have application potential in current sensors for power and energy meters.
2. **DC Current Sensor Using Switching-Mode Excited In-situ Current Transformer [J11]:** A novel design showing that standard high-accuracy AC current sensor can be combined with low-power DC sensing capabilities without modifications.
3. **Self-oscillating DC Current Transformer with Nanocrystalline Core [P3]:** This paper shows the future path for low-power fluxgate current sensor with extremely simple hardware.
4. **Magnetometric Localization and Measurement of Hidden AC Currents [P5]:** I have shown that electric current can be measured and localized by an array of magnetometers even without prior knowledge of its location. This was shown also for DC currents, where the influence of the Earth's field should be compensated.

8.1 Review of Objective Fulfillment

1. **Selecting suitable materials and fitting simulation models:** This point was eventually separated into two – selection of core material was needed in [P3], where the need for high inductance, low loss core led to the use of a nanocrystalline, tape wound toroid. The process of fitting parameters of an empirical model was done by Mr. Mirzaei in [P7], with my measurements as an input.
2. **Utilizing newly developed models for FEM simulations:** This area was eventually not given much attention. It was originally thought that the exact modeling of nonlinearities in electrodeposited nanowires would be needed to match theory and measurement, but after a closer inspection, not enough advantages of using nanowire arrays instead of solid films were found and the direction of research was changed to other areas.

3. **Optimizing the sensor performance using parametric methods:** Extensive parametric optimization was done during the design of current sensors for solid busbars [J9], although without any automated iterative procedure. The parameter space was searched in several steps, with candidates for next step selected manually.
4. **Building physical demonstrators and fixtures with fast prototyping methods:** Samples made with 3D printing, joined with polyamide bolts, are completely non-magnetic. Papers [J3], [J6], [J7], [J18], [J22], [P4] use coils made with winding machine over rectangular or cylindrical bobbins. 3D printed mold was used in [J10]. Custom non-magnetic sample holders were used in [J2]–[J4], [J7], [J8], [P2], [P3], [J18], [J21], [P7]. A complete sensor body made with 3D printing was used in [J6].
5. **Measurement of the properties of manufactured demonstrators and comparison with expected results:** All manufactured samples were compared with the theoretical values. Windings are simulated as one solid body, disregarding both their self-capacitance and inter-layer capacitance. Therefore simulation frequencies have to stay far away from coil resonance. On the other hand, on physical samples it is desirable to use large number of turns and high excitation frequency to extract a signal of a sufficient amplitude. This is one of the reasons why the frequency response of Rogowski coils [J10] cannot be accurately simulated up to its resonant frequency.

8.2 Suggestions for Further Research

There is definitely still a room for improvement in the field of electric current sensors. Electric drives have undergone extensive development in recent years due to increasing numbers of electric vehicles in production and current sensors are an important part of such systems.

For those applications it is not necessary to achieve extreme, metrology-grade accuracy and stability. Robustness and ease of manufacturing and installation are more important. Integration of magnetic circuits together with supporting electronics into a single silicon chip and embedding it into a magnetic yoke is one of prospective ways to make rugged, high performance sensors.

9 References

- [S1] D. X. Chen, J. A. Brug, and R. B. Goldfarb, “Demagnetizing factors for cylinders,” *IEEE Trans. Magn.*, vol. 27, no. 4, pp. 3601–3619, 1991, ISSN: 19410069. DOI: 10.1109/20.102932.
- [S2] D. X. Chen, E. Pardo, and A. Sanchez, “Fluxmetric and magnetometric demagnetizing factors for cylinders,” *J. Magn. Magn. Mater.*, vol. 306, pp. 135–146, 2006, ISSN: 03048853. DOI: 10.1016/j.jmmm.2006.02.235.
- [S3] W. Scholz, J. Fidler, T. Schrefl, *et al.*, “Scalable parallel micromagnetic solvers for magnetic nanostructures,” *Comput. Mater. Sci.*, vol. 28, no. 2, pp. 366–383, 2003, ISSN: 0927-0256. DOI: 10.1016/S0927-0256(03)00119-8.
- [S4] Y. P. Ivanov, M. Vázquez, and O. Chubykalo-Fesenko, “Magnetic reversal modes in cylindrical nanowires,” *J. Phys. D. Appl. Phys.*, vol. 46, no. 48, 2013, ISSN: 0022-3727. DOI: 10.1088/0022-3727/46/48/485001.
- [S5] O. Dmytriiev, U. A. Al-Jarah, P. Gangmei, *et al.*, “Static and dynamic magnetic properties of densely packed magnetic nanowire arrays,” *Phys. Rev. B*, vol. 87, no. 17, 2013, ISSN: 10980121. DOI: 10.1103/PhysRevB.87.174429.
- [S6] I. Ogasawara and S. Ueno, “Preparation and Properties of Amorphous Wires,” *IEEE Trans. Magn.*, vol. 31, no. 2, pp. 1219–1223, 1995, ISSN: 19410069. DOI: 10.1109/20.364811.
- [S7] I. Baraban, A. Litvinova, and V. Rodionova, “Amorphous ferromagnetic microwires: Methods of fabrication and measurements of the magnetic properties,” in *2017 IEEE 7th Int. Conf. Nanomater. Appl. Prop.*, IEEE, 2017, ISBN: 9781538628102. DOI: 10.1109/NAP.2017.8190415.
- [S8] H. Chiriac, N. Lupu, G. Stoian, G. Ababei, S. Corodeanu, and T. A. Óvári, “Ultrathin Nanocrystalline Magnetic Wires,” *Crystals*, vol. 7, no. 2, 2017, ISSN: 2073-4352. DOI: 10.3390/CRYST7020048.
- [S9] A. Zhukov, M. Ipatov, P. Corte-León, L. Gonzalez-Legarreta, J. M. Blanco, and V. Zhukova, “Soft magnetic microwires for sensor applications,” *J. Magn. Magn. Mater.*, vol. 498, 2020, ISSN: 0304-8853. DOI: 10.1016/J.JMMM.2019.166180.
- [S10] S. Atalay, P. Ripka, and N. Bayri, “Coil-less fluxgate effect in (Co_{0.94} Fe_{0.06})_{72.5} Si_{12.5} B₁₅ amorphous wires,” *J. Magn. Magn. Mater.*, vol. 322, no. 15, pp. 2238–2243, 2010, ISSN: 0304-8853. DOI: 10.1016/J.JMMM.2010.02.018.
- [S11] Y. Y. Zhao, H. Li, H. Y. Hao, M. Li, Y. Zhang, and P. K. Liaw, “Microwires fabricated by glass-coated melt spinning,” *Rev. Sci. Instrum.*, vol. 84, no. 7, 2013, ISSN: 00346748. DOI: 10.1063/1.4812331.
- [S12] J. Chen, J. Li, Y. Li, Y. Chen, and L. Xu, “Design and Fabrication of a Miniaturized GMI Magnetic Sensor Based on Amorphous Wire by MEMS Technology,” *Sensors*, vol. 18, no. 3, 2018, ISSN: 1424-8220. DOI: 10.3390/S18030732.
- [S13] J. Olivera, S. Aparicio, M. G. Hernández, *et al.*, “Microwire-Based Sensor Array for Measuring Wheel Loads of Vehicles,” *Sensors*, vol. 19, no. 21, 2019, ISSN: 1424-8220. DOI: 10.3390/S19214658.
- [S14] V. Torabinejad, M. Aliofkhaezai, S. Assareh, M. H. Allahyarzadeh, and A. S. Rouhaghdam, “Electrodeposition of Ni-Fe alloys, composites, and nano coatings—A review,” *J. Alloys Compd.*, vol. 691, pp. 841–859, 2017, ISSN: 0925-8388. DOI: 10.1016/J.JALLCOM.2016.08.329.

References

- [S15] A. Boodi, K. Beddiar, Y. Amirat, A. Ghaddar, F. Gloaguen, and J. Gieraltowski, "Magnetic properties of ferromagnetic nanowire arrays: Theory and experiment," *J. Phys. Conf. Ser.*, vol. 200, no. 7, 2010, ISSN: 1742-6596. DOI: 10.1088/1742-6596/200/7/072032.
- [S16] M. S. Salem, P. Sergelius, R. Zierold, J. M. Montero Moreno, D. Görlitz, and K. Nielsch, "Magnetic characterization of nickel-rich NiFe nanowires grown by pulsed electrodeposition," *J. Mater. Chem.*, vol. 22, no. 17, pp. 8549–8557, 2012, ISSN: 1364-5501. DOI: 10.1039/C2JM16339J.
- [S17] A. Santos and T. Kumeria, "Nanoporous anodic alumina for optical biosensing," in *Springer Ser. Mater. Sci.* Vol. 219, Springer, 2015, pp. 219–247. DOI: 10.1007/978-3-319-20334-8_7.
- [S18] A. Fert and L. Piraux, "Magnetic nanowires," *J. Magn. Magn. Mater.*, vol. 200, no. 1, pp. 338–358, 1999, ISSN: 0304-8853. DOI: 10.1016/S0304-8853(99)00375-3.
- [S19] M. M. Maqableh, L. Tan, X. Huang, *et al.*, "CPP GMR through nanowires," *IEEE Trans. Magn.*, vol. 48, no. 5, pp. 1744–1750, 2012, ISSN: 00189464. DOI: 10.1109/TMAG.2011.2174975.
- [S20] A. I. Martínez-Banderas, A. Aires, F. J. Teran, *et al.*, "Functionalized magnetic nanowires for chemical and magneto-mechanical induction of cancer cell death," *Sci. Rep.*, vol. 6, no. 1, 2016, ISSN: 2045-2322. DOI: 10.1038/srep35786.
- [S21] B. George, Z. Tan, and S. Nihtianov, "Advances in Capacitive, Eddy Current, and Magnetic Displacement Sensors and Corresponding Interfaces," *IEEE Trans. Ind. Electron.*, vol. 64, no. 12, pp. 9595–9607, 2017, ISSN: 02780046. DOI: 10.1109/TIE.2017.2726982.
- [S22] S. Fericean and R. Droxler, "New noncontacting inductive analog proximity and inductive linear displacement sensors for industrial automation," *IEEE Sens. J.*, vol. 7, no. 11, pp. 1538–1545, 2007, ISSN: 15581748. DOI: 10.1109/JSEN.2007.908232.
- [S23] A. Bertacchini, M. Lasagni, and G. Sereni, "Effects of the Target on the Performance of an Ultra-Low Power Eddy Current Displacement Sensor for Industrial Applications," *Electronics*, vol. 9, no. 8, 2020, ISSN: 2079-9292. DOI: 10.3390/ELECTRONICS9081287.
- [S24] K. D. Anim-Appiah and S. M. Riad, "Analysis and design of ferrite cores for eddy-current-killed oscillator inductive proximity sensors," *IEEE Trans. Magn.*, vol. 33, no. 3, pp. 2274–2281, 1997, ISSN: 00189464. DOI: 10.1109/20.573843.
- [S25] S. H. Yang, K. Hirata, T. Ota, and Y. Kawase, "Impedance Linearity of Contactless Magnetic-Type Position Sensor," *IEEE Trans. Magn.*, vol. 53, no. 6, 2017, ISSN: 00189464. DOI: 10.1109/TMAG.2017.2664074.
- [S26] A. Masi, S. Danzeca, R. Losito, P. Peronnard, R. Secondo, and G. Spiezia, "A high precision radiation-tolerant LVDT conditioning module," *Nucl. Instruments Methods Phys. Res. Sect. A Accel. Spectrometers, Detect. Assoc. Equip.*, vol. 745, pp. 73–81, 2014, ISSN: 0168-9002. DOI: 10.1016/J.NIMA.2014.01.054.
- [S27] J. De Pelegrin, B. M. De Carvalho, F. L. Bertotti, J. M. S. Lafay, and J. De Pelegrin, "Development and evaluation of a linear variable differential sensor," in *2nd Int. Symp. Instrum. Syst. Circuits Transducers*, IEEE, 2017, ISBN: 9781538620212. DOI: 10.1109/INSCIT.2017.8103523.
- [S28] K. Banerjee, B. Dam, and K. Majumdar, "A novel FPGA-based LVDT signal conditioner," in *2013 IEEE Int. Symp. Ind. Electron.*, IEEE, 2013, ISBN: 9781467351942. DOI: 10.1109/ISIE.2013.6563715.

- [S29] S. K. Mishra, G. Panda, and D. P. Das, “A novel method of extending the linearity range of linear variable differential transformer using artificial neural network,” *IEEE Trans. Instrum. Meas.*, vol. 59, no. 4, pp. 947–953, 2010, ISSN: 00189456. DOI: 10.1109/TIM.2009.2031385.
- [S30] W. Petchmaneelumka, W. Koodtalang, and V. Riewruja, “Simple Technique for Linear-Range Extension of Linear Variable Differential Transformer,” *IEEE Sens. J.*, vol. 19, no. 13, pp. 5045–5052, 2019, ISSN: 15581748. DOI: 10.1109/JSEN.2019.2902879.
- [S31] G. T. Laskoski, S. F. Pichorim, and P. J. Abatti, “Distance measurement with inductive coils,” *IEEE Sens. J.*, vol. 12, no. 6, pp. 2237–2242, 2012, ISSN: 1530437X. DOI: 10.1109/JSEN.2012.2185789.
- [S32] A. Masi, A. Danisi, R. Losito, and Y. Perriard, “Characterization of magnetic immunity of an ironless inductive position sensor,” *IEEE Sens. J.*, vol. 13, no. 3, pp. 941–948, 2013, ISSN: 1530437X. DOI: 10.1109/JSEN.2012.2220962.
- [S33] A. Danisi, A. Masi, R. Losito, and Y. Perriard, “Modeling of high-frequency electromagnetic effects on an ironless inductive position sensor,” *IEEE Sens. J.*, vol. 13, no. 12, pp. 4663–4670, 2013, ISSN: 1530437X. DOI: 10.1109/JSEN.2013.2271546.
- [S34] A. Danisi, A. Masi, and R. Losito, “Performance Analysis of the Ironless Inductive Position Sensor in the Large Hadron Collider Collimators Environment,” *Sensors*, vol. 15, no. 11, pp. 28 592–28 602, 2015, ISSN: 1424-8220. DOI: 10.3390/S151128592.
- [S35] O. Erb, G. Hinz, and N. Preusse, “PLCD, a novel magnetic displacement sensor,” *Sensors Actuators A Phys.*, vol. 26, no. 1-3, pp. 277–282, 1991, ISSN: 0924-4247. DOI: 10.1016/0924-4247(91)87005-N.
- [S36] X. Sun, T. Yamada, and Y. Takemura, “Output Characteristics and Circuit Modeling of Wiegand Sensor,” *Sensors*, vol. 19, no. 13, 2019, ISSN: 1424-8220. DOI: 10.3390/S19132991.
- [S37] C. C. Chang and J. Y. J. Chang, “Novel wiegand effect-based energy harvesting device for linear positioning measurement system,” in *2018 Asia-Pacific Magn. Rec. Conf.*, IEEE, 2019, ISBN: 9781538683781. DOI: 10.1109/APMRC.2018.8601059.
- [S38] K. Takahashi, T. Yamada, and Y. Takemura, “Circuit Parameters of a Receiver Coil Using a Wiegand Sensor for Wireless Power Transmission,” *Sensors*, vol. 19, no. 12, 2019, ISSN: 1424-8220. DOI: 10.3390/S19122710.
- [S39] FRABA B.V., *Wiegand Sensor WS-WFS-5-U0 Datasheet*, 2019. [Online]. Available: https://www.posital.com/media/posital%7B%5C_%7Dmedia/pictures%7B%5C_%7D1/wiegand/Datasheet-WS-WFS-5-U0.pdf.
- [S40] H. Sumali, E. P. Bystrom, and G. W. Krutz, “A displacement sensor for nonmetallic hydraulic cylinders,” *IEEE Sens. J.*, vol. 3, no. 6, pp. 818–826, 2003, ISSN: 1530437X. DOI: 10.1109/JSEN.2003.820333.
- [S41] J. Včelák, P. Ripka, and A. Zikmund, “Long-range magnetic tracking system,” *IEEE Sens. J.*, vol. 15, no. 1, pp. 491–496, 2015, ISSN: 1530437X. DOI: 10.1109/JSEN.2014.2345576.
- [S42] Z. Wang, M. Poscente, D. Filip, M. Dimanchev, and M. Mintchev, “Rotary in-Drilling alignment using an autonomous MEMS-based inertial unit for measurement-while-drilling processes,” *IEEE Instrum. Meas. Mag.*, vol. 16, no. 6, pp. 26–34, 2013, ISSN: 10946969. DOI: 10.1109/MIM.2013.6704968.
- [S43] Z. Liu and J. Song, “A Low-Cost Calibration Strategy for Measurement-While-Drilling System,” *IEEE Trans. Ind. Electron.*, vol. 65, no. 4, pp. 3559–3567, 2018, ISSN: 02780046. DOI: 10.1109/TIE.2017.2752149.

- [S44] S. Yang, G. Zhou, and Z. Wei, "Influence of high voltage DC transmission on measuring accuracy of current transformers," *IEEE Access*, vol. 6, pp. 72 629–72 634, 2018, ISSN: 21693536. DOI: 10.1109/ACCESS.2018.2874624.
- [S45] K. Draxler and R. Styblíková, "Demagnetization of instrument transformers before calibration," *J. Electr. Eng.*, vol. 69, no. 6, pp. 426–430, 2018, ISSN: 1339-309X. DOI: 10.2478/jee-2018-0066.
- [S46] J. Bauer, P. Ripka, K. Draxler, and R. Styblikova, "Demagnetization of current transformers using PWM burden," *IEEE Trans. Magn.*, vol. 51, no. 1, 2015, ISSN: 00189464. DOI: 10.1109/TMAG.2014.2356574.
- [S47] C. Zachariades, R. Shuttleworth, R. Giussani, and R. Mackinlay, "Optimization of a high-frequency current transformer sensor for partial discharge detection using finite-element analysis," *IEEE Sens. J.*, vol. 16, no. 20, pp. 7526–7533, 2016, ISSN: 1530437X. DOI: 10.1109/JSEN.2016.2600272.
- [S48] N. B. Narampanawe, K. Y. See, J. Zhang, E. K. Chua, and W. P. Goh, "Analysis of Ultra-Thin and Flexible Current Transformer Based on JA Hysteresis Model," *IEEE Sens. J.*, vol. 17, no. 13, pp. 4029–4036, 2017, ISSN: 1530437X. DOI: 10.1109/JSEN.2017.2705197.
- [S49] T. Yamashita, Y. Zhang, T. Itoh, and R. Maeda, "Development of thin film based flexible current clamp sensor using screen-printed coil," *Microsyst. Technol.*, vol. 22, no. 3, pp. 577–581, 2016, ISSN: 09467076. DOI: 10.1007/S00542-015-2601-9/FIGURES/10.
- [S50] K. Bohnert, A. Frank, G. Müller, *et al.*, "Fiber optic current and voltage sensors for electric power transmission systems," in *SPIE Commer. Sci. Sens. Imaging*, SPIE, 2018, ISBN: 9781510618190. DOI: 10.1117/12.2303945.
- [S51] K. Bohnert, C. P. Hsu, L. Yang, A. Frank, G. M. Müller, and P. Gabus, "Fiber-Optic Current Sensor Tolerant to Imperfections of Polarization-Maintaining Fiber Connectors," *J. Light. Technol.*, vol. 36, no. 11, pp. 2161–2165, 2018, ISSN: 07338724. DOI: 10.1109/JLT.2018.2803807.
- [S52] A. Gusarov, F. Descamps, M. Wuilpart, M. Aerssens, P. Mégret, and P. Moreau, "Influence of the optical fiber type on the performances of fiber-optics current sensor dedicated to plasma current measurement in ITER," *Appl. Opt.*, vol. 54, no. 19, pp. 5983–5991, 2015, ISSN: 2155-3165. DOI: 10.1364/AO.54.005983.
- [S53] S. Arakelyan, O. Galstyan, H. Lee, *et al.*, "Direct current imaging using a magneto-optical sensor," *Sensors Actuators A Phys.*, vol. 238, pp. 397–401, 2016, ISSN: 0924-4247. DOI: 10.1016/J.SNA.2016.01.002.
- [S54] G. Shan, D. F. Wang, and C. Xia, "Integrated piezoelectric direct current sensor with actuating and sensing elements applicable to two-wire dc appliances: theoretical considerations," *Meas. Sci. Technol.*, vol. 30, no. 2, 2019, ISSN: 0957-0233. DOI: 10.1088/1361-6501/AAF48A.
- [S55] M. H. B. Júnior, A. L. Magalhães, A. M. Bastos, *et al.*, "Piezoelectric ceramic sensor (PZT) applied to electric current measurements," *Microsyst. Technol.*, vol. 25, no. 2, pp. 705–710, 2019, ISSN: 09467076. DOI: 10.1007/S00542-018-3998-8/FIGURES/6.
- [S56] D. F. Wang, H. Liu, X. Li, *et al.*, "Passive MEMS DC Electric Current Sensor: Part II - Experimental Verifications," *IEEE Sens. J.*, vol. 17, no. 5, pp. 1238–1245, 2017, ISSN: 1530437X. DOI: 10.1109/JSEN.2016.2644722.

- [S57] J. Han, H. Hu, H. Wang, *et al.*, “Temperature-Compensated Magnetostrictive Current Sensor Based on the Configuration of Dual Fiber Bragg Gratings,” *J. Light. Technol.*, vol. 35, no. 22, pp. 4910–4915, 2017, ISSN: 07338724. DOI: 10.1109/JLT.2017.2766119.
- [S58] Z. Ding, Y. Du, T. Liu, K. Liu, B. Feng, and J. Jiang, “Distributed Optical Fiber Current Sensor Based on Magnetostriction in OFDR,” *IEEE Photonics Technol. Lett.*, vol. 27, no. 19, pp. 2055–2058, 2015, ISSN: 10411135. DOI: 10.1109/LPT.2015.2450237.
- [S59] Z. Wu, “A Wide Linearity Range Current Sensor Based on Piezoelectric Effect,” *IEEE Sens. J.*, vol. 17, no. 11, pp. 3298–3301, 2017, ISSN: 1530437X. DOI: 10.1109/JSEN.2017.2692258.
- [S60] G. Lou, X. Yu, and R. Ban, “A wide-range DC current sensing method based on disk-type magnetoelectric laminate composite and magnetic concentrator,” *Sensors Actuators A Phys.*, vol. 280, pp. 535–542, 2018, ISSN: 0924-4247. DOI: 10.1016/J.SNA.2018.08.029.
- [S61] X. Guo, X. Yu, and G. Lou, “A wide range DC current sensor based on disk-type magnetoelectric laminate composite with a feedback circuit,” in *IEEE Sensors Conf.*, IEEE, 2017, ISBN: 9781509010127. DOI: 10.1109/ICSENS.2017.8233978.
- [S62] J. Tong, Y. Jia, W. Wang, *et al.*, “Development of a Magnetostrictive FeNi Coated Surface Acoustic Wave Current Sensor,” *Appl. Sci.*, vol. 7, no. 8, 2017, ISSN: 2076-3417. DOI: 10.3390/APP7080755.
- [S63] W. Wang, Y. Jia, X. Liu, and Y. Liang, “Performance improvement of the SAW based current sensor incorporating a strip-patterned magnetostrictive FeCo film,” in *IEEE Int. Ultrason. Symp.*, IEEE, 2017, ISBN: 9781538633830. DOI: 10.1109/ULTSYM.2017.8091986.
- [S64] H. Yu, Z. Qian, H. Liu, *et al.*, “Circular Array of Magnetic Sensors for Current Measurement: Analysis for Error Caused by Position of Conductor,” *Sensors*, vol. 18, no. 2, 2018, ISSN: 1424-8220. DOI: 10.3390/s18020578. [Online]. Available: <http://www.mdpi.com/1424-8220/18/2/578>.
- [S65] A. Itzke, R. Weiss, and R. Weigel, “Influence of the Conductor Position on a Circular Array of Hall Sensors for Current Measurement,” *IEEE Trans. Ind. Electron.*, vol. 66, no. 1, pp. 580–585, 2019, ISSN: 02780046. DOI: 10.1109/TIE.2018.2826462.
- [S66] R. Weiss, R. Makuch, A. Itzke, and R. Weigel, “Crosstalk in Circular Arrays of Magnetic Sensors for Current Measurement,” *IEEE Trans. Ind. Electron.*, vol. 64, no. 6, pp. 4903–4909, 2017, ISSN: 0278-0046. DOI: 10.1109/TIE.2017.2674630.
- [S67] K.-L. Chen and N. Chen, “A New Method for Power Current Measurement Using a Coreless Hall Effect Current Transformer,” *IEEE Trans. Instrum. Meas.*, vol. 60, no. 1, pp. 158–169, 2011, ISSN: 0018-9456. DOI: 10.1109/TIM.2010.2049234.
- [S68] P. Mlejnek and P. Ripka, “AMR Yokeless Current Sensor with Improved Accuracy,” in *Proc. 30th Eurosensors Conf.*, vol. 168, Elsevier, 2016, pp. 900–903. DOI: 10.1016/j.proeng.2016.11.301.
- [S69] P. Mlejnek and P. Ripka, “Off-Center Error Correction of AMR Yokeless Current Transducer,” *J. Sensors*, vol. 2017, 2017, ISSN: 1687-725X. DOI: 10.1155/2017/6057634.
- [S70] W. Chen, H. Zhang, L. Chen, and S. Gu, “Wire-positioning algorithm for coreless Hall array sensors in current measurement,” *Meas. Sci. Technol.*, vol. 29, no. 5, 2018, ISSN: 0957-0233. DOI: 10.1088/1361-6501/AAEF0.

References

- [S71] P. Ripka, P. Mlejnek, P. Hejda, A. Chirtsov, and J. Vyhnanek, “Rectangular Array Electric Current Transducer with Integrated Fluxgate Sensors,” *Sensors*, vol. 19, no. 22, 2019, ISSN: 1424-8220. DOI: 10.3390/S19224964.
- [S72] K. Zhu, W. Han, W. K. Lee, and P. W. Pong, “On-Site Non-Invasive Current Monitoring of Multi-Core Underground Power Cables with a Magnetic-Field Sensing Platform at a Substation,” *IEEE Sens. J.*, vol. 17, no. 6, pp. 1837–1848, 2017, ISSN: 1530437X. DOI: 10.1109/JSEN.2017.2651886.
- [S73] A. Itzke, R. Weiss, T. Dileo, and R. Weigel, “The Influence of Interference Sources on a Magnetic Field-Based Current Sensor for Multiconductor Measurement,” *IEEE Sens. J.*, vol. 18, no. 16, pp. 6782–6787, 2018, ISSN: 1530437X. DOI: 10.1109/JSEN.2018.2849510.
- [S74] Y. Kuwabara, K. Wada, J. M. Guichon, J. L. Schanen, and J. Roudet, “Implementation and Performance of a Current Sensor for a Laminated Bus Bar,” in *IEEE Trans. Ind. Appl.*, vol. 54, IEEE, 2018, pp. 2579–2587. DOI: 10.1109/TIA.2018.2796538.
- [S75] J. Wang, D. Si, T. Tian, and R. Ren, “Design and Experimental Study of a Current Transformer with a Stacked PCB Based on B-Dot,” *Sensors*, vol. 17, no. 4, 2017, ISSN: 1424-8220. DOI: 10.3390/S17040820.
- [S76] J. Wu, Z. Chen, C. Wang, and L. Hao, “A Novel Low-Cost Multicoil-Based Smart Current Sensor for Three-Phase Currents Sensing of Overhead Conductors,” *IEEE Trans. Power Deliv.*, vol. 31, no. 6, pp. 2443–2452, 2016, ISSN: 08858977. DOI: 10.1109/TPWRD.2015.2402284.
- [S77] G. Geng, J. Wang, K. L. Chen, and W. Xu, “Contactless Current Measurement for Enclosed Multiconductor Systems Based on Sensor Array,” *IEEE Trans. Instrum. Meas.*, vol. 66, no. 10, pp. 2627–2637, 2017, ISSN: 00189456. DOI: 10.1109/TIM.2017.2711898.
- [S78] K. Hasegawa, S. Takahara, S. Tabata, M. Tsukuda, and I. Omura, “A new output current measurement method with tiny PCB sensors capable of being embedded in an IGBT module,” *IEEE Trans. Power Electron.*, vol. 32, no. 3, pp. 1707–1712, 2017, ISSN: 08858993. DOI: 10.1109/TPEL.2016.2606111.
- [S79] C. Hewson and J. Aberdeen, “An improved Rogowski coil configuration for a high speed, compact current sensor with high immunity to voltage transients,” in *IEEE Appl. Power Electron. Conf.*, IEEE, 2018, pp. 571–578, ISBN: 9781538611807. DOI: 10.1109/APEC.2018.8341069.

